Small Molecule Organic Acceptors: Relating Chemical Structure with Thin Film Device Performance

Helen Bristow

University of Oxford

A thesis submitted for the degree of
Doctor of Philosophy

January 2022

Abstract

The development of the class of small molecule organic semiconductors typically referred to as non-fullerene acceptors (NFA), has led to a resurgence of research interest on the topic of organic photovoltaic (OPV) devices, in which they have replaced fullerene derivatives as the electron acceptors of choice. This thesis contributes to understanding the relationship between the chemical structure of these small molecule organic semiconductors, their physical properties, optoelectronic properties, and performance in organic electronic thin film devices. A better understanding of this relationship is required to direct the development of novel small molecule organic semiconductors.

In the first part of this thesis the impact of aliphatic side chains on NFA intermolecular packing and mobility is investigated. The NFA O-IDTBR, which has been widely used in OPV applications, is also found to be a good candidate for organic thin film transistor (OTFT) applications. The high mobility of over 0.4 cm^2 V^{-1} s^{-1} achieved in OTFTs operating in the saturation regime is attributed to O-IDTBR's packing motif in the solid state.

In the second part of the thesis further chemical structure modifications to O-IDTBR's conjugated push-pull donor-acceptor structure as well as its aliphatic side chains are investigated. Through these structural modifications, the unique properties that the combination of the specific conjugated chromophore and octyl side chains present in O-IDTBR have given the material, allowing it to deliver high mobilities in OTFTs, are highlighted.

The third part of this thesis focuses on organic photodetectors (OPD), a relatively recently explored application for NFAs. Very little is currently known about the impact of OSC chemical structure on OPD performance metrics. In particular, achieving a low dark current at reverse bias has been a major limitation to the development of OPD technology. Two new blends based on NFAs for OPDs, PTQ10:O-FBR and PTQ10:O-IDTBR, are identified as delivering low dark current densities at reverse bias, resulting in high specific detectivities of over 10^{12} Jones.

The final part of the thesis focuses on NFAs with chemical structures tuned to allow absorption in the NIR region. Whilst OPVs were originally touted as a low-cost alternative to other solar cell technologies, the reduction in the cost of manufacturing silicon based solar panels has meant that, for OPV to realise its market potential, other advantages over competing solar technologies need to be exploited. One such application is transparent and

semi-transparent photovoltaics for which near-infra red (NIR), or specifically visible blind, NFAs are being developed. Similarly, a key OPD application is for detectors targeting NIR absorption, which have uses in biomedical imaging, substance identification and optical communications. The final results chapter explores the properties of several NIR absorbing NFAs and their application in both OPV and OPD applications.

Acknowledgements

First, I would like to thank my supervisor Prof. Iain McCulloch for giving me the opportunity to work in his group, his support and trust. I have learnt so much from working in your group and with your collaborators and am grateful for all the opportunities working for you has afforded me.

Thanks so much to Dr. Nicola Gasparini for initiating the photodetector work at Imperial and from who I learnt a great deal, it was a pleasure to work with you on this. I would also like to thank Prof. James Durrant, and especially his research group, thank you for inviting me into your research family, this has been a constant source of support for me over these years. In particular, I must thank Dr. Pabitra Shakya Tuladhar for her constant support of myself as well as all of the students in the Durrant group and that use the cleanroom at the MSRH.

Over the course of my PhD I have had the opportunity carry out research in several different laboratories and I would like to thank everyone I was lucky enough to meet, learn from and work alongside in RCS1 and the clean room in South Kensington; the AMD lab in Physics at Imperial; the cleanroom in MSRH; the B-lab in Physics at Oxford; the chemistry labs in Oxford; and the KAUST Solar Centre.

I am grateful to everyone who was with me at the start of my PhD and everyone who is here at the end. Your support, good advice, and constant kindness have made this possible for me. Most of all I am thankful to the members of the McCulloch group, past and present who have supported and taught me so much throughout my PhD.

Abbreviations

AC	As cast
AFM	Atomic force microscopy
Ag	Silver
Al	Aluminium
Au	Gold
BHJ	Bulk heterojunction
BT	2,1,3-benzothiadiazole
CB	Chlorobenzene
CV	Cyclic voltammetry
D*	Specific Detectivity
D-A	Donor-acceptor
DSC	Differential scanning calorimetry
DFT	Density functional theory
DOS	Density of states
DPO	Phen-NaDPO; 3-[6-(diphenylphosphinyl)-2-naphthalenyl]-1,10-Phenanthroline
EA	Electron affinity
E_g	Bandgap
EQE	External quantum efficiency
eV	Electron-volt
FF	Fill factor
GIWAXS	Grazing incidence wide angle X-ray scattering
HOMO	Highest occupied molecular orbital
IDT	Indacenodithiophene
i_n	Noise current
IP	Ionisation potential
ITO	Indium tin oxide
J_e	Electron transfer integral
J_{sc}	Short circuit current density
J_{mp}	Current density at point of maximum power
LE-IPES	Low energy inverse photoemission spectroscopy
LUMO	Lowest unoccupied molecular orbital
MoO_x	Molybdenum oxide

NFA	Non-fullerene acceptor
NIR	Near Infra-red
OPD	Organic photodetector(s)
OPV	Organic photovoltaic(s)
OSC	Organic semiconductor
OTFT	Organic thin film transistor
PC60BM	Phenyl-C61-butyric acid methyl ester
PC70BM	Phenyl-C71-butyric acid methyl ester
PCE	Power conversion efficiency
PESA	Photoelectron spectroscopy in air
PCE10	PTB7-Th; Poly[4,8-bis(5-(2-ethylhexyl)thiophen-2-yl)benzo[1,2-b;4,5-b']dithiophene-2,6-diyl-alt-(4-(2-ethylhexyl)-3-fluorothieno[3,4-b]thiophene-)-2-carboxylate-2-6-diyl)]
PDI	Perylene diimide
PDINO	2,9-Bis[3-(dimethyloxidoamino)propyl]anthra[2,1,9-def:6,5,10-d'e'f']diisoquinoline-1,3,8,10(2H,9H)-tetrone
PEDOT:PSS	Poly(3,4-ethylenedioxythiophene) polystyrene sulfonate
PEI	Polyethylenimine
PM6	PBDB-T-2F; Poly[(2,6-(4,8-bis(5-(2-ethylhexyl-3-fluoro)thiophen-2-yl)-benzo[1,2-b:4,5-b']dithiophene))-alt-(5,5-(1',3'-di-2-thienyl-5',7'-bis(2-ethylhexyl)benzo[1',2'-c:4',5'-c']dithiophene-4,8-dione)]
P_{in}	Incident light power density
R	Responsivity
SVA	Solvent vapour annealed
TA	Thermally annealed
$TBAPF_6$	Tetrabutylammonium hexafluorophosphate
T_{cc}	Cold crystallisation temperature
THF	Tetrahydrofuran
Tm	Melting temperature
UPS	Ultraviolet photoelectron spectroscopy
UV	Ultraviolet
V_{mp}	Voltage at point of maximum power
V_{oc}	Open circuit voltage
XRD	X-ray diffraction
ZnO	Zinc oxide

Table of Contents

Chapter 1: Introduction

1.1 Organic Electronics

Organic semiconductors have several advantages over their inorganic counterparts for next generation technologies and have already found commercial success in organic light emitting diodes (OLEDs), a several billion dollar industry in 2018.[1] The possibility to process OSCs with low-cost, low-temperature deposition techniques, such as roll-to-roll printing, means they are compatible with flexible substrates. The ability to tune the colour of and even produce transparent electronic devices, which at the same time exhibit mechanical flexibility and are light weight offers a range of exciting opportunities for OSCs, such as wearable electronic sensors, biometric monitoring, visibly transparent photovoltaics and conformable displays.[2] Organic thin film transistors (OTFTs), now demonstrate mobilities exceeding amorphous silicon, making them viable candidates for the backplanes of liquid crystal displays.[1] Solar cells based on OSCs, organic photovoltaics (OPVs), are lightweight and free of toxic elements. Recently, thanks to the development of so called non-fullerene acceptors, on which this thesis focuses, OPV has seen a resurgence in research and commercial interest.[3] The tunability of the absorption of organic semiconductors is exciting for organic photodetector (OPD) applications, as is the potential to use materials which absorb in the near-infra red to generate low-cost alternatives to inorganic photodetectors.[4] Colour selective responsivity, without the need to introduce filters is also possible with the correct selection of OSC materials.[5] On top of this there is also interest in using OPDs in conjunction with silicon based detectors to achieve high resolution imaging.[6] Light weight and flexible near infra-red responsive OPDs, have a variety of applications in biomedical monitoring and imaging.[7,8]

This diversity of OSC applications has generated a huge library of OSC materials. To better understand what makes good OSC materials for each application, the relationship between chemical structure, materials properties and device performance must be investigated intensively.

1.2 Organic Semiconductors

1.2.1 Fundamentals of Organic Semiconductors

The overlap of atomic orbitals from adjacent atoms in a molecule results in a splitting of energy levels and the formation of molecular orbitals. For a crystalline lattice or amorphous

solid, where a very large number of bonded atoms are present, this splitting results in a very large number of levels, which are close in energy and effectively form a continuum of states, commonly referred to as bands. The highest occupied band is known as the valence band and the lowest unoccupied band is known as the conduction band. Partial filling of the valence band or overlap of the conduction and valence bands are present for metals. Therefore, in metals, states with similar energy levels are readily available allowing facile excitation of charge carriers into empty states.

In semiconductors, there is a gap in energy between the full valence band and empty conduction band, known as a band gap.[9] Semiconducting materials typically possess band gaps of 0.5 – 3 eV.[10] For example, the inorganic semiconductors silicon, germanium and gallium arsenide have band gaps of 1.1 eV, 0.67 eV and 1.4 eV respectively.[11] Semiconductors have a limited conductivity in the dark at room temperature as few charge carriers will have enough energy to be thermally excited across the band gap. Meanwhile, electrically insulating materials possess an even larger band gap and so thermalisation of charge carriers across the band gap will be negligible.

In contrast, organic semiconductors (OSC) are conjugated molecules and polymers which do not possess the same long-range order as inorganic crystalline and amorphous solids. Organic molecules and polymers are made up of covalently bonded carbon and hydrogen atoms, which also often include various heteroatoms. As well as being carbon based, OSCs also exhibit semiconducting properties. There is a gap in energy between the frontier molecular orbitals of OSC polymers and molecules. This gap is due to the delocalised π electron system present in conjugated molecules, which results from the overlap of $2p_z$ orbitals from sp_2 hybridised carbon atoms.[11] This hybridisation of the $2p_z$ orbitals from sp_2 hybridised carbon atoms to give the frontier molecular orbitals of ethene and 1,3-butadiene is illustrated in figure 1. The highest occupied molecular orbital (HOMO) and lowest unoccupied molecular orbital (LUMO) are the frontier molecular orbitals of the individual organic semiconductor molecule/polymer. The specific chemical structures of OSC molecules and polymers will define their band gaps. By making slight modifications to the chemical structures, for example by adding electron withdrawing substituents, the band gaps and frontier molecular orbitals of the OSCs can be tuned.

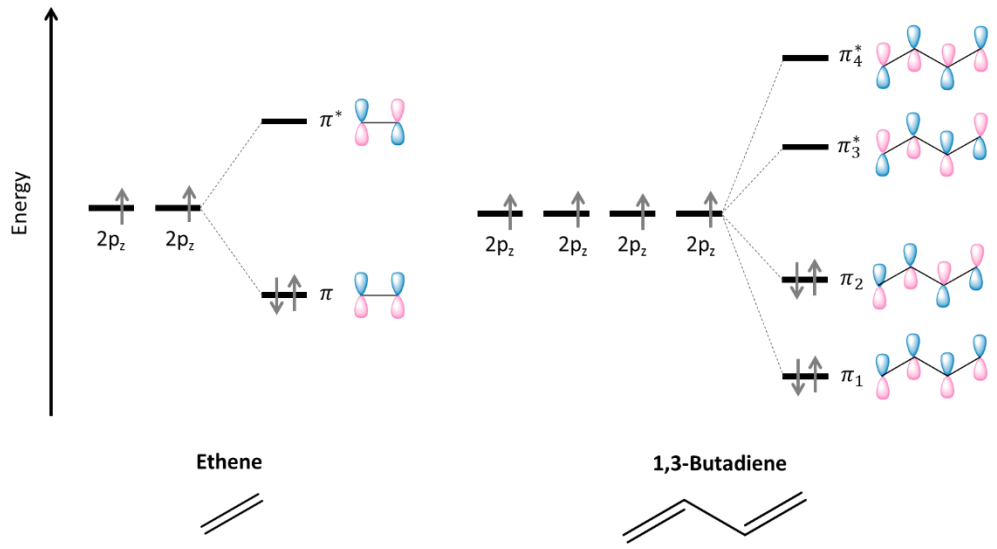

Figure 1| Illustrating hybridisation of sp_2 hybridised carbon atom $2p_z$ orbitals to give the bonding (π) and antibonding (π^*) molecular orbitals for ethene and 1,3-butadiene.

Discussing organic semiconductors in terms of orbital theory does not account for interactions between molecules/polymers in the solid state. The relatively weak intermolecular interactions between neighbouring organic semiconductor molecules, compared with covalently bonded inorganic semiconducting solids, results in weak delocalisation of orbitals across molecules. This has direct implications for charge transport in organic semiconductors. Despite the differences between covalent solids and molecules/polymers in the solid state, often band theory is applied to organic semiconductors with the HOMO and LUMO being approximated as the valence and conduction band, respectively.[11]

1.2.2 Excitations in Organic Semiconductors

The excited states of organic semiconductors can either be electrically or optically induced. The injection of charges, either holes or electrons, results in the formation of radical ions termed hole polarons and electron polarons respectively. Following the addition or removal of charge a redistribution in the molecular configuration to minimize energy occurs. Polarons are the combined charge and associated distortion of bond lengths and nuclear positions.[11] The new energy levels of the polarons exist within the HOMO-LUMO gap. Polarons, both the charge and associated molecular distortion, move through the OSC material.

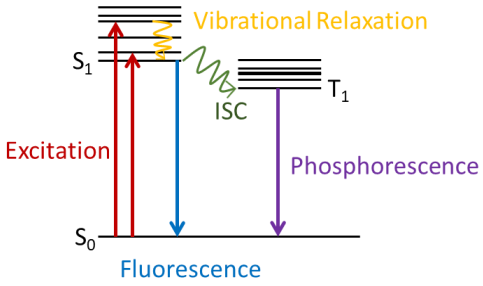

Figure 2| Simplified Jablonski diagram illustrating optical excitation from the ground state (S_0) to singlet excited state (S_1) and pathways for radiative decay back to the ground state via fluorescence or via intersystem crossing (ISC) to the triplet excited state (T_1) followed by phosphorescence to the ground state.

The electronic states of an OSC and transitions between them, for example optical excitation, can be demonstrated using a Jablonski diagram as in figure 2. On absorption of light, with appropriate energy, electrons are promoted across the band gap of the OSC, forming an exciton.[12] In contrast to the charge separated polaron states of injected carriers, excitons are coulombically bound electron and hole pairs. In organic semiconductors excitons are further stabilised relative to polarons due to the coulombic binding energy between the hole and electron as well as stabilising molecular lattice distortions. Excitons can also be formed from the combining of electrically injected polarons.

For inorganic semiconductors after photoexcitation, excitons are easily separated into charge separated polarons, this is due to the high relative dielectric permittivity (ε_r) of inorganic semiconductors, which screens charges from each other over relatively short distances. A typical inorganic semiconducting would have a ε_r of around 14.[13] In contrast, OSCs have much lower ε_r of around 2 – 4.[13,14] Therefore, in OSCs, dielectric screening of the charges is less than in inorganic semiconductors and excitons require an extra driving force to overcome the coulombic binding energy and dissociate into charge separated states.

1.2.3 Charge Transport in Organic Semiconductors

A key metric used to describe charge transport in a semiconductor is mobility, which is the velocity of charge carriers under an electric field and has units $cm^2\ V^{-1}\ s^{-1}$.[15] In the absence of an electric field charge transport in OSCs is purely diffusive. When an electric field is applied, a drift component will be introduced, which will dominate charge transport in the OSC. Charge carrier mobility in OSCs is dependent on many factors including temperature, intermolecular packing, impurities, electric field strength and charge carrier density.[16]

Whilst mobility is often treated as a material property, the mobility determined depends strongly on the method used to determine it.

There are several models used to describe charge transport in OSCs. For single crystals of OSC, which exhibit a relatively low degree of structural disorder and strong intermolecular interactions between the small molecule OSCs within the crystals, relatively high mobilities have been observed of up to 20 $cm^2 V^{-1} s^{-1}$.[1] These high mobilities can be explained by transient localisation models, in which "band-like" charge transport is considered.

Another model commonly used to describe charge transport in OSCs is multiple trapping and release.[17] Typically this model is used to describe OSCs with an observed microstructure consisting of crystalline domains separated by amorphous grain boundaries. This model has been used successfully to describe the observed temperature dependence of mobility, for example, in transistors based on the polymer PQT-12.[18] When charge carriers move between states they will be retained on that site for an amount of time after which they may be released to a new site or recombine with a charge carrier of opposing polarity. In the multiple trapping and release model, localised states which lie below the mobility edge will act as charge traps, retaining the charges before releasing them into higher energy mobile states. Trap sites are classed as shallow or deep depending on the retention time of charges.[11]

Most OSCs are disordered to the extent that charge carriers become highly localised, onto individual molecular sites, and in this case charge transport within such systems can be best described by a thermally activated hopping model. Hopping models for charge transport in OSCs build on the premise that charges hop between localised states. Such models have been used to explain mobilities of up to 0.5 $cm^2 V^{-1} s^{-1}$.[1] The distribution of energetic sites within the material results from anisotropy of local polarization and takes a gaussian shape, known as the density of states (DOS).[17] This disorder induced distribution of energetic levels is observed experimentally through the relatively broad optical spectra produced by OSCs.[19] The disorder in OSCs constitutes both variations in the energy of localised sites or in site position/separation, termed diagonal and off-diagonal disorder respectively.[16]

1.3 Organic Photovoltaics

1.3.1 Organic Photovoltaic Devices

Photovoltaics based on organic semiconductors were originally developed as low-cost, lightweight, and flexible alternatives to solar cell technologies based on inorganic

semiconductors. Significant improvements in the power conversion efficiencies achievable by this technology have been made in recent years, largely driven by the development of novel organic semiconductor materials. However, since the first development of organic photovoltaics (OPVs) the price of crystalline silicon based solar cells has significantly decreased, making OPV less of a cost competitive technology compared with established technologies than originally predicted.[20] In addition, other third generation light weight and solution processable photovoltaic technologies, such as lead based perovskites, have emerged.[21,22] Despite this, OPV still retains some critical advantages over these alternative technologies for specific applications such as indoor light harvesting and visibly transparent solar cells.[23,24]

One application where OPV can potentially dominate is in indoor photovoltaics.[25] The Internet of Things (IoT) is lauded as the future for technology. In the future numerous electronic devices in our homes and offices will be interconnected, key to this is that the devices will be off grid and being able to produce their own power, i.e. containing a solar panel is key to this. The aesthetic appeal of OPV is desirable for these types of products as well as their low weight and mechanical flexibility. The emission spectra of indoor lighting, fluorescent lamps and LEDs, is different to solar reference air mass 1.5 (AM1.5G) irradiance and the absorption of OSCs can be tuned to make OPVs matching this emission.[25]

The tunability of the absorption of organic semiconductors also means visibly transparent materials, able to absorb light in the near infra-red (NIR) or ultra-violet (UV) region can be synthesised. Visibly semi-transparent or transparent OPVs based on blends of these materials are desirable for building integrated photovoltaics and have been highlighted as particularly promising for greenhouse applications where the materials can be tuned to absorb outside of the wavelengths necessary for crop growth.[26,27]

Whilst many discount OPV due to the maturity of competing technologies the significant progress made over the course of this PhD, with record power conversion efficiencies (PCEs) jumping from 13 % in 2017 to over 18 % in 2021,[28,29] illustrates that there is still promise in this technology.

1.3.2 Organic Photovoltaic Operation

On photoexcitation of an OSC excitons form, which must overcome coulombic attraction in order to dissociate into free charge carriers and subsequently be extracted from the OPV.[30] In OPVs typically two OSC materials are used to facilitate this separation of

excitons into free charge carriers, known as a donor and acceptor material. The dissociation of photogenerated excitons into free charge carriers occurs at the physical interface between the donor and acceptor. At the interface excitons are separated though a charge-transfer state. The reduced free energy of the charge-transfer state relative to the exciton will drive this charge transfer process. From the charge-transfer state the electron and hole are further separated to form charge separated states. The charge separated hole and electron polarons will then be extracted at opposite electrodes.

To maximise the number of excitons which reach the donor:acceptor interface before recombining, an intermixed blend morphology, known as a bulk heterojunction (BHJ) is used. This BHJ active layer is sandwiched between the cathode, anode and other interlayers which assist charge extraction from the device as illustrated in figure 3.

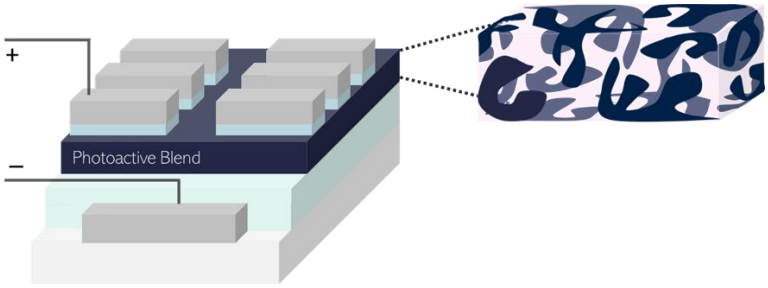

Figure 3| Illustration of an OPV stack containing a BHJ blend photoactive layer sandwiched between electrodes and interlayers.

Photovoltaic cells are designed to deliver electrical power from light irradiation, ideally delivering high power outputs over small surface areas. Power density is the product of current density and voltage extracted from the photovoltaic cell. The maximum voltage of the cell is achieved under open-circuit conditions (V_{oc}), where no current passes through the illuminated OPV as illustrated in figure 5. The short circuit current density (J_{sc}) is the current per unit area at short-circuit, which is when no voltage is applied to the device. Finally, the fill factor (FF) gives an idea of the squareness of the current-voltage characteristics and is related to the recombination and other processes in the device. The FF is the ratio of the maximum power output of the device, given at the max power point as illustrated in figure 5, to the theoretical maximum power output given by the product of J_{sc} and V_{oc}, equation 1.

$$FF = \frac{P_{max}}{P_T} = \frac{J_{max}V_{max}}{J_{sc}V_{oc}} \quad (1)$$

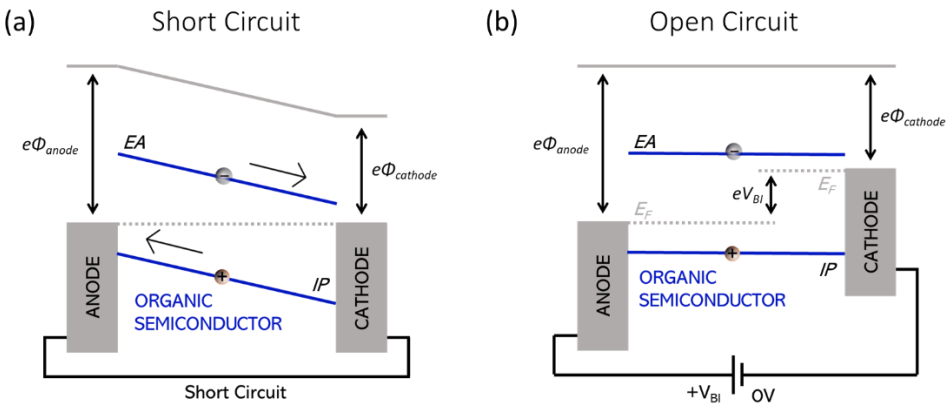

Figure 4| A simplified energy level diagram illustrating the shift in energy levels for a diode under illumination biased at (a) short circuit and (b) open circuit conditions.

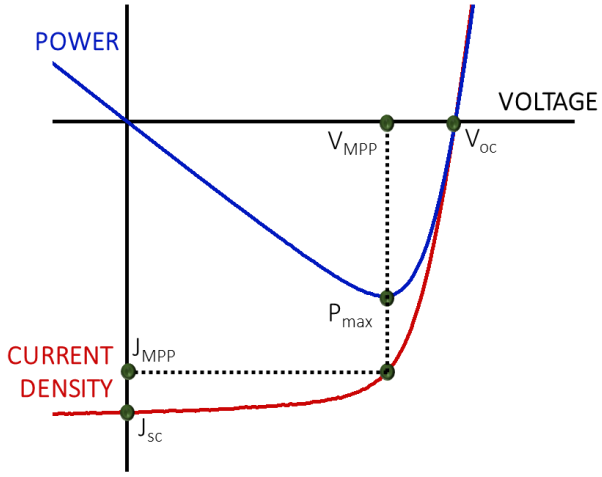

Figure 5| Diagram illustrating the current density – voltage (JV) characteristics of a solar cell. The short circuit current density (J_{sc}), open circuit voltage (V_{oc}), maximum power (P_{max}), current density at maximum power point (J_{MPP}) and voltage at maximum power point (V_{MPP}) are labelled.

The figure of merit for OPV operation is the power conversion efficiency (PCE), which is the ratio of maximum power output (P_{max}) from the photovoltaic cell to the incident power as in equation 2, which combines the short circuit current density (J_{sc}), open circuit voltage (V_{oc}) and fill factor (FF). The power output of an OPV will depend on the incident light source. The solar spectrum varies between geographical locations and with the time of day as well as year.

To allow comparison between research groups standard reporting to a predefined spectrum and intensity is needed, in most cases the AM1.5G spectrum is used for this. The AM1.5G standard reference spectrum was developed as a reasonable average condition, representing the terrestrial spectral irradiance through the atmosphere accounting for the fact the sun is most often not directly overhead and instead is at an angle to the earth's surface.

$$\frac{PCE}{100} = \frac{P_{max}}{P_{in}} = \frac{J_{SC}V_{OC}FF}{P_{in}}$$

(2)

1.3.3 Organic Photovoltaic Materials

The use of a mixed donor and acceptor blend active layer known as a bulk heterojunction (BHJ) was a huge breakthrough in OPV research giving power conversion efficiencies (PCEs) just over 3 %.[31,32] In particular, fullerenes and their derivatives were shown to be excellent electron accepting materials and combined with electron donating polymers in early OPV devices.[11] Over 10 years later replacement of these fullerene derivatives with so called non-fullerene acceptors (NFAs) lead to a resurgence of interest in the OPV field with PCEs over 14 % being realised.[33–35] Most recently, the development of the so called Y-series acceptors has led to OPVs with power conversion efficiencies over 18%.[36,37]

Fullerene Acceptors

To properly understand the emergence of the class of materials commonly referred to as non-fullerene acceptors, first fullerene-based acceptors are discussed. Buckminster fullerenes (C_{60}) are a hollow spherical allotrope of carbon which can undergo multiple reductions making them good candidates as acceptors for OPVs. Fullerenes themselves such as C_{60} are insoluble and therefore fullerene derivatives such as $PC_{60}BM$ and $PC_{70}BM$ (figure 6) were favoured for solution processed OPVs.[38,39] Charge transport in solid state fullerenes is isotropic, which is beneficial for OPVs in allowing efficient percolation of charges to the contacts independent of the materials orientation in the BHJ blend film.[40,41] Fullerene derivatives also have a propensity to form an optimal BHJ morphology for maximising power conversion efficiency and stability, with a variety of donor polymers.[42] The optimal morphology of the BHJ will vary depending on the specific OSCs used. Fullerene derivative based BHJs have been found to exhibit poor morphological stability. The fullerenes have been shown to aggregate resulting in phase segregation of the donor and acceptor material and leading to a degradation in OPV performance.

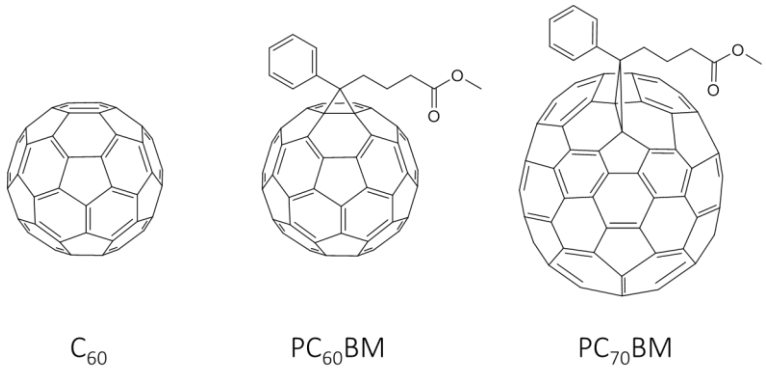

Figure 6| Chemical structure of the fullerene C_{60} and the fullerene derivatives $PC_{60}BM$ and $PC_{70}BM$, commonly used as electron accepting materials in OPVs.

OPVs based on a PffBT4T-2OD:$PC_{70}BM$ blend have achieved PCEs over 10 %, accompanied by notably high FFs over 70%.[43] One of the best understood material combinations for OPV applications is P3HT:$PC_{60}BM$ for which PCEs up to 5 % have been reported.[44]

A key attractive feature of fullerene derivates for use as acceptors in OPVs was their high electron mobilities. A high electron mobility helps to minimise efficiency losses by ensuring efficient charge separation and transport to the contacts. In this way recombination is minimised.[45] $PC_{60}BM$ has been determined to have an electron mobility of 10^{-3} cm^2 V^{-1} s^{-1} from analysing space-charge limited currents (SCLC) in single carrier diodes.[46–48] Electron mobilities of 0.1 cm^2 V^{-1} s^{-1} for $PC_{60}BM$ and 0.21 cm^2 V^{-1} s^{-1} for $PC_{70}BM$ have also been reported in OTFTs.[49]

Values reported for the EA of $PC_{60}BM$, determined using CV, range from 3.62 eV to 4.38 eV.[50] For $PC_{60}BM$ IP values around 5.0 eV are usually reported.[39,51,52] Synthetic modification can be used to tune the energetic properties of OSCs. However, possibilities for the synthetic modification of fullerenes are limited. This also restricts tuning of solubility and absorption.[38]

Other drawbacks to using fullerene derivatives as acceptors include their relatively high synthetic cost compared to other organic materials and complicated purification techniques.[53–55] They exhibit photo-instability in air and morphological instability in BHJ films.[41,56–58] PCBM blends have been shown to exhibit a reduction in performance over the first few hours of operation known as “Burn In”. OPVs based on a PffBT4T-2OD:$PC_{70}BM$ blend have been shown to exhibit a 20 % decrease in PCE over 60 hours of light soaking. This loss in performance was attributed to the formation of photoinduced trap states.[59]

As a result of the symmetrical nature of C_{60}, it exhibits many symmetry disallowed optical transitions. Therefore, $PC_{60}BM$ absorbs poorly in the visible region, with a molar extinction of only 4,900 mol^{-1} cm^{-1} at a peak wavelength of 400 nm in toluene.[60] C_{60} and its derivatives therefore have much weaker visible light absorption compared with most donor polymers. This means that, using a high ratio of fullerene based acceptor to donor can negatively impact absorption of the blend and thereby photocurrent generation.[48] C_{70} is less symmetrical than C_{60} and therefore $PC_{70}BM$ absorbs visible light better, however, this absorption is still limited to a molar extinction coefficient of 21,000 mol^{-1} cm^{-1} at a peak wavelength of 470 nm. Attempts to design fullerene derivatives with enhanced absorption of visible light have been made, for example the synthesis of $PC_{84}BM$.[60] However, the high synthetic cost of these acceptors is still a drawback. Absorption of OPV acceptors at longer wavelengths in the visible and infra-red region of the solar spectrum is also beneficial as these regions are more spectrally intense.[54,61]

Non-fullerene Acceptors

As discussed, replacement of fullerene derivatives as the acceptor of choice in OPVs was originally considered desirable due to their high synthetic costs, photo-instability in air, morphological instability in BHJ blend films and limited contribution to photocurrent generation.[41,56–58] The replacement materials, commonly referred to as non-fullerene acceptors (NFAs), were originally touted as low-cost alternatives to acceptors derived from fullerenes which would also deliver comparable performance. State of the art NFAs now consistently outperform PCBM as acceptors in BHJ OPVs.

Initially a variety of electron deficient chemical moieties were investigated as the basis for NFAs including perylenediimide (PDI), subphthalocyanine and diketopyrrolopyrrole .[58,62–64] The most successfully molecular design strategy was found to be combining electron rich and deficient units in a fused rod-like Acceptor-Donor-Acceptor (A-D-A) type of structure with pendant solubilising groups on the electron donating core leaving the terminal electron accepting units available for intermolecular pi stacking and charge transfer.[65] Research has predominantly focused on the development of these rod-like NFAs and it is with this style of NFA molecule that the best PCEs have been achieved.[36,37]

The motivation for developing NFAs with A-D-A structures was to obtain acceptors with a significantly enhanced contribution to photocurrent generation compared with PCBM.[65] Push-pull hybridisation between electron rich and deficient units in OSCs results in a narrowing of their band gap. By narrowing the band gap the absorption of NFAs is pushed towards the infra-red region which is more spectrally intense.[66] Strongly absorbing dyes

such as rhodanine were also chosen as the electron accepting units based on the premise that they would enhance light absorption.[54,65] Solubilising groups attached to the donor core leave the acceptor units available to facilitate exciton dissociation and intermolecular charge transfer. An A-D-A structure is synthetically versatile allowing variation of the donor and acceptor units as well as their synthetic modification to tune the band gap, frontier molecular orbitals and crystallinity of the acceptors.

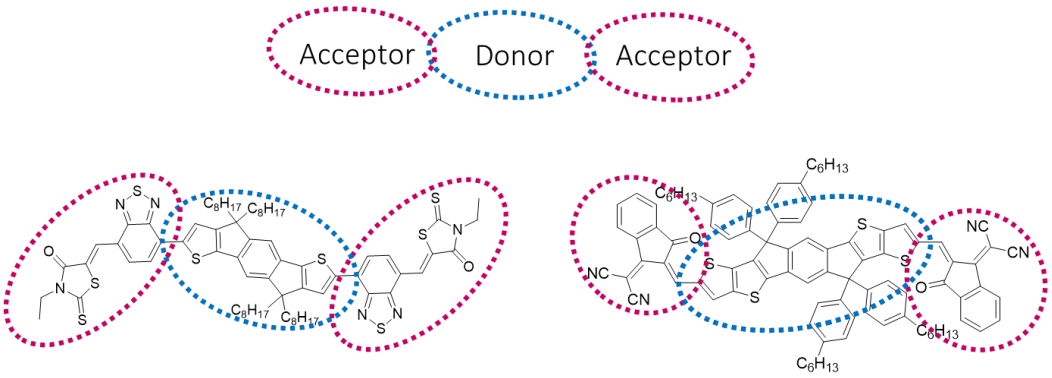

Figure 7| Illustrating the Acceptor-Donor-Acceptor structure of the typical non-fullerene acceptors O-IDTBR and ITIC.

Indacenodithiphene (IDT) and indacenodithieno[3,2-*b*]thiophene (IDTT) donor cores are common to many NFAs.[33,34] When first reported the early developed NFAs, O-IDTBR and EH-IDTBR both delivered impressive PCEs over 6 % when combined with the donor polymer P3HT. Since then over 10 % PCEs have been achieved with a variety of other donor polymers.[61,67,68] ITIC (figure 8) is another rod-like A-D-A NFA which has been widely investigated and has also delivered PCEs over 10 % in BHJ OPVs.[40] The structure contains a planar IDTT core flanked by 2-(3-oxo-2,3-dihydroinden-1-ylidene)-malononitrile acceptor units. When first reported ITIC yielded a PCE of 6.8 % when combined with the narrow band gap donor polymer PTB7-Th. The photovoltaic parameters for these devices were a V_{oc} of 0.81 V, FF of 0.59 and J_{sc} of 14.21 mA cm^{-2}.[69] In 2016 ITIC was combined with PBDB-T, which has a wider band gap and therefore complementary absorption, to give a PCE of 10.68 %.[40] This high performance at the time of publication can be linked to the impressively high FF of 75 %. Before the development of the Y-series of NFAs, Y6 being first published in 2019, a significant amount of the progress made in pushing up the power conversion efficiency of OPVs resulted from synthetically modifying the ITIC chemical structure.[69] Some of the ways ITIC has been modified include halogenation, changing the solubilising groups and extending the donor core.[28,33,34,42,70,71] The highest OPV efficiencies are currently achieved with the Y-series of

acceptors, in particular structural derivatives of Y6 (figure 8).[36,72] The highest OPV PCEs reported to date in 2021 now exceed 18 %.[29]

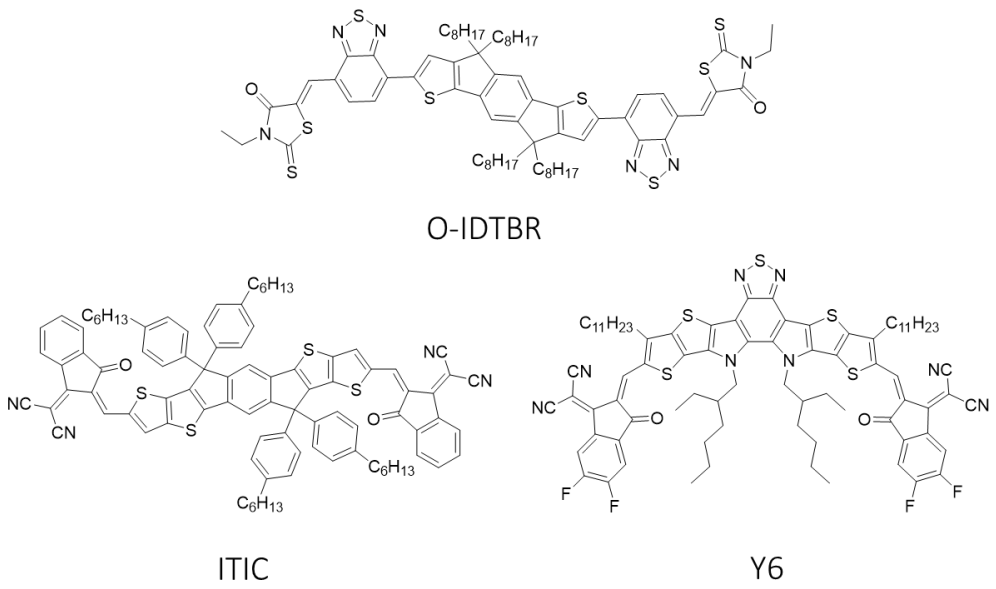

Figure 8| Chemical structures of the non-fullerene acceptors O-IDTBR, ITIC and Y6.

1.3.4 Charge Transport of Organic Photovoltaic Materials

Charge transport properties of NFAs are usually measured in bulk heterojunction blends where the NFAs are combined with an electron donating polymer. It is well established that the electron donating and accepting materials within these blends must have high and balanced charge carrier mobilities to effect efficient charge percolation within the active layer and charge extraction at the contacts. This is especially true for systems with a high density of tail states which act as charge traps, as is the case for most NFA based blends.[73,74] Therefore, understanding the relationship between chemical structure and charge transport is important for directing the development of improved OPV acceptors.

Charge extraction at linear increasing voltage (CELIV), in particular photo-CELIV, in which charge carriers photogenerated in an OPV held at open circuit are extracted by a linear voltage sweep, is widely used to analyse the bulk carrier mobility of OPV blends. This has benefits as the charge carriers are photogenerated and mobility is determined directly in the OPV device. However, for performing a comparison of NFA mobilities a technique which determines the mobility of a single component rather than a blend is preferable.

Charge transport properties of neat NFAs have predominantly been discussed in terms of space charge limited current (SCLC) mobilities. SCLC mobilities are usually calculated by

applying the Mott-Gurney law or one of its derivatives to the current-voltage characteristics of single carrier diodes. However, several studies have highlighted problems with this method of analysis when applied to organic semiconductors.[75–77] Problems include the requirement for ohmic contacts and for the semiconductor to be trap free. These conditions are not the practical reality for organic semiconductors and SCLC analysis has been shown to lead to mobility underestimations.[76,77] Another problem is that the intermediate voltage regime of single carrier diode current-voltage characteristics, which the Mott-Gurney equation is applicable to, is not always observed. Mobility extracted using SCLC analysis also depends on device architecture and active layer thickness. This dependence was highlighted in an inter-laboratory study comparing SCLC analysis of the same organic semiconductor across several research groups where differences in mobility over several orders of magnitude were obtained.[75] More concerningly, in the same work it was found that even when the groups were provided with the same raw data, the mobilities they calculated differed significantly.[75]

Another technique for determining mobility is time of flight (ToF). One drawback of ToF is that it requires film thicknesses of around a micron. For neat NFAs such thicknesses are not always achievable, mainly due to low solution viscosities for deposition. In a study comparing ToF mobilities of NFAs, the authors were unable to achieve thick enough O-IDTBR films and therefore only blend mobilities could be compared.[78] In this thesis the performance of NFAs in OTFTs will be explored.

1.4 Organic Thin Film Transistors

1.4.1 Organic Thin Film Transistor Devices

OSCs possess several desirable qualities for application in transistors, most notably the fact they can be processed at low temperatures using printing methods, making them compatible with plastic substrates. This contrasts with traditional inorganic, typically silicon, based transistors which are inflexible. Research into organic thin film transistors (OTFTs), commonly also referred to as organic field effect transistors, began in the 1980s.[79] As a result, understanding of the operation of OTFTs and their proper analysis are well understood compared with other emerging OSC technologies. A key parameter used to define how well a transistor performs is its mobility, which dictates how quickly the transistor can switch on and off. In this case, mobility is dependent on both the intrinsic charge transport properties of the organic semiconductor used as well as the conditions it is tested under, as is the case for all measurements of OSC mobility.

OTFTs, operating in accumulation mode, can be *p*-type or *n*-type depending on whether the transistor is operated to accumulate and transport holes or electrons in the channel. This thesis focuses on materials designed to transport electrons, so from here on unless otherwise stated *n*-type OTFTs will be discussed.

1.4.2 Organic Thin Film Transistor Operation and Characterisation

The basis of an OTFT is a metal-insulator-semiconductor (MIS) capacitor, in which a dielectric material is sandwiched between the organic semiconductor and a gating electrode (figure 9a). When a bias voltage is applied to the gating electrode, known as the gate voltage (V_G), the dielectric layer is polarised. For an n-type OTFT, application of a positive V_G results in the formation of a thin region of accumulated electrons in the OSC at its interface with the dielectric. The thin interfacial accumulation layer of charge carriers in the OSC forms the channel of the OTFT. Charge transport in the channel is between two symmetric electrodes. OTFTs have different configurations depending on the position of these electrodes in relation to the gate electrode and semiconductor layer. In this work, a top-gate bottom-contact OTFT configuration, also known as top-gate staggered configuration, is used (figure 9b). In general top-gate staggered and bottom-gate and bottom-gate coplanar architectures dominate OTFT research. This can partly be explained by the difficulty of processing source and drain electrodes on top of the OSC layer without damaging the OSC. Top-gate architectures have the further advantage of encapsulating the OSC active layer and for many materials higher mobilities have been achieved in top-gate configurations using polymer dielectrics compared with bottom-gate configurations, which typically use a silicon oxide dielectric.[80]

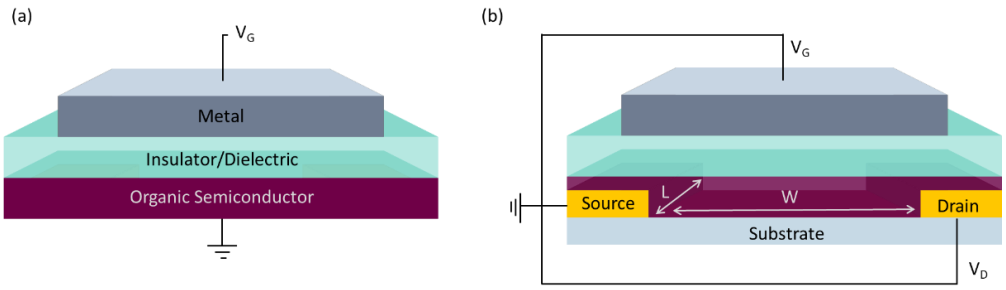

Figure 9| (a) Illustration of a MIS capacitor, (b) illustration of a top-gate bottom-contact OTFT with the channel length (L) and width (W) shown.

The channel dimensions of the OTFTs are defined by the separation of the source and drain electrodes, known as the channel length (L), and size of the electrodes, known as the channel width (W). In an OTFT a second bias is applied between the source and drain electrode, known as the drain voltage (V_D). The drain current, I_D, through the OTFT channel is modulated by the application of V_G and V_D.

OTFTs have three regimes of operation: cut-off, linear and saturation. For an ideal transistor, in the cut-off regime there is no charge accumulation in the OTFT channel and therefore $I_D = 0$ A. For an n-type transistor this is true when $[V_G - V_{th} \leq 0V]$. As V_G increases an accumulation layer of electrons forms in the channel and I_D flows between the source and drain electrode. In the linear regime this current increases linearly with V_D. This is true as long as the V_D is significantly below the V_G, $[0 < V_D << V_G - V_{th}]$. At higher V_D the channel will pinch-off, with a depletion region forming at the OSC channel interface with the drain electrode, resulting in a saturation of the I_D as it becomes independent of V_D, $[V_D >> V_G - V_{th} > 0V]$.

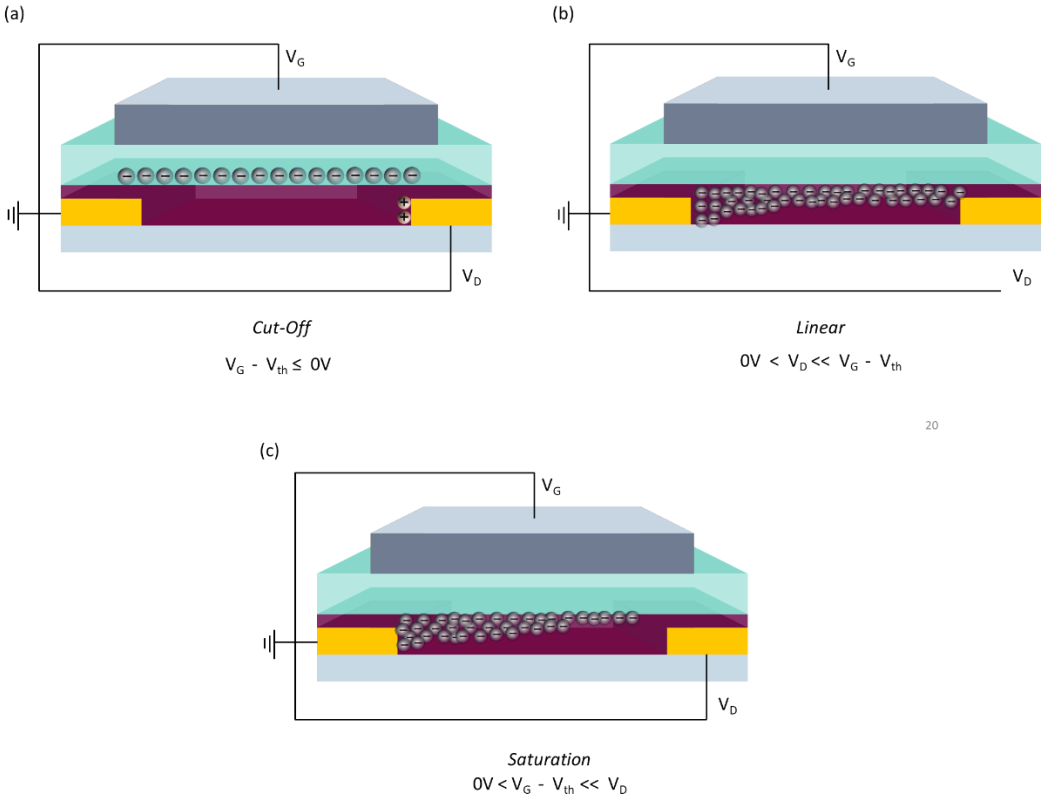

Figure 10| Illustration of the operating regimes of an OTFT. (a) Cut-off regime. (b) Linear regime, where drain current is proportional to source-drain voltage (V_D). (c) Saturation regime, where a pinch-off depletion region forms at the drain contact.

The areal density of mobile charge carriers accumulated at the OSC interface with the dielectric (Q_{mob}) is proportional to the applied gate voltage and dielectric capacitance (C) (equation 3). The threshold voltage (V_{th}) is the minimum gate voltage required for trap state in the OSC to be filled and mobile charge carriers to begin to accumulate in the channel. Assuming drift current dominates, the V_D will vary linearly between the source and drain electrode across the channel and be proportional to the channel width (W), Q_{mob}, the electric field at a particular position in the channel (dV/dx) and the mobility of charge carriers under the applied electric field (μ). The gradual channel approximation, equation 5, combines these two equation (3,4) and integrates over the potential difference across the channel length.

$$Q_{mob} = C(V_G - V_{th})$$

(3)

$$I_D = W\mu Q_{mob}\frac{dV}{dx}$$

(4)

$$I_D = \frac{W}{L}\mu C\left[(V_G - V_{th})V_D - \frac{V_D^2}{2}\right]$$

(5)

By approximating that $V_D << V_G$, equation 6, which gives the current between the source and drain for an OTFT operating in the linear regime, can be obtained. As I_D saturates with increasing V_D beyond $V_G - V_{th}$, the drain current in the saturation regime can be estimated by equation 7, where V_D is substituted for $V_G - V_{th}$.

$$I_D = \frac{W}{L}C\mu(V_G - V_{th})V_D$$

(6)

$$I_D = \frac{W}{2L}C\mu(V_G - V_{th})^2$$

(7)

When testing OTFTs, two types of current-voltage measurements are carried out. Current-voltage measurements where V_D remains constant and current as a function of V_G is

measured are known as transfer characteristics. Current-voltage measurements where V_D is swept over a series of constant V_G are known as output characteristics. Example transfer and output characteristics are displayed in figure 11.

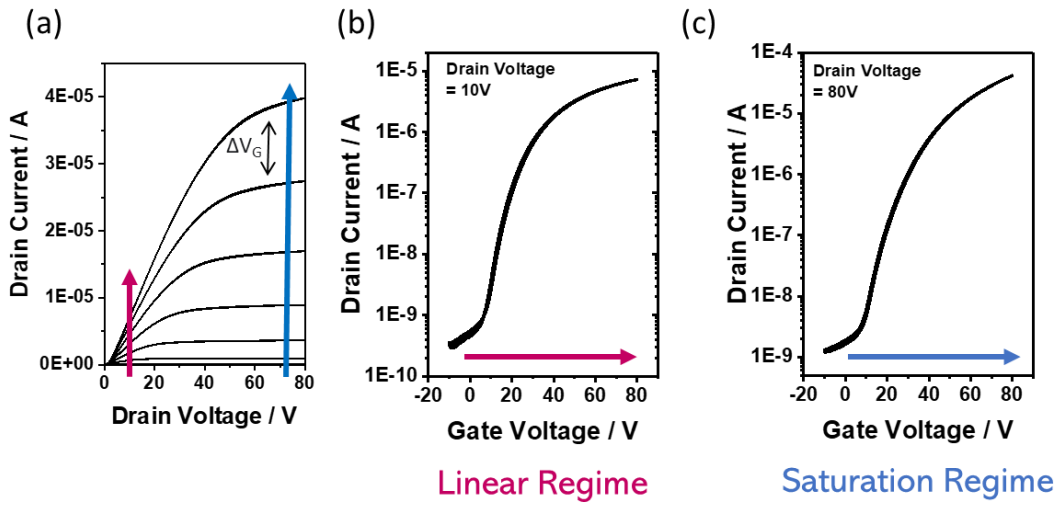

Figure 11| Example (a) output characteristics, (b) transfer characteristics in the linear regime and (c) transfer characteristics in the saturation regime.

1.4.3 Mobility in Organic Thin Film Transistors

Considering the gradual channel approximation, a mobility can be determined from OTFTs operating in either the linear or saturation regime, using equations 8 and 9 respectively.[81]

$$\mu_{lin} = \frac{L}{WCV_D}\left(\frac{\delta I_D}{\delta V_G}\right)$$

(8)

$$\mu_{sat} = \frac{2L}{WC}\left(\frac{\delta\sqrt{I_D}}{\delta V_G}\right)^2$$

(9)

OTFTs are commonly employed to determine the charge transport properties of single component thin films and single crystals of organic semiconductors. The limitations of mobility determination in OTFTs are well understood.[79,82,83] Previously misleading OTFT mobilities have been reported and therefore significant work has been done to standardise OTFT analysis and generate understanding around issues of mobility overestimation and underestimation.[83] These issues are usually related to contact resistance, non-linearity of the transconductance or a gate voltage dependence of mobility. Several studies have

established guidelines on how to present data to prevent misleading OTFT mobilities being reported.[79,83,84] In contrast, the application of SCLC analysis techniques to organic semiconductors is at a much earlier stage of development and the thickness dependence of this technique further complicates any materials comparison made using SCLC mobilities. Mobilities determined from OTFTs are thickness independent as transport is lateral through a thin layer of organic semiconductor rather than vertical through a bulk heterojunction blend as in an OPV. OTFTs also operate at relatively high charge carrier densities and as a result mobilities measured in OTFTs exceed those measured by other techniques.

N2200 is one of the most well studied solution processed OSC for *n*-type OTFTs. When first reported in 2009, N2200 delivered a relatively modest electron mobility of 0.002 $cm^2\ V^{-1}\ s^{-1}$.[85] Subsequently, through optimisation of the polymer molecular weight, OTFT configuration and material processing higher electron mobility values were achieved. For example, mobilities of between 0.1-0.85 $cm^2\ V^{-1}\ s^{-1}$ were reported, in top-gate OTFT architectures with a variety of different dielectrics.[80] Later, in 2015, processing N2200 by bar-coating pre-aggregated solutions of the polymer gave a fibrillar network of the polymer aligned parallel with the OTFT channel, leading to an impressive average electron mobility, extracted in the saturation regime, of 3.6 $cm^2\ V^{-1}\ s^{-1}$ being reported.[86] This highlights the importance of processing conditions and device configuration on the performance of a particular OSC in OTFTs. Similar considerations will be and are also true in emerging OSC technologies.

1.5 Organic Photodetectors

1.5.1 Organic Photodetector Devices

Another thin film OSC based device that has shown promise in recent years is organic photodetectors (OPD). Photodetectors absorb light and convert this into electrical signal and have applications in sensors, optical communications, and imaging. As with OPVs the synthetic versatility of non-fullerene acceptors makes them an attractive alternative to fullerene derivatives for bulk heterojunction OPDs. For photodetectors the spectrum of light absorbed by the device is critical depending on the specific application. For example, UV-visible absorbing OPDs have been used for indirect X-ray detection and NIR absorption is desirable for bioimaging and communications applications.[87–89] One key advantage of NFAs is that their chemical structures can easily be synthetically modified in order to modify the band gap of the acceptors and thereby the wavelengths detected by the OPD. The absorption of OSCs can also be tuned to near infra-red (NIR) wavelengths, 800 – 2500 nm.[90] For example, replacement of the alkyl side chains on the non-fullerene

acceptor CTIC-4F with alkoxy side chains narrowed the band gap from 1.4 eV to 1.1 eV.[91] In a blend with PTB7-Th, the alkoxy substituted acceptor delivered an impressive responsivity of 0.37 AW^{-1} at 995 nm, however, the specific detectivity was limited by the high dark current density of the device. Commercial NIR responsive photodetectors are based on inorganic materials including germanium, indium gallium arsenide (InGaAs) and mercury cadmium telluride (HgCdTe).[90] Photodetectors based on these materials are costly, making OPDs a desirable lower cost alternative. In addition to this, for wearable sensors and biomedical imagining the mechanical flexibility of OPDs is also beneficial. Several examples of skin conformable photodetectors for biomedical monitoring have recently been reported.[2,92]

Another target market for OPDs is wavelength selective photodetectors, which would not require colour filters as their inorganic counterparts do. One example where wavelength selective OPDs have been used effectively is in a hybrid colour image sensor, where a green light selective OPD was integrated on top of a silicon based complementary metal-oxide semiconductor (CMOS) sensor, which provided the red and blue pixels. In the hybrid sensor larger pixel sizes and thereby a higher resolution were realised.[6] This type of hybrid sensor has been reported in work involving Samsung.[93] There has also been recent commercial interest in OPDs which utilise the optical effects of microcavities to achieve tuneable narrowband responsivity in the NIR, by the Germany based start-up Senorics GmbH.[94]

1.5.2 Organic Photodetector Operation

The type of organic photodetector investigated in this work, organic photodiodes, are closely related to OPVs. Both technologies employ a diode architecture with a bulk heterojunction active layer consisting of a mixture of electron donating and accepting organic semiconductor material. OPVs are operated in forward bias to facilitate power extraction from the device whereas OPDs are operated in reverse bias, which is favourable for maximising charge extraction from the device, as illustrated in figure 12.

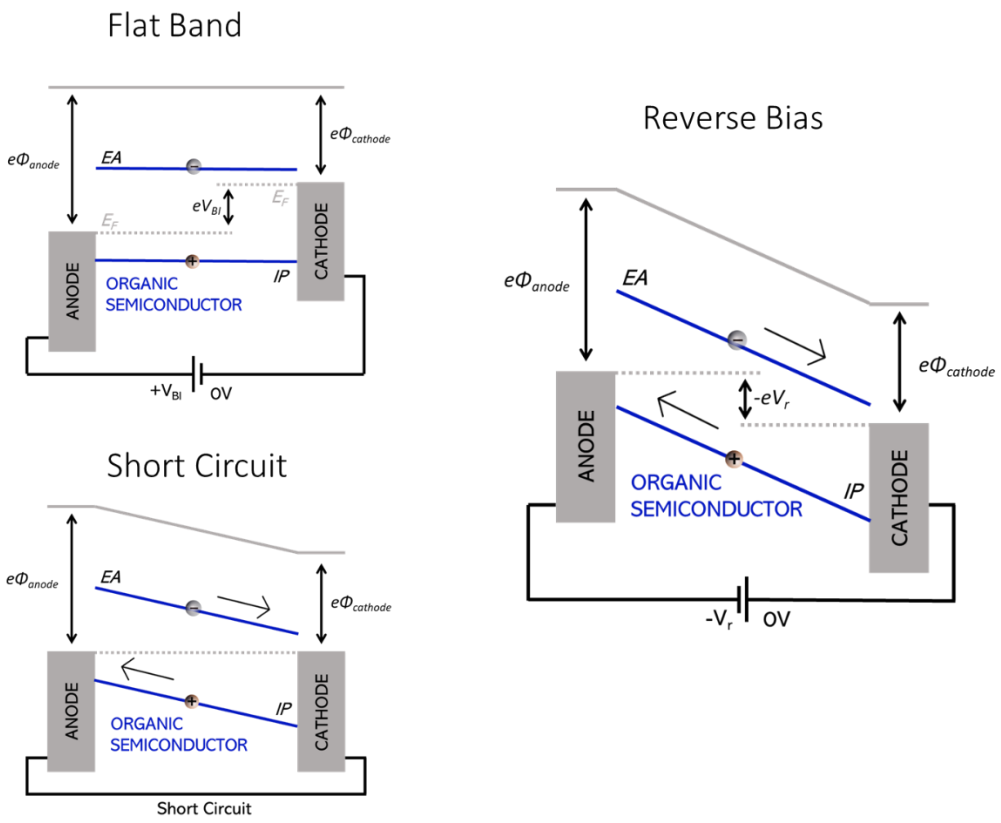

Figure 12| Simplified energy level diagrams illustrating flat band, short circuit and reverse bias diode operation under illumination. At reverse bias the electric field in the device is increased and thereby charge extraction from the device is enhanced.

Whilst in OPVs, power conversion efficiency is the key parameter used to define how well a device performs, in OPDs performance is assessed using several parameters. The key metrics used to define how well an OPD performs are Responsivity (R), Dark Current (J_D), noise equivalent power (NEP), linear dynamic range (LDR), Specific Detectivity (D*), transient times and cut-off frequency. The simultaneous optimisation of these parameters can be challenging.[95,96] For example, typically the external quantum efficiency and therefore the responsivity of a device will decrease with active layer thickness. In contrast, employing thick active layers is one method to reduce the dark current in OPDs. The speed of response of the device is also likely to be decreased for thicker OPDs.

To date very little is understood about the relationship between the chemical structure of the OSCs employed in OPDs and the performance metrics for these devices. Until recently most work on OPDs has focused on fullerene derivative based OSC blends. In this thesis, several NFAs are explored in OPDs.

1.6 Motivation and Thesis Outline

NFAs have received a large amount of research interest in recent years, pushing power conversion efficiencies closer to values which will make OPV a commercially relevant technology. The bulk of research in the field of OPVs analyses blends of donor and acceptor material. This thesis has two aims. First, to further understanding of how the chemical structure of this relatively new class of solution processable small molecule organic semiconductors relates to their performance in thin film technologies. Second, following the success of NFAs as a class of materials for OPVs the thesis explores if these materials can work well in other thin film technologies, specifically OTFTs and OPDs. By better understanding the relationship between chemical structure and thin film device performance it is hoped that this can help to direct the development of new OSC materials for a variety of thin film technologies.

The structure of the thesis is as follows: in *Chapter 2* the effect of branched vs. linear aliphatic side chain on IDTBR intermolecular packing and mobility in OTFTs is investigated. The importance of the influence of solid-state packing on the material properties of NFAs is highlighted. Based on the identification of O-IDTBR as a promising material for OTFTs, solvent vapour annealing and contact engineering are explored to learn more about the material properties and to enhance its performance in OTFTs. In *Chapter 3*, based on the promising performance of O-IDTBR in OTFTs, structural derivatives of the NFA are characterised and applied in OTFTs. The structural modifications explored include changes to the linear aliphatic side chain length as well as varying the nature of the terminal electron deficient acceptor unit and electron rich donor core.

Chapter 4, explores O-IDTBR and its derivative O-FBR as materials for organic photodetectors (OPD), a relatively new OSC thin film technology. Blends of the NFAs with the donor polymer PTQ10 are found to deliver exceptionally low dark currents. Finally, in *Chapter 5*, NFAs designed to have near infra-red (NIR) absorption for visibly transparent OPV and NIR responsive OPD applications are investigated. In *Chapter 6*, a summary of the work and outlook highlighting future work based on the results of this thesis is given. Finally in *Chapter 7*, the experimental details of the previous chapters are laid out.

Chapter 2: Impact of Non-fullerene Acceptor Side Chain Variation on Transistor Mobility

It is well established that by modifying the chemical structure of NFAs, the optical absorption, energy levels and bulk heterojunction morphology can be tuned. However, the effect of chemical structure modifications, in particular the choice of aliphatic side chains, on the charge transport properties of NFAs is not well understood. In this chapter, the relationship between chemical structure, molecular packing, and charge transport, as measured in organic thin film transistors (OTFTs), is investigated for the branched and linear side chain analogues of the NFA IDTBR, EH-IDTBR and O-IDTBR respectively. Whilst both IDTBR analogues have been shown to deliver similar performances in OPVs, here they are shown to exhibit very different packing motifs and electron mobilities. The aim of this study was to determine if the choice of aliphatic side chain impacted the charge transport properties of the NFAs EH-IDTBR and O-IDTBR and if any differences could be rationalised in terms of the intermolecular packing of the molecules. During the study, O-IDTBR was found to perform particularly well in OTFTs and further optimization of OTFTs based on O-IDTBR through solvent vapour annealing and modification of the transistor source/drain contacts was therefore also explored.

A large portion of this chapter is published in the paper entitled "Impact of Nonfullerene Acceptor Side Chain Variation on Transistor Mobility"[97] *and the rest is as yet unpublished work. Many thanks to Weimin Zhang, who synthesised and purified the NFA molecules used in this and many other studies included in this thesis; Andrew J. P. White, who collected the single crystal XRD data; Karl J. Thorley, who carried out the transfer integral calculations, as well as Julianna Panidi and Jan Kosco, who helped to perform the AFM measurements in this chapter.*

2.1 Background

Aliphatic side chains are included in organic semiconductors to endow them with good solubility in organic solvents allowing them to be processed from solution. These aliphatic side chains must be long enough to give good solubility but are also electrically insulating so must not impair charge transport between the molecules.[98] In NFAs, the side chains are pendant to the electron donating core of the molecules to leave the electron deficient terminal units, on which the LUMO of the molecules will be localized, accessible to facilitate charge transport between the molecules.[54] In the design of OSCs, typically the optimization of side chains will come after the identification of a promising target NFA. A good example of this is BTP-eC9, which was identified through a systematic study optimizing the chlorinated analogue of the NFA Y6.[99] This optimization typically focuses on thin film device optimization and less consideration is given to how the side chains may affect the charge transport properties of the NFAs.

Charge transport in molecular organic semiconductors is directly related the intermolecular packing of the molecules, which will dictate the overlap of adjacent molecular orbitals and thereby the efficiency of charge transfer between molecules.[1,100] Solubilising groups, such as alkyl chains, play an important role in determining the intermolecular packing and single crystal packing motifs of small molecule organic semiconductors. Crystal engineering via solubilising group variation has resulted in high performance small molecule p-type materials for OTFTs[101] and work has been done to explore the role that aliphatic side chains play in dictating crystal packing.[102]

At the time this study started, previous reports of the packing motifs of NFAs were limited. For the NFA 6TIC-4F, the X-ray crystallographic structure was reported, revealing that the phenylhexyl side chains orientate almost perpendicularly to the donor 6T core.[37] Strong π stacking of the fluorinated terminal acceptor units and outermost thienothiophene units of the donor core was also reported. These interactions were highlighted as important for efficient intermolecular charge transport but electronic coupling between the NFAs was not investigated.

The intermolecular packing in thin films of ITIC has been previously modelled using molecular dynamics simulations.[31] These simulations demonstrated that the terminal electron accepting units of ITIC form π stacks. From the simulated π stacked pairs of ITIC molecules electronic couplings between 20 – 80 meV were calculated. It was concluded that acceptor unit π stacking is the predominant method for charge transport in thin films

of ITIC. In contrast, in the same study, for single crystals of ITIC a crossed edge-to-face orientation of adjacent chromophore units was reported.[31] More recently, subsequent to the publication of the work discussed in this chapter, in a detailed investigation into the intermolecular packing and transport properties of a variety of NFAs, the packing motif in single crystals of ITIC was identified as Herringbone, which has zero dimensionality (0D) of π-π stacking.[103] The study highlighted the importance of considering the intermolecular packing of NFAs, a factor that can fundamentally limit their charge transport properties, for the development of NFAs with higher charge carrier mobilities which are necessary for the commercialisation of OPV to be possible.[103]

In this chapter, the effect of the choice of either branched ethyl-hexyl or linear octyl side chains for the NFA IDTBR on its intermolecular packing and thereby charge transport properties is explored. Since NFAs are the electron accepting materials in OPVs, their n-type mobility is investigated. However, recently NFAs have been investigated as materials for both n-type and ambipolar OTFTs.[104–106] For OTFTs based on ITIC, a relatively modest n-type saturation mobility of 0.014 $cm^2 V^{-1} s^{-1}$ has previously been reported.[104] In contrast, for the linear C16 side chain analogue of ITIC, known as IDTTIC, a higher mobility of 0.50 $cm^2 V^{-1} s^{-1}$ has been reported.[104,105] This illustrates the effect on mobility of changes in NFA chemical structure as well as the promise of these types of small molecule OSC for OTFT applications. For context, the best performing small molecules developed for n-type OTFTs include perylenediimide (PDI) and naphthalenediimide (NDI) derivatives, for which in some cases mobilities exceeding 1 $cm^2 V^{-1} s^{-1}$ have been achieved.[107,108]

The linear (octyl) and branched (ethyl-hexyl) chain analogues of IDTBR, referred to as O-IDTBR and EH-IDTBR respectively (Figure 13), were initially reported as acceptors for OPVs in 2016, when they were combined with P3HT in blends exhibiting good ambient stability.[109] Since then, work combining EH-IDTBR with other donor polymers has delivered blends exhibiting low voltage losses, burn in free photovoltaic performance and high quantum efficiencies.[59,110] Meanwhile, work on O-IDTBR has delivered blends exhibiting low recombination rates and high efficiencies with small molecule donors.[74,111]

Given the promising performance of other NFAs in OTFTs, IDTBR was seen as a good candidate for investigating in this application. In OTFTs a single OSC component is typically used. This allows the properties of that OSC to be investigated independent of other OSCs, which would be present in a BHJ blend. Surprisingly little work has been done to date investigating the subtle differences in performance of the two molecules as a result of their differing side chains. By investigating EH-IDTBR and O-IDTBR in single component devices, in this case OTFTs, any difference in their performance could be related back to their chemical structures.

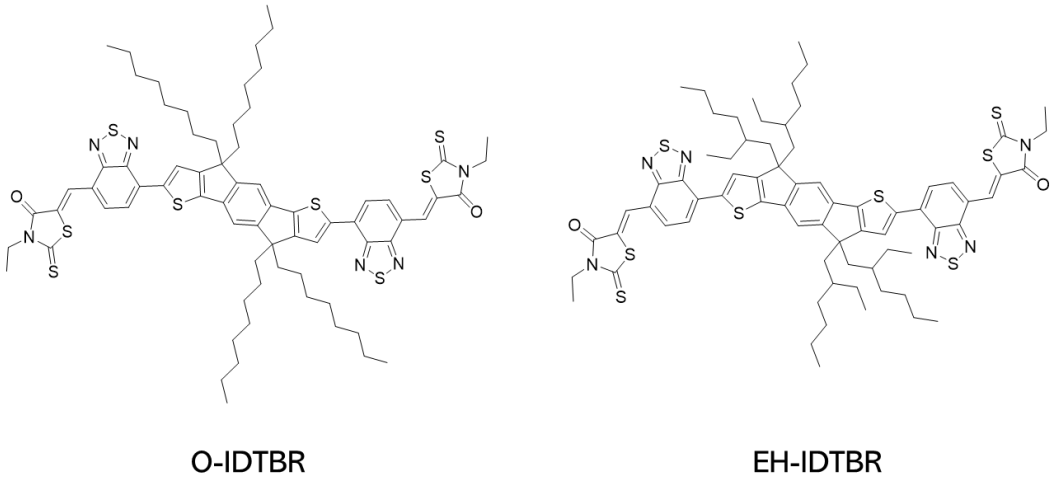

Figure 13| Chemical structures of O-IDTBR and EH-IDTBR.

2.2 Performance of OTFTs based on O-IDTBR and EH-IDTBR

To investigate if any differences in charge transport properties of O-IDTBR and EH-IDTBR can be observed experimentally, OTFTs based on thin films of the two neat materials were fabricated. The processing conditions of the organic semiconductor film in the OTFTs will influence the structural order of molecules in the solid state and thereby their optical and electronic properties. Therefore, first suitable processing conditions for the thin films on which the OTFTs were to be based were identified.

Temperatures which may be relevant to the structural order of O-IDTBR and EH-IDTBR samples were identified using differential scanning calorimetry (DSC). In DSC a solid sample is heated at a controlled rate allowing the identification of its thermal transitions. It should be noted that for many OSCs certain thermal transitions, for example the glass transition (T_g) temperature, cannot always be observed using DSC and in these cases higher sensitivity techniques such as rapid heat-cool calorimetry or dynamic mechanical thermal

analysis can be used.[112–114] Prior to running the DSC, the two materials were dissolved in chloroform and drop cast to remove any thermal or crystallisation history of the sample. This is important as differing thermal and crystallisation histories between samples can affect the T_g.[112] It is important to note that the microstructure of OSCs deposited by spin coating is likely to differ from those of a drop cast film, as a result of the faster drying speed and thickness of the wet films differing significantly.[115] Despite this DSC on drop cast samples can give a good indication of which temperature processing conditions may result in relevant microstructure changes in the NFA thin films.

The first and second heating cycle thermograms of O-IDTBR and EH-IDTBR are displayed in figures 14b and 14c. Differences between the first and second heating cycles can be attributed to irreversible transitions that take place during the first cycle. O-IDTBR exhibits a cold crystallisation exotherm at 120 °C. Such cold crystallisations are typically associated with side chain reorganisation. Annealing thin films of O-IDTBR at 120 °C results in a red-shift in the absorbance of the films (figure 14a), indicating a change in the structural order.

Already for the two side chain analogues of IDTBR difference in behaviour can be observed from the DSC. In the second heating cycle of EH-IDTBR three distinct endotherms are observed at 119 °C, 182 °C and 222 °C. These endotherms indicate the presence of three EH-IDTBR phases. The suppression of the melt endotherm (T_m) at 222 °C in the second heating cycles indicates that the crystalline phase which forms at high temperatures is less accessible from the melt phase than the as cast morphology.[116] The endothermic transition at 119 °C can be associated with side chain melting, which is of interest for the optimisation of OTFT performance. Previously batch to batch variation has been observed in the DSC of EH-IDTBR, as highlighted in the thesis of Dr. Zeinab Hamid.[116] The variations observed were attributed to the chirality of the EH-IDTBR side chains, which leads to a mixture of stereoisomers forming during synthesis. For the experiments discussed in this thesis the same batch of EH-IDTBR was used throughout.

Table 1| For the NFAs O-IDTBR and EH-IDTBR. Onset temperature of melt (T_m), of cold crystallisation exotherm (T_{cc}), and of lowest temperature endotherm (T_1). As well as peak absorption wavelength for as cast thin films ($\lambda_{max,AC}$) and for thin films annealed at 120 °C ($\lambda_{max,TA}$) .

NFA	T_m / °C	T_{cc} / °C	T_1 / °C	$\lambda_{max,AC}$ / nm	$\lambda_{max,TA}$ / nm
O-IDTBR	223	118	-	690	733
EH-IDTBR	212/222	-	119	673	665

Figure 14 displays the UV-vis absorbance of as cast O-IDTBR and EH-IDTBR thin films as well as thin films annealed at 120 °C, which corresponds to just above the T_{cc} for O-IDTBR and above the lowest temperature endotherm (T_1), observed in the second heating cycle of the DSC, for EH-IDTBR. For O-IDTBR a large red shift in absorption of 43 nm is observed on annealing, meanwhile for EH-IDTBR a slight blue shift of 8 nm is observed. This difference between O-IDTBR and EH-IDTBR in the thin film UV-vis already indicates weaker electronic coupling between molecules in the case of EH-IDTBR, which is likely due to looser intermolecular contacts associated with the branched side chains.[117]

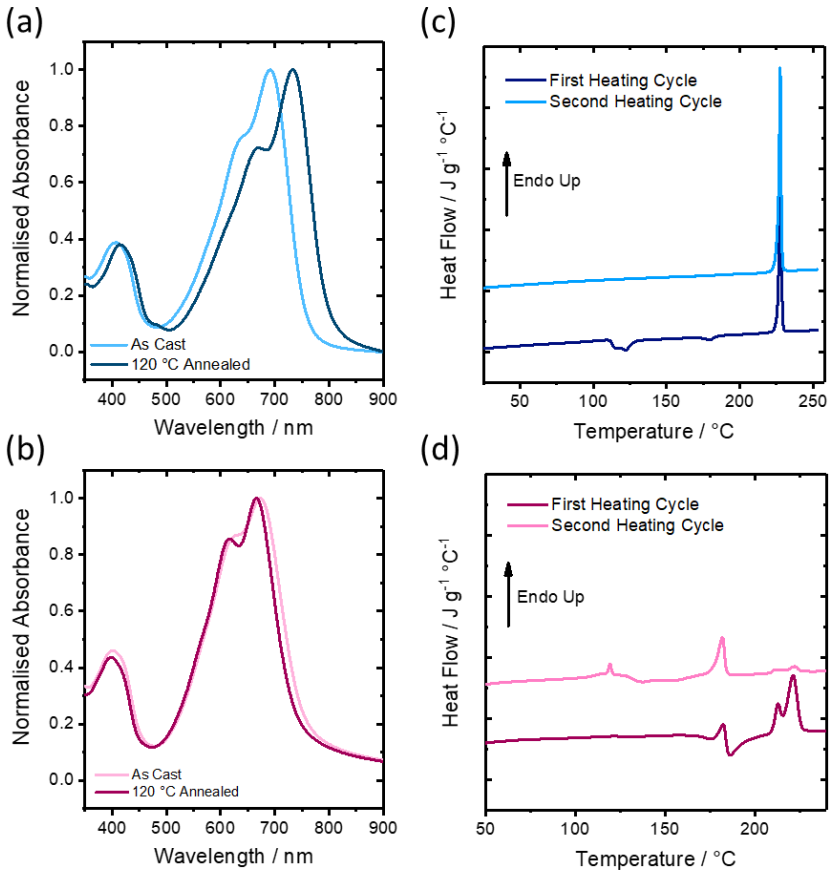

Figure 14| (a) Normalised UV-vis absorbance of as cast and thermally annealed (120 °C) thin films of O-IDTBR. (b) Normalised UV-vis absorbance of as cast and thermally annealed (120 °C) thin films of EH-IDTBR. (c) First and second DSC heating cycle of O-IDTBR (ramp rate 5 °C min^{-1}). (d) First and second DSC heating cycle of EH-IDTBR (ramp rate 5 °C min^{-1}).

OTFTs were fabricated based on NFA films annealed at different temperatures, corresponding to thermal transitions identified in the DSC. The OTFTs had a top-gate, staggered configuration as illustrated in figure 15. Table 2 gives the mobilities extracted in the linear and saturation regimes for OTFTs based on O-IDTBR and EH-IDTBR thin films

annealed at the various temperatures. In figure 16 example saturation regime transfer characteristics and a plot of the gate voltage dependence of mobility for these OTFTs are displayed.

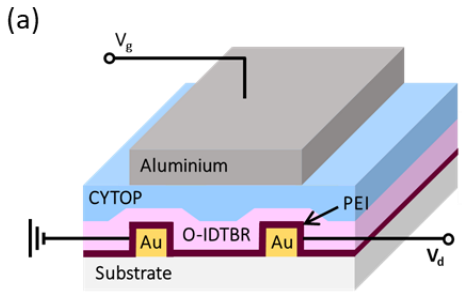

Figure 15| (a) n-channel OTFT device architecture used in this work. CYTOP is used as the dielectric with polyethyleneimine (PEI) modified gold (Au) source and drain electrodes. A gate voltage (V_g) and drain voltage (V_d) are applied to the aluminium gate electrode and gold drain electrodes respectively.

For OTFTs based on as cast thin films of both O-IDTBR and EH-IDTBR, similar mobilities were obtained, 0.04 ± 0.03 $cm^2 V^{-1} s^{-1}$ for EH-IDTBR and 0.07 ± 0.04 $cm^2 V^{-1} s^{-1}$ for O-IDTBR in the saturation regime. For EH-IDTBR thermal annealing was found to be detrimental to the OTFT performance. Although higher mobilities were obtained for films of EH-IDTBR annealed at 120 °C, of 0.06 ± 0.02 $cm^2 V^{-1} s^{-1}$, compared with as cast films, from figure 16d the mobility in these OTFTs is highly gate voltage dependent. From figure 16c, the on-currents for OTFTs based on EH-IDTBR decrease with increasing anneal temperature. Therefore, for EH-IDTBR based OTFTs the best performance and highest mobility is achieved when no thermal annealing is performed on the OSC film.

In contrast, for O-IDTBR a significant increase in OTFT performance, relative to the as cast devices, is achieved when the OSC thin film is annealed at 120 °C, with a mobility of 0.3 ± 0.0 $cm^2 V^{-1} s^{-1}$ being determined in the linear regime and 0.4 ± 0.0 $cm^2 V^{-1} s^{-1}$ being determined in the saturation regime, averaged over 25 transistors across 5 substrates. This enhancement of mobility can be associated with an increase in structural order of the O-IDTBR molecules on annealing, as discussed in the next section. In figure 17, example transfer and output characteristics for O-IDTBR and EH-IDTBR based OTFTs, fabricated using the processing conditions which give the best performance are given. These processing conditions are a 120 °C annealed films of O-IDTBR and as cast films of EH-IDTBR.

Table 2| For O-IDTBR and EH-IDTBR. Mobility values extracted in the linear (μ_{lin}) and saturation (μ_{sat}) regime for OTFTs based on as cast thin films and thin films annealed at varying temperatures, selected based on the DSC thermograms.

Film Processing	O-IDTBR		EH-IDTBR	
	μ_{lin} / cm^2 V^{-1} s^{-1}	μ_{sat} / cm^2 V^{-1} s^{-1}	μ_{lin} / cm^2 V^{-1} s^{-1}	μ_{sat} / cm^2 V^{-1} s^{-1}
AC	0.02 ± 0.03	0.07 ± 0.04	0.04 ± 0.05	0.04 ± 0.03
120 °C	0.3 ± 0.0	0.4 ± 0.0	0.04 ± 0.02	0.06 ± 0.02
175 °C	n/a	n/a	0.01*	0.03 ± 0.01
190 °C	0.08 ± 0.05	0.3 ± 0.1	n/a	n/a
240 °C	n/a	n/a	-	0.003*

[a]*Where a thermal anneal condition was not tested, not applicable (n/a) is marked in the table.* [b]*Means and standard deviations taken over at least 5 transistors for each processing condition. OTFT channel dimensions 40/1000 µm.*Averages not provided for these processing conditions as most OTFTs were not switching and had high gate leakage currents*

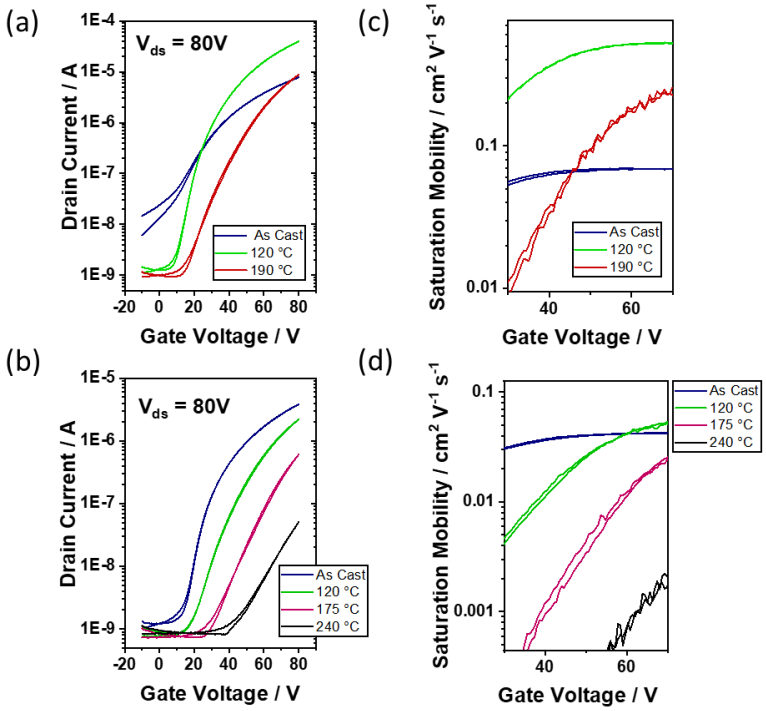

Figure 16| Saturation regime transfer (V_{ds} = 80 V) characteristics and gate voltage dependence of mobility for OTFTs based on (a,c) O-IDTBR and (b,d) EH-IDTBR annealed at various temperatures, selected based on the DSC thermograms. [Channel dimensions 40/1000µm, CYTOP dielectric 900 nm.]

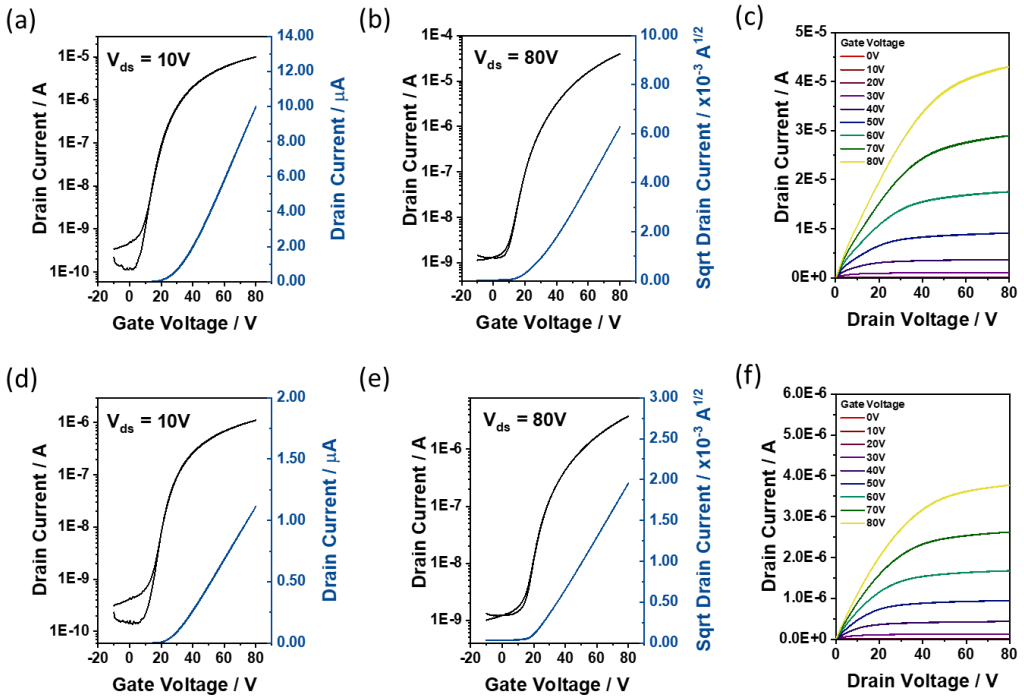

Figure 17| Transfer characteristics in the (a) linear regime (V_{ds} = 10V) and (b) saturation regime (V_{ds} = 80V) as well as (c) output characteristics for OTFTs based on films of O-IDTBR annealed at 120 °C/10mins. Transfer characteristics in the (d) linear regime (V_{ds} = 10V) and (e) saturation regime (V_{ds} = 80V) as well as (f) output characteristics for OTFTs based on as cast films of EH-IDTBR. [Channel dimensions 40/1000µm, CYTOP dielectric 900 nm.]

As charge transport in OTFTs is through a thin interfacial accumulation layer formed at the interface of the OSC with the dielectric, trap states as a result of a poor interface can detrimentally affect OTFT performance. If the OSC has a high surface roughness, this can induce trap states, for example at grain boundaries, resulting in charge trapping. To investigate if the OTFT performance could have been affected by differences in the morphology of the as cast and annealed (120 °C) NFA thin films the surface topography was analysed using Atomic Force Microscopy (AFM).

In figure 18 the AFM topography images of 3 x 3 µm^2 areas of the thin films are presented and table 3 gives the route means squared roughness (RMS) derived for each film. A significant increase in surface roughness was observed upon annealing EH-IDTBR. In contrast, interestingly O-IDTBR films exhibited a decrease in surface roughness upon annealing. As surface roughness is inherently linked to charge trapping at the dielectric interface, the low surface roughness observed for the annealed O-IDTBR film likely in part contributes to the improved OTFT performance observed.

Table 3| Route mean square (RMS) roughness of as cast and annealed (120 °C/ 10 minutes) films of O-IDTBR and EH-IDTBR measured by AFM.

	O-IDTBR	EH-IDTBR
As Cast	1.2 nm	0.3 nm
Annealed 120 °C/ 10mins	0.3 nm	1.2 nm

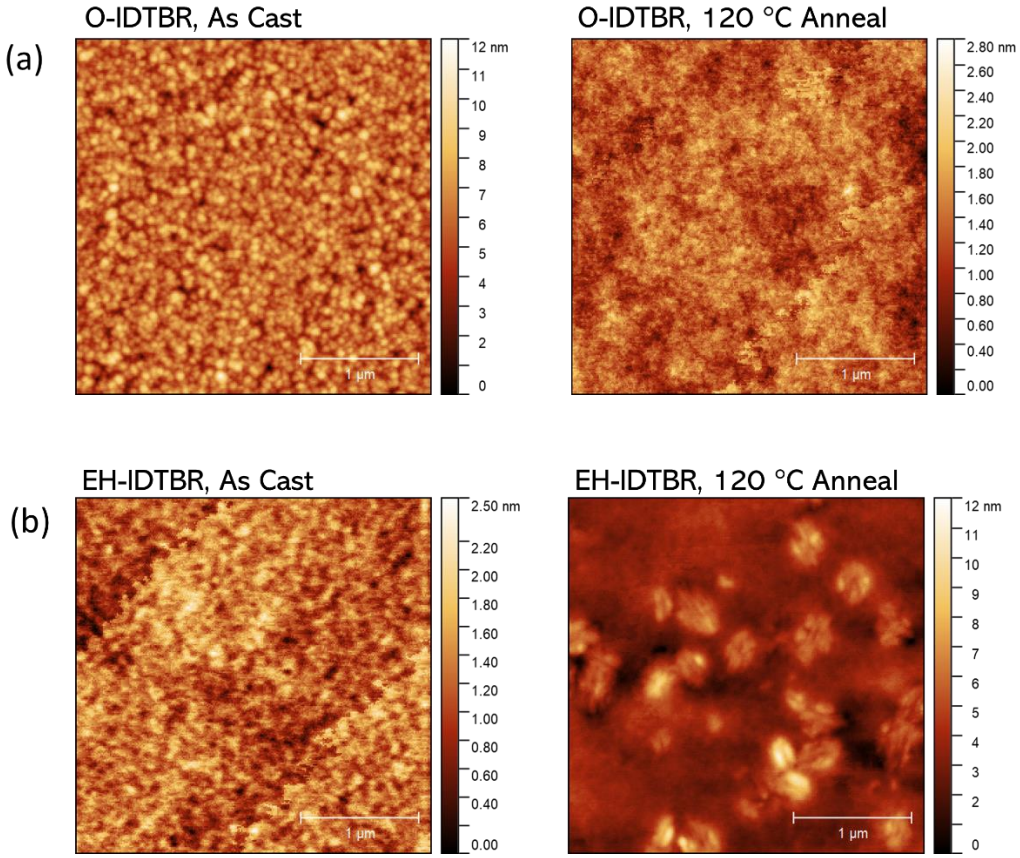

Figure 18| AFM tapping mode topography images of as cast and annealed (120 °C) thin films of (a) O-IDTBR and (b) EH-IDTBR.

2.3. Intermolecular Packing of O-IDTBR and EH-IDTBR

Differential scanning calorimetry (DSC), Grazing Incidence X-ray Diffraction (GIXRD) and the bathochromic shift in absorption observed on annealing have shown O-IDTBR thin films to be more crystalline than those of EH-IDTBR.[109] Even though differences in crystallinity, i.e. the degree of structural order in thin films, have been established, the precise intermolecular interactions between these NFAs have not been investigated. As the mobility of small molecule OSCs is related to their intermolecular packing, to rationalise the differences in OTFT mobility observed, the intermolecular interactions and electronic coupling between the NFAs were investigated.

OSC thin films typically exhibit a high degree of structural disorder and therefore the precise intermolecular packing arrangement can be difficult to determine experimentally from thin films.[31,34] Grazing Incidence Wide Angle X-ray Scattering (GIWAXS) provides insight into the degree of crystallinity, orientation of molecules relative to the substrate and in some cases lamella packing and π stacking distances. GIWAXS patterns of thin films of O-IDTBR and EH-IDTBR have been reported elsewhere.[109,118,119]

Here, to investigate the intermolecular packing of O-IDTBR and EH-IDTBR, single crystals were grown by the antisolvent vapour diffusion method using a chlorobenzene/methanol solvent system. Antisolvent vapour diffusion is one of the most common techniques for growing single crystals of small molecules.[103,120] From the crystals the NFA packing motif was then determined using X-ray crystallographic analysis. The refined crystal structures are available from the Cambridge Crystallographic Data Centre, CCDC 1889754 and 1889755 for O-IDTBR and EH-IDTBR respectively.

Table 4| Crystal Data, Data Collection and Refinement Parameters for the crystal structures of O-IDTBR and EH-IDTBR

Data	O-IDTBR	EH-IDTBR
formula	$C_{72}H_{88}N_6O_2S_8$	$C_{72}H_{88}N_6O_2S_8$
formula weight	1325.96	1325.96
colour, habit	purple blocky needles	dark purple blocks
temperature / K	173	173
crystal system	monoclinic	triclinic
space group	$P2_1/c$ (no. 14)	P-1 (no. 2)
a / Å	13.7663(2)	10.0709(8)
b / Å	15.81032(17)	12.3721(7)
c / Å	32.7146(3)	16.3680(8)
α / deg	90	78.476(5)
β / deg	96.2928(12)	73.057(6)
γ / deg	90	66.120(7)
V / Å^3	7077.43(15)	1776.1(2)
Z	4	1 [c]
D_c / g cm^{-3}	1.244	1.240
radiation used	Cu-Kα	Mo-Kα
μ / mm^{-1}	2.709	0.300
2θ max / deg	147	56
no. of unique reflns measured (R_{int})	13647 (0.0259)	6999 (0.0176)
obs, $\|F_o\| > 4\sigma(\|F_o\|)$	10573	5084
no. of variables	839	448
R_1(obs), wR_2(all) [a]	0.0647, 0.1898	0.0708, 0.2309

[a] $R_1 = \Sigma||F_o| - |F_c||/\Sigma|F_o|$; $wR_2 = \{\Sigma[w(F_o^2 - F_c^2)^2] / \Sigma[w(F_o^2)^2]\}^{1/2}$; $w^{-1} = \sigma^2(F_o^2) + (aP)^2 + bP$.
[c] The molecule has crystallographic C_i symmetry.

Table 4 provides a summary of the crystallographic data for the structures of O-IDTBR and EH-IDTBR. The unit cells and packing motifs of both NFAs are illustrated in figure 19. For both O-IDTBR and EH-IDTBR, the terminal electron accepting units of the NFAs π stack as expected. However, the packing motifs exhibit significant differences. In the single crystals, EH-IDTBR exhibits a 1D slipped stack packing motif. On the other hand, for the O-IDTBR single crystals an interdigitated columnar packing motif was identified. Within this interdigitated packing, the O-IDTBR electron accepting units, the rhodanine and adjacent benzothiadiazole unit, assemble in columns. The O-IDTBR molecules interdigitate between these columns resulting in a 3D network. It has been shown that packing motifs allowing isotropic charge transport in two or three dimensions, will exhibit a higher tolerance of carrier transport towards disorder and therefore lead to higher mobilities, compared with one dimensional packing motifs.[1] Therefore, the three dimensional packing motif of O-IDTBR could qualitatively be expected to allow more

effective and disorder tolerant charge transport within the material. It is also interesting to note that in the two packing motifs O-IDTBR and EH-IDTBR exhibit different conformations to each other. It is not clear if this will have an effect on the charge transport properties of the molecules.[97]

Next, to quantitatively assess differences in intermolecular charge transfer for the two different packing motifs, transfer integrals were calculated. The concept of transfer integrals originates from Marcus theory and relates to the strength of coupling between orbitals on two sites.[121] Electron transfer integrals (J_e) were calculated with the Gaussian 09 software package[122], using the orbital projection method[123] at the B3LYP/6-31G* level. For the J_e calculations, pairs of molecules within the packing motifs were selected based on their apparent π stacking interactions, as illustrated in figure 20. For the calculations the pairs of molecules selected were treated with the aliphatic side chains removed to reduce the complexity of the calculations.

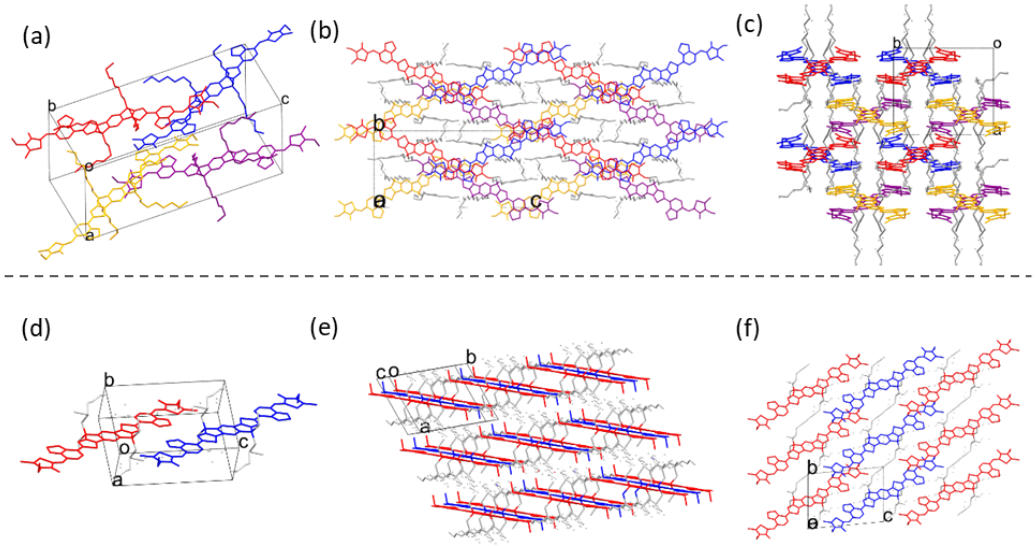

Figure 19| X-ray crystallographic packing motifs of (a,b,c) O-IDTBR and (d,e,f) EH-IDTBR (a) O-IDTBR unit cell. (b,c) O-IDTBR 2x2x2 packing motif. (d) EH-IDTBR unit cell. (e,f) EH-IDTBR 3x3x2.5 packing motif. Colours added arbitrarily and hydrogen atoms omitted for clarity.

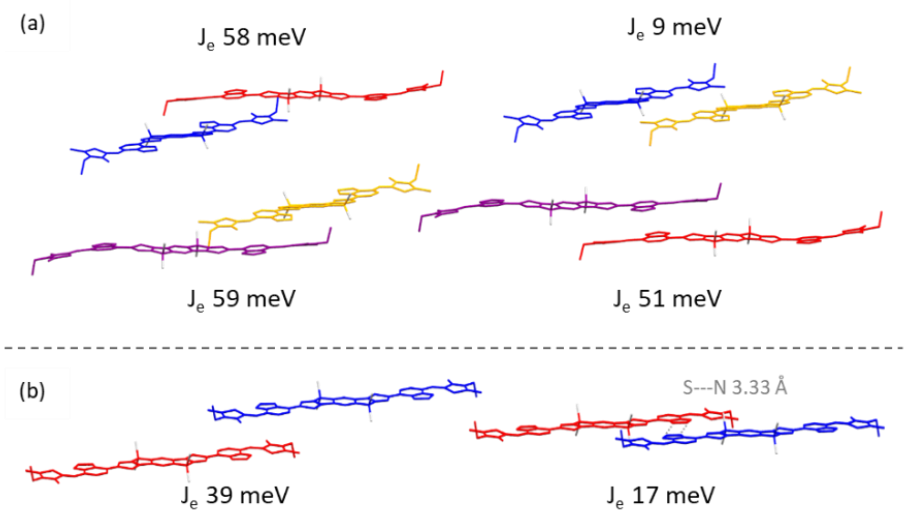

Figure 20| Electron transfer integrals (J_e) calculated for pairs of molecules taken from the single crystal structures of (a) O-IDTBR and (b) EH-IDTBR with truncated side chains. Colours match those used in figure 19 to aid identification of molecular pairs.

A high magnitude J_e indicates strong electronic coupling between molecules and therefore efficient electron transfer between them. However, the number of possible pathways for charge transport can be more important than the magnitude of J_e. A packing motif with dominant transfer integrals in several directions is associated with more defect tolerant charge transport and therefore higher mobilities compared with packing motifs exhibiting dominant transfer integrals in only one direction.[1] An example of this is a comparison between TIPS-pentacene and TES-pentacene. TIPS-pentacene, one of the best p-type small molecule OTFT materials, has two J_e values of magnitudes 54 meV and 65 meV within its 2D brickwork packing motif. This contrasts with TES-pentacene which packs in a 1D slipped stack motif and has a higher magnitude transfer integral of 94 meV. Despite the higher J_e of TES-pentacene in the solid state it delivers lower OTFT mobilities compared with TIPS-pentacene.[124,125]

In the 1D slipped stack packing motif of EH-IDTBR each molecule has only two nearest neighbours with which it forms a π stack. For these π stacked pairs of molecules the J_e is 39 meV. In addition to the π stacked neighbouring molecules, there is also a close contact between adjacent molecules within the packing motif (figure 20b). This close contact appears to be related to short contact interactions between the BT unit sulphur and nitrogen atoms on adjacent EH-IDTBR molecules. Previously similar S---N contacts between BT units were shown to contribute to the self-assembly of small molecule OSCs.[126] This S---N square interaction within the 1D slipped stack packing arrangement of EH-IDTBR allows moderate charge transport in a second direction, with a calculated J_e of 17 meV.

For O-IDTBR, within each π stacked column in the packing motif there are four different molecular pairings. For three out of four of these pairings, J_e over 50 meV were calculated (figure 20a). For the final pair of O-IDTBR molecules, a comparatively low J_e of 9 meV was calculated, corresponding to an unfavourable overlap of the LUMOs and therefore limiting vertical transport through the columns. Despite this, intramolecular transport between columns allows charge transport in 3D.

Calculation of the electron transfer integrals confirmed that the 3D packing motif observed in single crystals of O-IDTBR allows 3D charge transport within the material. This contrasts with EH-IDTBR, where transport in the solid state packing motif identified is at best limited to 2D. The n-type mobility calculated in the saturation regime of 0.4 $cm^2\ V^{-1}\ s^{-1}$ for OTFTs based on thin films of O-IDTBR can be understood in terms of its propensity to form an interdigitated packing motif with relatively high J_e between molecules allowing isotropic electron transport in the solid state. In contrast, for EH-IDTBR, which exhibits a 1D slipped stack packing arrangement, the lower mobilities observed can be in part explained by the more limited directionality of the transport pathways within the solid state packing motif.

2.4 Side Chain Dependence of Intermolecular Packing

Although necessary for solution processing of OSCs, aliphatic side chains are insulating and therefore can inhibit charge transport between the conjugated backbones of OSCs depending on their positioning within a packing motif.[54] Whilst intermolecular packing depends on many different factors, it can be described as a balance between a variety of attractive or repulsive non-covalent interactions. As expected, the terminal acceptor units of O-IDTBR and EH-IDTBR have been shown to π stack in the solid state, which is beneficial for intermolecular electron transport and a feature which has been identified for many of the best performing NFAs.[103] On top of these π stacking interactions, intermolecular interactions between the aliphatic side chains will also influence the packing motifs of OSCs. The non-covalent interactions between aliphatic side chains help to stabilise the solid state packing motif. The influence of side chains is dependent on the specific structure of the conjugated chromophore, so will vary depending on the NFA being investigated.[98]

For EH-IDTBR and O-IDTBR it is clear that the differences in orientation of the octly and 2-ethylhexyl side chains result in very different packing motifs, which, as shown already, have a large impact on IDTBRs charge transport properties. In the single crystals of EH-IDTBR, disorder in the 2-ethyl-hexyl side chains meant it was not possible to resolve

the exact position of all eight of the carbon atoms in the chains. As the positions were not resolved, the interactions between aliphatic side chains could not be quantified using computational methodology. Despite this, some general conclusions about the interactions involving the aliphatic side chains can be drawn from the single crystal packing motifs obtained.

There are four types of non-covalent van der Waals interactions: exchange, electrostatic, induction and dispersion. In the case of side chain interactions, the induction and electrostatic energies will be minimal as these originate from permanent dipoles. The magnitude of C-H bond dipoles is small as the electronegativity difference between carbon and hydrogen is small. The interaction energy between two alkyl chains is a balance between repulsive exchange energy, i.e. electron-electron repulsions, and attractive dispersion energy, i.e. induced dipole-induced dipole interactions. The position of the side chains is largely dictated by the physical size of the atoms, however, the resulting interactions between chains should overall stabilise the packing motif by dispersion interactions.

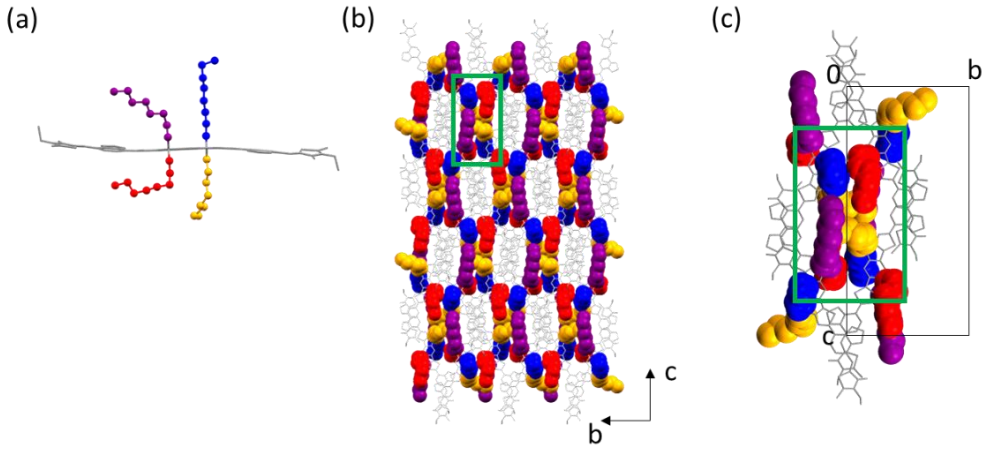

Figure 21| Illustrating the packing of octyl side chains in the intermolecular packing motif of O-IDTBR, determined using X-ray crystallography. (a) Colouration of the different octyl side chains used to help distinguish them within the following diagrams. (b) Macroscopic packing arrangement of octyl side chains viewed from the [100] direction. (c) Highlighting one column of side chain packing within the macroscopic network which spans two unit cells viewed from the [100] direction.

For linear aliphatic side chains, the stabilisation by dispersion interactions is maximised when the chains are in close proximity to each other, either aligned or intertwined. When the atom-atom distances are greater than the sum of van der Waals radii of the atoms, the arrangement is overall stabilising. Analysis of the single crystal structure of O-IDTBR reveals a columnar network of octyl side chains, which intertwine, packing closely together and complementing the network of conjugated chromophores (figure 21). The flexibility of the four octyl side chains allows each to adopt a different conformation (figure 21a).

For the O-IDTBR packing motif, some of the key interchain alignments of the octyl side chains are highlighted in figure 22. The octyl side chain arrangements shown are based on the positions of majority occupancy. As highlighted in figure 21a, two of the octyl side chains (purple and red) are less straight than the other two (blue and yellow). As illustrated in figure 22, the chains twist around or align with each other in a packing motif of their own, filling the space between the network of conjugated chromophores. For example, the two bent chains wrap around the C6-C8 carbon positions of a chain from a second molecule (yellow). Another example is the side chains highlighted in blue, which lie parallel to the C1-C3 of a purple side chains and C1-C4 of a red side chain on a non-adjacent molecule. Similarly, the C4-C8 of the purple chains of non-adjacent molecules align themselves with each other. The close and ordered packing arrangement of the octyl side chains are important in dictating the interdigitated columnar packing motif observed in single crystals of O-IDTBR.

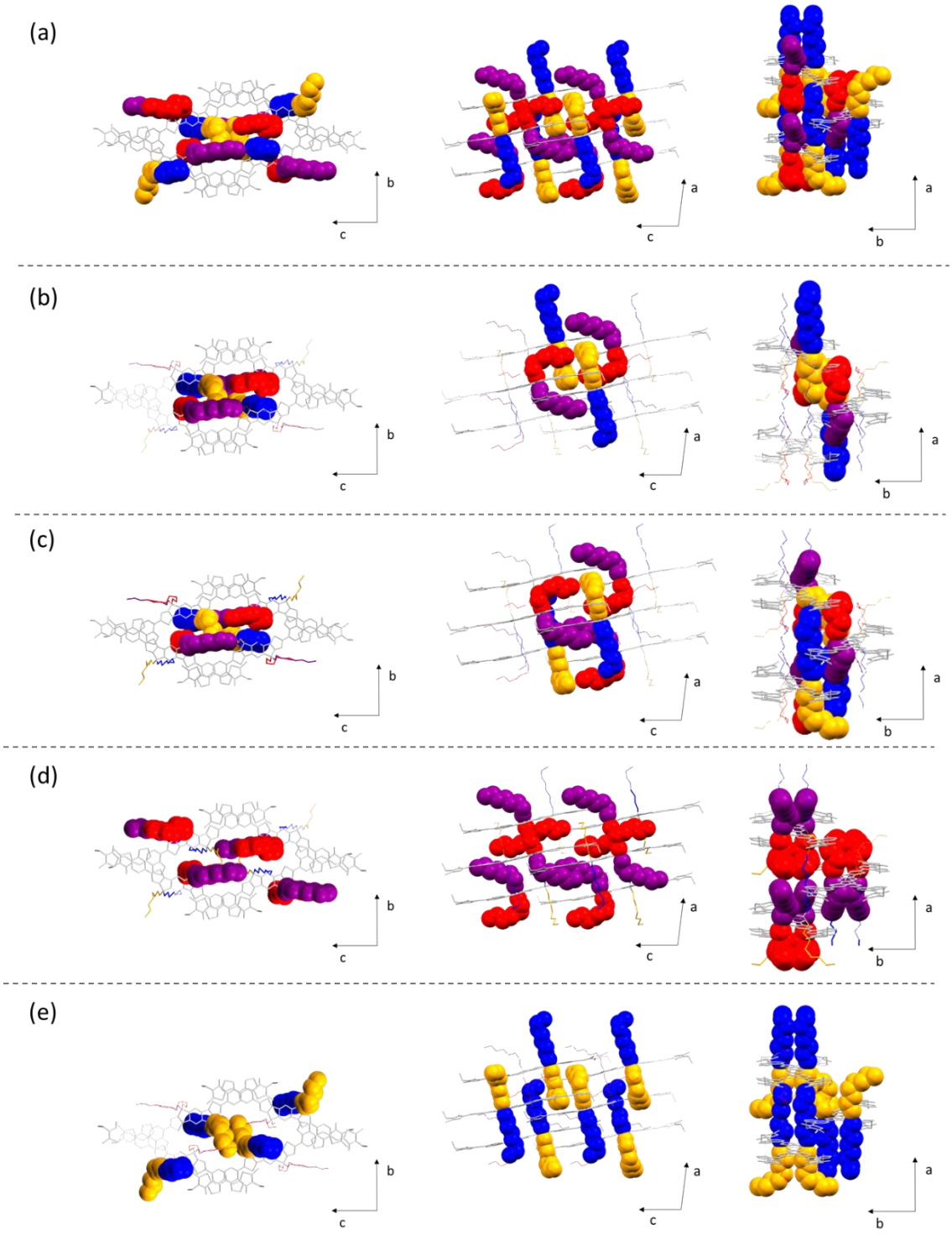

Figure 22| Illustration highlighting some key octyl chain interactions within the single crystal packing motif of O-IDTBR shown left to right in the [100], [010] and [001] directions for six interdigitating O-IDTBR molecules. (a) Illustration with all octyl side chains space filled. (b-e) Illustration with various octyl side chains space filled to show specific interactions. Colours chosen to highlight specific side chain conformations based on the same colour scheme as figure 21.

As the octyl and 2-ethylhexyl chains are structural isomers of each another, similar dispersion stabilisation could be expected. For the aliphatic hydrocarbons equivalent to the side chains, octane and 3-methylheptane, the van der Waals volumes are 88.720 $cm^3 mol^{-1}$ and 88.710 $cm^3 mol^{-1}$ respectively.[127] Where the van der Waals volume is the volume occupied by the molecule, into which another molecule cannot encroach. In the single crystals of O-IDTBR the volume of the side chain is directed away from the electron donating core whereas for EH-IDTBR this volume is concentrated around the core (figure 23). Branched 2-ethylhexyl side chains are less flexible and extend less far from the conjugated backbone than linear octyl side chains.

As previously mentioned, there is significant disorder in the 2-ethylhexyl side chains of EH-IDTBR within the crystal packing motif determined in this work. This disorder is illustrated by grey dots in figure 23a, which represent alternative positions for the side chain carbon atoms. In addition to differences in the orientation of the side chains, the first carbon of the 2-ethylhexyl side chain was not fully resolved in the X-ray diffraction pattern. This generates uncertainty around the position of the whole side chain relative to the conjugated backbone. Another complication associated with the 2-ethylhexyl chains is that they contain a stereochemical centre. It has been shown that isolating enantiomers with specific side chain chirality improves the performance of OTFTs based on p-type diketopyrrolopyrrole small molecules.[128] The EH-IDTBR used in this work was not necessarily enantiomerically pure which could have contributed to disorder within the crystal packing motif. Therefore, only general conclusions about the positions and packing of the 2-ethylhexyl side chains are drawn.

In the packing motif determined for EH-IDTBR, the 2-ethylhexyl side chains align themselves parallel with the conjugated IDTBR backbones. Figure 23b illustrates that this alignment does not block the terminal acceptor units from forming π stacks or the S---N interactions between BT units on adjacent molecules. Each EH-IDTBR molecule possesses four 2-ethylhexyl side chains which can be split into two categories: those coloured in yellow in figure 23 and those coloured green. Typically, the longer branches extend towards the centre of the molecular backbone, aligning parallel with it and the C2 branches extend towards the rhodanine units. However, some of the C6 branches of these chains extend towards the terminal units rather than along the IDT core and this results in uncertainty in the positioning of the side chains in the EH-IDTBR crystal structure. The alternative positions are shown as grey spheres in figure 23a.

In contrast with O-IDTBR, for which the octyl side chains interacted only with chains on other molecules within the packing arrangement, for EH-IDTBR the side chains both above and below the plane of the molecule interact with each other as well as side chains from molecules adjacent to them within the slip stack. Again it is clear that the 2-ethylhexyl side chains are playing an important role in dictating the intermolecular packing motif of EH-IDTBR.

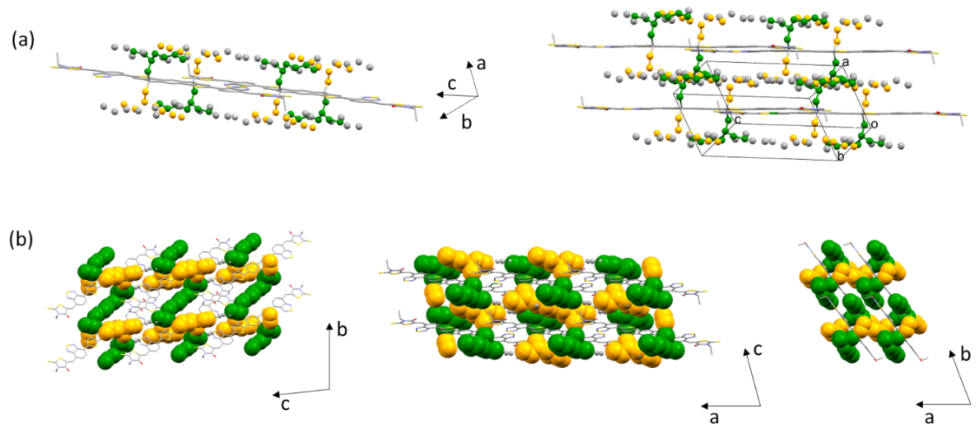

Figure 23| (a) Illustration highlighting positional disorder of the 2-ethylhexyl carbon atoms within the single crystal packing motif of EH-IDTBR. 2-ethylhexyl side chain carbon atoms are represented by spheres. Eight carbons were chosen to represent each chain and coloured in yellow and green. Alternative carbon positions are represented by grey spheres. (b) Illustrations with coloured atoms space filled viewed left to right from the [100], [010] and [001] direction.

2.5 Literature Context

Ideally, transistors based on single crystals would have been investigated as the thin films will contain grain boundaries which will limit charge transport. Several attempts were made to fabricate single crystal OTFTs across various laboratories and with various collaborators with no success. The reason for this is not clear but it is possible that the fragility of the crystals was a problem and that a good contact was not able to be formed between the crystals and the electrodes or dielectric. The conclusions here rely on the packing motif observed in single crystals corresponding to the packing in thin films. As the best performing EH-IDTBR based OTFT was the as cast device it is likely that this film is relatively structurally disordered, however, other studies have shown that even in structurally disordered thin films the single crystal packing motif can be identified in the grazing incidence wide angle X-ray scattering (GIWAXS) pattern.[103]

For O-IDTBR, based on studies following this work, it is certain that the intermolecular packing observed in the single crystal is also present in the annealed thin film.[118,119,129] In one study, micropowder X-ray diffraction identified the same packing motif as present in the single crystals in a powder sample of O-IDTBR.[129] Another study simulated the intermolecular packing of O-IDTBR in the solid state, giving identical packing to the single crystals.[118] Finally, from detailed analysis of the GIWAXS of thin films annealed at 120 °C, X-ray scattering peaks corresponding to the same unit cell as the single crystal were determined.[119]

2.6 Further Optimisation of O-IDTBR based OTFTs through Solvent Annealing

Based on the promising initial performance of O-IDTBR in OTFTs its performance was further explored. The thermal properties of NFAs are highly important in dictating the microstructure of OPV active layers. As has been demonstrated here for O-IDTBR, and elsewhere for other NFAs, the T_g or cold crystallisation (T_{cc}), if they exhibit one, can be used to understand how a thin film including the material should be processed post deposition by thermal annealing to obtain the optimum microstructure for good device performance in OPVs and OTFTs. Thermal annealing (TA) is not the only method by which OSC films are processed post deposition.

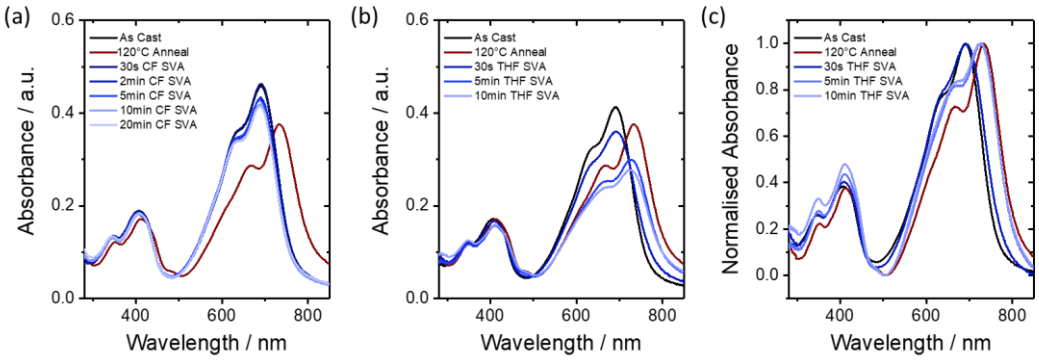

Figure 24| UV-vis absorbance of O-IDTBR thin films after solvent vapour annealing (SVA) and thermal annealing at 120 °C (a) SVA with chloroform (CF), (b) SVA with tetrahydrofuran (THF), (c) normalised UV-vis absorbance of O-IDTBR thin films SVA with THF.

Another post deposition processing technique is solvent vapour annealing (SVA), which is commonly used to optimise the active layer morphology of OPVs and has also been used to improve the performance of OTFTs.[130] The process of SVA involves exposing films of organic semiconductor to a solvent vapour within an enclosed environment, for example a petri dish. The solvent vapour solvates the organic semiconductor material facilitating the

rearrangement of the molecules into a more ordered microstructure. Previously, all small molecule based OPVs using O-IDTBR as the acceptor material in the active layer have exhibited enhanced performance when SVA was used.[111]

To investigate the effect of SVA on the microstructure and charge transport properties of O-IDTBR, OTFTs based on SVA thin films were fabricated. Both chloroform and tetrahydrofuran (THF) were investigated as the solvent vapour. As illustrated in figure 24, SVA with chloroform had no effect on the UV-vis absorption of the thin film, indicating that no structural reorganisation of the O-IDTBR molecules occurs. The reduced absorbance intensity of the SVA thin films relative to the as cast thin film is likely due to some of the absorbing material, O-IDTBR, being dissolved during the process. In contrast, for THF a shift in absorption similar to that observed on thermally annealing the thin film, was observed (figure 24b, c).

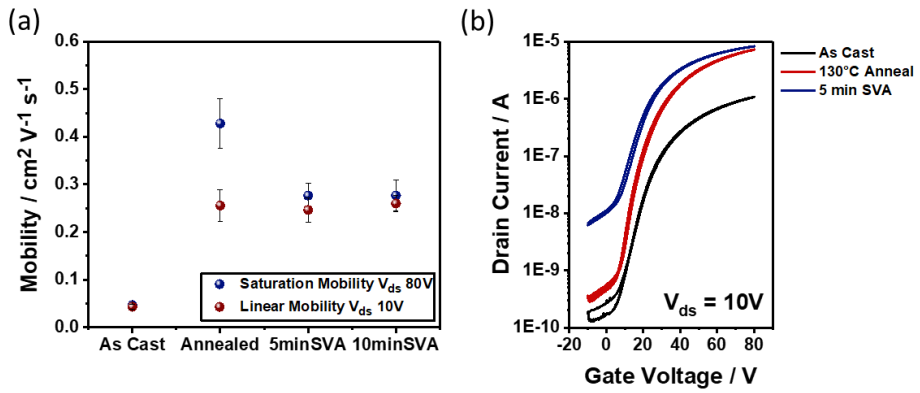

Figure 25| For OTFTs based on thin films of O-IDTBR as cast or post processed by either thermally annealing at 120 °C for 10mins or solvent vapour annealed (SVA) for either 5mins or 10mins. (a) Comparison of linear and saturation mobility with averages taken across 6 OTFTs. (b) Transfer characteristics of the OTFTs operating in the linear regime. [The OTFTs have channel dimensions L/W 40/1000 µm and a 900 nm thick CYTOP dielectric.]

OTFTs based on O-IDTBR thin films SVA with THF for either 5 or 10 minutes were fabricated. As can be seen in figure 25, in the linear regime mobilities equivalent to the OTFTs based on TA thin films were achieved. The saturation mobility extracted from the OTFTs is lower than for TA films, at 0.3 $cm^2 V^{-1} s^{-1}$ for films SVA for 5 mins. However, the saturation and linear mobility match well, which is often not the case in OTFTs. It has been shown that linear and saturation mobilities which match well indicate low energetic disorder in the OSC.[81] As can be seen in figure 25b, for the SVA film based OTFTs the off-currents are much higher than for the thermally annealed devices. It is not clear what causes this increase in off-current but it could be associated with a higher charge carrier

density in the SVA film. Figure 26 displays the linear and saturation transfer characteristics as well as output plot and gate voltage dependence of mobility for OTFTs based on O-IDTBR exposed to THF SVA for 5 minutes. It has been shown successfully that as an alternative to thermally annealing, which is not always possible depending on what substrate the transistor is fabricated on, SVA can be used.

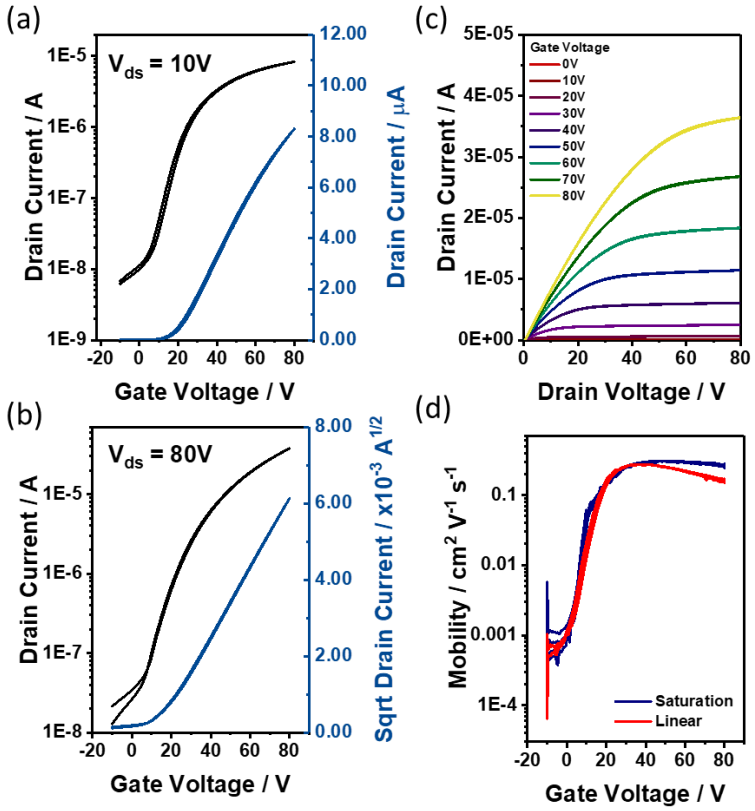

Figure 26| For OTFTs based on thin films of O-IDTBR SVA with THF for 5 minutes: (a) Linear (V_{ds} = 10 V) transfer characteristics, (b) Saturation (V_{ds} = 80 V) transfer characteristics, (c) Output characteristics and (d) Mobility as a function of gate voltage. [Channel dimensions 40/1000μm, CYTOP dielectric 900 nm.]

2.7 Contact Engineering in O-IDTBR based OTFTs

The performance and therefore mobility of organic semiconductors in OTFTs is highly dependent on the device architecture and choice of contacts.[131–133] In order to minimise the barrier to charge injection and reduce contact resistance, the workfuction of the source and drain contacts can be aligned with the electron affinity (EA) of the OSC material in the case of electron transport and the ionisation potential (IP) in the case of hole transport.

Table 5| For as cast and thermally annealed films of O-IDTBR the ionisation potentials (IP) determined using PESA and optical band gap (E_g) estimated from UV-vis absorption.

Conditions	IP / eV	E_g / eV
O-IDTBR, As Cast	5.59	1.55
O-IDTBR, Anneal 120°C/10mins	5.50	1.50

Several methods for determining the IP and EA of OSCs are used in literature. The use of ultra-violet photoelectron spectroscopy (UPS) to determine the IP, combined with low energy inverse photoemission spectroscopy (LE-IPES) to determine the EA has been highlighted as a good to characterise the energy levels of OSCs.[9,134] Previously, the IP and EA of O-IDTBR have been determined using these techniques as 5.67 eV and 3.55 eV respectively.[135,136] Photoelectron spectroscopy in air (PESA), which differs from UPS in that it uses lower intensity UV irradiation and is performed under ambient conditions rather than vacuum, can also be used to determine the IP of OSCs. In this work, using PESA, an IP of 5.59 eV was determined for as cast thin films of O-IDTBR. This is in good agreement with the previously reported PESA determined IP value for O-IDTBR of 5.6 eV.[136] Another commonly used technique to determine the IP and EA of an OSC is cyclic voltammetry (CV). Previously using CV IP and EA values of 5.45 eV and 3.90 eV were determined for O-IDTBR.[110] Notably these CV derived values differ significantly from the UPS/IPES values. Previously good correlation between IPES and CV derived EAs has been reported.[134]

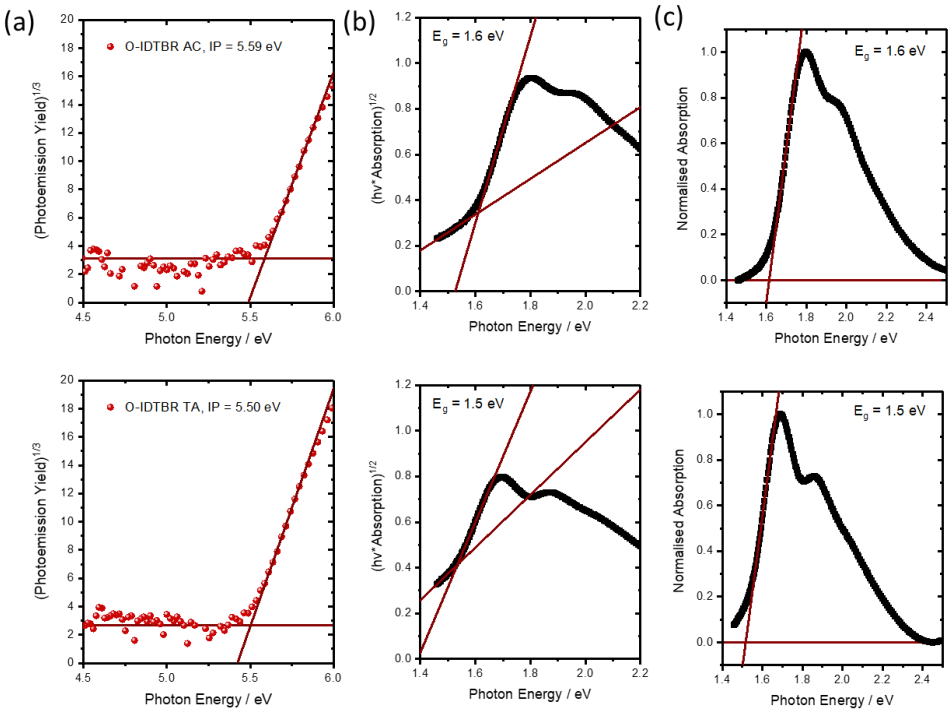

Figure 27| (a) Plots of the cube root of photoemission yield against photon energy, (b) Tauc plots and (c) extrapolated normalised absorbance plots for thin films of O-IDTBR either as cast (AC) or thermally annealed (TA) at 120 °C.

As is clear from the UV-vis absorption spectra of as cast and annealed films of O-IDTBR (figure 14) there is a large red shift in absorption on annealing at just above the cold crystallisation temperature. Therefore, the annealed film has a smaller optical band gap (E_g) and the energy levels of the material have changed. The E_g can be roughly estimated from the UV-vis absorption of the OSC, either using a Tauc plot (figure 27b) or extrapolating the normalised absorption (figure 27c).[134,137] The E_g corresponds to the energy of the long wavelength edge of absorption and will be less than the gap between the IP and EA, due to the binding energy of excitons.[134] Elsewhere it has been reported that E_gs of OSCs can be reported with an accuracy of ± 0.05 eV when determined by extrapolating the optical absorption.[134] Here, an E_g of 1.50 eV was determined from the onset of absorption of as cast thin films and 1.55 eV from thin films annealed at 120 °C. The E_g can also be determined from the intersection of the thin film UV-vis absorption and photoemission spectra, elsewhere using this technique a wider E_g for O-IDTBR of 1.74 eV was reported.[136]

The observed red-shift in absorption on thermally annealing thin films of O-IDTBR at just above the cold crystallisation temperature, 120 °C, will also relate to a shift in the IP and

EA of the material. Here, PESA was used to assess the difference in IP between an as cast and annealed thin film of O-IDTBR (table 5). The cube root of the photoemission yield as a function of photon energy for as cast and annealed films of O-IDTBR are shown in figure 24a. To assess the error in the measurement of IP using PESA, the IP measurement for the as cast film was repeated on a different day with a freshly coated film and consistent results were obtained, 5.585 eV and 5.587 eV. This indicates that the observed difference in IP between the as cast and annealed film is accurate.

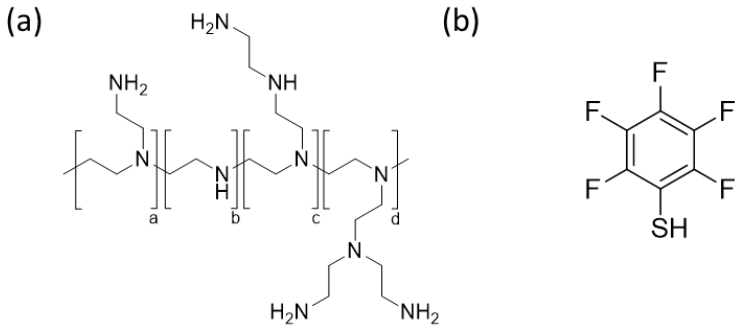

Figure 28| Chemical structures of (a) polyethylenimine (PEI) and (b) pentafluorobenzenethiol (PFBT).

The highest mobilities for n-channel OTFTs based on O-IDTBR reported here were achieved using evaporated gold electrodes coated with a thin layer of polyethylenimine (PEI) (figure 28). Upon physisorption of the PEI to the electrode, due to the aliphatic amine groups a large molecular dipole is induced, thereby decreasing the workfunction of the metal contact and enhancing electron injection/extraction.[138] This low workfunction electrode blocks hole injection into the channel making it electron selective.[132,139] Previously PEI has been introduced to give unipolar electron transporting OTFTs using ambipolar OSCs.[139,140] As shown in figure 29a, the EA of O-IDTBR is well aligned with the workfunction of PEI modified gold, which has previously been reported as 3.94 eV.[132]

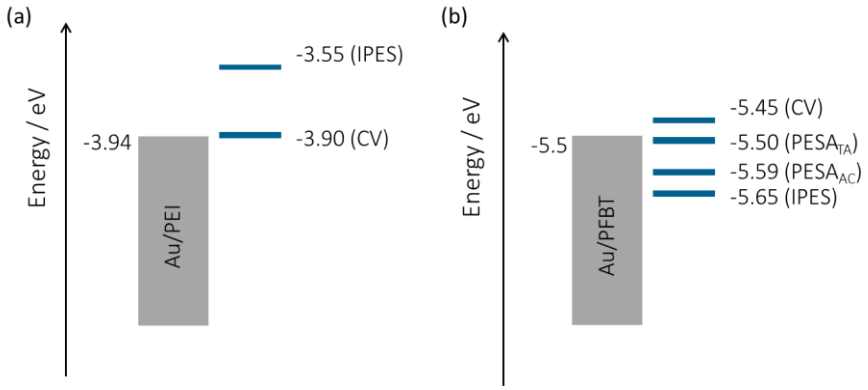

Figure 29| Schematic illustrating the alignment of the workfunction of (a) polyethyleneimine (PEI) modified gold[132] with the EA of thin films of O-IDTBR, which has previously been determined as 3.55 eV using LE-IPES and 3.90 eV using CV.[110,136] (b) of pentafluorobenzenethiol (PFBT) modified gold[141] with the IP of thin films of O-IDTBR. In this work the IPs of as cast (AC) thin films and thin films thermally annealed at 120 °C (TA) were determined using PESA. Previously the IP has been determined as 5.45 eV using CV and 5.65 eV using IPES.[110,136]

For p-type OTFTs often a pentafluorobenzenethiol (PFBT) self-assembled monolayer (SAM) is used to increase the workfunction of the metal contacts and better align them with the IP of the OSC. A polar monolayer will form on the metal surface inducing a potential energy shift. A workfunction of 5.5 eV has previously been reported for PFBT modified gold.[109,141] As shown in figure 29b, the workfunction of PFBT modified gold source and drain contacts is well aligned with the IP of annealed thin films of O-IDTBR.

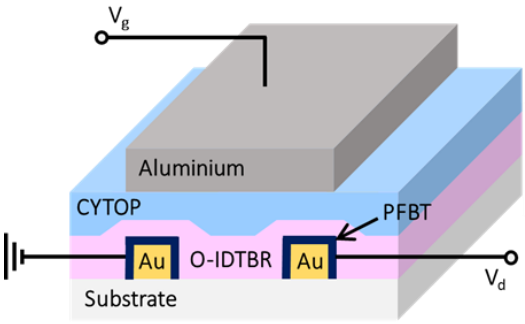

Figure 30| Device architecture of O-IDTBR OTFTs employing PFBT modified gold (Au) source/drain contacts and a CYTOP dielectric.

To investigate if O-IDTBR exhibits ambipolar charge transport, top-gate staggered OTFTs based on O-IDTBR were fabricated using PFBT modified gold source and drain electrodes as illustrated in figure 30. These OTFTs did exhibit ambipolar charge transport, meaning OTFT operation at positive and negative gate biases were observed, demonstrating that both holes and electrons are able to accumulate and be extracted from the OTFT channel. Example transfer and output plots for the ambipolar O-IDTBR based OTFTs are displayed

in figure 31. From these OTFTs, electron mobilities of 0.1 cm^2 V^{-1} s^{-1} and 0.2 cm^2 V^{-1} s^{-1} were extracted for the linear (V_{ds} 40 V) and saturation (V_{ds} 160 V) regime respectively. Hole mobilities of 0.06 cm^2 V^{-1} s^{-1} and 0.1 cm^2 V^{-1} s^{-1} were extracted for the linear (V_{ds} -40V) and saturation (V_{ds} -160V) regime respectively. The electron mobilities determined are lower than those extracted from OTFTs with PEI modified gold source and drain contacts and this likely results from the significantly larger barrier to electron injection in OTFTs employing a PFBT rather than PEI source/drain contact modification.

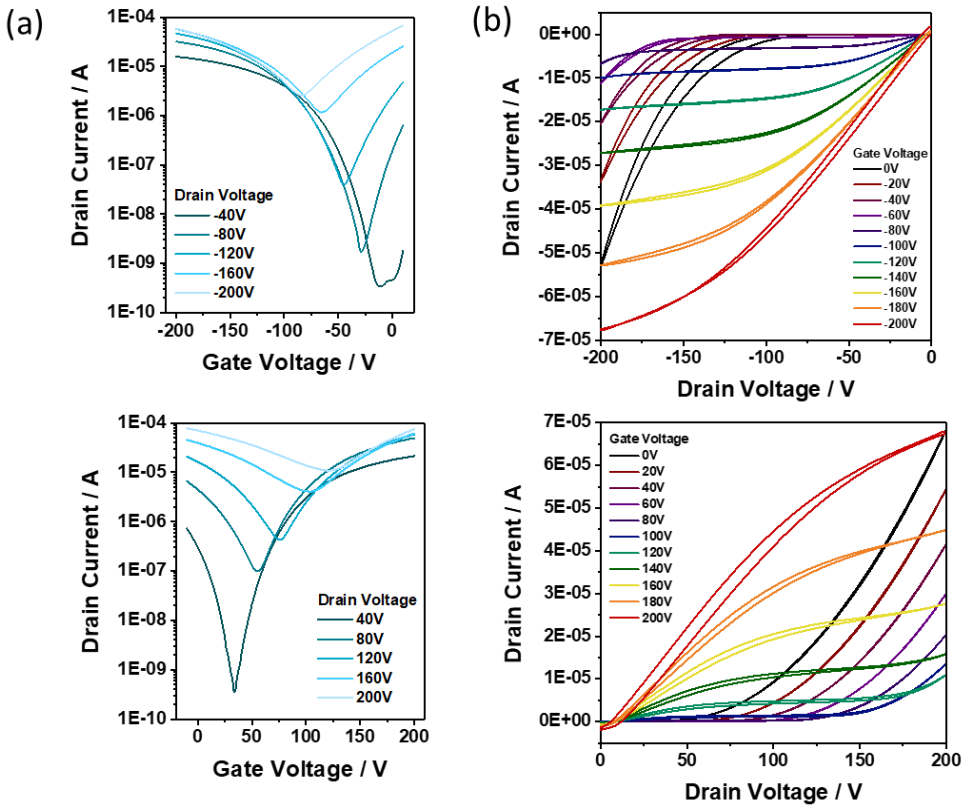

Figure 31| (a) Saturation regime forward scan transfer characteristics for p-type (V_{ds} = –40 to –200 V) and n-type (V_{ds} = 40 to 200 V) operation and (b) output characteristics for OTFTs based on O-IDTBR thin films annealed at 120 °C and employing PFBT modified gold source/drain electrodes with channel dimensions L50/W1000 µm.

The implications of organic photovoltaic (OPV) acceptors exhibiting both electron and hole transport are significant.[142,143] In general, the acceptor material in an OPV is considered to form a percolating network allowing transport of electrons from the interface between the acceptor and donor material, where photogenerated excitons are separated into free charges, to the cathode. The fact that holes can also be transported in the acceptor domain could have significant implications for charge transport and recombination in OPVs. Similar ambipolar transport has been observed for $PC_{60}BM$, for which hole and electron mobilities of 0.1 $cm^2\ V^{-1}\ s^{-1}$ and 0.4 $cm^2\ V^{-1}\ s^{-1}$ were reported in similar voltage regimes and with very similar transfer and output characteristics.[142,144] Previous to this, approximately equal hole and electron mobilities were observed for $PC_{60}BM$ based ambipolar OTFTs and therefore its promise as a material that could be used in the development of complementary logic circuits was highlighted.[145]

2.8 Conclusion

By comparing the intermolecular packing and performance in OTFTs of O-IDTBR and EH-IDTBR, the choice of aliphatic side chain has been shown to have a significant impact on intermolecular packing and thereby on electron mobility. Using single crystal X-ray diffraction, the packing motif of EH-IDTBR was shown to be a slipped stack arrangement, which leads to dominant transfer integrals in only one dimension. It has been shown that packing motifs exhibiting transfer integrals isotropic in different directions will exhibit a higher tolerance of carrier transport towards disorder and therefore lead to higher mobilities.[1] The packing motif of O-IDTBR is shown to have a three-dimensional structure, yielding three dominant transfer integrals isotropic in different directions. These differences in packing motif are found to be largely dictated by the choice of side chain.

In line with this, films of O-IDTBR annealed at 120 °C, which corresponds to the cold crystallisation exotherm, are shown to deliver impressive saturation and linear electron mobilities in OTFTs, of 0.4 $cm^2\ V^{-1}\ s^{-1}$ and 0.3 $cm^2\ V^{-1}\ s^{-1}$ respectively. In contrast, for EH-IDTBR based OTFTs the mobilities were an order of magnitude lower. This difference in mobility is related back to the intermolecular packing in the solid state determined from single crystals. Based on further studies, it is known with relative certainty that the intermolecular packing motif present in the single crystals of O-IDTBR is also present in the thin films annealed at just above the cold crystallisation exotherm.[118,119,129] It is important to note that this observed microstructure does not necessarily correspond to the microstructure within the O-IDTBR thin film in which the charges are accumulated and

transported during OTFT operation, however, with currently available characterisation techniques this is not possible to elucidate.[146]

Based on the good performance achieved in the initial study for O-IDTBR, this material was further explored in OTFTs. Solvent vapour annealing (SVA) of O-IDTBR thin films was shown to deliver similar linear mobilities of 0.3 $cm^2 V^{-1} s^{-1}$ to those achieved thermally annealing the thin film at just above the cold crystallisation exotherm, 120 °C. Therefore, SVA can be used as an alternative to thermal annealing which is not always compatible with the fabrication of OTFTs and OPVs, for example on plastic substrates. Finally, by aligning the workfunction of the source/drain contacts with the IP of O-IDTBR thin films, ambipolar transport in O-IDTBR is observed. This has implications for the conventional thinking that only electron transport occurs in domains of acceptor material in OPVs.

Chapter 3: Impact of O-IDTBR Structure Variation on Thin Film Device Performance

In Chapter 2 the importance of aliphatic side chains in dictating the intermolecular packing and thereby charge transport properties of IDTBR was highlighted. In this chapter the effect of varying the chemical structure of O-IDTBR on its OTFT performance is further explored. By varying the length of the aliphatic side chains, terminal electron accepting units and electron donating core of O-IDTBR it was hoped that enhanced performances in OTFTs and OPVs would be achieved. Many thanks to Weimin Zhang, who synthesized and purified the O-IDTBR derivatives used in this chapter and to Rachael Found, who performed the O-IDTBCN DSC included in this chapter and worked with many IDTBR derivatives during her master's thesis.

3.1 Background

The general design of the types of calamitic NFAs investigated in this thesis are to include an electron rich donor core unit, flanked by terminal electron deficient acceptor units and with pendant aliphatic side chains on the donor core, as described in the introduction. A large body of work has been done varying the chemical structure of NFAs and investigating how these structural modifications affect OPV performance.[147] Less work has focused on how modifications to the chemical structure affect the charge transport properties of the neat materials.

3.2 Investigating Linear Side Chain Derivatives of IDTBR

Having identified, during the work outlined in Chapter 2, that the linear octly side chain derivative of IDTBR (O-IDTBR or C_8-IDTBR) delivered such good OTFT performance, other linear side chain analogues, hexyl and decyl (C_6-IDTBR and C_{10}-IDTBR), were investigated. The chemical structures of the three materials are shown in figure 32.

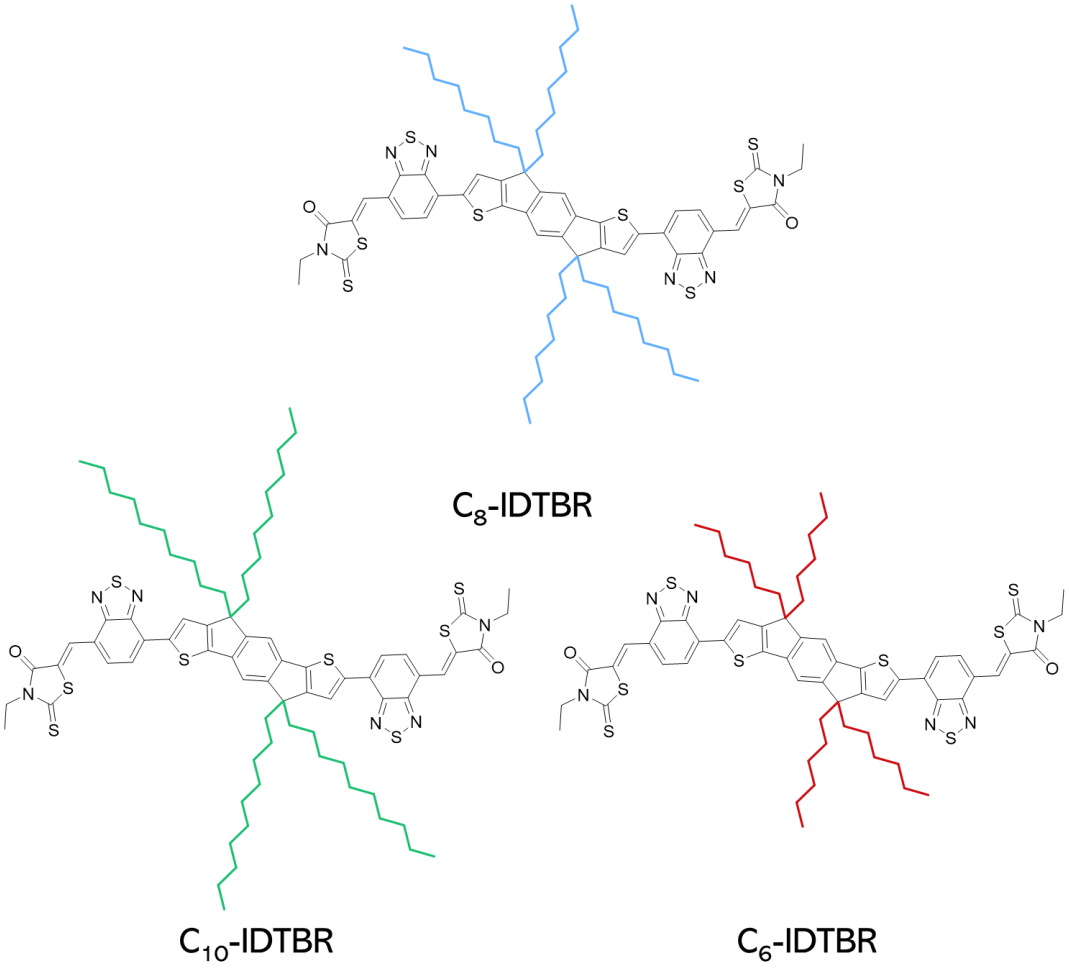

Figure 32| Chemical structures of C_{10}-IDTBR, C_8-IDTBR (O-IDTBR) and C_6-IDTBR.

First the material properties of the new NFAs were investigated and compared with that of C_8-IDTBR. The first and second cooling and heating cycles of the three materials are shown in figure 33. The third heating cycles were also performed and resembled the second cycle. The key peaks which may be observed in the DSC thermogram of an OSC are the glass transition temperature (T_g), cold crystallisation temperature (T_{CC}) and melt temperature (T_m). The glass transition is an endothermic process in which the material changes from a glassy solid to viscous state on heating.[148] It has previously been noted that peaks at the T_g are commonly not observed in DSC experiments on OSCs.[148,149] For NFAs often a cold crystallisation is observed, which is an exothermic crystallisation of the material in its viscous state.

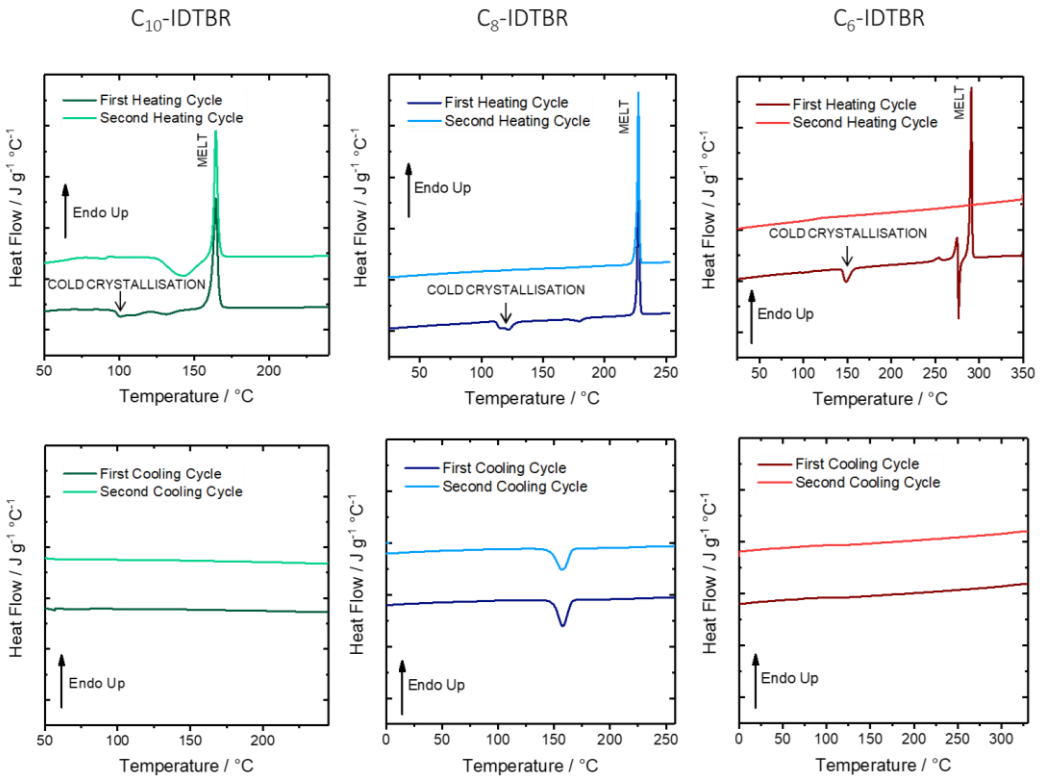

Figure 33| First and second differential scanning calorimetry heating and cooling thermograms of C_6-IDTBR, C_8-IDTBR and C_{10}-IDTBR. The thermograms are offset for clarity and were taken at a scan rate of 5 °C min^{-1}.

Both the T_g and T_{CC} typically occur at temperatures relevant for the optimisation of the OSC layer in thin film devices, for example by thermal annealing, and also have implications for the thermodynamic stability of devices based on the OSC.[149] The melt occurs at much higher temperatures and is the transition from solid to liquid state, marked by a large endotherm. In studies investigating other NFAs it has been suggested that the cold crystallisation peak likely masks the glass transition and can be used as a proxy for the T_g.[148] The T_g of NFAs has been related to the morphological stability of OPVs, NFAs with a higher T_g will have lower diffusion coefficients and so morphological instability of the BHJ blends will be lower.[148,150]

All three materials exhibit a cold crystallisation in the first heating cycle, which is not present on subsequent cycles. For C_6-IDTBR, C_8-IDTBR and C_{10}-IDTBR the peaks of these exotherms are at 147 °C, 118 °C and 101 °C respectively. For the longer side chain analogue, C_{10}-IDTBR, both the cold crystallisation and crystalline phase melt occur at lower temperatures than for C_8-IDTBR and for the shorter side chain analogue, C_6-IDTBR these occur at higher temperatures (table 6). Cold crystallisation is associated heating a

non-crystalline sample, for example a sample which has been cooled quickly and not had time to recrystallise. The slow cooling cycle performed in the DSC experiments means that the sample does have time to recrystallise and so the cold crystallisation will not be observed in subsequent cycles.

For C_6-IDTBR the absence of a melt peak in subsequent cycles after the first heating cycle is possibly due to the degradation or ablation of the sample during the high temperature scan, up to 360 °C, performed to elucidate the melt peak at 290 °C. It is not clear what causes the preceding endothermic and exothermic peaks in the cycle between 245 – 285 °C. Only in the cooling cycle of C_8-IDTBR are any features observed, this exothermic peak is associated with a phase transition of the material. For C_{10}-IDTBR it is not clear what cases the feature in the heating cycles with an onset at 125 °C, which becomes prominent in the second and third cycles.

Table 6| For C_{10}-IDTBR, C_8-IDTBR (O-IDTBR) and C_6-IDTBR the temperature of melt onset (T_m) and of cold crystallisation peak (T_{cc}). As well as peak absorption wavelength for as cast thin films and for thin films annealed at just above their T_{cc}.

NFA	T_m / °C	T_{cc}	Abs max. / nm	Abs max. at T_{cc} / nm
C_{10}-IDTBR	157	101	690	684
C_8-IDTBR	223	118	690	733
C_6-IDTBR	285	147	690	682

As was demonstrated in *Chapter 1* for C_8-IDTBR, the cold crystallisation temperature is important in dictating changes in the morphology of neat films of the NFA. Figure 34 displays the UV-vis absorbance of C_6-IDTBR, C_8-IDTBR and C_{10}-IDTBR thin films. As cast thin films of all three materials exhibit a peak absorption at 690 nm. Unlike for C_8-IDTBR, for C_6-IDTBR and C_{10}-IDTBR a prominent red-shift in absorption on annealing the thin films of material at just above their cold crystallisation temperatures is not observed. This indicates that the same highly ordered microstructure identified for C_8-IDTBR might not be forming for the other NFAs. For both C_{10}-IDTBR and C_6-IDTBR a slight blue shift in peak absorption is observed on annealing at just above the onset of cold crystallisation (110 °C for C_{10}-IDTBR and 160 °C for C_6-IDTBR), to 684 nm and 682 nm respectively. This is similar to the blue shift in absorption observed when annealing thin films of EH-IDTBR, from 673 nm to 665 nm.

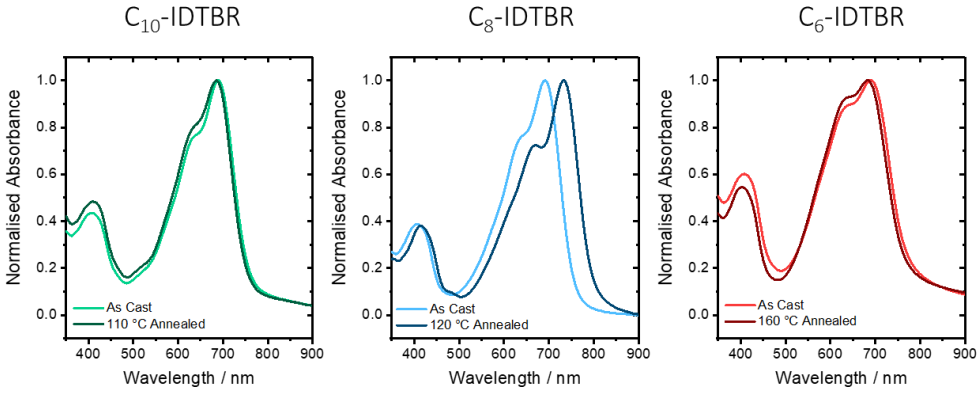

Figure 34| UV-vis absorbance for as cast and annealed thin films of C_6-IDTBR, C_8-IDTBR and C_{10}-IDTBR. Plots are normalised to the peak absorbance of each film.

As discussed in *Chapter 1*, for OTFTs based on EH-IDTBR the best performance and highest mobility were achieved for as cast thin films. OTFTs based on as cast thin films of C_6-IDTBR delivered average saturation and linear mobilities of 0.02 $cm^2\ V^{-1}\ s^{-1}$ and 0.03 $cm^2\ V^{-1}\ s^{-1}$, respectively. Example OTFT transfer and output characteristics are displayed in figure 35 and averages are given for 5 transistors with channel dimensions of 40/1000 µm. In contrast to OTFTs based on EH-IDTBR and O-IDTBR, these OTFTs exhibit non-ideal transfer characteristics, with a non-linear drain current observed as a function of gate voltage. As a result, the calculated mobility has a strong dependence on the gate voltage, meaning these mobilities are possibly overestimated. It was not possible to record transfer plots for OTFTs based on films of C_6-IDTBR annealed at 160 °C. It is not clear why this is the case, however, two possible reasons could be that annealing of the PEI coated electrodes at 160 °C may have resulted in degradation of the material or that the surface roughness of the C_6-IDTBR may have increased resulting in significant charge trapping at the interface between the OSC and dielectric. Overall, it is clear that C_6-IDTBR based OTFTs do not perform as well as either C_8-IDTBR or EH-IDTBR transistors.

Table 7| For OTFTs based on the NFAs C_{10}-IDTBR, C_8-IDTBR (O-IDTBR) and C_6-IDTBR: mobility values extracted in the linear (μ_{lin}, V_{ds} = 10V) and saturation (μ_{sat}, V_{ds} = 80 V). Thin films of the NFAs, on which the OTFTs were based, were as cast or annealed at just above the cold crystallisation temperatures determined using DSC (table 6)

	As cast		Thermally Annealed	
NFA	μ_{lin} / $cm^2\ V^{-1}\ s^{-1}$	μ_{sat} / $cm^2\ V^{-1}\ s^{-1}$	μ_{lin} / $cm^2\ V^{-1}\ s^{-1}$	μ_{sat} / $cm^2\ V^{-1}\ s^{-1}$
C_{10}-IDTBR	0.06 ± 0.02	0.04 ± 0.01	0.2 ± 0.0	0.08 ± 0.01
C_8-IDTBR	0.06 ± 0.03	0.07 ± 0.04	0.3 ± 0.0	0.4 ± 0.0
C_6-IDTBR	0.03 ± 0.00	0.02 ± 0.00	-	-

[a] Means and standard deviations taken over at least 5 transistors for each processing condition with channel dimensions 40/1000 µm and a 900 nm CYTOP dielectric. [b] Thermally annealed C_6-IDTBR based OTFTs did not give transfer characteristics.

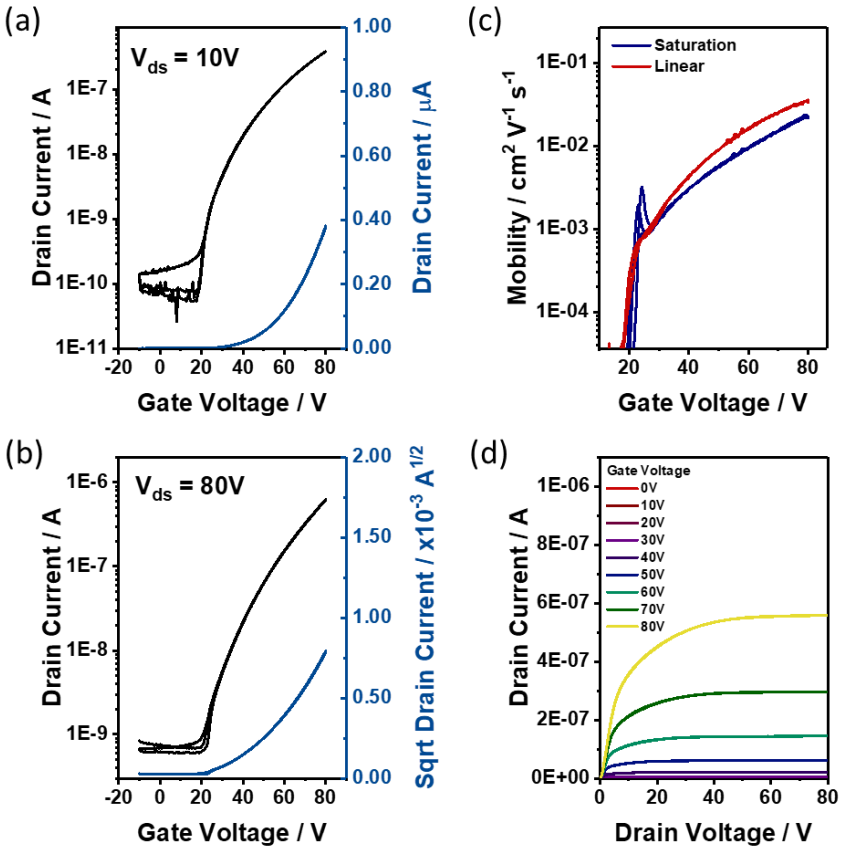

Figure 35| For OTFTs based on as cast films of C_6-IDTBR, representative (a) linear (V_{ds} = 10 V) transfer characteristics, (b) saturation (V_{ds} = 80 V) transfer characteristics, (c) calculated mobility plotted as a function of gate voltage and (d) output characteristics. [Channel dimensions L/W 40/1000 µm, 900 nm CYTOP dielectric]

For OTFTs based on as cast thin films of C_{10}-IDTBR linear and saturation mobilities of 0.06 cm^2 V^{-1} s^{-1} and 0.04 cm^2 V^{-1} s^{-1} were calculated. For OTFTs based on films of C_{10}-IDTBR annealed at 110 °C a large improvement in linear mobility to 0.2 cm^2 V^{-1} s^{-1} was observed. This enhancement is despite no shift in absorption being observed when C_{10}-IDTBR is annealed at just above the cold crystallisation temperature, which indicates the same structural reorganisation observed for C_8-IDTBR is not being observed for C_{10}-IDTBR. Example OTFT transfer and output characteristics for the annealed devices are displayed in figure 36. As for C_6-IDTBR, these OTFTs exhibit a gate voltage dependence of mobility (figure 36c) with a bowing shape observed in the transfer characteristics (figure 36a, b). This bowing is often associated with an overestimation of mobility values.[79]

Based on these results C_6-IDTBR and C_{10}-IDTBR both exhibit inferior OTFT performance and lower mobilities than C_8-IDTBR. This highlights that the selection of not just linear

side chains, but specifically octyl side chains when O-IDTBR was first designed was particularly intuitive or fortunate.

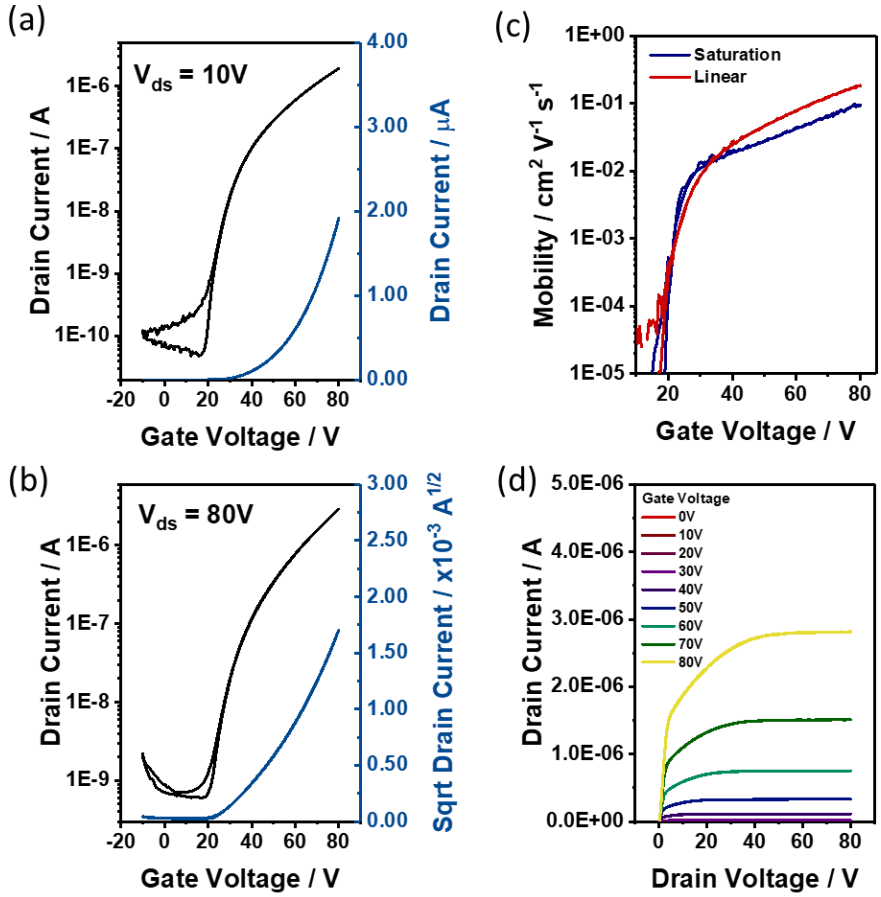

Figure 36| For OTFTs based on thin films of C_{10}-IDTBR annealed at 110 °C, representative (a) linear (V_{ds} = 10 V) transfer characteristics, (b) saturation (V_{ds} = 80 V) transfer characteristics, (c) calculated mobility plotted as a function of gate voltage and (d) output characteristics. [Channel dimensions L/W 40/1000 µm, 900 nm CYTOP dielectric]

3.3 Impact of End Group Modulation on Transistor Mobility

The type of NFAs investigated in this thesis are designed to have their terminal electron deficient acceptor units accessible for π-π stacking to facilitate charge transport between the molecules.[54] As was shown in *Chapter 2* for IDTBR, and has been shown for many other NFAs, including Y6 and ITIC, these acceptor units π-π stack within the intermolecular packing motif of the molecules.[103] Since the LUMO of the NFAs will be localised on these terminal acceptor units, changing them should have a significant effect on electron mobility. In O-IDTBR, the electron acceptor unit consists of a benzothiadiazole combined with rhodanine. Here two end-group derivatives of O-IDTBR are investigated,

where rhodanine is replaced with either dicyanovinyl (O-IDTBCN) or 1,1-dicyanomethylene-3-indanone (O-IDTBIC) terminal units. The chemical structures of O-IDTBR, O-IDTBCN and O-IDTBIC are shown in figure 37.

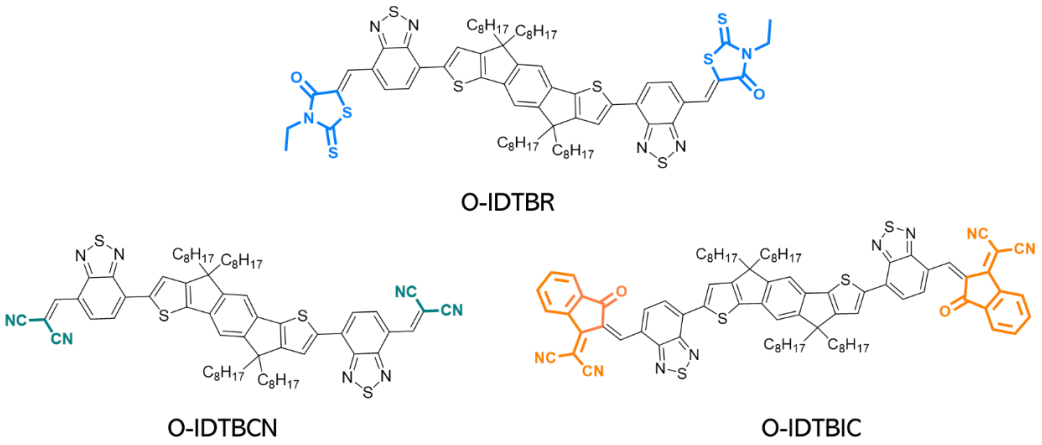

Figure 37| Chemical structures of O-IDTBR, O-IDTBCN and O-IDTBIC.

First to identify suitable anneal temperature for the O-IDTBCN based OTFTs, DSC was carried out. From the DSC thermograms shown in figures 38b and c there are no clear endotherms or exotherms below the melt peak at 197 °C in either the heating or cooling cycles. It has previously been highlighted that often for NFAs the glass transition temperature cannot be identified from DSC but can be observed from the shift in UV-vis absorbance of thin films on annealing relative to the as cast films.[151] Similarly to O-IDTBR, a red-shift in peak absorption is observed on annealing thin films at 130 °C, from 725 nm to 760 nm (figure 38a). This shift can be associated with increased structural order in the film.

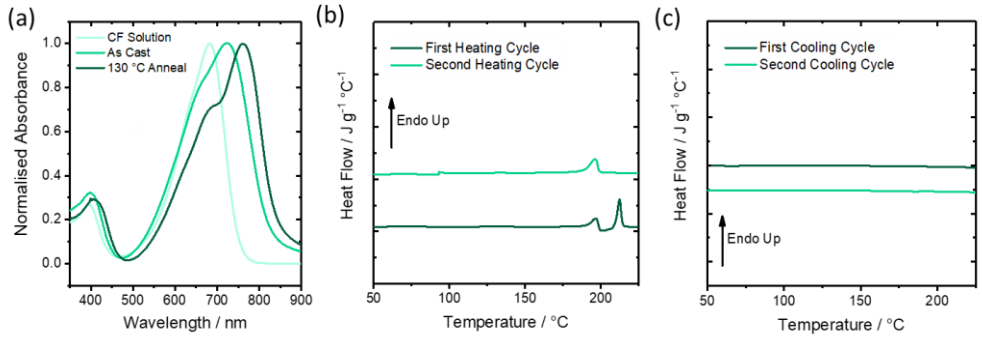

Figure 38| UV-vis absorbance of O-IDTBCN in chloroform (CF) solution, as cast thin films and thin films annealed at 130 °C. (b) First and second differential scanning calorimetry heating thermograms of O-IDTBCN. (c) First and second differential scanning calorimetry cooling thermograms of O-IDTBCN. The thermograms are offset for clarity and were taken at a scan rate of 10 °C min^{-1}.

Next, OTFTs based on both as cast thin films of O-IDTBCN and thin films annealed at 130 °C were fabricated. Figure 39 displays the transfer and output characteristics of the best performing OTFTs based on O-IDTBCN, for which the OSC layer was thermally annealed at 130 °C. Table 8 presents the average linear and saturation mobilities of as cast and thermally annealed O-IDTBCN based OTFTs. Electron mobilities of 0.03 $cm^2\ V^{-1}\ s^{-1}$ were determined for OTFTs operating in both the linear and saturation regime. As cast films of O-IDTBCN yielded an inferior performance with mobilities of 0.01 $cm^2\ V^{-1}\ s^{-1}$, achieved in both the linear and saturation regime. Unlike for O-IDTBR where annealing the thin films at the temperature associated with the red-shift in absorption led to an order of magnitude increase in electron mobility, for O-IDTBCN only a small increase in mobility is observed.

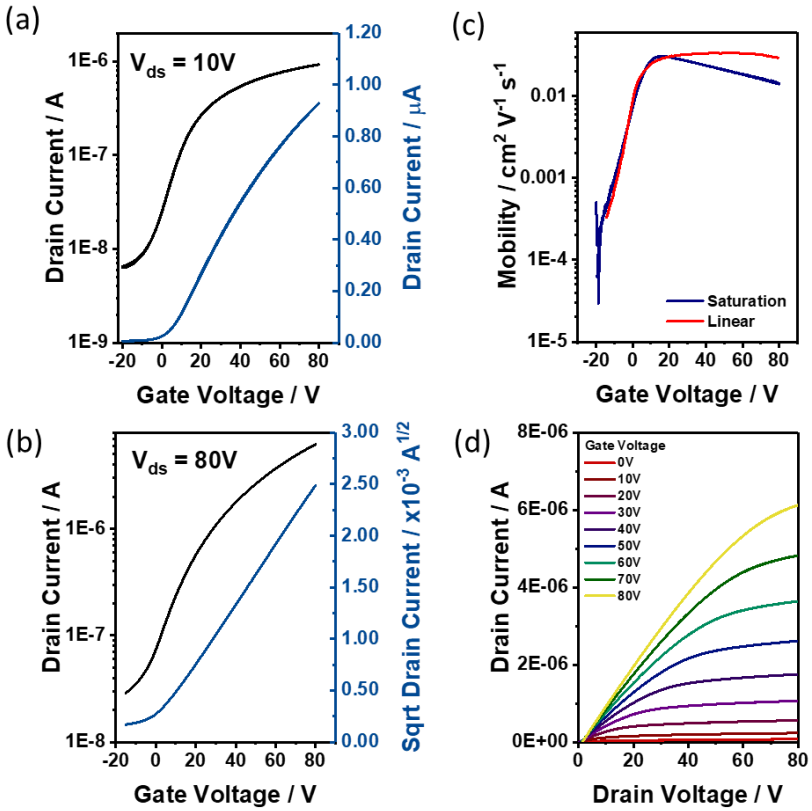

Figure 39| For OTFTs based on thin films of O-IDTBCN annealed at 130 °C, representative (a) linear (V_{ds} = 10 V) transfer characteristics, (b) saturation (V_{ds} = 80 V) transfer characteristics, (c) calculated mobility plotted as a function of gate voltage and (d) output characteristics. [Channel dimensions L/W 40/1000 µm, 900 nm CYTOP dielectric]

Table 8| For the NFAs O-IDTBCN, O-IDTBR and O-IDTBIC. Mobility values extracted in the linear (μ_{lin}, V_{ds} = 10V) and saturation (μ_{sat}, V_{ds} = 80 V) regime for OTFTs based on as cast thin films and thin films annealed at 120 °C, 130 °C and 140 °C for O-IDTBR, O-IDTBCN and O-IDTBIC respectively.

	As cast		Thermally Annealed	
NFA	μ_{lin} / cm^2 V^{-1} s^{-1}	μ_{sat} / cm^2 V^{-1} s^{-1}	μ_{lin} / cm^2 V^{-1} s^{-1}	μ_{sat} / cm^2 V^{-1} s^{-1}
O-IDTBCN	0.009 ± 0.003	0.01 ± 0.00	0.03 ± 0.01	0.03 ± 0.00
O-IDTBIC	0.003 ± 0.001	0.006 ± 0.002	0.002 ± 0.001	0.003 ± 0.002
O-IDTBR	0.06 ± 0.03	0.07 ± 0.04	0.3 ± 0.0	0.4 ± 0.0

[a] *Means and standard deviations taken over at least 5 transistors for each processing condition with channel dimensions 40/1000 µm and 900 nm CYTOP dielectric.*

The second terminal acceptor unit derivative of O-IDTBR investigated is O-IDTBIC. O-IDTBIC contains a 1,1-dicyanomethylene-3-indanone (IC) terminal unit, which is combined with a benzothiadiazole (BT) unit to give the electron deficient parts of the molecule. The IC unit is present in ITIC and Y1, which can both be regarded as breakthrough materials in the development of OPVs.[36,69,72] Disproportionately, NFAs containing the IC terminal accepting unit or a modification of this unit have been developed and for this reason it was an interesting moiety to investigate.[147] After the development of both ITIC and Y1 a range of NFAs with derivative chemical structures were and continue to be developed. However, the IC unit has not previously been investigated in combination with the BT unit as in O-IDTBIC.

DSC was again carried out to first investigate the thermal properties of O-IDTBIC and the first and second heating and cooling cycles are presented in figures 40a and 40b. In the first heating cycle an exotherm, with an onset at 134 °C is observed, which is assigned as the cold crystallisation (T_{CC}). On annealing thin films of O-IDTBIC at just above the T_{CC}, at 140 °C, a red-shift in peak absorbance is observed from 815 nm to 840 nm.

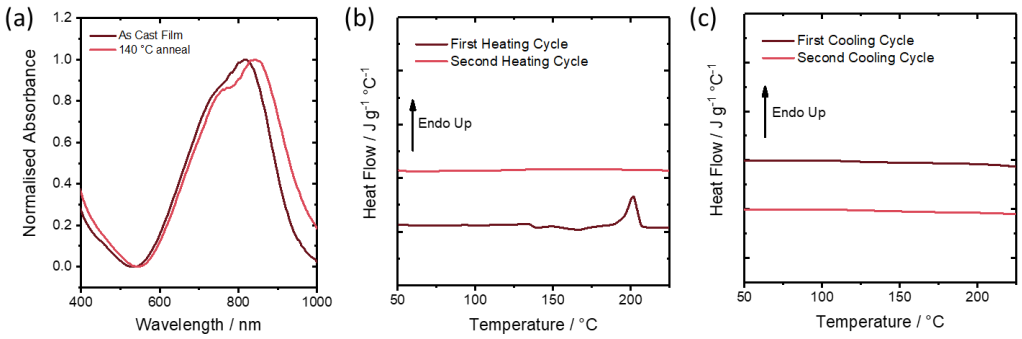

Figure 40| a) UV–vis absorbance spectra of as cast films of O-IDTBIC and films annealed at 140 °C. (b) First and second differential scanning calorimetry heating thermograms of O-IDTBIC. (c) First and second differential scanning calorimetry cooling thermograms of O-IDTBIC. The thermograms are offset for clarity and were taken at a scan rate of 5 °C min^{-1}.

Based on this change in thin film structural order observed when annealing at 140 °C, OTFTs based on as cast films of O-IDTBIC as well as films annealed at 140 °C were fabricated. Representative plots for the characterisation of the O-IDTBIC based OTFTs are displayed in figure 41. For O-IDTBIC based OTFTs the highest electron mobilities were achieved for as cast films of the NFA, with mobilities of 0.006 ± 0.002 cm^2 V^{-1} s^{-1} and 0.003 ± 0.001 cm^2 V^{-1} s^{-1} being achieved in the saturation and linear regimes respectively averaged over five transistors (table 8). Lower mobilities were obtained for O-IDTBIC films annealed at 140°C of 0.003 cm^2 V^{-1} s^{-1} in the saturation regime.

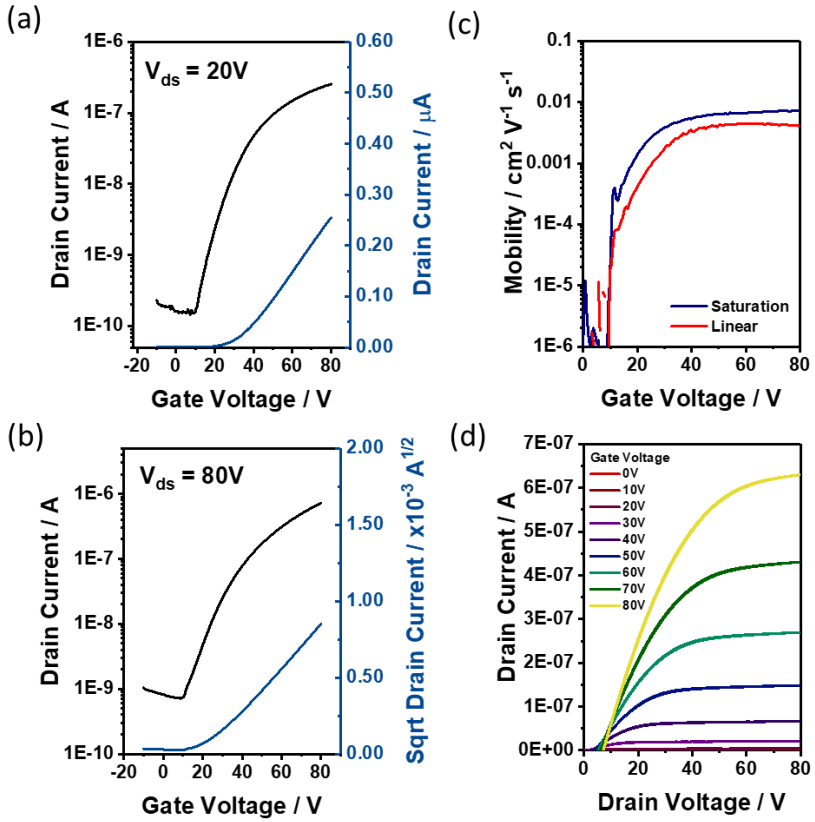

Figure 41| For OTFTs based on as cast thin films of O-IDTBIC, representative (a) linear (V_{ds} = 10 V) transfer characteristics, (b) saturation (V_{ds} = 80 V) transfer characteristics, (c) calculated mobility plotted as a function of gate voltage and (d) output characteristics. [Channel dimensions L/W 40/1000 µm, 900 nm CYTOP dielectric]

3.4 Impact of End Group Modulation on OPV Performance

The end group derivative of O-IDTBR, O-IDTBCN, was also found to perform well as an acceptor in OPVs. The PCE10:EH-IDTBR blend has previously demonstrated some of the best OPV performances of blends employing IDTBR.[59,61] Therefore, the performance of O-IDTBCN was initially investigated with PCE10 (figure 42). Figure 43 displays the current density-voltage characteristics of the best performing OPVs and table 9 displays the performance parameters.

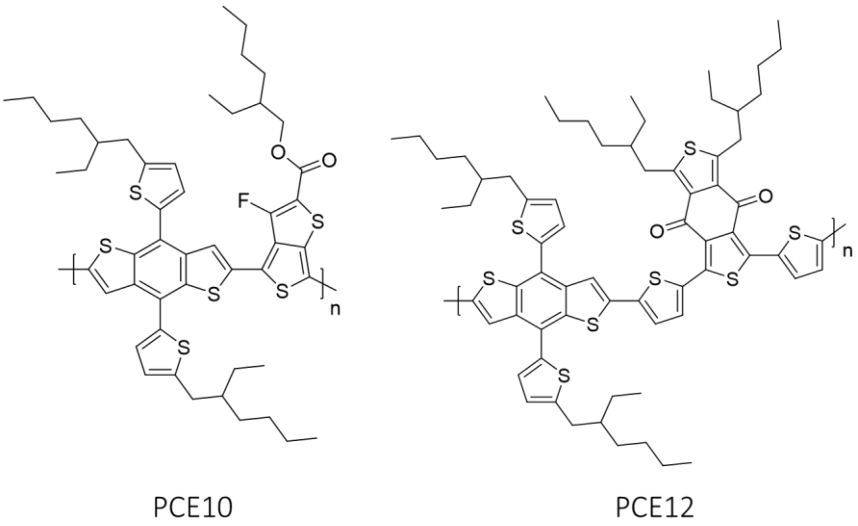

Figure 42| Chemical structure of the donor polymers PCE10 and PCE12.

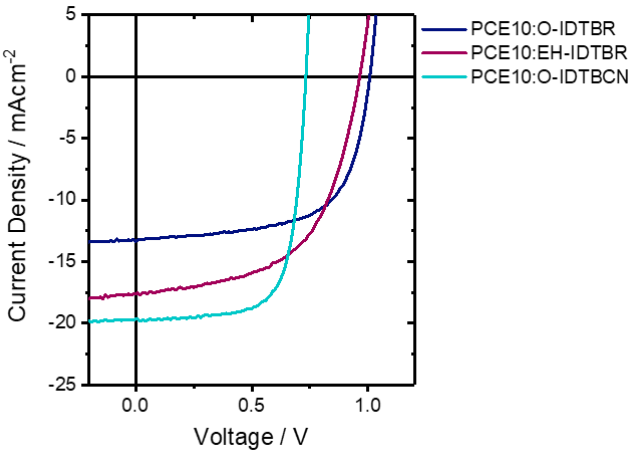

Figure 43| Current density-voltage characteristics of OPVs based on PCE10 combined with either O-IDTBR, EH-IDTBR or O-IDTBCN in a 1:2.5 ratio.

Table 9| OPV performance of blends based on PCE10 combined with either O-IDTBR, EH-IDTBR or O-IDTBCN in a 1:2.5 ratio.

Blend	J_{sc} / $mAcm^{-2}$	V_{oc} / V	FF	PCE / %
PCE10:O-IDTBR	14.2 ± 0.8	1.02 ± 0.01	0.55 ± 0.01	8.0 ± 0.4
PCE10:EH-IDTBR	18.1 ± 2.4	1.00 ± 0.02	0.57 ± 0.02	10.4 ± 1.5
PCE10:O-IDTBCN	21.0 ± 1.9	0.726 ± 0.007	0.68 ± 0.03	10.3 ± 0.9

[a]Mean values and standard deviations determined from 5 OPVs with pixel areas of 0.045 cm^2.

Extending this OPV study comparing O-IDTBCN with O-IDTBR it was found that in blends with PCE10 a more balanced hole and electron mobility was achieved for the PCE10:O-IDTBCN blend as determined by analysing space charge limited currents (SCLC) in single carrier diodes.[152] High and balanced hole and electron mobilities are important for achieving high performance OPVs, although this is an oversimplification of the complex processes occurring in the photoactive blend.[153] The SCLC electron mobility of 4.8 x 10^{-5} cm^2 V^{-1} s^{-1} reported for a PCE10:O-IDTBR blend is much lower than 2.2 x 10^{-4} cm^2 V^{-1} s^{-1} for the PCE10:O-IDTBCN blend. In neat films, O-IDTBR and O-IDTBCN exhibit comparable SCLC electron mobilities of 2.0 x 10^{-4} cm^2 V^{-1} s^{-1} and 1.8 x 10^{-4} cm^2 V^{-1} s^{-1} respectively.[152] More recently, the higher FF and J_{sc} of the PCE10:O-IDTBCN blend have been related to the larger quadrupole moment of O-IDTBCN relative to O-IDTBR, which was shown to result in a reduction of the recombination in the blend.[135]

Table 10| OPV performance of blends based on PCE12 combined with O-IDTBCN in a 1:1 ratio, either as cast or annealed.

Blend, Processing	J_{sc} / $mAcm^{-2}$	V_{oc} / V	FF	PCE / %
PCE12:O-IDTBCN, As Cast	17.8 ± 0.08	0.791 ± 0.006	0.59 ± 0.02	8.3 ± 0.4
PCE12:O-IDTBCN, 130 °C/10 min	21.0 ± 1.7	0.697 ± 0.002	0.69 ± 0.00	10.1 ± 0.8
PCE12:O-IDTBCN, 150 °C/10 min	21.5 ± 1.2	0.689 ± 0.003	0.63 ± 0.01	9.4 ± 0.6

[a]Mean values and standard deviations determined from 4 OPVs with pixel areas of 0.045 cm^2.

PCE12 (figure 42) is another commonly used donor in OPVs, most often used in combination with the NFA ITIC.[154] When ITIC was first reported it delivered a PCE of only 6.8 % when combined with PCE10, later a PCE of over 11 % was achieved using the, at that time newly developed, donor PCE12.[40,69] Notably, contrasting with this, relatively low PCEs, the best being just over 7 %, are achieved for blends of PCE12:O-IDTBR.[155] The donor polymer choice will have a large impact on the performance of OPVs, both due to the energetics of the material and its degree of miscibility with the acceptor. The NFA O-IDTBCN was also investigated in blends with the donor PCE12. Figure 44a displays the current density- voltage characteristics and table 10 presents the OPV performance metrics.

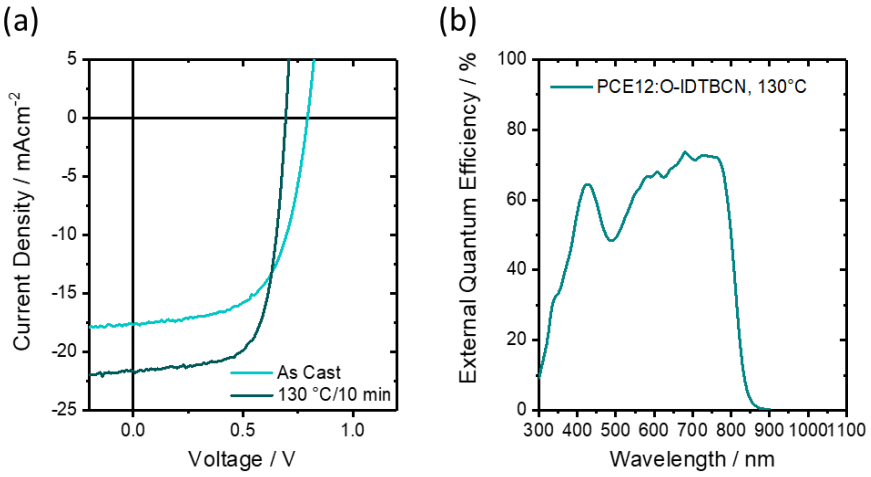

Figure 44| (a) Current density-voltage characteristics of OPVs based on PCE12 combined with O-IDTBCN in a 1:1 ratio, either as cast or annealed at 130 °C/ 10 minutes. (b) External Quantum Efficiency of an OPV based on an active layer of PCE12:O-IDTBCN annealed at 130 °C/ 10 minutes.

It is likely that the observed significant drop in V_{oc} on thermally annealing the blend, is related to the pre-aggregation behaviour of PCE12. When first reported, PCE12 was shown to exhibit a higher PCE for devices processed from a solution which had first been heated to 90 °C compared with OPVs fabricated from a solution prepared at room temperature. The V_{oc} of a PCE12:$PC_{60}BM$ was shown to drop from 0.86 V to 0.79 V on changing this process.[154] In contrast, here for the PCE12:O-IDTBCN blend the highest V_{oc} is achieved for OPVs processed from a cold solution. However, higher J_{sc} values are achieved when the BHJ active layer is processed from the hot solution, contributing to the overall higher PCE achieved. In table 11 the OPV performance parameters for OPVs processed from a chlorobenzene solution which had been heated to 60 °C and a solution prepared at ambient temperature are presented. When comparing the thermally annealed OPVs prepared using these two solutions a V_{oc} of 0.796 V is achieved for the OPV prepared from an ambient

temperature solution, which drops to 0.694 V for the OPV processed from hot solution. It is interesting to note that while a drop in V_{oc} on annealing is observed for the OPVs processed from 60 °C solution, this drop is not observed for the active layer deposited from the solution prepared under ambient conditions. Analysis of the morphology of these blends prepared by different techniques would give an indication of the source of the observed voltage losses as well as the increase in J_{sc} and FF observed for the best performing PCE12:O-IDTBCN based OPVs.

Table 11| OPV performance of blends based on PCE12 combined with O-IDTBCN processed from solutions in chlorobenzene at ambient temperature or 60 °C.

Processing	J_{sc} / $mAcm^{-2}$	V_{oc} / V	FF	PCE / %
Hot Solution, 130 °C/10 min	21.1 ± 0.7	0.694 ± 0.003	0.65 ± 0.02	9.5 ± 0.2
Hot Solution, As Cast	18.3 ± 0.8	0.788 ± 0.008	0.57 ± 0.03	8.2 ± 0.2
Ambient Temp. Solution, 130 °C/10 min	17.4 ± 0.8	0.796 ± 0.002	0.58 ± 0.01	8.0 ± 0.3
Ambient Temp. Solution, As Cast	17.8 ± 0.7	0.789 ± 0.001	0.58 ± 0.00	8.2 ± 0.3

[a]*Mean values and standard deviations determined from 5 OPVs with pixel areas of 0.045 cm^2.*

3.5 Impact of Varying Electron Rich Core on Transistor Mobility

The final chemical structure modification investigated is the effect of changing the electron rich core of O-IDTBR. O-IDTTBR (figure 45), contains an indacenodithieno[3,2-b]thiophene (IDTT), rather than indacenodithiophene (IDT), electron rich donor core. Previously, in a study comparing the IDTT containing NFA IDTTIC with IDT containing NFA IDTIC, a higher saturation electron mobility of 0.5 $cm^2\ V^{-1}\ s^{-1}$ compared with 0.12 $cm^2\ V^{-1}\ s^{-1}$ was obtained for IDTTIC based OTFTs.[105] This higher mobility was attributed to the extended conjugation in the core unit. Based on this it was hoped that O-IDTTBR would exhibit a similarly enhanced mobility relative to O-IDTBR.

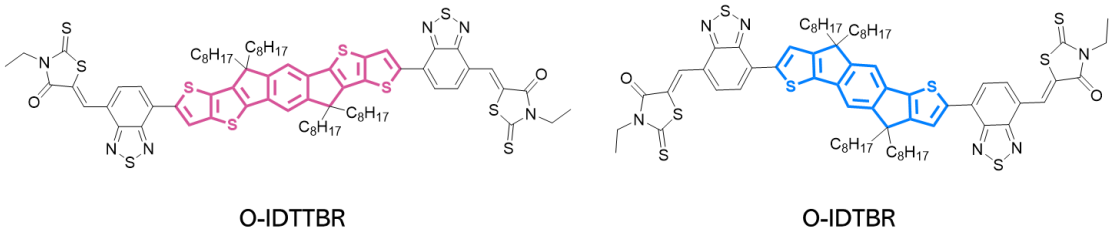

Figure 45| Chemical structures of O-IDTBR and O-IDTTBR.

First the optical and thermal properties of O-IDTTBR are investigated and compared with O-IDTBR. Table 12, compares the optoelectronic properties of O-IDTBR and O-IDTTBR. It could be expected that on increasing the size of the electron donating core of the molecule that the optical band gap would be reduced as a result of increased push-pull hybridisation. It is clear from the solution UV-vis, shown in figure 46a, that this is not the case with the peak absorption of O-IDTTBR being identical, 650 nm. This is in contrast to IDTIC and IDTTIC, which employ the same IDT and IDTT core as O-IDTBR and O-IDTTBR, for which a red-shift in absorption onset of 50 nm was observed in solution on extending the electron donating core unit from IDT to IDTT.[105]

Table 12| Optoelectronic properties of the NFAs O-IDTBR and O-IDTTBR. Peak absorptions in chloroform solution ($\lambda_{max,sol}$) as well as cast thin film ($\lambda_{max,AC}$). Ionisation potentials obtained using PESA (IP) and optical band gap ($E_{g,\ AC}$) determined using a Tauc plot.

NFA	$\lambda_{max,sol.}$ / nm	$\lambda_{max,AC.}$ / nm	IP / eV	$E_{g,\ AC}$ / eV
O-IDTBR	650	690	5.59	1.55
O-IDTTBR	650	669	5.33	1.57

Whilst DSC is a very useful technique to understand the thermal transitions of an NFA, it typically requires at least 3 mg of material. For NFAs, to remove the thermal history of the material before running the DSC the NFAs are drop cast from chloroform solution. This, therefore, requires around 12 mg of material to run one DSC measurement, which is problematic when new OSCs are often synthesised in very small quantities. It has been shown that shifts in UV-vis on sequential annealing, from which a deviation metric can be calculated, can be used to probe the thermal transitions of NFAs and determine the T_g or T_{CC}.[151,156] For O-IDTBIC very little deviation in absorbance for the as cast film was observed on annealing.

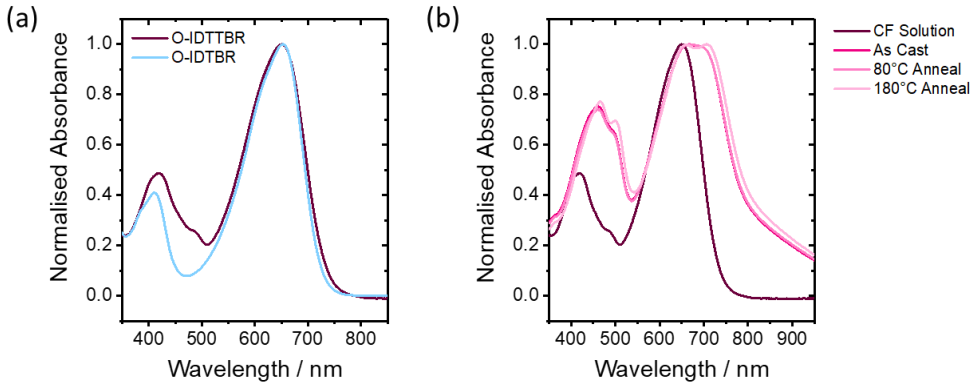

Figure 46| (a) UV-vis absorbance of O-IDTTBR and O-IDTBR solutions in chloroform. (b) UV-vis absorbance of O-IDTTBR in thin films and chloroform solution. Plots are normalised to the peak absorbance of each film.

From as-cast thin films of the O-IDTBR and O-IDTTBR optical band gaps of 1.55 eV and 1.57 eV were estimated respectively, by plotting Tauc plots. The band gaps for the two NFAs can be thought of as the same within the error of the estimations made using this technique.[137] To further investigate the difference in energy levels between O-IDTTBR and O-IDTBR the ionisation potential (IP) was determined using PESA (figure 47b). Whilst the optical band gap of O-IDTTBR and O-IDTBR are the same, there is an offset in the energy levels of the two materials relative to each other. From PESA the IPs for as cast thin films of O-IDTTBR and O-IDTBR are 5.33 eV and 5.59 eV respectively. The HOMO O-IDTTBR can be roughly approximated as its IP. The addition of a more electron rich donor core unit, for example IDTT, is expected to destabilise the HOMO leading to a shallowing of the HOMO energy, this matches the difference in IP observed between O-IDTBR and O-IDTTBR.

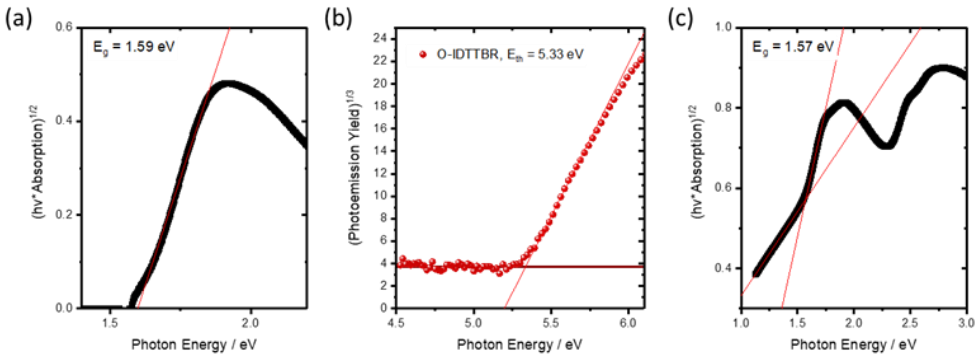

Figure 47| (a) Optical band gap determined from Tauc plot based on solution UV-vis absorbance of O-IDTTBR in chloroform. (b) Extrapolation of the cube root of photoemission yield from PESA to obtain ionisation potential (IP) of as cast films of O-IDTTBR. (c) Tauc plot used for the determination of the optical band gap of O-IDTTBR from an as cast thin film.

Since post deposition thermal annealing had little effect on the optoelectronic properties of O-IDTTBR until the high temperature of 180 °C, OTFTs based on just as cast films of O-IDTTBR were investigated. The transfer, output and mobility plots of these OTFTs are given in figure 48. Mobilities of 0.03 $cm^2 V^{-1} s^{-1}$ and 0.04 $cm^2 V^{-1} s^{-1}$ were extracted in the linear and saturation regimes respectively. These mobilities are around half of those achieved with as cast films of O-IDTBR. Unfortunately, the approach of elongating the donor core to improve charge carrier mobility as was previously shown for IDTIC compared with IDTTIC has not worked in the case of O-IDTBR.

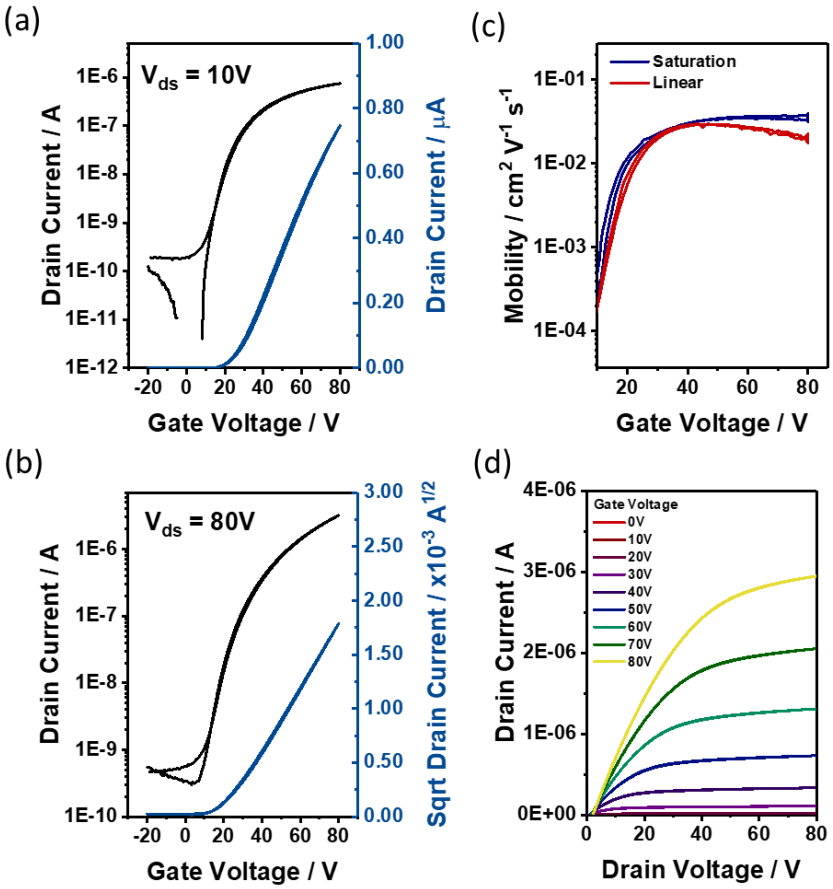

Figure 48| For OTFTs based on as cast thin films of O-IDTTBR, representative (a) linear (V_{ds} = 10 V) transfer characteristics, (b) saturation (V_{ds} = 80 V) transfer characteristics, (c) calculated mobility plotted as a function of gate voltage and (d) output characteristics. [Channel dimensions L/W 40/1000 µm, 900 nm CYTOP dielectric]

3.6 Conclusion

Several structural derivatives of O-IDTBR were investigated in an attempt to tune its charge transport properties, thereby yielding higher mobilities and better OTFT performances. Despite the high mobility of the linear octyl side chain NFA O-IDTBR, derivatives with hexyl and decyl side chains performed poorly in comparison. As was highlighted in *Chapter 2*, the octyl side chains are critical in stabilising the interdigitated packing motif of O-IDTBR and it is likely that the hexyl and decyl side chains are not able to provide this stability.

Varying the end group of O-IDTBR to dicyanovinyl in O-IDTBCN and 1,1-dicyanomethylene-3-indanone in O-IDTBIC also did not yield higher transistor mobilities. Both O-IDTBIC and O-IDTBCN exhibit a red-shift in absorption on thermally annealing, similar to the behaviour observed for O-IDTBR, which can be attributed to an

increase of structural order in the thin films. O-IDTBCN has been shown to perform well when combined with PCE12 and PCE10 in OPVs, delivering PCEs over 10 %. In particular this is interesting as previously O-IDTBR has been shown to perform poorly in blends with PCE12. There are few examples of NFAs which perform well with both PCE10 and PCE12. Changing the electron rich donor core from indacenodithiophene (IDT) in O-IDTBR to indacenodithieno[3,2-b]thiophene (IDTT) in O-IDTTBR also did not enhance the mobilities extracted from OTFTs, unlike in a previous study where this had been shown to be a successful approach.

Investigating hexyl and decyl side chain derivatives of O-IDTBR also highlighted the importance of side chain length in dictating the thermal transitions of NFAs. It was found that for C_6-IDTBR both the cold crystallisation exotherm and melt endotherm occurred at higher temperatures than for C_8-IDTBR and for C_{10}-IDTBR the transitions occurred at lower temperatures. This has implications for designing NFAs with good thermodynamic stability as it suggests that shorter side chains are desirable to achieve higher transition temperatures, which are associated with lower diffusion coefficients and therefore higher morphological stability.

This chapter highlights the dramatic difference that small changes in chemical structure can make to the properties of NFAs and the importance of considering how the molecules will pack in the solid state as well as the expected energetics of the monomeric species when designing novel NFAs. One can question how many promising NFAs have been discarded that with only minor tweaks to the chemical structure could have delivered greatly improved performances. It also highlights the unique properties of O-IDTBR, which has demonstrated resilience in the field of OPV, amongst a variety of closely related structural analogues. The selection of not just linear side chains, but specifically octyl side chains when O-IDTBR was first designed was particularly intuitive or fortunate.

Chapter 4: Achieving Low Organic Photodetector Dark Currents with Non-Fullerene Acceptors

The work in this chapter originated from a desire to better understand the relationship between the chemical structure of small molecule organic semiconductors and their performance in organic photodetectors (OPD). For organic photodetectors (OPD), not only is the responsivity of the device to light important, but also the sensitivity and speed of this response depending on the application the device is designed for. Simultaneously optimising the different parameters for OPD operation can be difficult. In particular, fabricating an OPD which is sensitive to low light intensities, whilst having a high responsivity has been problematic. The work in this chapter aimed to identify combinations of polymer donor and non-fullerene acceptor which can deliver a high sensitivity in OPDs. Here, O-IDTBR and O-FBR are combined with the upscalable polymer PTQ10 to fabricate high sensitivity OPDs. Minimal dark current densities on the order of nanoamperes per centimetre squared are achieved for both the O-IDTBR and O-FBR based detectors. Detectivities on the order of 10^{11}-10^{12} Jones calculated from the noise equivalent power of the devices are also achieved.

The bulk of work in this chapter is reported in the publication entitled "Nonfullerene-Based Organic Photodetectors for Ultrahigh Sensitivity Visible Light Detection"[157] *Many thanks to Nicola Gasparini, who supervised this work and introduced me to the field of photodetectors. Specifically in this chapter, thanks to Nicola for analysing the frequency dependence of the noise current given here. Thanks to Alberto Scaccabarozzi for measuring, analysing and interpreting the GIWAXS data for my samples. Again thanks to Weimin Zhang, who synthesised and purified the O-IDTBR used in this and many other studies. Thanks also to Mark Little for synthesising and purifying the O-FBR used in this chapter.*

4.1 Background

4.1.1 OPD Sensitivity

One of the most critical considerations for photodetectors is to achieve a high signal to noise ratio (SNR). In order to do this, a simultaneously high responsivity, low current in the dark and low noise level must be realized. Some level of current will pass through all photodetectors in the absence of light. Dark current is literally the current in the device

when there is no illumination, i.e., the device is in the dark. In a photodetector, the aim is to distinguish the signal due to photogenerated current from the signal due to a baseline dark current in the device. A low dark current allows the conversion of low levels of light into a detectable electrical signal, without the need to apply a significant external bias.[96,158] Random statistical variations in the OPD current measured are due to noise and it is this noise that ultimately limits the sensitivity of a photodetector.

Dark currents obtained for OPDs are wide ranging and depend on both the materials employed and the architecture of the photodetector. Currently, the lowest dark current density (J_d) values range between 10^{-9}-10^{-10} A cm^{-2}.[159] High J_d values are typically attributed to dark injection from the metal contacts into the active layer or thermal generation of charge carriers within the bulk heterojunction.[96] High dark current density has been a persistent problem limiting OPD technology.[4,96] [160] It has been shown that trap states contribute significantly to the noise current in OPDs.[4] The relationship between open-circuit voltage, dark current and non-radiative recombination losses has also been highlighted.[90] These studies bring important insight into the sensitivity limitations of OPDs, but are not focused on how the chemical structures of the organic semiconductors selected relate to this.

There are several methods utilised to reduce the dark current of OPDs.[87] Use of thick active layer has been associated with reduced leakage currents, in particular due to less pinholes present in the film.[158] In addition, a variety of different hole and electron blocking layers have been employed to successfully reduce dark currents in OPDs, relative to traditional OPV diode architectures.[87,161] Variations in device interlayer are not investigated here but, as will become clear, this is necessary for achieving stable and low dark currents in the future.[162] At the time of this work, very little was known about the relationship between the chemical structure of the acceptor material and the performance of OPDs.[4,96] A trend of lower dark current with increased effective band gap of the active layer had recently been highlighted for a series of polymers combined with $PC_{70}BM$.[96] Before understanding of how chemical structure relates to OPD performance a blend exhibiting low dark current densities needed to be identified and, as discussed in the next sections, PTQ10 proved a good choice as a donor polymer for OPDs.

4.1.2 Polymer Selection

The quinoxaline polymer PTQ10, shown in figure 49a, was selected as the donor material for this OPD study and was a promising candidate for several reasons. When first reported it was highlighted that PTQ10 can be synthesised in high yield from low-cost precursors,

with relatively few synthetic steps, making it viable for commercial organic electronic applications.[163] In addition to this, unlike many other blends for OPVs, which exhibit a reduction in current density and fill factor on increasing the thickness of the BHJ active layer, the PTQ10:IDIC blend exhibited thickness tolerant performance. OPVs based on PTQ10:IDIC maintained a PCE of over 10 % at an active layer thickness of 300 nm.[163] More recently, helping to explain this, PTQ10 was shown to exhibit a particularly long charge carrier diffusion lengths of 19 nm, compared with 5-10 nm for most conjugated polymers.[164] The thickness tolerance of OPVs based on PTQ10 was an indication that it could be a good polymer candidate for OPD applications where thick active layers are often used to minimise dark currents.[163] The use of relatively thick active layers is also necessary for commercialisation of OSC technologies, where printing techniques will be used. For OPVs, PTQ10 is also one of the few polymers which has achieved over 15% efficiency when combined with the state-of-the-art non-fullerene acceptor Y6 or its derivatives.[165]

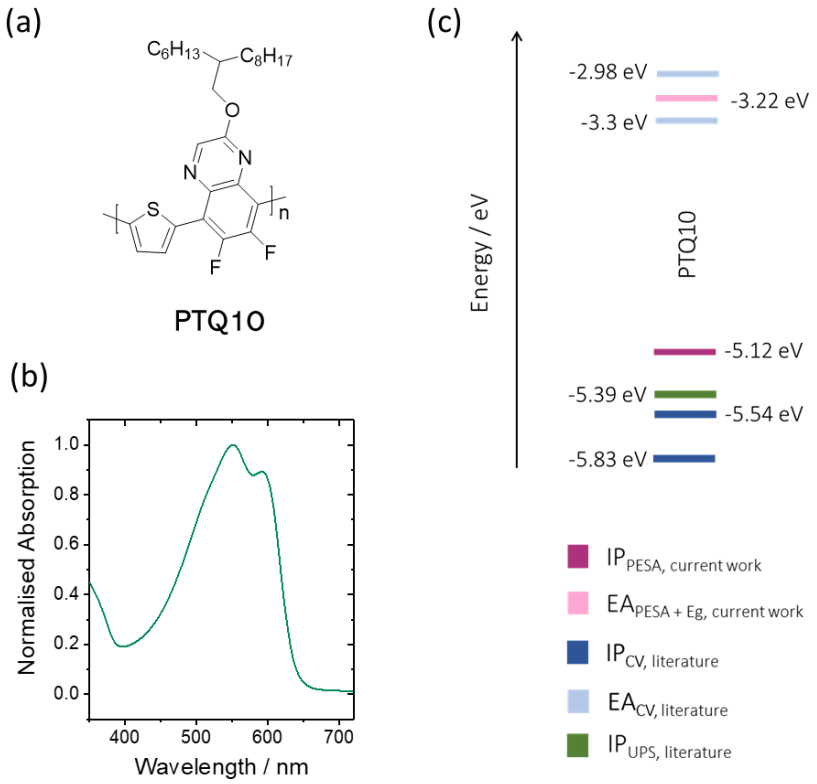

Figure 49| (a) Chemical structure of PTQ10, (b) UV-vis Absorbance of an as cast PTQ10 thin film, (c) Energy levels of PTQ10. Estimated in this study using photoelectron spectroscopy in air (PESA) and the optical band gap (E_g) of 1.9 eV. In previous literature energy levels have been determined using either cyclic voltammetry (CV),[163][166] or ultraviolet photoelectron spectroscopy (UPS) to obtain the IP.[167]

The IP of PTQ10 was determined as 5.12 eV using PESA and this was combined with the optical band gap of 1.9 eV to give an estimated EA of 3.22 eV. Although this method is widely used to estimate the EAs of OSCs, it does not account for the binding energy of excitons and therefore gives overestimated EA values. As illustrated in figure 49c, there is significant variation in the energy levels of PTQ10 reported throughout literature. This can have implications for investigations looking at the offset in energetics between donor and acceptor in OPVs and how they relate to voltage losses in the system. With such varied energy levels reported it become unclear which blends are expected to have a type two offset in energetics, a good predictor of whether the formation of a charge-transfer state between a donor and acceptor material will be energetically favourable. To confirm the relatively small IP determined for PTQ10 by PESA, measurements were performed on two batches of PTQ10 from different suppliers. The cube root of the photoemission yield for these measurements are shown in figure 50. The IPs determined of 5.12 eV, for the batch used in this work, and 5.15 eV, for a second batch, are in good agreement with each other.

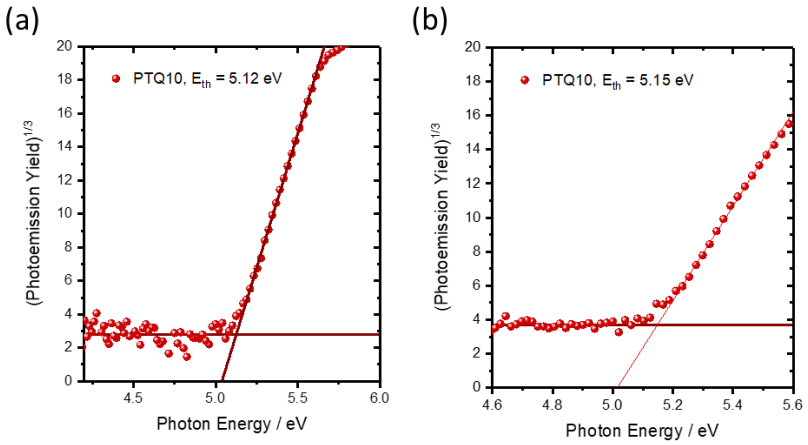

Figure 50| Cube root of photoemission yield from PESA measurements for two different batches of PTQ10 with different molecular weights. (a) PTQ10 batch from 1-Material©. (b) PTQ10 batch from Brilliant Materials© Mn/Mw 17/49 kg mol^{-1}.

4.1.3 Non-fullerene Acceptor Selection

To fabricate OPDs, PTQ10 was combined with either the NFA O-IDTBR or O-FBR, which can be seen as a derivative of O-IDTBR – containing a fluorene rather than IDT core (figure 51a). O-FBR was one of the first reported NFAs, delivering a PCE of 4.1 %, with a notably high V_{oc} of 0.82 V when combined with the donor polymer P3HT.[54] The comparatively high V_{oc} for a P3HT:O-FBR based OPV (P3HT:$PC_{70}BM$ gives 0.59 V) can be attributed to O-FBR's shallow EA level of 3.75 eV. Given the indication in previous studies that a large effective band gap of the active layer blend is beneficial for achieving

low dark current densities in OPDs, PTQ10:O-FBR appeared to be a promising candidate for high sensitivity OPDs.[96] More recently, the direct relationship between open-circuit voltage and noise current in OPDs has been demonstrated.[90]

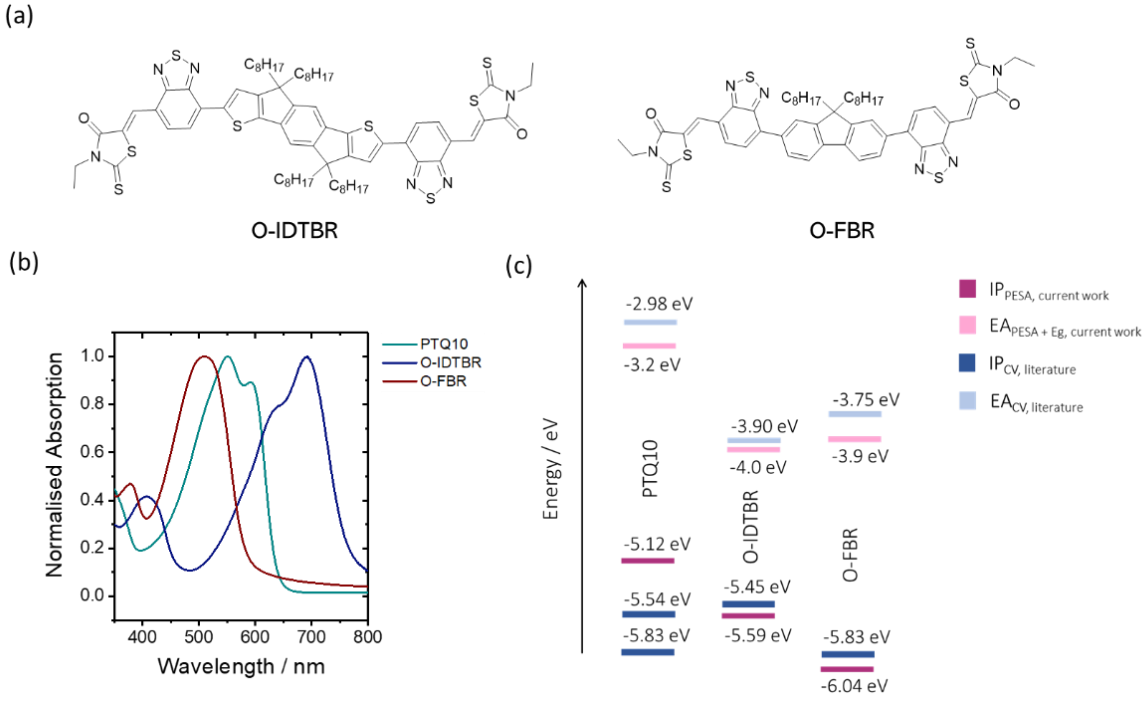

Figure 51| (a) Chemical structures of O-IDTBR and O-FBR. (b) UV-vis Absorbance of O-IDTBR, O-FBR and PTQ10. (c) Energy levels for the OSCs: previously reported in literature using cyclic voltammetry (CV)[110,163,166] and determined in this work using PESA for the ionisation potential (IP) and IP + Optical Band gap for the electron affinity (EA).

The twisted fluorene unit of O-FBR compared with the planar and more electron rich IDT unit in O-IDTBR results in significantly different band gaps and energy levels as illustrated in figure 51. The optical band gaps (E_g) were determined from as cast films of O-FBR and O-IDTBR as 2.1 eV and 1.6 eV respectively. The complementary absorption of the two molecules can be seen in figure 51b, O-FBR absorbs strongly in the visible region of the electromagnetic spectrum, with a peak absorption at 509 nm for as cast thin films of the material. As cast films of O-IDTBR exhibit a peak absorption at 690 nm, on the edge of the visible region. Based on the IPs determined from PESA measurements a type two offset in energetics between PTQ10 and both NFAs is present so efficient exciton dissociation at the donor-acceptor interface could be expected. However, based on the literature cyclic voltammetry values, from which the HOMO level can also be estimated, there may be a negligible HOMO-HOMO offset between PTQ10 and O-IDTBR, which could limit photocurrent generation in the blend.

4.2 Organic Photodetector Fabrication

For the OPDs fabricated in this study, the active layers were deposited using a doctor blade under ambient conditions. Doctor blade coating is more comparable with high throughput production techniques favoured by industry, such as slot-die coating, compared with spin-coating, which is commonly used in research laboratories. In general, thicker active layers can also be achieved using doctor blade coating compared with spin-coating. In this study, the active layer thicknesses were close to 450 nm for both blends. The active layers comprise a 1:2 ratio by mass of either PTQ10:O-FBR or PTQ10:O-IDTBR and the OPDs were fabricated with an inverted ITO/ZnO/PTQ10:Acceptor/MoO_x/Ag architecture as detailed in *Chapter 7*, the experimental section.

4.3 Organic Photodetector Characterisation

Depending on the application that an OPD is used for, different parameters will be of more significant importance. For example, communications applications may require a fast response time to read a signal, whereas bio-imagers may require a high sensitivity to detect very weak optical signals, but speed of response will be less important. The focus of this study was to identify potential organic semiconductor blends that could deliver OPDs with a high sensitivity, i.e., a low dark current density at reverse bias.

For good photodetection an efficient conversion of photons to electrons by the OPD is required. The external quantum efficiency (EQE) at a specific wavelength is the ratio of power extracted from the device to power incident on the device. EQE is typically reported for OPVs and is related to the responsivity of the device by equation 10, where λ is the wavelength, q is the elementary charge, h is Planck's constant and c is the speed of light. Responsivity accounts for the differences in energy between photons of different wavelengths and is therefore more relevant for OPD applications where a quantitative assessment of the incident light is required.

$$R(\lambda) = \mathrm{EQE}\frac{\lambda q}{hc} \tag{10}$$

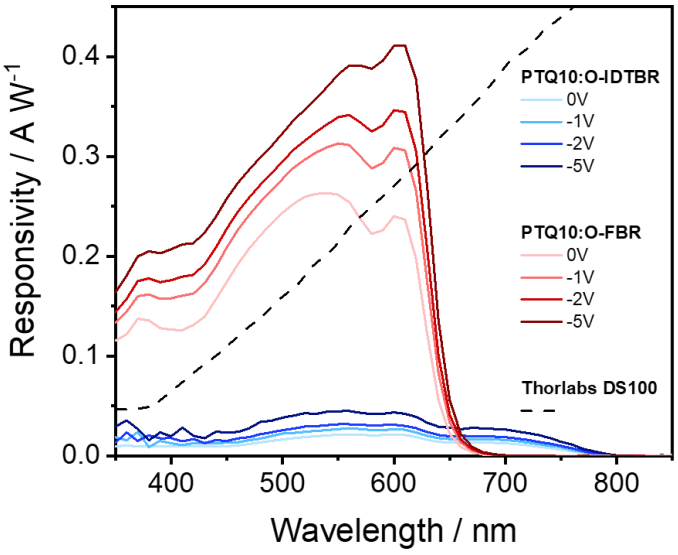

Figure 52| Responsivity of OPDs based on PTQ10:O-FBR and PTQ10:O-IDTBR as a function of bias, as well as Thorlabs© DS100 silicon photodetector measured in parallel.

The responsivities of the two OPDs under short-circuit conditions as well as applied reverse bias are displayed in figure 52. The peak responsivity under short-circuit conditions of the PTQ10:O-FBR blend, which is at 600 nm, is 0.23 A W^{-1}. The responsivity almost doubles to 0.41 A W^{-1} when a bias voltage of – 5 V is applied. This is expected as at increased reverse bias the extraction efficiency is improved and is why OPDs are typically operated at reverse bias.[87] This high responsivity for the PTQ10:O-FBR based OPD competes with values reported for the best performing OPDs. At short-circuit the PTQ10:O-FBR blend responsivity also exceeds that of a commercially available silicon photodiode, a Thorlabs DS100, at wavelengths below 550nm.

In contrast, the peak responsivity of the PTQ10:O-IDTBR blend is lower, 0.02 A W^{-1} at 550 nm under short-circuit conditions. Again, this responsivity doubles, to 0.04 A W^{-1}, on application of a – 5 V bias. As mentioned in section 4.2, in OPDs and OPVs, a blend of donor and acceptor material is used to aid separation of coulombically bound photogenerated excitons through the formation of charge-transfer states at the interface between the donor and acceptor.[30] For a long time, it was commonly accepted that an interfacial energy offset between the donor and acceptor material was required making the charge transfer state more energetically favourable than excitons of either the donor or acceptor material.[168] From the low responsivity achieved for the PTQ10:O-IDTBR based OPD, of less than 0.05 A W^{-1}, it seems likely that the offset in IP was insufficient for efficient exciton separation at the interface between the two materials. Despite this the

responsivity of the PTQ10:O-IDTBR blend extends through all visible wavelengths from 350-800 nm.

Next the dark current in the OPDs is considered. The current density-voltage characteristics of the two OPDs, PTQ10:O-FBR and PTQ10:O-IDTBR, under no illumination and one sun equivalent illumination are presented in figure 53. For the OPDs made in this study, at – 2 V, the dark current density of the PTQ10:O-FBR blend is 0.17 nA cm^{-2} and of the PTQ10:O-IDTBR blend is 0.84 nA cm^{-2}. For OPDs, dark currents are often seen to increase at high reverse bias voltages due to dark injection from the metal contacts into the active layer and in particular this is observed for the PTQ10:O-FBR based OPDs reported here.

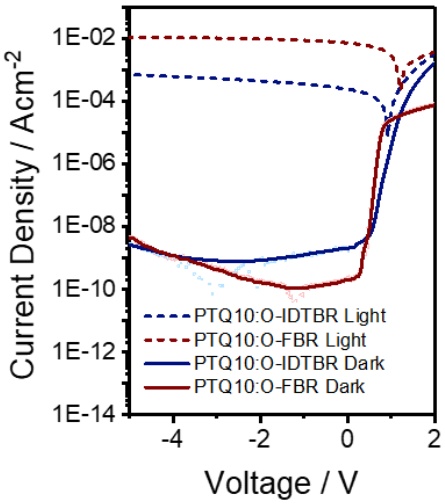

Figure 53| Current density-voltage characteristics of OPDs based on PTQ10:O-FBR and PTQ10:O-IDTBR operating under AM1.5G simulated illumination (Light) and in the dark.

The figure of merit for OPDs is the specific detectivity (D*), which combines the responsivity and sensitivity of an OPD in one metric. Often D* is calculated directly from the dark current density (J_d) using equation 11, where q is the elementary charge. This calculation assumes shot noise is the major contributor to noise in the output current and ignores the contributions of all other types of noise.[95,160] Ignoring the contribution of thermal noise to the output signal of OPDs has been highlighted to lead to significant overestimations in noise equivalent power (NEP) and D*.[169] In good agreement with this, the D* values determined here using equation 11 are significantly overestimated, with maximum D* values of 4.7 x 10^{13} Jones and 1.8 x 10^{12} Jones being calculated for the PTQ10:O-FBR and PTQ10:O-IDTBR based OPD respectively at their peak R. D* values as a function of wavelength for both blends calculated in this way are plotted in figure 54.

$$D^* = \frac{R}{\sqrt{2qJ_d}}$$

(11)

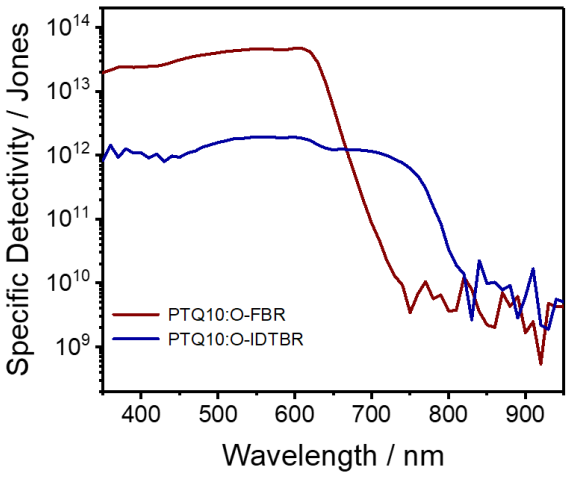

Figure 54| Overestimated Specific Detectivity calculated from the OPD dark current densities using equation 11 at an applied bias of – 2V.

When reporting the sensitivity of an OPD, the noise current (i_n) associated with the current measured in the device is a key consideration. This noise arises due to the discrete nature of electrons and their resulting thermal and statistical fluctuations (thermal and shot noise).[169] The above method, using equation 11, is an oversimplification as the dark current only accounts for a portion of the noise current in the OPD, specifically the shot noise. The noise current in an OPD can be estimated according to equation 12, where q is the elementary charge, i_d is the dark current, k is the Boltzmann constant, T is the temperature and R_{shunt} is the shunt resistance.[170] The first term, including the dark current, accounts for the shot noise (S_{shot}) and the second term derived from the shunt resistance is for the thermal noise ($S_{thermal}$). The shunt resistance was determined from the dark J-V characteristics and this value along with the other calculated parameters are given in table 13.

$$(i_n)^2 = \left(2qi_d + \frac{4kT}{R_{shunt}}\right)$$

(12)

Table 13| Peak responsivity (R), Dark Current (i_d), shunt resistance (R_{shunt}), Calculated shot noise current (S_{shot}), Calculated thermal noise current ($S_{thermal}$), calculated noise current (i_n) and noise equivalent power at peak responsivity (NEP) for 0.045 cm^2 OPDs combining either O-IDTBR or O-FBR with PTQ10 and operating at either – 2 V or – 5 V applied bias.

NFA and Applied Bias	R / A W^{-1}	i_d / A	R_{shunt} / Ω	S_{shot} / A^2	$S_{thermal}$ / A^2	i_n / A	NEP / W
O-FBR (-2V)	0.35	7.6 x 10^{-12}	2.6 x 10^7	2.4 x 10^{-30}	6.2 x 10^{-28}	2.6 x 10^{-14}	7.6 x 10^{-14}
O-FBR (-5V)	0.41	1.9 x 10^{-10}	2.6 x 10^7	6.2 x 10^{-29}	6.2 x 10^{-28}	3.3 x 10^{-14}	8.0 x 10^{-14}
O-IDTBR (-2V)	0.03	3.8 x 10^{-11}	5.9 x 10^8	1.2 x 10^{-29}	2.8 x 10^{-29}	8.7 x 10^{-15}	2.7 x 10^{-13}
O-IDTBR (-5V)	0.05	1.1 x 10^{-10}	5.9 x 10^8	3.6 x 10^{-29}	2.8 x 10^{-29}	1.1 x 10^{-14}	2.5 x 10^{-13}

Noise current is also frequency and light intensity dependent. By measuring the dark current through the device as a function of time the frequency dependence of the noise current can be assessed. Figure 55 displays the noise power spectra of the OPDs as a function of frequency, which is obtained by performing a fast Fourier transform of the noise current taken over a long time period. The spectral density is shown to be relatively frequency independent and therefore the approximation made using equation 12, which negates to account for the contribution of flicker noise to the OPD noise current, is valid in this case. The noise floor has been reached at a frequency as low as 0.1 Hz, suggesting that the flicker noise is negligible for frequencies above 0.1 Hz.

From the noise current, the noise equivalent power (NEP), which is the incident light intensity at which no photocurrent response can be distinguished from the noise in the output signal, can be calculated using equation 13.

$$NEP = \frac{i_n}{R} \quad (13)$$

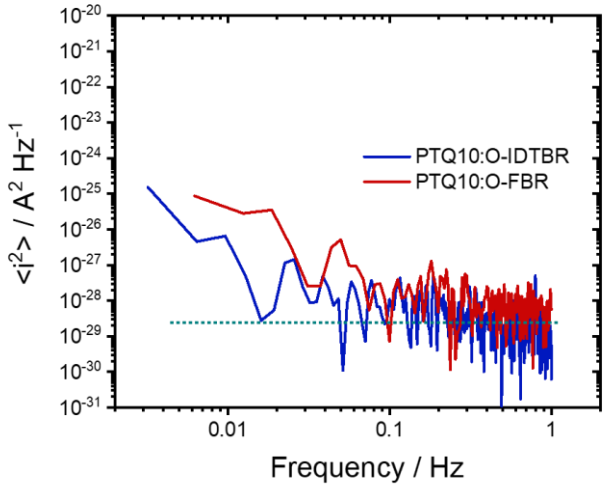

Figure 55| Noise power spectral density of OPDs based on PTQ10:O-FBR and PTQ10:O-IDTBR operated at an applied bias of – 2 V.

D* can then be calculated more accurately from the NEP according to equation 14. Δf is the bandwidth of the system and A is the photodetector area, in this case 0.045 cm^2.

$$D^* = \frac{\sqrt{A\Delta f}}{NEP} = \frac{\sqrt{A\Delta f}R}{i_n} \quad (14)$$

Plots of D* as a function of wavelength calculated using this method at an applied reverse bias of both – 2 V and – 5 V are presented in figure 56. The PTQ10:O-IDTBR blend exhibits a highly uniform D* extending into the near infra-red. In contrast, the PTQ10:O-FBR blend exhibits specific detectivities of over 10^{12} Jones up to a wavelength of 610 nm where it peaks at 2.8 x 10^{12} Jones, when operated under an applied bias of -2V. The dominant contribution of thermal noise to the noise current means that the D* achieved for the PTQ10:O-FBR blend is relatively bias independent.

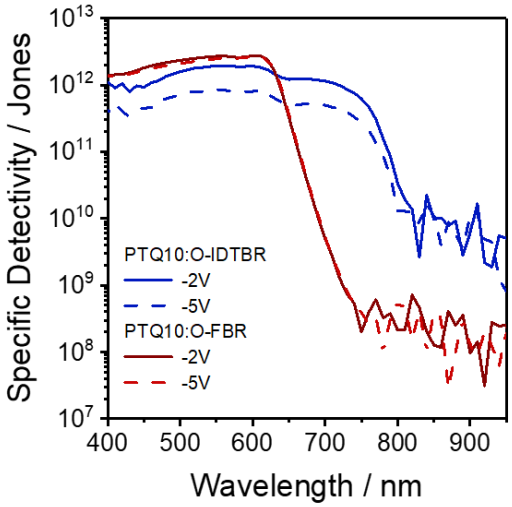

Figure 56| Specific Detectivity of PTQ10:O-IDTBR and PTQ10:O-FBR based OPDs as a function of wavelength, calculated from the shot and thermal noise current using equation 14.

In addition to detection of low light levels a linear responsivity to varying light intensity is also desirable for many applications. For applications which require high contrast detection, such as image sensors, a large difference between the minimum and maximum signal extracted is important. The metric which gives an assessment of this breadth of sensitivity of an OPD is the linear dynamic range (LDR). LDR expresses the ratio of photocurrent at high light intensity (j_{max}) to photocurrent at low light intensity (j_{min}) in decibels according to equation 15.

$$LDR = 20\log\left(\frac{j_{max}}{j_{min}}\right) \quad (15)$$

In order to calculate the LDR in this study, the light intensity incident on the OPDs was varied using neutral density filters and an AM1.5G solar simulator. A plot of the current density of the OPDs under varying light intensity is shown in figure 57. At an applied bias of – 2 V LDR values of 75 dB and 71 dB were calculated for the PTQ10:O-FBR and PTQ10:O-IDTBR based OPDs respectively. Unfortunately, these LDR values are likely significantly underestimated compared with the real values as it was difficult to block all background light in the setup used to measure the LDR. This is clear from the plots in figure 57, where a significantly increased dark current is observed relative to when all background light is blocked (figure 53). At the maximum light intensity investigated, 1 sun AM1.5G illumination given by a Xenon light source calibrated with a silicon reference cell,

current densities at – 2 V applied bias of 4.5 x 10^{-4} A cm^{-2} and 9.5 x 10^{-3} A cm^{-2} were obtained for the PTQ10:O-IDTBR and PTQ10:O-FBR based OPDs respectively. Assuming that the light intensity dependence of the OPD photocurrent is linear to the noise floor, these values of photocurrent under 1 sun conditions can be combined with the dark current density values of 1.7 x 10^{-10} A cm^{-2} for the PTQ10:O-FBR based OPD and 8.4 x 10^{-10} A cm^{-2} for the PTQ10:O-IDTBR based OPD to give estimated LDRs of 155 dB and 115 dB respectively. Of course, the response may not be linear in this full range and studies have suggested a sublinear response at low light intensities can be expected and is related to intra band gap trap states.[171] The upper limit of the linear response of these photodetectors was also not investigated.

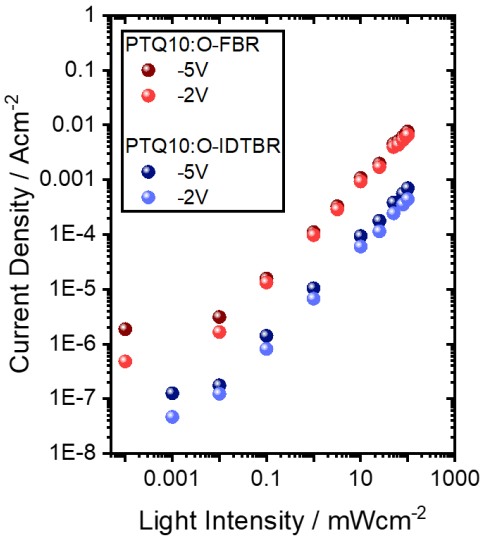

Figure 57| Current density as a function of light intensity for OPDs based on PTQ10:O-FBR and PTQ10:O-IDTBR operating at – 2 V and – 5 V reverse bias.

The response speed of a photodetector is especially important for video imaging applications where they need to respond to a certain frequency of incident light without a drop in signal intensity being observed. If the modulation frequency of the incident light is faster than the combined rise and fall time of the photodetector then the maximum photocurrent will not be obtained in this time period and thereby the response signal will be limited.

To investigate the speed of response of the OPDs, first the rise and fall times were measured by illuminating them with a 0.5 ms square wave pulse of white LED light. Here the rise time is defined as the time taken to achieve 99% maximum photocurrent intensity from 1% photocurrent intensity and the fall time is the converse. From figure 58, which shows the

rise time for the two OPDs, it is clear that the PTQ10:O-FBR based OPD responds faster with a rise time of 12 μs compared with 20 μs for the PTQ10:O-IDTBR based OPD.

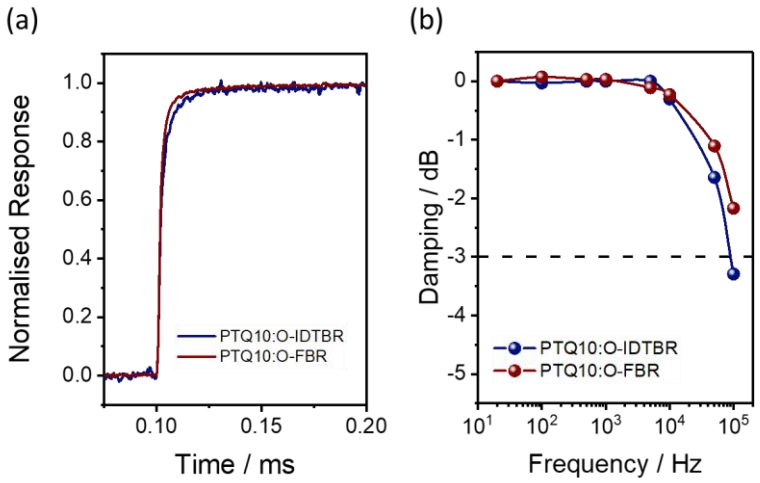

Figure 58| (a) Normalised rise-time transients for OPDs based on PTQ10:O-FBR and PTQ10:O-IDTBR. (b) Normalised photoresponse of OPDs based on PTQ10:O-FBR and PTQ10:O-IDTBR at increasing frequency of incident white LED light for determination of the cut-off frequency.

In general, the frequency at which the photoresponse drops to $1/\sqrt{2}$ times the maximum photocurrent intensity is known as the -3 dB limit and this is the level generally used to define the cut-off frequency of an OPD. This -3 dB limit is calculated according to equation 16 where i_{max} is the maximum photocurrent intensity and i_{freq} is the photocurrent intensity for a specific frequency of incident light. In this case the cut-off frequencies were measured using a sinusoidal pulse of white LED light of frequencies between 20 Hz – 100 kHz and a plot of the damping as a function of frequency is displayed in figure 58b. Here the cut-off frequencies were determined as 110 kHz for the PTQ10:O-FBR based OPD and 90 kHz for PTQ10:O-IDTBR based OPD. For most video applications a cut-off frequency of 10 kHz is sufficient, i.e., the photodetector responds to incident 0.1 ms light pulses without a drop in photocurrent intensity greater than the – 3 dB limit being observed. Both blends investigated in this study exceed this specification.

$$Damping(freq) = -20\log\left(\frac{i_{max}}{i_{freq.}}\right) \quad (16)$$

4.4 Understanding the OPD Performance

To try and better understand the differences in performance between the two blends, the morphology was compared using grazing incidence wide angle X-ray scattering (GIWAXS). GIWAXS is used ubiquitously in the analysis of OSC blends to investigate the degree of structural order in the films, which can be related to energetic order and recombination present.[146] Previously it was concluded that active layers exhibiting a highly ordered microstructure lead to excellent D* and LDR values, compared with active layers demonstrating a less ordered microstructure.[172] Whilst GIWAXS has been proven a very useful technique for assessing the degree of structural order in the OSC active layers of thin film devices and furthering understanding of how OSCs work, it is important to note that the observed microstructure may not directly correlate to the performance observed for the devices.[173]

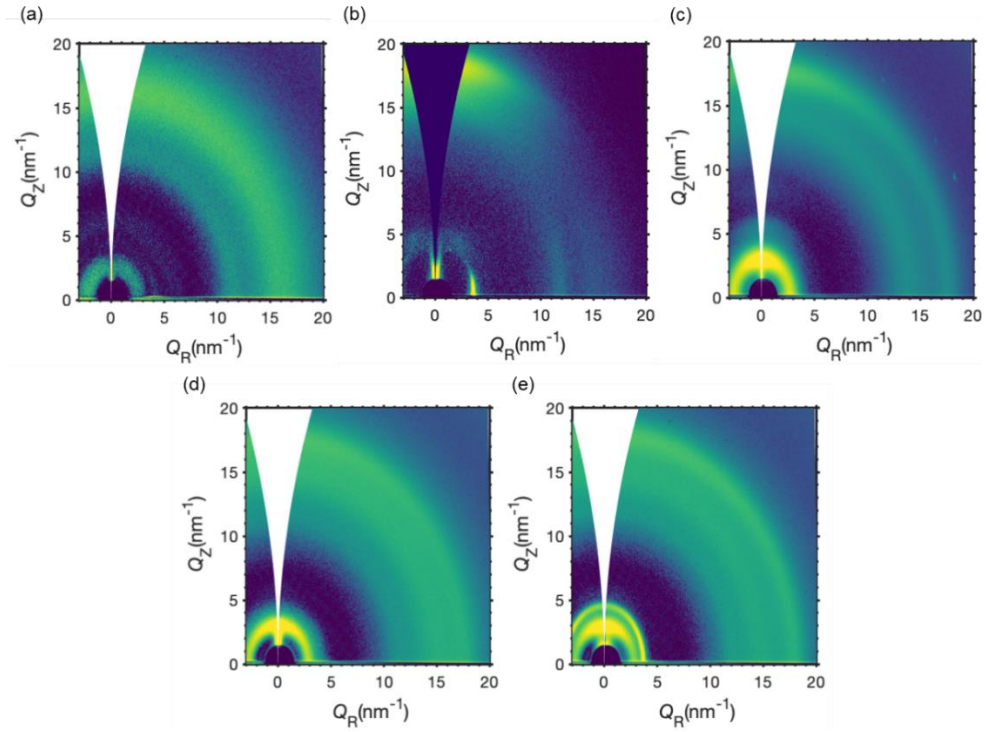

Figure 59| 2D GIWAXS patterns for as cast films of (a) O-FBR, (b) O-IDTBR, (c) PTQ10, (d) PTQ10:O-FBR, and (e) PTQ10:O-IDTBR.

Figure 59 presents the 2D GIWAXS patterns for as cast films of O-FBR, O-IDTBR and PTQ10 as well as the two blends. The as cast films of O-IDTBR exhibit a narrow in-plane diffraction peak associated with lamellar stacking in the direction of the alkyl chains and a broader out-of-plane diffraction peak corresponding to π–π stacking, which together indicate a face-on orientation of the molecules with respect to the substrate. In contrast, the

2D GIWAXS of the O-FBR as cast film does not exhibit distinctive diffraction peaks and the broad scattering halo observed in the 2D GIWAXS is indicative of an amorphous microstructure. The 2D GIWAXS pattern of PTQ10 exhibits rings, which indicates an isotropic distribution of crystallites in the film. The rings at low scattering q-values are associated with lamellar packing and at higher q-values with π–π stacking.

On blending the NFAs with PTQ10 similar features as in the neat films are observed. For the PTQ10:O-IDTBR blend the distinct diffraction patterns of both O-IDTBR and PTQ10 are still observed. However, the lamellar stacking peak of O-IDTBR arcs around the pattern in the blend, indicating a distribution of orientations is present compared to the face-on orientation observed for the neat film. Figure 60 presents the out of plane and in plane scattering profiles of the films and it is clear from these that there is no appreciable shift in the peak positions of the scattering profiles between the neat and blended films. This indicates that the crystal structure of both materials is preserved in the blend. For the PTQ10:O-FBR blend the microstructural order of the PTQ10 is also preserved in the blend film. The degree of microstructural order in the film is likely to play a role in dictating the dark current in OPDs. It could be suggested that the higher microstructural order in PTQ10:O-IDTBR blends might be responsible for the reduced bias dependence displayed by the OPDs relative to the PTQ10:O-FBR OPDs at high reverse voltages, where the effect of dark injection is higher.

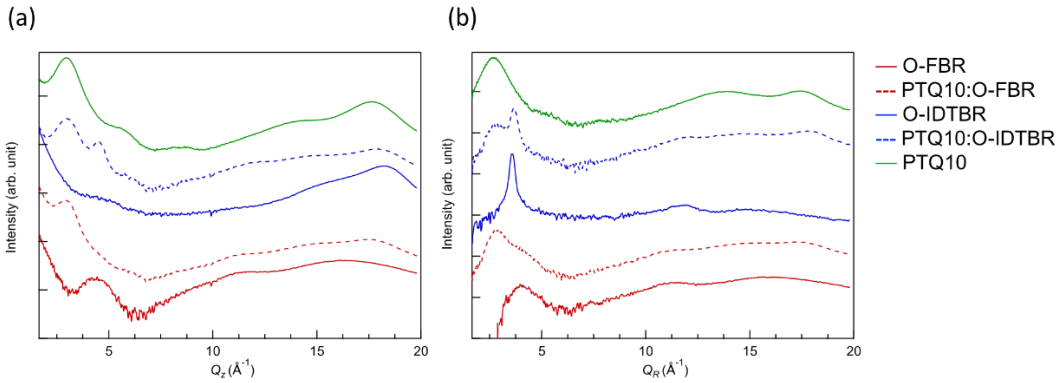

Figure 60| (a) Out-of-plane and (b) in-plane scattering profiles integrated from the 2D-GIWAXS patterns for as cast films of O-FBR, O-IDTBR and PTQ10 as well as their blends.

4.5 The Limitations of Zinc Oxide as an Interlayer

The results here demonstrate that the combination of PTQ10 with the NFAs O-IDTBR and O-FBR can be blade coated in air to fabricate OPDs which deliver low dark currents. In the case of O-FBR this is achieved along with a simultaneously high responsivity, comparable to a silicon photodetector in the visible range. The contacts and interlayers can have a large impact on the selectivity of charge extraction in OPDs and thereby the dark current of the devices.[87] The focus of this study was the OSC materials in the active layer and work was not done to optimise the contacts. The commonly used electron transport (ETL) layer zinc oxide (ZnO) was used. However, it has recently been highlighted that ZnO is not a good ETL for OPDs.[162,174] It has been reported that soaking ZnO layers with a light source that contains a UV component is necessary to fill sub-gap trap states and to enable efficient charge extraction from OPV active layers.[175] For OPDs it has been shown that light soaking leads to an undesirable increase in dark current. In a study investigating this, similarly low dark currents were obtained using a tin oxide (SnO_2) ETL as were achieved using a ZnO ETL before light soaking.[162] This suggests that ZnO is not a good choice as an OPD interlayer, however, it does indicate that similarly low dark currents as achieved for PTQ10:O-FBR and PTQ10:O-IDTBR here should be achievable using other ETLs.

4.6 Conclusion

In summary, two new blends for organic photodetector applications have been proposed based on the combination of the acceptors O-FBR and O-IDTBR with the polymer PTQ10. For these photodetectors specific detectivity values, determined from their noise equivalent power, of over 10^{12} Jones for the PTQ10:O-FBR based detector and over 10^{11} Jones for PTQ10:O-IDTBR based detector are reported. Both blends exhibit exceptionally low dark currents at a -2 V applied bias of 0.17 nA cm^{-2} and 0.84 nA cm^{-2} respectively. The OPD active layers were blade coated and all three of the materials have the potential to be produced economically at large scale making these blends good candidates for commercial OPD applications. Further work is needed to better understand how the chemical structures of the organic semiconductors relate to their good performance as active layer components for OPDs.

Chapter 5: Near Infra-red Absorbing Non-fullerene Acceptors for Photovoltaics and Photodetectors

An area of emerging interest in the fields of organic photovoltaics (OPV) and organic photodetectors (OPD) is the development of near infra-red absorbing (NIR) non-fullerene acceptors (NFA) for visibly transparent OPVs, and OPDs able to detect NIR wavelengths. To date there are only a few examples of NFAs absorbing in the NIR and for these applications novel NFAs targeting absorption in this wavelength region need to be developed. This chapter focuses on the characterisation and application in OPVs and OPDs of newly developed NIR absorbing NFAs.

Many thanks to Weimin Zhang, who synthesised and purified the molecules discussed in this chapter and to Maxime Babics who led the study applying O4TFIC in OPDs, "Non-fullerene-based organic photodetectors for infrared communication."[88]

5.1 Background

5.1.1 Near Infra-red Absorbing Non-fullerene Acceptors

The near infra-red region of the electromagnetic spectrum is typically considered as 800-2000 nm, although sometimes wavelengths above 750 nm are included in this definition.[90,176] The development of NFAs exhibiting absorption in this region is desirable for both OPD and OPV applications. For the commercialisation of OPV, one of the key target markets is now seen as visibly transparent OPVs, for which, as will be discussed, the development of NIR absorbing NFAs is desirable.[22,24,176] Meanwhile many of the key applications of OPDs, for example bioimaging, optical communications and substance identification, require NIR to mid-IR wavelength detection.[94,176,177]

To date, relatively few NFAs with absorption onsets in the NIR, above 800 nm, have been reported. Some of the most prominent examples are IEICO-4F, Y6, COTIC-4F and CO1-4Cl, which have absorption onsets in thin films at 931 nm, 1000 nm, 1127 nm and 1240 nm respectively.[36,176,178–180] For both OPD and OPV applications the design and synthesis of new NFAs, to expand the library of available materials absorbing in the NIR region, is desirable.

5.1.2 Semi-transparent Organic Photovoltaics

Much progress has been made in the achievable PCEs of OPVs with the development of NFAs which absorb in the NIR. Several NFAs have been developed which absorb in this region, targeting enhanced OPV photocurrent generation, and thereby high PCEs.[181] Blends using these NIR absorbing NFAs are able to harness more of the solar spectrum thereby leading to high photocurrent densities. For example, for the PM6:Y6 blend a photocurrent density of over 23 mA cm^{-2} can be obtained.[36] Another example is PCE10:IEICO-4F based OPVs for which photons are harvested up to 1000 nm, contributing to the high J_{sc} of 27.3 mA cm^{-2}.[42] Aside from achieving higher OPV J_{sc}s, and thereby PCEs, research into NIR absorbing NFAs is also of interest for the development of semi-transparent OPVs.

OSC-based photovoltaics were originally designed as a low-cost alternative to silicon photovoltaics. However, the substantial reduction in the cost of silicon based photovoltaics over recent years means that for commercial success, OPV must find specific applications where it's performance metrics can outcompete silicon.[24,27] One such application is visibly transparent OPVs for building integrated photovoltaics. The tunability of the absorption of organic semiconductors means that materials can be specifically designed to harvest light outside of the photopic response of the human eye, which is the response of the eye under well-lit conditions and is shown in figure 61. Related to OPVs which appear transparent to the human eye, another application of OPV which has received significant attention is greenhouse rooves, where absorption outside the window of light required by the plants for photosynthesis and pollination is desirable.[27] For greenhouses applications, the OPVs should transmit wavelengths of 400 – 600 nm, which are involved in plant photosynthesis, and also UV wavelengths which are used by plant pollinators.[182]

The spectrum of light which will be incident on an OPV operating in outdoor conditions can be approximated by the reference air mass 1.5 spectrum (AM1.5G) plotted in figure 61.[183,184] As can be seen from the relative irradiance, the NIR region has a higher solar irradiance than the UV region and therefore higher power outputs are expected for OPVs utilizing materials which absorb in the NIR region compared with UV region.

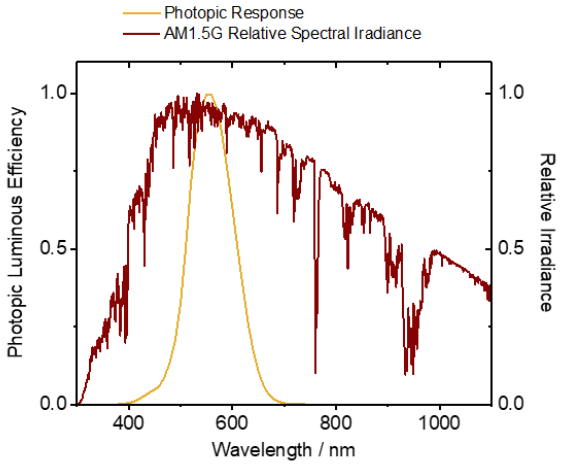

Figure 61| Normalised photopic luminous efficiency and AM1.5G spectral irradiance plotted as a function of wavelength. Photopic luminous efficiency was obtained from the colour and vision research laboratory.[185] Reference air mass 1.5 spectrum (AM1.5G) was obtained from NREL.[186]

For semi-transparent OPVs, as well as the PCE, the degree of transparency is also an important metric in defining the performance of the device. The degree of transparency is given by the average visible transmittance (AVT), equation 17. AVT is the percentage transmission (*T*) of the OPV device weighted for the photopic response of the human eye (*V*).[187] For OPVs there is a trade-off between PCE and AVT. When using narrow band gap acceptors, the maximum open-circuit voltage (V_{oc}) of a blend, is limited compared with when wider band gap materials are used. A metric for the overall performance of a semi-transparent OPV is the light utilisation efficiency (LUE), which is the product of the PCE and AVT.[26]

$$AVT = \frac{\int T(\lambda)V(\lambda)AM1.5G(\lambda)d\lambda}{\int V(\lambda)AM1.5G(\lambda)d\lambda}$$

(17)

For window applications, transmission of light by the OPVs which gives a perceived neutral tinge is desirable, i.e. it is desirable that the colours of an object observed through a semi-transparent OPV can be perceived correctly.[26,188] The metric which gives an assessment of how well the light transmitted through the semi-transparent OPV resembles the incident AM1.5G radiation is the colour rendering index (CRI).[187]

Over the past decade the PCEs achieved by semi-transparent OPVs have increased significantly. In 2011, for an OPV with an AVT of 65 %, based on a small molecule donor and C_{60} acceptor, a PCE of only 1.3 % was reported.[189] Since the development of NFAs,

significant progress has been made in the field of semi-transparent OPVs. For example the narrow band gap, NIR absorbing, NFA IEICO-4F was developed for OPV applications in 2017 and has subsequently been used in some of the best performing semi-transparent OPVs.[71,183,188,190] The state-of-the-art NFA Y6 also exhibits a peak absorption in the NIR, making it a good candidate for semi-transparent OPVs.[188,191,192] Semi-transparent OPVs based on PM6:Y6 and PCE10:IEICO-4F blends and utilizing a solution processable silver nanowire top electrode previously delivered PCEs of 9.79 % and 7.49 % combined with AVTs of 23 % and 33 % respectively.[188] When considered independently, the PCE10:IEICO-4F active layer was able to achieve AVT values of 59.6 %, however, this AVT was reduced on inclusion of the transport layers and electrodes.[190] The best performance so far achieved by this blend for semi-transparent OPVs is a PCE of 11 % combined with a AVT of 30 %.[193] Notably, whilst both Y6 and IEICO-4F absorb in the NIR, the two donors PCE10 and PM6 absorb in the visible region, limiting the AVT.

Whilst the development of NIR absorbing NFAs has led to progress in the development of semi-transparent OPVs, to be commercially viable for window applications AVT values of over 50% need to be realized.[24] Therefore, more progress in the development of new OSC blends delivering simultaneously high PCEs and AVTs is required. Part of the focus of this chapter will be on investigating chemical structure modifications of NFAs to improve their visible light transparency. The design of suitable NFAs for visibly transparent photovoltaics is more complex than for opaque OPVs as the PCE, AVT and CRI all need to be considered.[26,187]

5.1.3 Near Infra-red Responsive Organic Photodetectors

Photodetectors sensitive to NIR wavelengths are desirable for optical communications and substance identification as well as biometric monitoring and imaging.[8,88–90] Commercial detectors responding into the NIR region are based on epitaxially grown inorganic materials, including silicon or various III-V semiconductors. These materials are brittle and inflexible, making them incompatible with applications requiring mechanically flexible photodetectors. Therefore, the development of NIR responsive OPDs is particularly attractive for biometric monitoring applications, where having a flexible, conformable and light weight detector is desirable.[177,194] Photodetectors for biometric monitoring applications utilise NIR wavelengths to monitor various biological processes. One proven application of NIR absorbing NFA based OPDs is in pulsed oximeters, which quantify the concentration of oxygenated and deoxygenated haemoglobin in blood using the ratio of absorbance of red and NIR (or red and green) light.[89] Specifically, for pulsed oximeters a

photodetector responsive to light with wavelengths between 740nm – 950nm is required.[89] Only a few blends employing NIR absorbing NFAs exhibiting responsivities up to 1000 nm have been reported.[180] Furthermore, bioimaging in the second NIR window, 1000 – 1350 nm, is desirable for applications such as fat tissue imaging. However, progress in the development of OSCs delivering responsivities up to 1400 nm has so far been limited.[90,195]

Typically blends employing NIR absorbing NFAs will give a broadband photoresponse across the visible and NIR region. To obtain narrowband responsivity in the NIR one strategy that has been explored is charge collection narrowing in thick bulk heterojunction active layers by which the efficacy of collection of shorter wavelengths is reduced leading to a narrowband response near the onset of absorption of the blend.[196] On top of using NIR absorbing OSCs, to obtain OPD responsivity in the NIR another strategy that has been successfully applied is using microcavities to tune the absorption of the intermolecular charge-transfer state giving photodetectors with NIR photoresponses.[197] This provides an excellent way to obtain a narrowband NIR OPD photoresponses at tuneable wavelengths. Notably both of these approaches deliver relatively low responsivities.[87,198]

The NFAs with absorption tuned to the NIR region, is a desirable approach for achieving OPDs with high NIR responsivities. To date, few NIR absorbing NFAs have been designed for OPD applications. One example is CO1-4Cl, which has been used in OPDs delivering a responsivity over 0.5 A W^{-1} in the 920 – 960 nm region.[179] Other analogues of this structure have also been explored and delivered high OPD responsivities. The detectivities of OPDs based on CO1-4Cl and its derivatives have been limited by the relatively high dark currents obtained.[199] As mentioned in *Chapter 4*, high dark currents in OPDs have been related to noise currents arising from intra-gap trap states and this has been highlighted as a particular problem for OPDs employing narrow band gap NIR absorbing OSCs.[4,87] To better understand this limitation, and how it might relate to the chemical structure of the NFAs, studies investigating OPDs based on a range of blends employing NIR absorbing NFAs would be useful. For this to be possible, first the library of available NIR absorbing NFAs applied in OPDs needs to be extended. This chapter will explore the NFAs O-IDTBCN and O4TFIC as materials for NIR responsive OPDs.

5.2 Near Infra-red Absorbing O-IDTBR Derivatives

Throughout this thesis the effect of chemical structure modifications on O-IDTBR have been explored. O-IDTBR absorbs strongly in the visible region with absorption peaks in thin films thermally annealed at 120 °C at 414 nm, 670 nm and 733 nm, making it

unsuitable for transparent OPV applications. The peak absorption for thermally annealed thin films of O-IDTBR at 733 nm is right on the edge of the visible region, with the absorption tail extending into the NIR. Therefore, O-IDTBR has been used in NIR responsive OPDs. For example, an OPD based on P3HT:O-IDTBR has been shown to exhibit low dark current densities of 21 nA cm^{-2} at – 5 V applied bias and has also been successfully employed in a pulsed oximeter where the NIR wavelength absorbing properties of the blend were exploited for blood oxygen level monitoring.[160,200] In *Chapter 4*, a PTQ10:O-IDTBR based OPD with a dark current density of 0.8 nA cm^{-2} at – 2 V reverse bias was presented.[157] The responsivity of these unannealed O-IDTBR based blends extends to 740 nm. The ideal wavelength range of response for pulsed oximeters operating in the NIR is 740 – 950 nm.[89] Indeed, the NIR is typically considered as wavelengths from 800 – 2500 nm.[90] It is therefore advantageous to extend the responsivity of OPDs further into the NIR than O-IDTBR allows.

Initially, it was hoped that by modifying the chemical structure of O-IDTBR, in order to narrow its optical band gap, that NFAs more suitable for both NIR photodetection and semi-transparent OPV applications could be obtained. As discussed in *Chapter 3*, to further narrow the band gap of O-IDTBR, the electron accepting rhodanine unit in the Acceptor-Donor-Acceptor chemical structure can be exchanged for a more electron deficient unit, shifting the NFA's absorption into the NIR as a result of enhanced intramolecular charge transfer. Figure 62 displays the chemical structures of the end group derivatives of O-IDTBR: O-IDTBCN and O-IDTBFIC. In O-IDTBCN, which is also discussed as a material for OTFTs and OPVs in *Chapter 3*, a dicyanovinyl unit replaces the rhodanine. In O-IDTBFIC a fluorinated 1,1-dicyanomethylene-3-indanone (FIC) unit, which is widely used in many of the best performing NFAs including Y6 and IEICO-4F, is implemented.

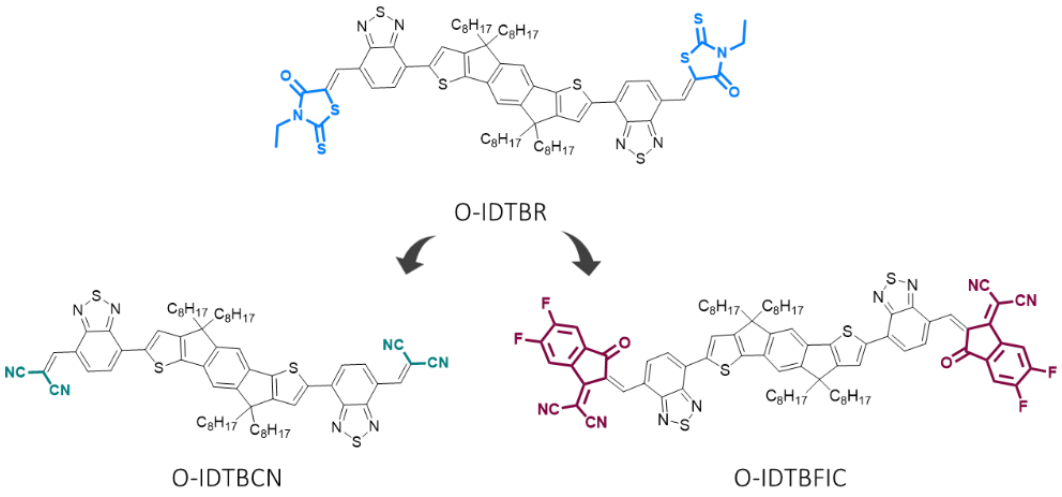

Figure 62| (a) Chemical structures of O-IDTBR, O-IDTBCN and O-IDTBFIC.

The peak absorption of thin films of O-IDTBCN annealed at 130 °C, for which the UV-vis absorption is presented in figure 38 (*Chapter 3*), of 763 nm, relative to 733 nm for O-IDTBR, makes it a desirable candidate for NIR responsive OPDs. O-IDTBCN is not suitable for visibly transparent OPV applications as it absorbs strongly in the 400 – 700 nm region.

Following the success of the PTQ10 based OPDs discussed in *Chapter 4*, again PTQ10 was investigated here as the donor polymer in OPDs, combining it this time with O-IDTBCN. In *Chapter 4* it was highlighted that exciton dissociation in PTQ10:O-IDTBR based OPDs was likely limited by the lack of offset in IP between the donor and acceptor.

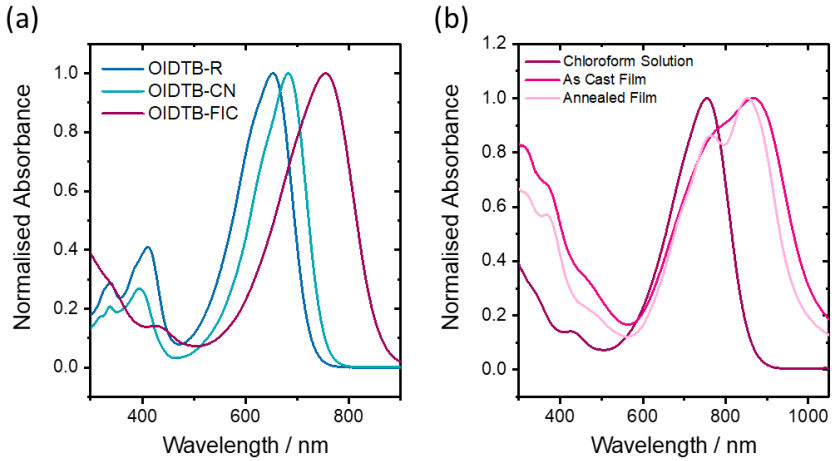

Figure 63| (a) Normalised UV-vis absorbance of OIDTBR, OIDTBCN and OIDTBFIC in chloroform solution at 0.005 mg ml^{-1}. (b) UV-vis absorbance of OIDTBFIC in chloroform solution, as cast thin film and thin film thermally annealed at 150°C.

To assess the offset in IP between PTQ10 and O-IDTBCN, the IP of O-IDTBCN was determined using PESA. Here, for thin films of O-IDTBCN annealed at 130 °C, an IP of 5.86 eV was determined. Similarly, from as cast thin films of O-IDTBCN, the IP was determined to be 5.72 eV. This difference in IP between as cast and annealed films is more significant than for either O-IDTBR or O-IDTBFIC, for which the IPs are shown in figure 64. The change in energy levels observed on annealing again highlights the difficulties in understanding the differences in energy levels between the monomolecular species and OSC in the solid-state. In a bulk heterojunction blend a variety of energy levels associated with the OSCs will be present.[201] The IP of O-IDTBCN in both as cast and annealed thin films determined using PESA is deeper than that of PTQ10, which can be expected to enable the energetically favourable formation of a charge-transfer state in the blend and resulting exciton dissociation into charge separated states. The values of IP are in good agreement with the value of 5.80 eV determined previously using ultraviolet photoelectron spectroscopy (UPS).[135] As mentioned previously, UPS can be combined with low-energy inverse photoemission spectroscopy (LE-IPES) to determine the EA of OSCs. Elsewhere, using LE-IPES, the EA of O-IDTBCN has been determined as 3.80 eV.[135] It is worth noting that LE-IPES is a specialist technique which would not be readily available to many labs working on OSCs.c

Figure 64| Ionisation potentials (IP) determined from PESA for as cast (AC) and thermally annealed (TA) thin films of O-IDTBR, O-IDTBCN and O-IDTBFIC. Thin films were annealed at either 120 °C for O-IDTBR, 130 °C for O-IDTBCN, or 150 °C for O-IDTBFIC.

To fabricate the OPDs, PTQ10:O-IDTBCN blends with a 1:1.5 ratio of donor to acceptor were blade coated from chlorobenzene. The OPVs had an ITO/ZnO/Active-Layer/MoO_x/Ag architecture. As discussed in *Chapter 4*, this is not the ideal architecture for OPDs but is used here to investigate the initial viability of the PTQ10:O-IDTBCN blend for OPD applications. Figure 65 displays the OPV and OPD

performance of 880 nm thick PTQ10:O-IDTBCN based devices. From figure 65a and 65c, the EQE is above 50 %, which is impressive at this large film thickness. For context, typically the thicknesses of optimised OPV blends are below 150 nm. For the active layer annealed at 100 °C, the responsivity of the device extends to a peak of 0.36 A W^{-1} at a wavelength of 775 nm. This responsivity is recorded under short circuit conditions, and it is expected that the responsivity will increase when an external field is applied. For comparison the peak responsivity under short circuit conditions of the PTQ10:O-FBR blend discussed in *Chapter 4* is 0.23 A W^{-1} and almost doubles to 0.41 A W^{-1} when an external bias of – 5V is applied.

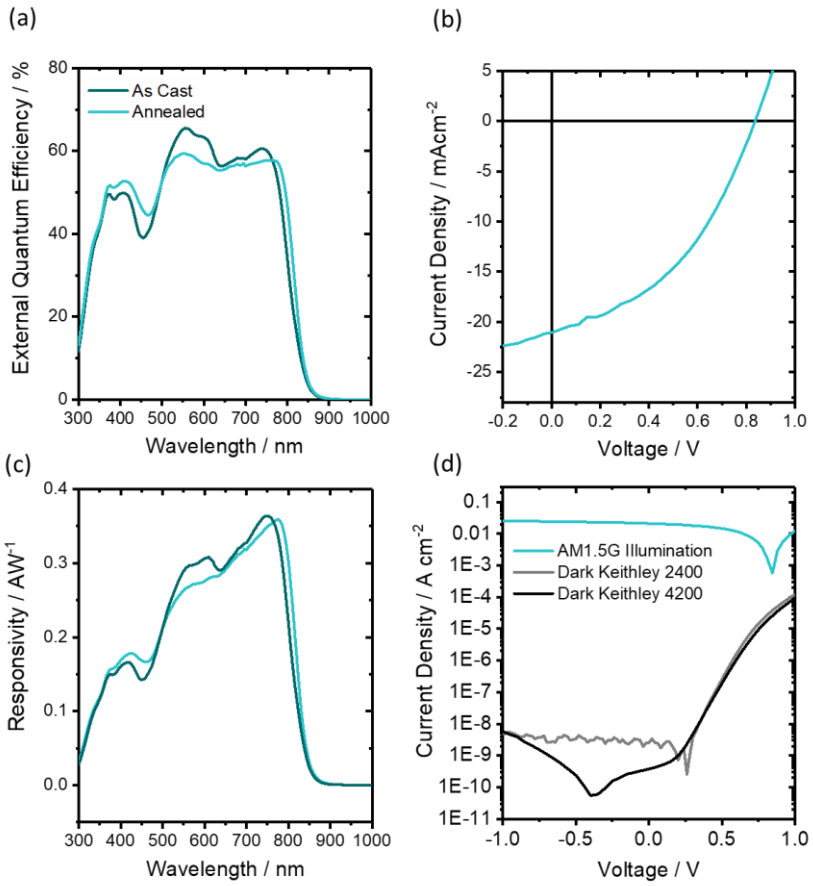

Figure 65| For a PTQ10:O-IDTBCN based device: (a) External Quantum efficiency of devices based on an as cast active layer or active layer thermally annealed at 100 °C. (b) Current density-voltage characteristics of a thermally annealed device. (c) Responsivity of an as cast and 100 °C annealed device. (d) Dark and illuminated current density-voltage characteristics of the device thermally annealed at 100 °C. The dark current densities measured on both a Keithley 4200 and 2400 source-measurement unit are shown.

Relative to PTQ10:O-IDTBR, the replacement of O-IDTBR with O-IDTBCN simultaneously extended the OPD responsivity into the NIR, making it more useful in specific OPD applications. As mentioned, the O-IDTBCN based OPDs also exhibited a significantly higher peak responsivity compared with those based on O-IDTBR. From figure 65b, despite the relatively high current density achieved for this 880 nm thick active layer, a relatively low FF of 42 % is achieved, when the device is considered as an OPV. FF is not a parameter considered in OPD performance, where typically the devices are operated at reverse bias. Figure 65d displays the dark and illuminated current density of the thermally annealed PTQ10:O-IDTBCN device.

Across six devices, dark currents of $5.8 \pm 0.3 \times 10^{-8}$ A cm^{-2} were measured at a reverse bias of – 1 V using a Keithley 2400 source-measurement unit. This corresponds to a direct current reading of around 10^{-10} A for a device with pixel area of 0.045 cm^2 and is at the limit of the sensitivity of a Keithley 2400. In contrast, measuring on a Keithley 4200 source-measurement unit, which has a higher sensitivity, lower dark currents were achieved, as illustrated in figure 65d. It is not clear what causes the minimum at – 0.4 V which can be seen in figure 65d, but similar features can be observed in literature for blends with very low dark currents.[96] It is possible that this is related to the circuitry with which the devices are measured or alternatively not being able to achieve total darkness under laboratory conditions. Under short circuit conditions a dark current density of 3.8×10^{-9} A cm^{-2} was measured using the Keithley 4200. This dark current achieved for the PTQ10:O-IDTBCN based devices is impressively low for a NIR responsive blend and, combined with the simultaneously high responsivity achieved, suggests that PTQ10:O-IDTBCN blends could be promising in OPD applications, especially applications where NIR detectivity is required. In order to properly assess the NEP and thereby D* for these PTQ10:O-IDTBCN based OPDs, proper measurements of the contributions of noise to the current density in the devices would need to be made.

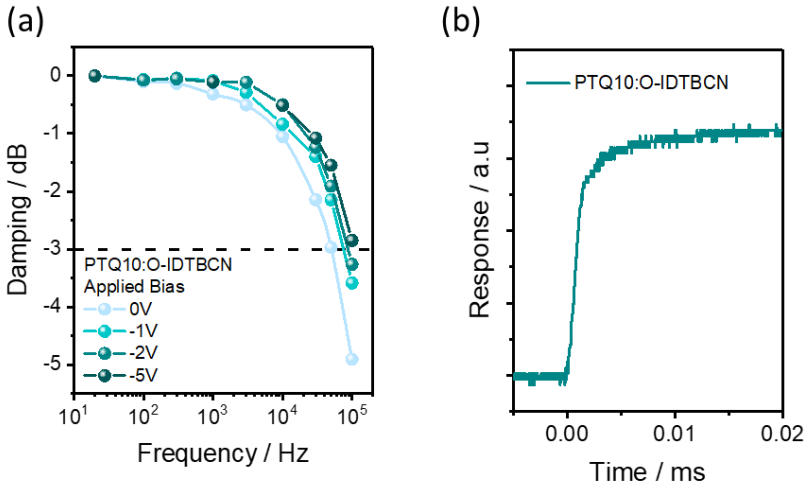

Figure 66| For OPDs based on a PTQ10:O-IDTBCN blend with a 1:1.5 ratio of donor to acceptor and annealed at 100 °C (a) Normalised photoresponse at increasing frequency of white LED light, for determination of the – 3dB cut-off frequency at varying applied bias. (b) Transient response to white LED light under short circuit conditions.

The response time and cut-off frequency of the thermally annealed PTQ10:O-IDTBCN based OPDs were also investigated. Figure 66a displays plots from which the – 3dB cut-off frequencies at 0 V, – 1 V, – 2 V and – 5 V were determined. Figure 66b displays the transient response of the OPD. The rise times, fall times and cut-off frequencies of a representative OPD are given in table 14. As the OPD is based on a relatively thick, 880 nm, active layer film a relatively slow response could be expected. In fact, here a comparatively fast response is observed with cut-off frequencies of more than 50 kHz under both short circuit conditions and – 2 V applied bias. For context, it has been reported that a response to frequencies of 10 – 15 kHz is sufficient for imaging applications and that for high speed imaging 100 kHz is required.[202]

Table 14| Rise and fall times as well as cut-off frequency for a representative OPD based on a PTQ10:O-IDTBCN blend with a 1:1.5 ratio of donor to acceptor and annealed at 100 °C. Measured at 0V and -2V applied bias.

NFA	At 0 V	At -2 V
Rise Time / µs	19	6
Fall Time / µs	12	6
Cut-off frequency / kHz	50	85

5.3 Near Infra-red Absorbing Non-fullerene Acceptors with Oxygen Bridged Cores

In section 5.2 it was highlighted that the strong absorption of O-IDTBR and its derivatives in the visible region, 400 – 700 nm, meant these NFAs are unsuitable for visibly transparent OPV applications. Therefore, significantly different NFA chemical structures, employing a highly electron rich oxygen bridged core donor unit, are explored in this section. After initial characterisation of the optoelectronic properties, these materials are explored in opaque OPVs, which could in the future be further optimised for transparency. The materials are then explored in NIR responsive OPDs, which are shown to be promising for optical communications applications.[88]

Previously oxygen-bridged electron donating core units have been used in the NFA CO_i6DFIC and its derivatives.[203,204] These NFAs benefit from strong intramolecular charge transfer in the Acceptor-Donor-Acceptor structure, between the electron rich oxygen-bridged core and electron withdrawing fluorinated IC units, giving them relatively narrow optical band gaps. CO_i6DFIC exhibits a peak absorption in solution at 760 nm.[203] Here the newly designed NFA O4TFIC, for which the chemical is given in figure 67, is investigated. In contrast with CO_i6DFIC, O4TFIC exhibits a more red-shifted absorption, with a maximum at 800 nm in chloroform solution. This difference can be attributed to the differing position of the oxygens within the alkoxy bridged core. In the core of CO_i6DFIC the oxygen is located adjacent to the thienothiophene central moiety, whereas in O4TFIC the oxygen is at the neighbouring position. O4TFIC also possess linear octyl side chains rather than the bulkier phenyl-hexy side chains present in CO_i6DFIC.

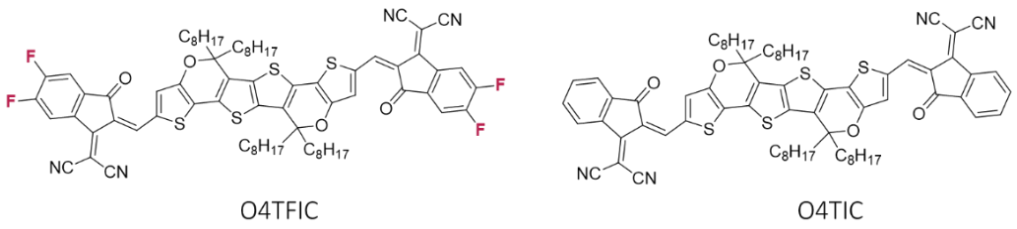

Figure 67| Chemical structures of O4TFIC and O4TIC.

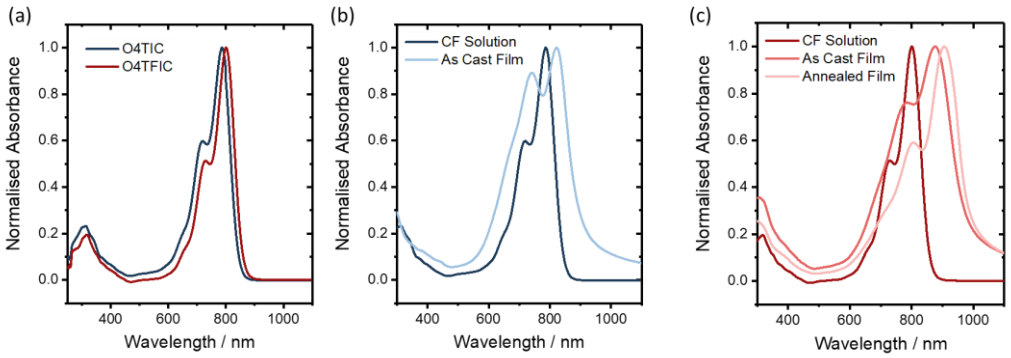

Figure 68| (a) Normalised solution UV-vis absorbance of O4TIC and O4TFIC in chloroform, concentration 0.005 mg ml^{-1}. (b) Normalised solution and as cast thin film absorbance for O4TIC. (c) Normalised absorbance of O4TFIC for a solution in chloroform, as cast thin film and thin film annealed at 130 °C for 10 minutes.

The effect of fluorination of the 1,1-dicyanomethylene-3-indanone (IC) end group is relatively well understood, exemplified here in the comparison between O4TIC and O4TFIC (figure 67). Previously, in the acceptor ITIC, increasing the number of fluorine substituents on the IC unit has been correlated with closer intermolecular π-π stacking in single crystals, resulting in higher coupling constants between molecules and increased electron mobility, as well as a red shift of the NFAs absorption in solution and the solid state.[205] From the plot of absorbance in chloroform solution displayed in figure 68a, fluorination of the end group results in a relatively small shift in absorption of 13 nm from 787 nm for O4TIC to 800 nm for O4TFIC. This is in line with the similarly small shift in peak absorption in solution on moving from ITIC, to its fluorinated analogue IT-4F, of 17 nm.[28]

In contrast, in the solid state a much more significant red shift in absorption is observed for O4TFIC compared with O4TIC. In figure 68b a clear broadening of the absorption of O4TIC on moving from solution to thin film is observed. No shift in absorption is observed on annealing O4TIC thin films relative to the as cast films. In contrast, for O4TFIC a red shift in absorption is observed on moving from the solution to the as cast thin film (figure 68c) and a further red shift is observed on thermally annealing the thin film at 130 °C/10 minutes. From this it is clear that the fluorinated end group of O4TFIC is having a significant effect on the solid-state intermolecular packing of the material. Overall, from solution to annealed thin film, a shift in peak absorption of 105 nm, from 800 nm to 905 nm, is observed for O4TFIC. This shift is likely due to structural reorganisation of the molecules in the thin films. Such structural reorganisation is currently difficult to predict when designing novel small molecule organic semiconductors. The formation of J-aggregates or other intermolecular packing interactions can significantly alter the absorption compared

with that predicted for the monomolecular species.[206] It has been shown that the combination of different long range coulombic as well as short range orbital interactions in the slip stacked packing motifs of Y6 and its derivatives result in the large red-shift and spectral broadening observed in its absorbance in the solid state relative to solution.[206] A similarly large red-shift and broadening of the absorbance of O4TFIC on moving from the monomolecular (solution absorbance) to solid state (thin film absorbance) is observed here. Figure 69 helps this large shift in absorbance between solution and solid state to be visualised for Y6 and O4TFIC.

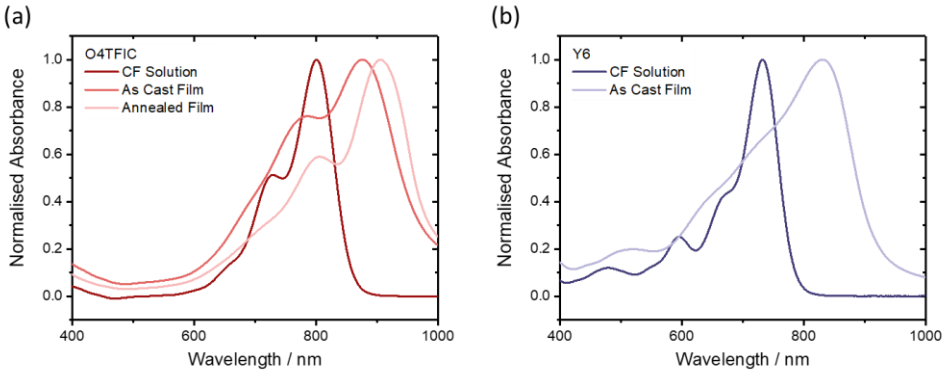

Figure 69| (a) Normalised absorbance of O4TFIC in chloroform solution, as cast thin film and thin film annealed at 130 °C for 10 minutes. (b) Normalised absorbance of Y6 in chloroform solution and as cast thin film.

5.3.1 Near Infra-red Absorbing Non-fullerene Acceptors with Oxygen Bridged Cores for Organic Photovoltaic Applications

From the UV-vis absorbance in thin films, it is clear that O4TFIC is a promising candidate for visibly transparent OPVs in terms of having a low absorbance in the 400 – 700 nm range. To pair O4TFIC with a suitable donor material the energy levels are determined. The IP and E_g of O4TIC and O4TFIC thin films, both as cast and annealed, are shown in table 15. The IPs were determined using PESA and the E_g was determined from the onset of absorption in thin films.

Table 15| For the NFAs O4TFIC and O4TIC in as cast or thermally annealed (TA) thin films: Ionisation potentials obtained using PESA (IP) and optical band gaps (E_g) obtained from the onset of UV-vis absorption. Peak absorbance of the as cast and annealed thin films (λ_{max}).

Sample	IP / eV	E_g / eV	λ_{max} / nm
O4TIC, As Cast	5.59	1.35	822
O4TFIC, As Cast	5.70	1.25	877
O4TFIC, TA at 130°C	5.66	1.25	905

The performance of O4TFIC as an acceptor in OPVs was then investigated. Initially, PCE10 was selected as a potential donor with which to pair O4TFIC. This selection was made based on the previous pairing of CO_i6DFIC and its derivatives with PCE10.[203] The PCE10:O4TFIC based OPV performances are given in table 16. Unfortunately, only low PCEs, with an average of 3.5 %, were achieved. This is likely due to an unfavourable blend morphology and poorly aligned energetics of the two OSCs.

Table 16| Photovoltaic performance of OPVs based on a PCE10:O4TFIC and PCE10:O4TIC active layer blends. Current density (J_{sc}), Open Circuit Voltage (V_{oc}), Fill Factor (FF) and Power Conversion Efficiency (PCE).

Blend	J_{sc} / mAcm^{-2}	V_{oc} / V	FF	PCE / %
PCE10:O4TIC	8.8 ± 0.6	0.750 ± 0.002	0.46 ± 0.01	3.0 ± 0.2
PCE10:O4TFIC	13.0 ± 1.1	0.551 ± 0.003	0.50 ± 0.01	3.5 ± 0.3

[a]Mean values and standard deviations determined from 5 OPVs with pixel areas of 0.045 cm^2.

The OPV performance of O4TFIC was next tested by combining it with PM6. OPVs based on PM6:O4TFIC, in a 1:1 weight ratio, were prepared from chlorobenzene solutions and annealed at 130 °C/10 mins. Figure 70a displays the current density-voltage characteristics of the best performing PM6:O4TFIC based OPV and figure 70b displays the EQE. For the PM6:O4TFIC blend, a higher V_{oc} of 0.672 V was obtained compare with the PCE10:O4TFIC blend. Notably, this V_{oc} is still lower than the best performing blends used in transparent OPVs to date. For comparison semi-transparent OPVs based on PM6 combined with a Y6 derivative delivered a V_{oc} of 0.89 V, which drops to 0.84 V when the blend is optimised for transparency.[207] Therefore, in the future finding alternative donor polymers to pair with O4TFIC that yield higher V_{oc}s would be desirable. The transparency of the O4TFIC based OPVs was not optimised but it is important to note that on optimisation of the AVT the PCE is likely to drop.[190]

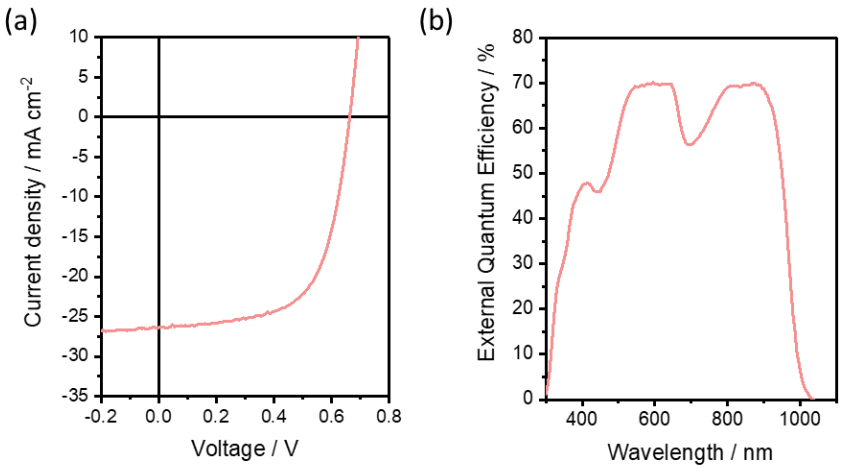

Figure 70| (a) Current Density-Voltage characteristics under AM1.5G illumination of a PM6:O4TFIC based OPV with a 100 nm active layer. (b) External Quantum Efficiency of a PM6:O4TFIC based OPV with a 100 nm active layer.

Table 17| Photovoltaic performance of OPVs based on a PM6:O4TFIC active layer blend. Current density (J_{sc}), Open Circuit Voltage (V_{oc}), Fill Factor (FF) and Power Conversion Efficiency (PCE).

Blend, Thickness	J_{sc} / mAcm^{-2}	V_{oc} / V	FF	PCE / %
PM6:O4TFIC, 100 nm	27.3 ± 0.5	0.672 ± 0.001	0.60 ± 0.01	11.0 ± 0.4
PM6:O4TFIC, 200 nm	23.1 ± 2.6	0.643 ± 0.026	0.44 ± 0.02	6.5 ± 0.5

[a]*Mean values and standard deviations determined from 5 OPVs with pixel areas of 0.045 cm^2.*

Next it was considered if, by modifying the chemical structure of O4TFIC, the V_{oc} of OPVs based on it could be enhanced, whilst maintaining good visible transparency. The V_{oc} of an OPV is related to the energy of the intermolecular charge-transfer state, which forms at the interface of the donor and acceptor material.[30] The charge-transfer state energies of NFA based blends have been shown to be lower than the interfacial energy offsets, i.e. the offsets between the IP of the donor and EA of the acceptor. It was hoped that by adjusting the chemical structure of O4TFIC to shallow its energy levels an enhanced V_{oc} could be obtained for OPVs on which it is based. At the same time, it was desirable to maintain a narrow optical band gap, necessary for transparency to visible light. To achieve this O6TFIC, which extends the electron rich core of O4TFIC with two extra thiophene units, was designed (figure 71). By adding electron density to the donor core of the molecule in this way, it was predicted that both frontier molecular orbitals of the monomeric species should be shifted closer to vacuum, thereby giving lower IPs and EAs.

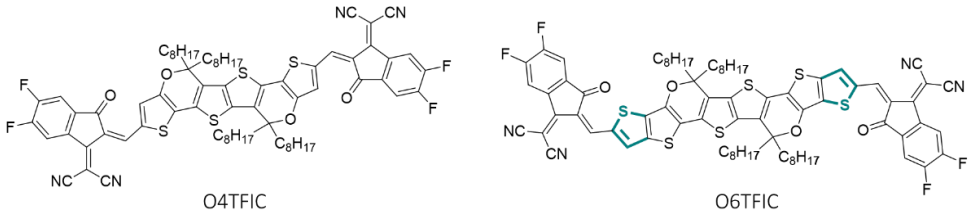

Figure 71| Chemical structure of O6TFIC, with O4TFIC again for comparison.

The IPs, derived from PESA, and optical band gaps (E_g), estimated from the onset of absorption, are given in table 18. By comparing the IPs for as cast thin films, of 5.70 eV and 5.46 eV for O4TFIC and O6TFIC respectively, it is clear that introducing additional electron density onto the core of the molecule has reduced the IP as was expected. Only a slight change in optical band gap was observed from the onset of absorption. This is desirable as whilst a large red-shift in peak absorption would move the absorption associated with ground to singlet excited state (S0-S1) transition out of the visible region it would also shift other peaks, for example that corresponding to the S0-S2 transition, into the visible region.

Figure 72a, displays the normalised solution UV-vis absorbance of O4TFIC and O6TFIC in chloroform. A new peak is observed in the solution UV-vis for O6TFIC at 455 nm. As can be seen in figure 72b this peak also appears in the UV-vis absorbance of the as cast thin film. As a result of this extra absorbance thin films of O6TFIC are a pale green colour and less visibly transparent than O4TFIC. The origin of the new absorption peak is unclear. It is also interesting to note that, whilst for O4TFIC a large red shift in absorbance is observed on annealing, which is likely related to the reorganisation of molecules in the thin film into a more ordered state, for O6TFIC no such shift is observed.

Table 18| For the NFAs O4TFIC and O6TFIC in as cast or thermally annealed (TA) thin films: Ionisation potential obtained from PESA (IP) and optical band gap (E_g) estimated from the onset of UV-vis absorption. Peak absorbance of the thin films (λ_{max}).

Sample	IP / eV	E_g / eV	λ_{max} / nm
O4TFIC, As Cast	5.70	1.25	877
O4TFIC, TA at 130°C	5.66	1.25	905
O6TFIC, As Cast	5.46	1.18	887

When O6TFIC was tested in OPVs combined with the donor polymer PM6, a very poor OPV performance was recorded with a PCE of only 0.71 % being achieved for devices with an active layer thickness of 110 nm. As O6TFIC also exhibits worse visibly transparency than O4TFIC its performance was not further explored. In the future it is hoped that other chemical structure derivatives of O4TFIC can deliver simultaneously high PCEs and narrow optical band gaps.

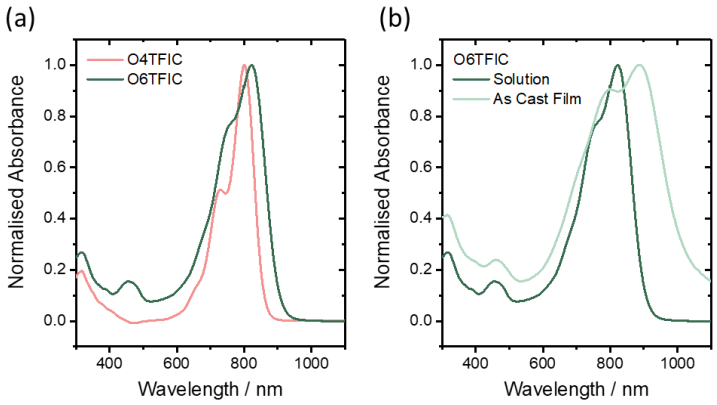

Figure 72| (a) Normalised UV-vis absorbance of O6TFIC and O4TFIC in chloroform solution at 0.005 mg ml^{-1}. (b) Normalised UV-vis absorbance of a chloroform solution and as cast thin film of O6TFIC.

5.3.2 Near Infra-red Absorbing Non-fullerene Acceptors with Oxygen Bridged Cores for Organic Photodetector Applications

For OPD applications, the peak absorbance of thermally annealed thin films of O4TFIC at 905 nm and the high EQEs achieved for PM6:O4TFIC based OPVs made it a desirable candidate for NIR responsive OPDs. Therefore, PM6:O4TFIC based OPDs were used to demonstrate the potential of OSCs for optical communications applications.[88] For optical communications applications a fast response speed and high specific detectivity are desirable. PM6:O4TFIC OPDs delivered a high responsivity of 0.50 A W^{-1} at 890 nm under short-circuit conditions and were able to transcribe the signal from a commercial remote control.[88] Figure 73 displays the damping and transient response of the OPDs. The limitation of these devices is their relatively high dark currents, 8.3 x 10^{-7} A cm^{-2} at – 2 V applied bias. This is in part likely related to the relatively thin active layer, of only 90 nm, the unoptimized device architecture and also the narrow band gap of the acceptor, as it has been shown that noise current limitations to the detectivity of OPDs are more significant in the NIR region.[4,158]

For optical communications applications a fast photoresponse is a key requirement because signals of pulsed rather than continuous light are used to avoid overheating of the device.

PM6:O4TFIC based photodetectors were shown to deliver a fast photoresponse to an LED emitting at 880 nm. Figure 73a displays the normalised transient response under short-circuit conditions and – 2V applied bias. A very fast rise time of 8.1 µs, which decreases to 3.8 µs on applying a – 2 V reverse bias, was measured. Here the rise time corresponds to the time taken for the device to go from 10 % to 90 % of the steady state photoresponse. This response is significantly faster than the other OPDs discussed in this thesis. From the normalised plot of photoresponse as a function of frequency (figure 73b), it is clear that for these OPDs the – 3dB cut-off frequency is not reached within the frequency range of the function generator used to modulate the IR LED emission. The frequency range required for IR communication is 38 – 52 kHz and the PM6:O4TFIC device is shown to perform well within this range.[88]

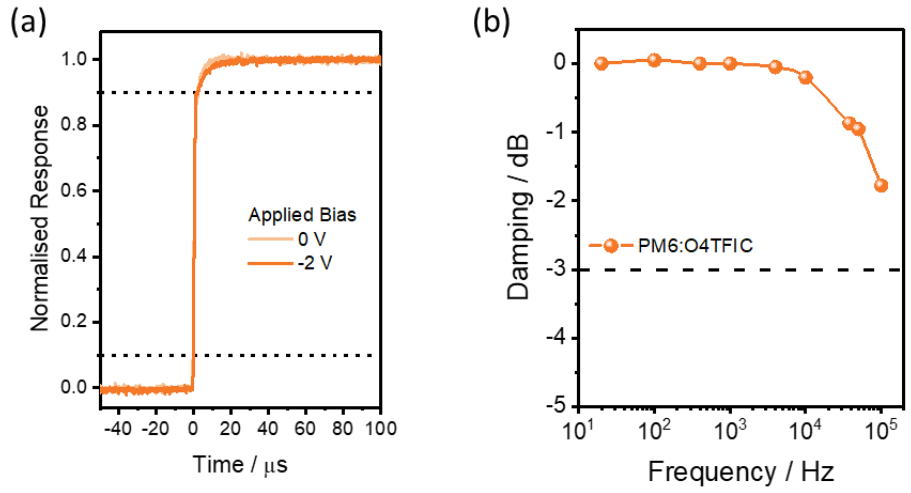

Figure 73| For OPDs based on a PM6:O4TFIC blend (a) The transient response under an applied bias of 0 V or – 2V. (b) The normalised photoresponse at increasing frequency of incident IR LED light (880 nm).

The fast response of the OPDs, necessary for optical communications applications, could be associated with a high mobility of O4TFIC. In line with *Chapters 2* and *3*, O4TFIC was also investigated in OTFTs. Based on the shift in UV-vis absorbance of thin films of O4TFIC annealed at 130 °C, the same anneal temperature was applied in the fabrication of the OTFTs. Again, a PEI electron selective interlayer was used and therefore exclusively n-type unipolar transport was observed. Figure 74 displays the transfer and output characteristics of OTFTs based on as cast and thermally annealed thin films of O4TFIC. In figure 75, the mobility calculated in the saturation and linear regime is plotted as a function of gate bias for these OTFTs. For the OTFTs based on the annealed thin films, higher on-currents were achieved in both the saturation and linear regime. Interestingly, the off-currents of the devices were also higher in the annealed OTFTs, indicating an increase in the conductivity of the transistor channel. High off-currents are detrimental to OTFT performance as the ratio of on to off current is important for the switching of a transistor. However, the relatively high off-current observed relates to a higher channel conductivity, which is indicative of a higher charge carrier density in annealed O4TFIC films. Conductivity is proportional to the product of mobility and charge carrier density. Similar linear mobilities, of 0.05 $cm^2\ V^{-1}\ s^{-1}$, are extracted for both the as cast and thermally annealed O4TFIC films. For OTFTs based on an annealed O4TFIC films a higher saturation mobility of 0.08 $cm^2\ V^{-1}\ s^{-1}$ is obtained, compared with 0.06 $cm^2\ V^{-1}\ s^{-1}$ for the as cast film. The high off-currents observed in these OTFTs mean that O4TFIC is not a promising material for transistor applications, however, the overall the performance indicates good transport properties for O4TFIC.

Table 19| Mobilities calculated in the linear (μ_{lin}, V_{ds} = 10 V) and saturation (μ_{sat}, V_{ds} = 80 V) regimes for OTFTs based on as cast or thermally annealed (130 °C) films of O4TFIC.

Processing	μ_{lin} / $cm^2\ V^{-1}\ s^{-1}$	μ_{sat} / $cm^2\ V^{-1}\ s^{-1}$
As Cast	0.05 ± 0.00	0.05 ± 0.00
Thermally Annealed	0.06 ± 0.00	0.08 ± 0.00

[a] *Means and standard deviations taken over at least 5 transistors for each processing condition with channel dimensions 40/1000 µm and a 900 nm CYTOP dielectric.*

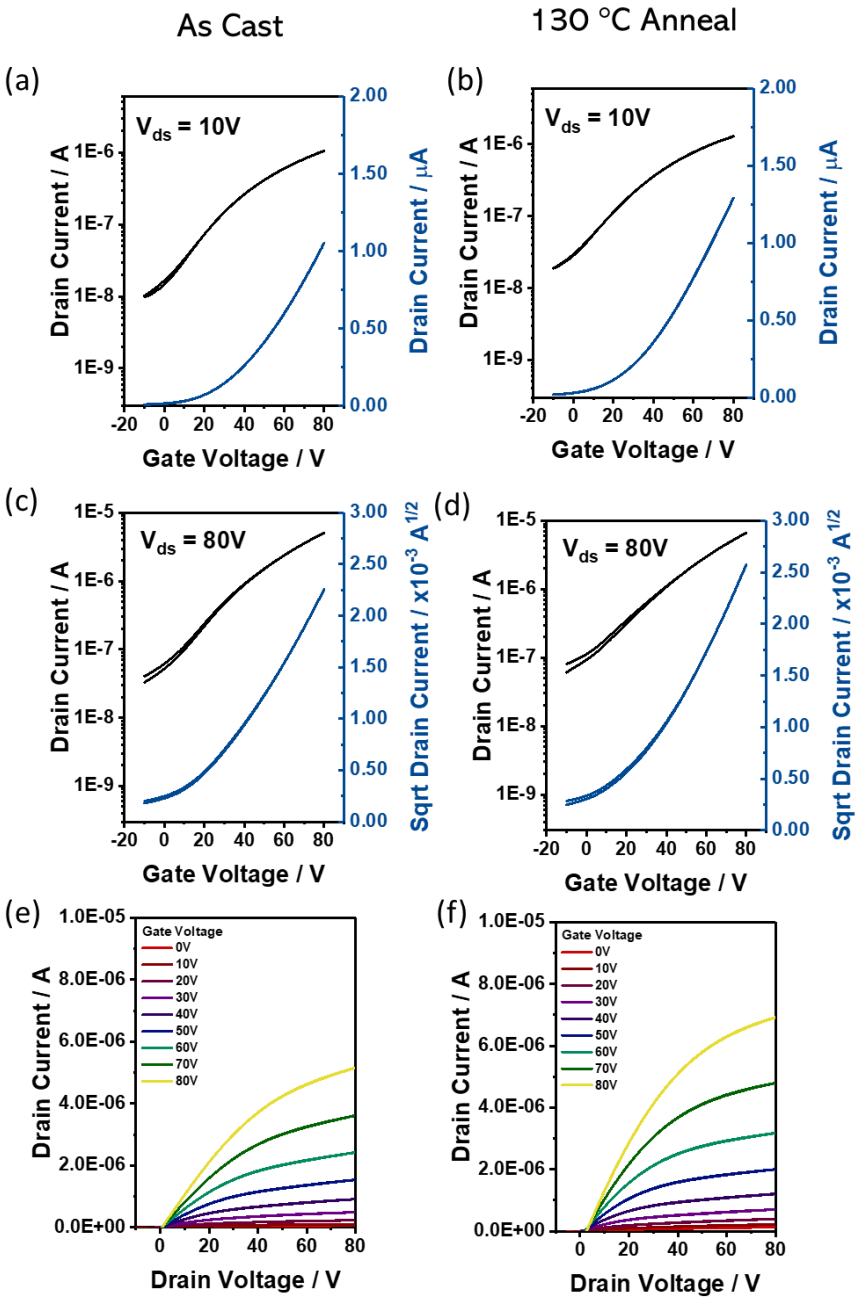

Figure 74| For OTFTs based on thin films of O4TFIC, either as cast or thermally annealed (130 °C/10 mins): (a,b) linear (V_{ds} = 10 V) transfer characteristics, (c,d) saturation (V_{ds} = 80 V) transfer characteristics, and (d,e) output characteristics. [Channel dimensions L/W 40/1000 µm, 900 nm CYTOP dielectric].

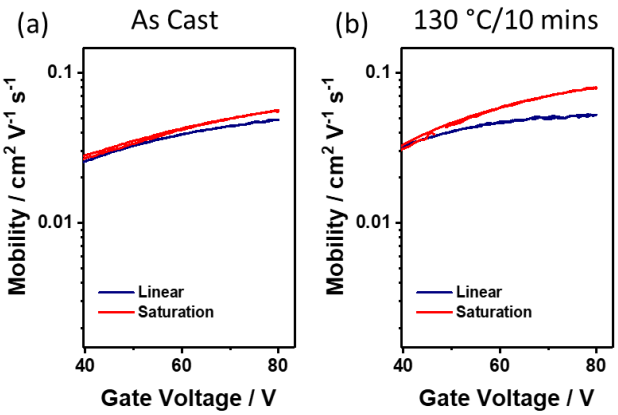

Figure 75| Mobility as a function of gate voltage calculated in the linear (V_{ds} = 10 V) and saturation (V_{ds} = 80 V) regime for OTFTs based on thin films of O4TFIC either (a) as cast or (b) annealed at 130 °C/10 mins. [channel dimensions L/W 40/1000 µm, 900 nm CYTOP dielectric]

5.4 The Near Infra-red Absorbing Non-fullerene Acceptor RS-Y6

So far in this chapter NIR absorbing O-IDTBR derivatives have been explored as well as NFAs containing a novel oxygen bridge core. Whilst these materials have shown promise for OPV and OPD applications, their efficiencies in opaque OPVs have not achieved PCEs approaching those of OPVs employing the Y-series NFAs. Y6 and its derivatives have been used in some of the best performing opaque OPVs to date, which have yielded PCEs approaching 18%.[36,208] This subclass of NFAs are often referred to as Y-series acceptors and typically exhibit absorption in the NIR. Since the development of the Y-series of acceptors, significant research has been done into improving the performance of Y6 through minor chemical structure modifications. For example, the acceptor N3 emerged from a study carefully analysing the effect on OPV performance of varying the alkyl side chain on the central core unit of Y6.[209] Another example is the acceptor BTP-eC9, which for a long time delivered the best performances in OPV. BTP-eC9 has nonyl side chains on the outer thiophene unit of the Y6 core as well as chlorine rather than fluorine substituents on the terminal IC units.[99]

Here, a novel derivative of Y6, RS-Y6 (figure 76) is presented. RS-Y6 contains a thiol side chain on the outer thiophene of the Y6 core unit. It was hoped that this structure modification would increase the electron density on the NFAs core and as a result that the energetic levels of RS-Y6 would be shallowed relative to Y6, thereby leading to potentially higher V_{oc}s in OPV blends compared with Y6, whilst also maintaining a narrow optical band gap.

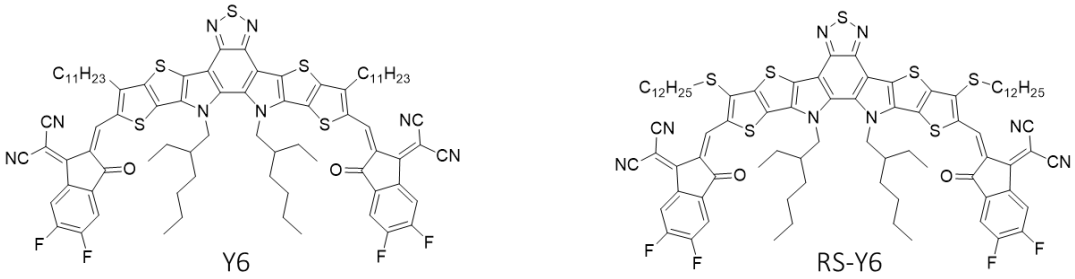

Figure 76| Chemical structures of Y6 and RS-Y6.

First the material and optoelectronic properties of RS-Y6 were compared with those of Y6. In solution UV-vis a more pronounced shoulder is observed for Y6 compared with RS-Y6 (figure 77a). Y6 is known to aggregate in solution, however, even at concentrations down to 0.0002 mg ml^{-1}, no shift in peak absorption was observed (figure 78b). This indicates that the fine structure observed in the solution UV-vis is not due to dimer formation. Similar molar extinction coefficients of 1.9 x 10^5 dm^3 mol^{-1} cm^{-1} and 1.2 x 10^5 dm^3 mol^{-1} cm^{-1} were determined for Y6 and RS-Y6 respectively. For context the molar extinction coefficients of a variety of IDTBR derivatives discussed in this thesis are given in table 20. For Y6 and RS-Y6 much higher extinction coefficients were determined compared with the IDTBR derivatives. Notably systematic errors in the concentrations of the solutions used to determine of the molar extinction coefficient can lead to distortions of value. Here sequential dilutions were performed using a micropipette.

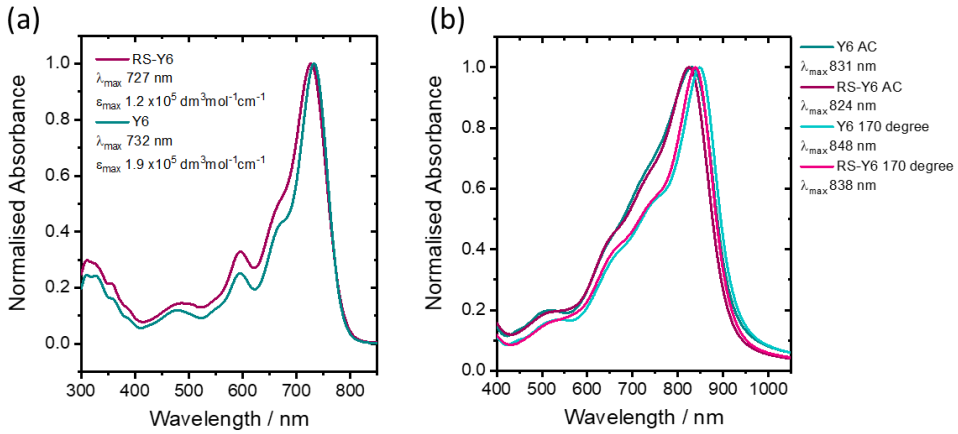

Figure 77| For the NFAs Y6 and RS-Y6: (a) Solution UV-vis absorbance in chloroform and (b) thin film UV-vis absorbance of as cast and annealed thin films.

Table 20| Molar extinction coefficients (ε) of various NFAs determined from solution UV-vis absorbance in chloroform as well as the wavelength of peak absorption in solution, at which ε is calculated ($\lambda_{max, sol.}$).

NFA	ε / dm^3 mol^{-1} cm^{-1}	$\lambda_{max, sol.}$ / nm
Y6	1.9 x 10^5	732
RS-Y6	1.2 x 10^5	727
O-IDTBR	1.0 x 10^5	653
O-IDTBCN	1.0 x 10^5	682
EH-IDTBR	1.0 x 10^5	653

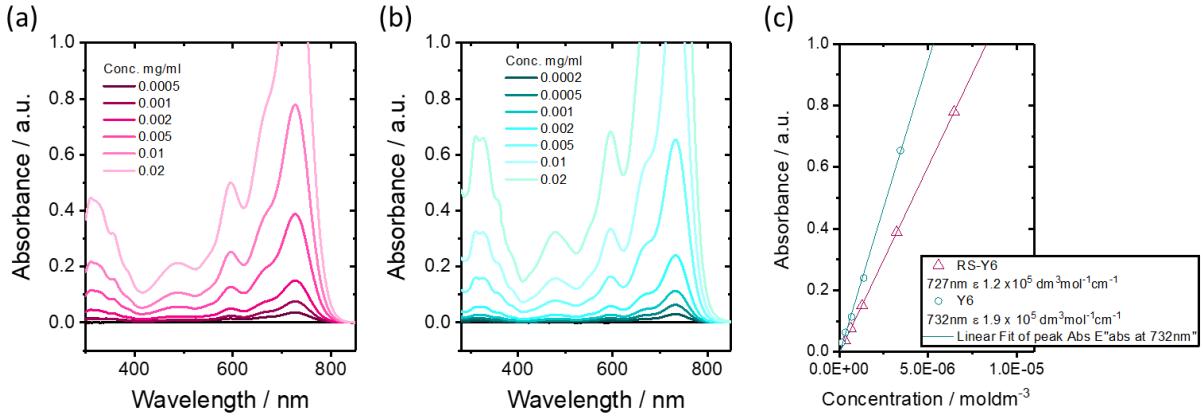

Figure 78| Solution UV-vis absorbance in chloroform of (a) RS-Y6 and (b) Y6. (c) Determination of the molar extinction coefficient of Y6 and RS-Y6 from solution UV-vis absorbance.

For both RS-Y6 and Y6, on moving from solution to the solid state, a broadening of the absorption is observed accompanied by a large red-shift in peak absorbance from 732 nm to 831 nm for Y6 and 727 nm to 824 nm for RS-Y6. Annealing thin films of the two NFAs at increasing temperature results in a gradual increase and red shift in absorbance (figure 79a).

Previously it has been shown that a pronounced peak corresponding to either the cold crystallization or glass transition temperature of Y6 does not appear in DSC measurements.[148,210] However, it is clear from the UV-vis of sequentially annealed thin films that a transition in the structural order is occurring (figure 77b). The deviation in the absorbance of annealed thin films compared with the as cast film absorbance can be used to determine the low temperature transitions of OSCs. Equation 18, gives the deviation metric, which is the sum of the squared deviation in absorbance between as cast (I_{AC}) and annealed thin films (I_T).[156] Previously a low temperature transition of 102 °C was determined for Y6 by calculating the deviation metric.[148] Figure 79, displays the UV-vis of sequentially annealed films of Y6 and RS-Y6 as well as the deviation metric plotted as

a function of temperature. The low temperature transition for RS-Y6 appears at lower temperatures than for Y6, 91 °C and 102 °C respectively. These values were determined from linearly fitting the deviation metric following previously reported procedures.[148,156] The lower transition temperature of RS-Y6 compared with Y6 is expected based on the longer dodecyl (C_{12}) side chain relative to the undecyl (C_{11}) side chain of Y6. The low temperature thermal transitions of several Y6 derivatives have previously been determined.[150,151] Derivatives with longer side chains demonstrated lower transition temperatures, in line with what was observed for the IDTBR side chain derivatives discussed in *Chapter 3*.[150] The conclusion of the previous study into Y6 and its derivatives, was that Y6 derivatives with shorter side chains, and therefore higher glass transition temperatures and lower diffusion constants, were necessary for the development of thermodynamically stable blends based on Y6 derivatives.[150] However, shorter side chains are detrimental to solubility and processability and therefore it was suggested that the Y-series of acceptors may never be viable for a stable commercial product.[150]

$$Deviation\ Metric = \sum_{\lambda_{min}}^{\lambda_{max}} [I_{AC}(\lambda) - I_T(\lambda)]^2 \quad (18)$$

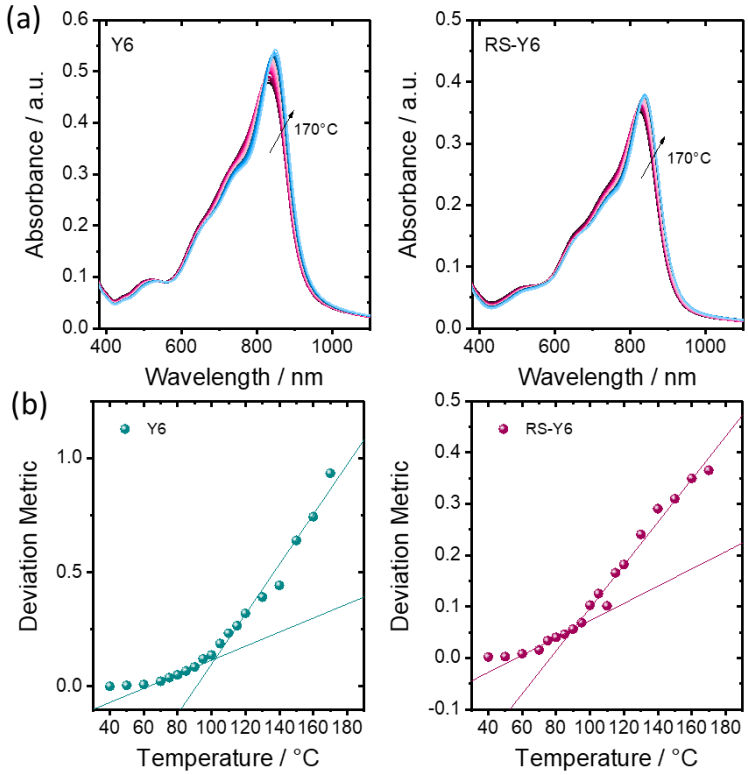

Figure 79| (a) Thin film UV-vis absorbance of Y6 and RS-Y6 with sequential annealing. (b) Deviation metrics calculated from the sequentially annealed thin film UV-vis absorbance of RS-Y6 and Y6.

Next the energy levels of the two NFAs were compared. NFA energy levels are almost exclusively determined in the solid state, either by photoelectron spectroscopy or cyclic voltammetry. As mentioned, ultraviolet photoelectron spectroscopy (UPS) combined with low energy inverse photoemission spectroscopy (LE-IPES) has been highlighted as an excellent way to assess the IP and EA of NFAs, however, this is a highly specialist technique not available ubiquitously. Using UPS and LE-IPES previously the IP and EA of Y6 have been determined as 5.8 eV and 4.1 eV respectively.[136] In the same study, using PESA a notably shallower IP of 5.65 eV was determined for Y6. This is in good agreement with the values determined here using PESA on as cast and thermally annealed thin films of Y6, 5.67 eV and 5.65 eV respectively (table 21). Figure 80 displays the linear fit of the cube root of photoemission yield from PESA measurements. The IP of the NFAs was determined both for as cast thin films and thin films annealed at 170 °C, for which the maximum red shift in absorbance was observed (figure 79). The IPs determined for as cast and thermally annealed thin films of RS-Y6 were similar to Y6 (table 21).

Table 21| For as cast and thermally annealed Y6 and RS-Y6: Ionisation potentials (IP) determined using PESA and optical band gaps (E_g) estimated from the onset of UV-vis absorption. As well as peak absorption in the thin films ($\lambda_{max, film}$).

Conditions	$\lambda_{max, film}$ / nm	IP / eV	E_g / eV
Y6, As Cast	831	5.67	1.37
Y6, Anneal 170 °C/10mins	848	5.65	1.35
RS-Y6, As Cast	824	5.62	1.32
RS-Y6, 170 °C/10mins	838	5.66	1.31

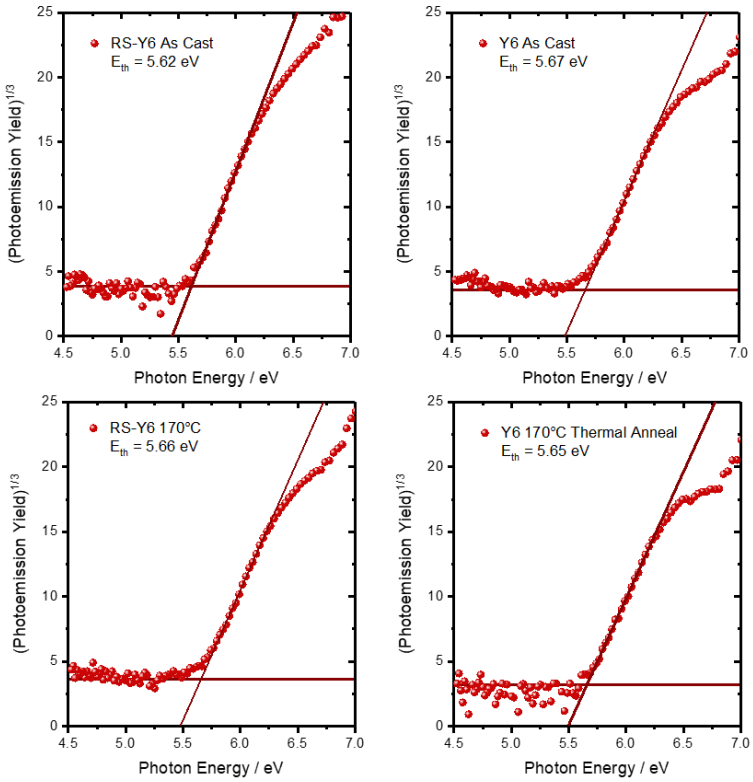

Figure 80| Cube root of photoemission yield for Y6 and RS-Y6 thin films measured by photoelectron spectroscopy in air (PESA) with fits to determine ionisation potential (IP).

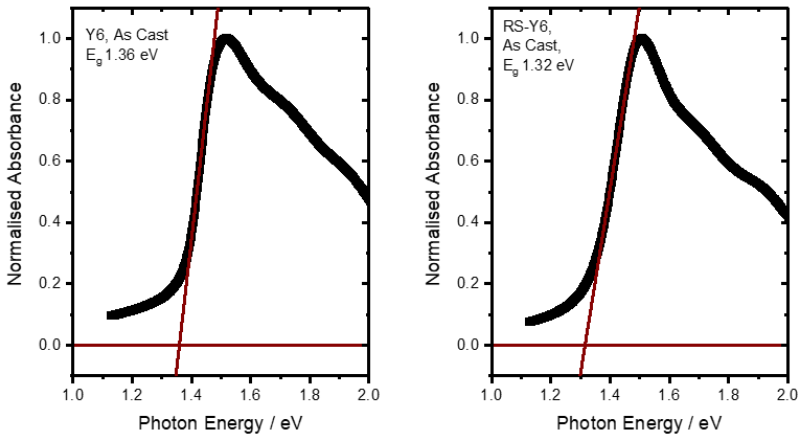

Figure 81| Optical band gaps (E_g) of Y6 and RS-Y6 determined from the onset of absorption of as cast thin films deposited from CF solution by spin coating.

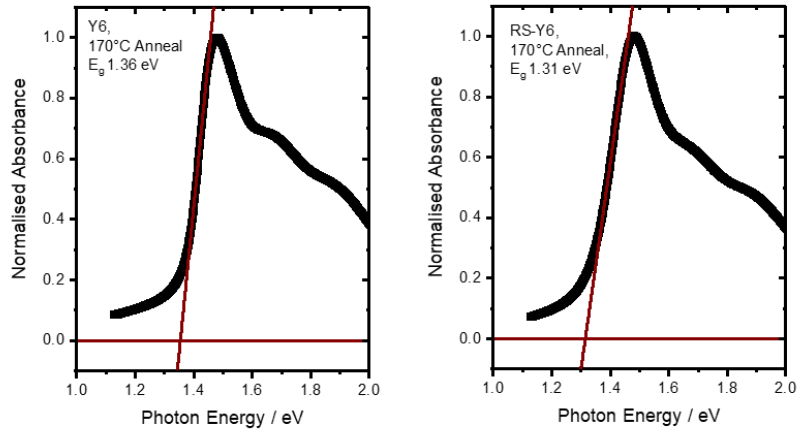

Figure 82| Optical band gaps (E_g) of Y6 and RS-Y6 determined from the onset of absorption of thin films deposited from CF solution by spin coating and thermally annealed in air at 170 °C for 10 minutes

Despite the peak absorption in thin films of Y6 occurring at longer wavelengths than films of RS-Y6, a larger E_g was determined for Y6, in both as cast and thermally annealed thin films, (table 21) by extrapolating the onset of thin film absorption as shown in figures 81 and 82. The broader absorbance of RS-Y6 leads to this smaller estimated band gap, relative to Y6, despite RS-Y6 having a less red-shifted peak absorbance. This highlights that using the E_g determined from the UV-vis absorbance as an estimate may not be the best method to determine the E_g. Optical band gaps can also be determined from the intercept of the normalised absorption and photoemission. Elsewhere, using this method, a wider optical band gap of 1.45 eV has been determined for Y6.[136]

Cyclic voltammetry (CV) is another commonly used technique to determine the energy levels of NFAs. Due to their typically poor solubility in solvents commonly used for CV, OSC CV is usually performed on thin film samples. It has recently been highlighted that a significant number of erroneous energy level values may have emerged as a result of variations in the formal potential of the ferrocenium/ferrocene (Fc^+/Fc) redox couple as well as standard electrode potentials used in the calculation of energy levels from the onset of reduction and oxidation of OSCs vs. Fc^+/Fc.[211] Here a redox potential of 5.1 eV vs. the Fermi scale is used, but values of 5.4 eV and 4.8 eV are also common in literature and it is not always stated what assumption was used when CV derived values are presented.[211] It is clear that a 0.3 eV difference in the methodology used to estimate the energy levels makes comparison between literature values confusing. A second problem for carrying out CV to determine the energy levels of NFAs is that, for CVs of solid-state samples, often the NFAs will delaminate or degrade during the cyclic voltage sweep of the experiment.

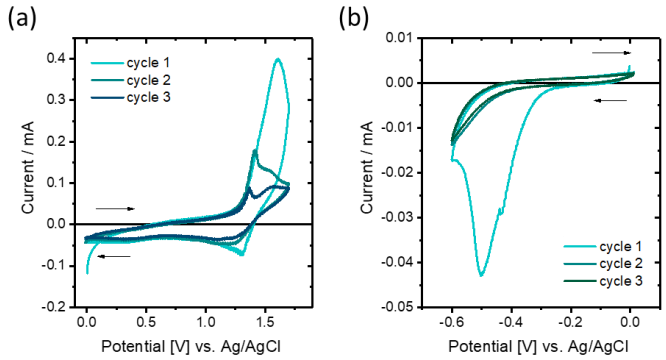

Figure 83| Sequential cyclic voltammograms of Y6. Arrows indicate the direction of the scan sweep. (a) Oxidation cycles. (b) Reduction cycles.

Figure 83 displays three sequential cyclic voltammograms of as cast films of Y6. For the cycles at positive applied potentials, during which the acceptor is oxidized, the signal intensity reduces on cycling but the onset of oxidation remains similar. From the second cycle the onset of oxidation was determined as 1.30 V for both acceptors, as shown in figure 84, which then corresponds to an IP of 5.95 eV. The onset of oxidation of Y6 is in good agreement with the previously reported value, from which an IP of 5.65 eV was estimated likely using a redox potential vs the fermi scale of 4.8 eV for the Fc^+/Fc couple.[36,211]

Table 22| Energy levels of Y6 and RS-Y6 determined from UV-vis, cyclic voltammetry (CV) and photoelectron spectroscopy in air (PESA) measurements.

Conditions	Oxidation Onset / V	IP_{CV} / eV	Reduction Onset / V	EA_{CV} / eV	IP_{PESA} / eV
Y6, As Cast	1.30	5.95	-0.33	4.32	5.67
RS-Y6, As Cast	1.30	5.95	-0.41	4.24	5.62

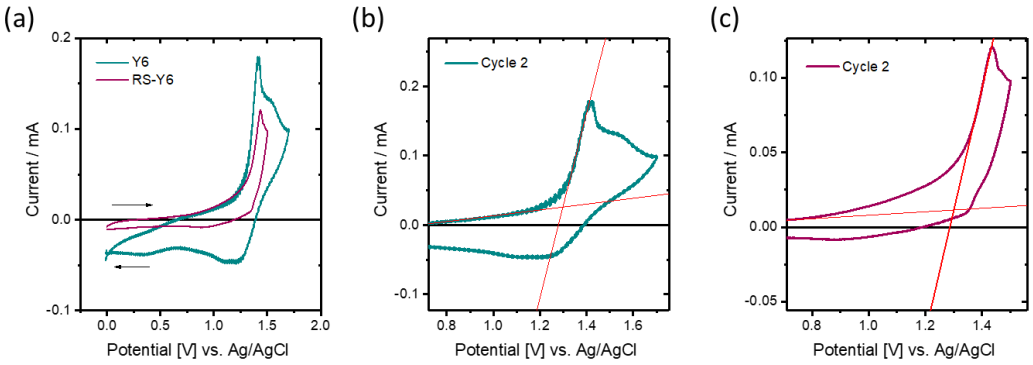

Figure 84| Cyclic voltammograms for Y6 and RS-Y6 versus a silver/silver chloride (Ag/AgCl) reference electrode. Arrows indicate the direction of the scan sweep. (a) Second oxidation cycle of Y6 and RS-Y6. (b) Determination of the onset of oxidation from the second oxidation cycle of Y6 and (c) RS-Y6.

On cycling films of both Y6 and RS-Y6 at negative potentials the thin films delaminated. This can be seen for Y6 in figure 83b, where whilst a peak corresponding to reduction of Y6 is observed in the first cycle, this disappears in subsequent cycles. To determine the onset of reduction the first cycles of Y6 and RS-Y6 were used, as shown in figure 85. From the reduction onsets of – 0.33 V and – 0.41 V for Y6 and RS-Y6 respectively, the EAs were approximated as 4.32 eV and 4.24 eV respectively. Notably there is a significant difference in the IPs determined for Y6 by UPS, PESA and CV (5.8 eV[136], 5.67 eV, 5.95 eV).

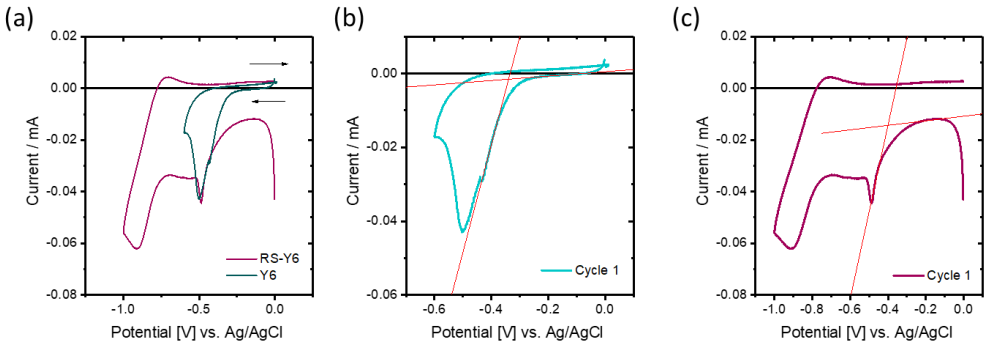

Figure 85| Cyclic voltammograms for Y6 and RS-Y6. (a) First reduction cycle of Y6 and RS-Y6. (b) Determination of the onset of reduction from the first reduction cycle of Y6 and (c) Determination of the onset of reduction from the first reduction cycle of RS-Y6.

From this in depth characterisation of RS-Y6, it is clear that it has very similar optical and electronic properties to Y6. Unfortunately, no significant difference between the EAs of the two NFAs was observed (table 22). Despite this, the new acceptor RS-Y6 was compared with Y6 in BHJ based OPVs with the donor polymer PM6.The chemical structure of PM6 is shown in figure 86 as well as its absorbance, which is complementary to that of Y6 and RS-Y6. The IP of PM6, determined using PESA, and optical band gap determined by extrapolating the onset of absorption are given in table 23.

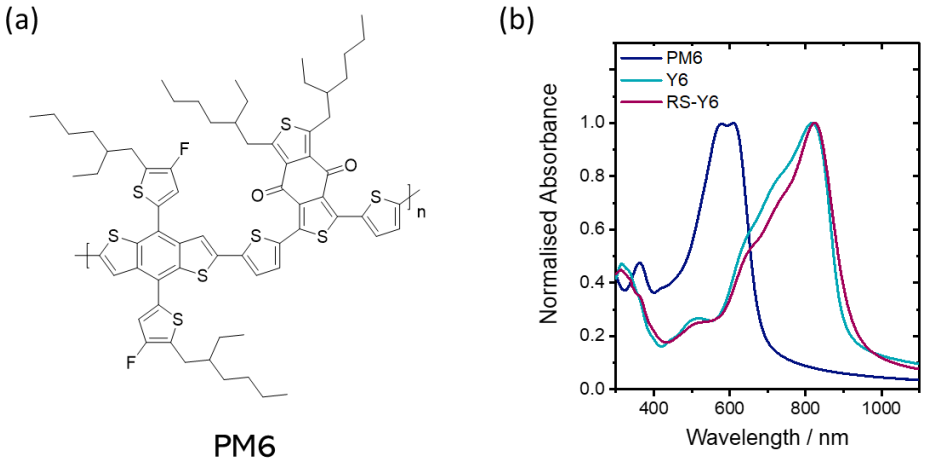

Figure 86| (a) Chemical structure of the donor polymer PM6. (b) Normalised absorbance of as cast thin films of PM6, Y6 and RS-Y6.

PM6:Y6 is a widely studied blend for OPVs. Typically the blend is deposited by spin coating from a chloroform solution containing a 0.5 % v/v high boiling point solvent additive such as 1-chloronaphthalene or 1,8-diiodooctane.[36] Here a similar fabrication procedure is used for both the PM6:Y6 and PM6:RS-Y6 active layer blend, with the new blend optimized for thickness by varying the spin coating speed (figure 87b). Both blends

were deposited by spin coating from a 1:1.2 donor to acceptor ratio solution in chloroform containing 0.5 % v/v 1-chloronaphthalene. The performance of the OPVs utilizing two different electron transport layers (ETL), DPO and PDINO, was investigated. It was decided to investigate two ETLs as previously limitations in V_{oc} arising from recombination at OPV contacts have been highlighted.[30]

Table 23| Peak absorption wavelengths for as cast thin films of PM6 ($\lambda_{max,\ film}$) as well as the ionisation potential (IP) determined using PESA and optical band gap (E_g) determined from the absorption onset of an as cast thin film.

Conditions	$\lambda_{max,\ film}$ / nm	Eg / eV	IP_{PESA} / eV
PM6, As Cast	362, 577, 609	1.78	5.13

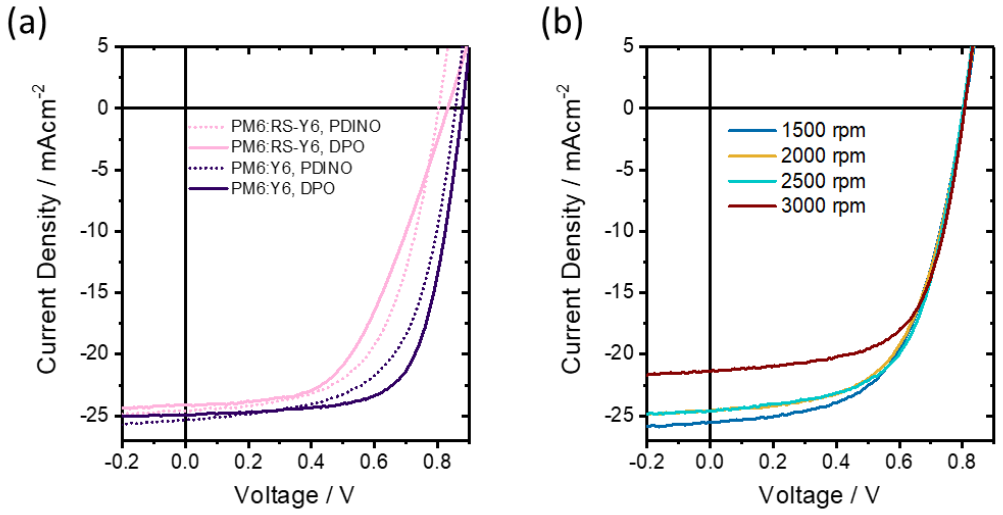

Figure 87| (a) Current density-voltage characteristics for OPVs based on PM6 combined with either the NFA Y6 or RS-Y6 and using either DPO or PDINO as the electron transport layer (ETL). (b) Current density-voltage characteristics for OPVs based on a PM6:RS-Y6 blend deposited at varying spin speeds with a PDINO ETL.

The performance parameters of the OPVs based on Y6 and RS-Y6 utilizing the two interlayers are presented in table 24 and the current density-voltage characteristics are displayed in figure 87a. Using both interlayers a lower V_{oc} is achieved for the PM6:RS-Y6 blend relative to PM6:Y6. For the DPO interlayer, which gave higher V_{oc}s, a 35 mV difference in V_{oc} is observed and for the PDINO interlayer a 60 mV difference in V_{oc} is observed between OPVs based on the two blends. Due to the lower V_{oc} observed for the RS-Y6 based blend, relative to the Y6 blend, this acceptor was not further explored.

Table 24| Performance metrics for OPVs based on PM6 combined with either the NFA Y6 or RS-Y6 and using either DPO or PDINO as the electron transport layer (ETL).

NFA, ETL	J_{sc} / $mAcm^{-2}$	V_{oc} / V	FF	PCE / %	No. Cells
Y6, DPO	24.5 ± 0.4	0.875 ± 0.003	0.67 ± 0.02	14.4 ± 0.6	6
RS-Y6, DPO	25.3 ± 0.0	0.840 ± 0.002	0.58 ± 0.00	12.4 ± 0.1	6
Y6, PDINO	25.7 ± 0.3	0.861 ± 0.005	0.60 ± 0.00	13.2 ± 0.9	5
RS-Y6, PDINO	23.0 ± 0.5	0.805 ± 0.004	0.62 ± 0.01	11.5 ± 0.5	6

[a]Mean values and standard deviations determined from the number of OPV cells indicated, with pixel areas of 0.045 cm^2.

5.5 Conclusion

In this chapter the need to expand the library of available NIR absorbing NFAs for semi-transparent OPV applications and OPD applications was highlighted. Several new NIR absorbing NFAs were characterised and applied in OPVs and OPDs.

Initially, O-IDTBR chemical structure derivatives were explored. Modulation of the end group of O-IDTBR to either dicyanovinyl or fluorinated 1,1-dicyanomethylene-3-indanone (FIC), in O-IDTBCN and O-IDTBFIC respectively, effectively shifts the NFA absorbance into the NIR. In particular, O-IDTBCN was shown to be a promising NFA for NIR responsive OPD applications. An OPD based on an 880 nm thick active layer of PTQ10:O-IDTBCN delivered a high responsivity of 0.36 A W^{-1} at 775 nm and dark current density of 3.8 x 10^{-9} A cm^{-2} under short-circuit conditions. Further optimisation of the device architecture should lead to even lower dark currents and this blend is particularly promising for biometric monitoring applications, where photoresponse in the 740 – 900 nm region is required and achieving low dark current densities has previously proved elusive.

As O-IDTBR and its derivatives exhibit absorption in the visible region, 400 – 700 nm, these NFAs were not explored for semi-transparent OPV applications. Novel NFAs with an electron rich oxygen bridged core unit were explored as an alternative. One of these NFAs, O4TFIC, delivered a good OPV performance in blends with PM6, giving a PCE of 11.0 %. In the future, O4TFIC should be explored in combination with other donor polymers with which higher V_{oc}s, than the relatively low V_{oc} of 0.672 V obtained with PM6, can be achieved. From this chapter, O4TFIC also emerged as a good candidate in OPDs for NIR optical communications applications. OPDs based on a blend of PM6:O4TFIC

were shown to exhibit simultaneously high responsivities and fast response times well within the range required for NIR photodetectors for optical communications.

Whilst O4TFIC was shown to have potential for OPV applications, the PCE achieved lags significantly behind the state of the art Y-series acceptors for which PCEs consistently above 15 % are achieved.[21] For this reason the novel Y-series acceptor, RS-Y6, was explored. RS-Y6 is a chemical structure derivative of Y6 containing a thiol side chain on the outer thiophene of the core unit and gives a peak absorption in the NIR region at 824 nm in as cast thin films. Characterisation of the material and optoelectronic properties of RS-Y6 demonstrated limited differences compared with Y6. Applied in OPVs, blends of RS-Y6 with PM6 achieved PCEs of 12.4 %.

Chapter 6: Summary and Future Outlook

Throughout this thesis the importance of better understanding the relationship between the chemical structure of OSCs and their performance in thin film devices is highlighted as critical to the development of new materials and better understanding the performance of the devices themselves.

In *Chapter 2* the critical role that the choice of aliphatic side chain has on the charge transport properties of the NFA IDTBR was highlighted. Charge transport in OSCs is related to the intermolecular packing of the molecules/polymers in the solid state. The intermolecular packing motifs of O-IDTBR and EH-IDTBR were compared using single crystal X-ray diffraction and the differences in structure were found to be largely dictated by the choice of aliphatic side chains. The packing motif of EH-IDTBR was shown to be a slipped stack arrangement, leading to dominant transfer integrals calculated in only one dimension. In contrast, the packing motif of O-IDTBR has a three-dimensional structure, for which dominant transfer integrals were calculated in isotropic directions. It has been reported that OSC packing motifs exhibiting transfer integrals isotropic in different directions will exhibit a higher tolerance of carrier transport towards disorder and therefore lead to higher charge carrier mobilities.[1]

In good agreement with this, in n-channel OTFTs, O-IDTBR was shown to give an order of magnitude higher electron mobility, of 0.4 $cm^2\ V^{-1}\ s^{-1}$, compared with EH-IDTBR, 0.04 $cm^2\ V^{-1}\ s^{-1}$. Based on other studies, the intermolecular packing motif in the single crystals of O-IDTBR is known to also be present in thin films annealed at just above its cold crystallisation exotherm, 120 °C.[118,119,129] Therefore, the difference in OTFT mobility between O-IDTBR and EH-IDTBR observed was explained using the differences in intermolecular packing determined from the single crystals. It is important to highlight that it is not possible to prove absolutely that the functional microstructure of the OTFT active layers contains the same packing motif as that obtained from the single crystals or any other microstructure characterisation technique. However, this result does indicate that the aliphatic side chains of IDTBR have a significant impact on its intermolecular interactions and charge transport properties.

Currently, prediction of the intermolecular packing of solution processible NFAs, with aliphatic side chains, from their chemical structures is not possible. Computational studies typically rely on the single crystal X-ray diffraction determined intermolecular packing motifs of NFAs to predict bulk heterojunction microstructures and solid state

optoelectronic properties, this means that the material must be synthesised before the computational work can begin.[212] In the future, predictions of intermolecular packing and optoelectronic properties based only on the chemical structure would greatly assist the development of novel high performance NFAs.

Based on the higher mobility obtained for the O-IDTBR based n-channel OTFTs, alternative processing techniques and device architectures for the OTFTs were also explored in *Chapter 2*. First, solvent vapour annealing of the O-IDTBR films was investigated as an alternative method with which to process the n-channel OTFTs, leading to mobilities of 0.3 $cm^2\ V^{-1}\ s^{-1}$ in both the linear and saturation regime. Solvent vapour annealing is thereby shown to be an alternative method for processing O-IDTBR based OTFTs when thermally annealing might not be compatible with other previously deposited layers in the thin film devices. One way to improve mobility in OTFTs is to dope the OSC material and, subsequent to the work reported here, doping of O-IDTBR was reported elsewhere to lead to mobilities of over 1 $cm^2\ V^{-1}\ s^{-1}$.[119] By aligning the contacts of the transistors with the IP of O-IDTBR, ambipolar OTFTs were realized. From these ambipolar OTFTs, a hole mobility of 0.1 $cm^2\ V^{-1}\ s^{-1}$ was determined for O-IDTBR. Future work could further explore the hole transport of other NFAs in OTFTs.

In *Chapter 3*, *c*hemical structure variants of O-IDTBR were investigated. By varying the linear side chain length, terminal electron deficient moieties and electron rich core unit, unfortunately inferior OTFT performances were realized, as compared to O-IDTBR, in all cases investigated. Whilst the O-IDTBR derivatives did not perform well in n-channel OTFTs, O-IDTBCN in particular was shown to give a good performance in OPVs. This went on to be explored further elsewhere.[152] Two linear side chain analogues of O-IDTBR were investigated, C_6-IDTBR and C_{10}-IDTBR, and it is interesting to highlight the inferior performance of these two materials as often aliphatic side chains are chosen rather arbitrarily when new OSCs are designed. This draws into question how many promising target materials have been disregarded which with subtle tweaks to their chemical structures could have been promising OSC materials for thin film device applications. O-IDTTBR, which possesses an extended electron rich core, relative to O-IDTBR, also did not yield improved OTFT performance. In a previous study a similar core extension did yield enhanced mobility in n-channel OTFTs.[105] Notably, in that study C_{16} side chains were used with the more extended electron donating IDTT core unit. Therefore, exploring IDTTBR with longer side chains could be an interesting direction for future work, as from *Chapter 2* the space filling of the side chains appears critical in dictating the intermolecular

packing motifs of NFAs. Future work could also explore other NFAs as OTFT materials. For example, recently an impressive mobility of 2.4 $cm^2 V^{-1} s^{-1}$ was reported for n-channel OTFTs based on the NFA Y6.[213]

In *Chapter 4*, impressively low dark current densities were achieved for PTQ10:O-IDTBR and PTQ10:O-FBR based OPDs, of 0.84 nA cm^{-2} and 0.17 nA cm^{-2} respectively at – 2 V reverse bias. Unfortunately, strong conclusions about the relationship between the chemical structures of the OSCs and the OPD performance could not be made as the devices were likely limited by the use of zinc oxide as an interlayer. Further work exploring these blends could use alternative interlayers, for example PEI or tin oxide which have both shown promise in OPDs delivering low and stable dark currents.[159,162]

Several recent studies have highlighted that developing NIR absorbing OSCs for OPD and OPV technologies is of interest for specific applications where these technologies can have a commercial impact, for example in semi-transparent OPVs and photodetectors for biometric monitoring and substance analysis.[22,24,94,176] The current library of NFAs is vast, whereas NFAs with absorptions extending beyond 800 nm, into the NIR, are limited to tens of materials.[176] Therefore, it is desirable to explore novel NFA chemical structures and their derivatives to expand this class of materials. This is especially necessary to allow further investigation of some of the fundamental limitations of low optical band gap materials which have recently been highlighted. These limitations include relatively higher noise currents, reduced open-circuit voltages and increased non-radiative recombination.[4,90,136] In *Chapter 5* several novel NIR NFAs are presented and initially explored in OPD and OPV applications.

Whilst O-IDTBR based OPDs give a response which reaches into the edge of the NIR region, utilizing NFAs with a more red-shifted absorbance is desirable to maximise responsivity in this region. Building on the work presented in *Chapter 4*, where PTQ10 is shown to be a promising donor polymer for high sensitivity OPDs, in *Chapter 5*, O-IDTBCN, which has a red-shifted absorbance relative to O-IDTBR, is shown as a promising OPD candidate. The PTQ10:O-IDTBCN blend delivered a peak responsivity of 0.36 A W^{-1} at 775 nm. Further characterisation of the noise currents in the OPDs and their responsivity under applied reverse bias will allow the specific detectivity under likely operating conditions to be determined. Again, exploration of alternative interlayers to zinc oxide such as PEI or tin oxide should lead to lower and more stable dark currents.

Aside from O-IDTBCN, in *Chapter 5* two other NIR absorbing NFAs, RS-Y6 and O4TFIC, were also explored. In opaque OPVs the PM6:RS-Y6 blend and PM6:O4TFIC blend

achieved PCEs of 12.4 % and 11.0 % respectively. These blends were not optimised for visible light transparency and further work could look at optimising the light utilisation efficiency of the active layers as well as the OPV electrodes and interlayers. For example, the use of silver nanowires as the top electrode in semi-transparent OPVs has led to some of the highest average visible transmittances achieved to date.[188]

PM6 absorbs strongly in the visible region. By employing donor and acceptor OSCs which absorb selectively outside of the visible region much higher AVTs can be achieved.[26,183] Therefore, exploring combining the NIR absorbing NFAs with donor polymers which also absorb outside of the visible region is important if semi-transparent OPVs with average visible transmittances of over 50 %, necessary for window applications, are to be achieved in a commercial product.[24] So far the PCEs of semi-transparent OPVs based on blends employing a donor and acceptor which both absorb in the NIR lag behind those using donors absorbing in the visible region. For example, an active layer visible transmittance of 60 % in the 400-600 nm region was achieved when the narrow band gap donor DPP2T was combined with IEICO-4F in OPVs, however, this was combined with a PCE of only 5.74 %.[183] In *Chapter 5*, O4TFIC was tested in OPVs with both PM6 and PCE10, in both cases giving V_{oc}s below 0.7 V. Finding a more suitable donor material for which the blend charge-transfer state energy is higher and thereby increased V_{oc}s might be achieved is also desirable to boost the efficiency of OPVs based on O4TFIC. O4TFIC exhibits a peak absorbance in thermally annealed thin films at 905 nm. Further tuning of the chemical structure of O4TFIC can be explored to realise narrower optical band gaps and already several tuned chemical structures are being explored.

The PM6:O4TFIC blend was shown to be promising for OPDs, exhibiting a fast response time in the NIR.[88] Here the limitations of the OPDs were the high dark current densities observed at reverse bias, which can, at least in part, be attributed to the use of PEDOT:PSS and DPO as interlayers as well as the comparatively thin active layer. By investigating this blend in other device architectures, with different interlayers, the intrinsic limits of the dark current can be investigated.[4] Especially for narrow band gap OSCs, a significant number of recent studies have highlighted sub band gap trap states could be critical in limiting the performance of thin film devices.[4,90,171,214,215] Future work attempting to better understand the relationship of chemical structure, solid state microstructure and sample history with these trap states will be critical to the improvement of thin film devices and the development of new NFAs.

Chapter 7: Experimental Procedures

7.1 Materials

All solvents used in this thesis were purchase from Sigma Aldrich. Pentafluorobenzenethiol (PFBT) and polyethylenimine (PEI) were also purchased from sigma Aldrich.

The NFAs investigated in this work were synthesised and purified my Weimin Zhang as specified in each chapter, apart from Y6 which was obtained from Brilliant Materials. Phen-NaDPO was purchased from 1-Material.

PCE10 was purchased from 1-Material. PM6 was obtained from Brilliant Materials. PCE12 was purchased from Ossila and had a M_w 70,532, M_n 33,138 and PDI 2.1. The PTQ10 used was purchased from 1-Materials and gave similar properties when compared to a batch of PTQ10 obtained from Brilliant Materials.

7.2 OSC Material Properties Characterisation

7.2.1 Differential Scanning Calorimetry (DSC)

DSC samples of the OSCs were prepared by drop-casting from chloroform solutions to remove the thermal history of the materials. A TA instruments Q20 DSC was used to perform the measurements. Unless otherwise stated in each case two heating and cooling cycles were recorded at a temperature ramp rate of either 5° min^{-1} or 10° min^{-1} as stated in the text.

7.2.2 Cyclic Voltammetry (CV)

Cyclic voltammetry (CV) can be used to determine the reduction and oxidation processes of organic semiconducting materials. In the analysis of organic semiconductors by CV, typically linear forward and reverse voltage sweeps are applied to a stationary electrode onto which the redox active species being investigated has been deposited, immersed in an electrolyte. When a potential at which redox processes are accessible is reached a wave will appear in the cyclic voltammogram.

Cyclic voltammograms were recorded using a three-electrode setup connected to a Metrohm Autolab PGSTAT101 potentiostat. A platinum wire and a Ag/AgCl electrode (3 mol dm^{-3} $NaCl/H_2O$) were used as the counter and reference electrodes respectively. The working electrode was a glassy carbon electrode, onto which the organic semiconductors were drop cast from chloroform solution. The measurements were carried out using an anhydrous acetonitrile solution of Tetrabutylammonium hexafluorophosphate

(0.01 mol dm^{-3}) as the supporting electrolyte, which was degassed with nitrogen for at least 60 mins prior to the measurements. The voltammograms were collected at scan rates of 50 mV s^{-1} under nitrogen. A Ferrocenium/Ferrocene (Fc^+/Fc) redox couple was used as an internal standard.

Significant variations in the methodology used within the organic photovoltaic field have been highlighted as a problem for comparing the derived IP and EAs of different NFAs.[211] A variety of different Fc^+/Fc potentials have been used in literature, however, a review of these concluded that there was a general consensus around a 0.40 V potential vs. the saturated calomel electrode (SCE) in acetonitrile. As the standard potential of the SCE is 0.24 V, the Fc^+/Fc couple has a potential of 0.64 V vs. the normal hydrogen electrode (NHE). Based on this, the formal potential of the Fc^+/Fc redox couple should be 5.1 eV or 5.39 eV. However, a value of 4.8 eV is also widely used in literature.[211]

From this formal potential, the measured half-wave potential of the Fc^+/Fc couple in the CV experiment (E_{Fc}), and the onset of oxidation/reduction for the material being investigated (E_{ox}/E_{red}), equations 19 and 20 can be used to estimate the IP and EA respectively. The oxidation and reduction potentials were estimated from the onset potential of the wave relating to the relevant redox process. The onset potential corresponds to the potential at which the initial injection of holes (IP) or electrons (EA) is observed.

$$-IP = -(E_{ox} - E_{Fc} + 5.1)\ eV$$

$$-EA = -(E_{red} - E_{Fc} + 5.1)\ eV$$

(19, 20)

7.2.3 Photoelectron Spectroscopy in Air

In Ambient Photoemission Spectroscopy (APS), also known as Photoelectron Spectroscopy in Air (PESA), the measurement is carried out under ambient conditions. This is in contrast with Ultraviolet Photoelectron Spectroscopy (UPS) measurements, which are performed under vacuum and use much higher energy photons than APS measurements.

In this work, APS measurements were carried out on a KP Technology Ltd. APS02 system. The system combines a Kelvin Probe system with the APS measurement.

Photoelectron spectroscopy is used to measure the ionisation potential (IP) of organic semiconductors, which are typically between 4 – 6 eV. The sample is irradiated with UV photons of varying energy and if of sufficient energy these photons can liberate electrons

from the materials surface. These released electrons ionise atmospheric species such as N_2 and O_2 to form N_2^- and O_2^-. The ions then drift towards a positively charged probe tip and an ion current is measured, which is the photoemission yield.[216] This process is illustrated in figure 88.

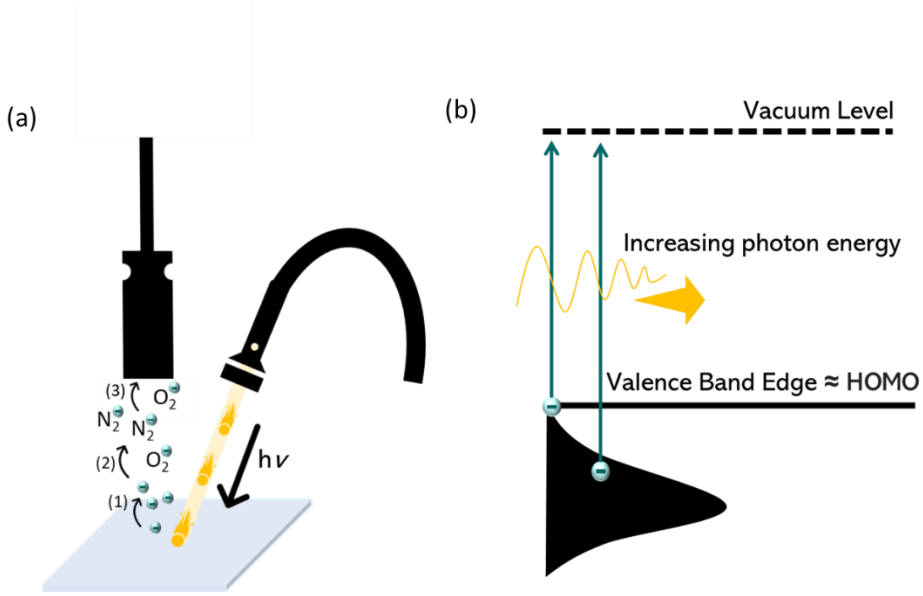

Figure 88| Illustrating how photoemission spectroscopy works. (a) The sample is irradiated with UV photons which photoexcite electrons generating an electron cloud at the sample surface (1). The released electrons are scattered by larger atmospheric species, such as N_2, O_2 and H_2O. Atmospheric ions such as N_2^- and O_2^- are generated (2). These ions drift towards the positively biased probe tip and an ion current is detected (3). In this case the metal probe tip is a 2 mm diameter gold tip. (b) Incident UV photons above a threshold energy needed to liberate electrons from the valence band of the material to the vacuum level. For an organic semiconductor, rather than a band as in conventional semiconductors there is a distribution of states, known as a density of states from which electrons are photoexcited. The Ionisation Potential corresponds to the lowest energy photon for which an electron is liberated from the material.

From the photoemission yield the onset of ionisation, the IP of the material, can be determined. It has been shown that the best fit for the photoemission yield data for organic semiconductors is to extrapolate the cube root of the photoemission yield according to equation 21, where Y is photoemission yield and hv is the incident photon energy. This is illustrated in figure 89 for as cast films of the polymer C_{16}-IDTBT.

$$Y = (hv - E_{th})^3 \quad (21)$$

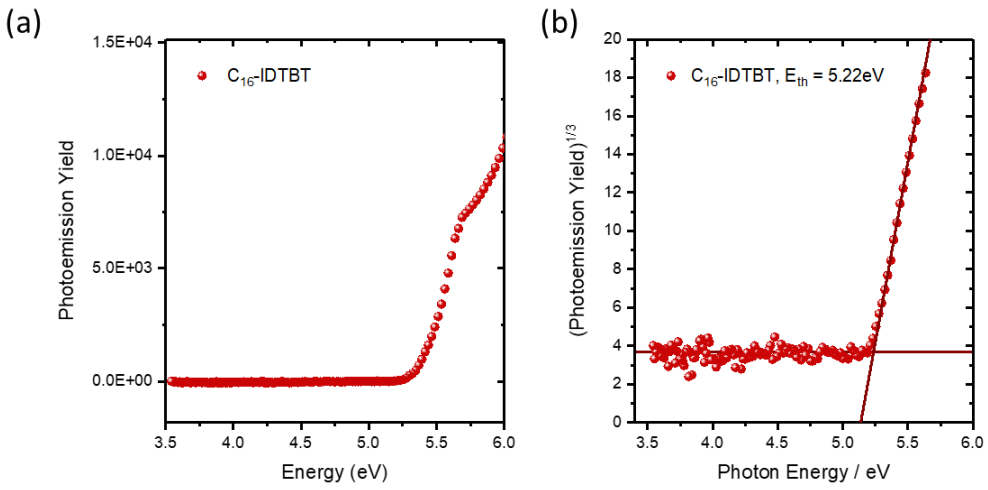

Figure 89| (a) Photoemission yield for a PESA measurement on an as cast thin film of the polymer C_{16}-IDTBT. (b) Extrapolation of the cube root of the photoemission yield to extract the threshold energy (E_{th}), which is the IP.

Samples for PESA were prepared by spin coating dynamically onto ITO coated glass substrates from solutions in chloroform and applying post deposition treatments as reported in the text. To ensure that the samples were not degraded whilst performing the APS measurement surface fermi level measurements, the equivalent of a workfunction measurement for a metal, were carried out using the Kelvin Probe setup before and after the APS measurements were performed.

7.2.4 Ultraviolet Visible (UV-vis) Spectroscopy

Thin film UV-vis Absorbance spectra were obtained using either a UV-1601 Shimadzu spectrometer, Cary 60 UV-Vis spectrophotometer or Perkin Elmer Lambda 1050 UV/Vis/NIR spectrometer. Solution UV-vis spectra were obtained on either a UV-1601 Shimadzu spectrometer or Cary 5000 UV-vis-NIR Spectrophotometer and the OSCs were dissolved in chloroform unless otherwise stated.

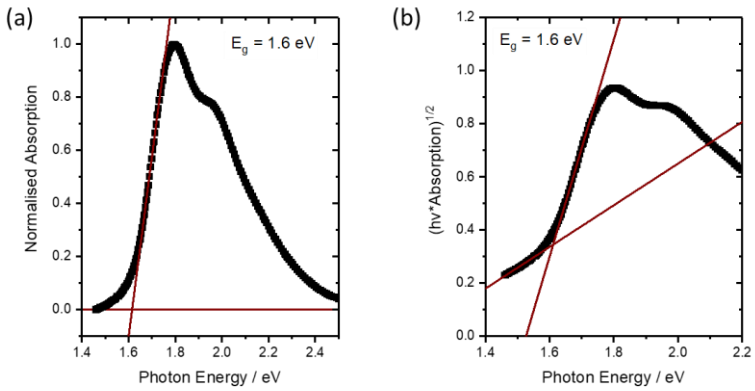

Figure 90| Illustrating the determination of the optical band gap (E_g) from both the (a) normalised absorption and (b) Tauc plot of as cast films of O-IDTBR.

The optical band gap (E_g) is often estimated from the UV-vis absorption of a material. Often this is done by extrapolating the onset of the normalised absorption or by plotting a Tauc plot, as illustrated in figure 90.[137] For the OSCs investigated in this thesis, both methods were used and similar E_g values were determined in each case.

Another, arguably more accurate, method for determining the E_g is to infer it from the intersection of the normalised absorption and photoluminescence spectra.[217] Whilst this may be a preferable method, which will be less affected by the breadth of the absorption tail of the OSC, for many NFAs, and in particular NIR absorbing NFAs, the photoluminescence will be at NIR wavelengths which requires a photoluminescence detector capable of responding in the NIR, something not always available as standard. Elsewhere this method has been used to determine the E_g of as cast films of some common NFAs.[136] Notably wider band gaps are obtained for both Y6 and O-IDTBR using the intersection of the normalised absorption and photoluminescence spectra, 1.45 eV and 1.74 eV respectively, compared with 1.36 eV and 1.55 eV estimated here by extrapolating the UV-vis absorption.

7.2.5 Grazing Incidence Wide Angle X-ray Scattering (GIWAXS)

In GIWAXS X-rays are directed at the sample at a very shallow angle of incidence, α_i, and the scattering of these X-rays is recorded using a 2D detector. This scattering gives information about the in-plane, Q_z, and out of plane, Q_R, packing of the material being analysed.

Samples for GIWAXS were prepared by depositing as cast thin films onto highly doped silicon substrates. As cast thin films of O-FBR (10 mg ml^{-1}, chlorobenzene), O-IDTBR

(10 mg ml^{-1}, chlorobenzene), PTQ10 (10 mg ml^{-1}, chlorobenzene), PTQ10:O-FBR (20 mg ml^{-1}, chlorobenzene) and PTQ10:O-IDTBR (10 mg ml^{-1}, chlorobenzene) were all deposited by spin-coating at 1000 rpm/30sec under ambient conditions.

The GIWAXS measurements reported here were carried out by Alberto Scaccbarozzi at the noncrystalline diffraction beamline (BL11-NCD-Sweet) at the ALBA Synchrotron Radiation Facility in Barcelona (Spain). A detector (Rayonix, WAXS LX255-HS) with a resolution of 1920 × 5760 pixels was used to collect the scattering signals. The sample holder position was calibrated with a chromium oxide (Cr_2O_3) standard. The incident energy was 12.4 eV, and the sample-to-detector distance was set at 200.93 mm. The angle of incidence α_i was set between 0.1 and 0.15, and the exposure time was 5 s. 2D GIWAXS patterns were corrected as a function of the components of the scattering vector with a Matlab script developed by Aurora Nogales and Edgar Gutiérrez.

7.2.6 Atomic Force Microscopy (AFM)

AFM was carried out to map the topography of as cast and annealed (120 °C/10 minutes) thin films of O-IDTBR and EH-IDTBR, spin coated on glass at 1000 rpm/45 seconds. Scans were carried out on 3 × 3 μm surface areas. A Bruker Dimension Icon was used in tapping mode with a scanning speed of 1 ln/sec. Data analysis was performed using Gwyddion software.

7.2.7 Single Crystal Growth and Analysis

Solutions of either O-IDTBR or EH-IDTBR in chlorobenzene (1 mg ml^{-1}, 0.5 ml) were placed in 2 ml glass vials. These vials were placed into larger vials containing methanol (2.5 ml) which were then sealed. Equilibration via vapor diffusion occurred over 3 to 10 days after which crystals were analysed. Crystallographic data was collected by Andrew J. P. White. Data for O-IDTBR was collected using an Agilent Xcalibur PX Ultra A diffractometer and for EH-IDTBR using a Xcalibur 3 E diffractometer. The structures were refined using the SHELXTL and SHELX-2013 program systems.[218,219]

7.2.8 Transfer Integral Calculations

Pairs of molecules were isolated from the packing motif determined by single crystal XRD within the Mercury crystallography software. The molecular coordinates were imported into the Avogadro software, in which the structures were edited to remove the side chains and replace them with methyl groups. Electron transfer integrals were then calculated, with the help of Karl J. Thorley, using the Gaussian 09 software package,[122] with the orbital projection method[123] at the B3LYP/6-31G* level.

7.3 Thin Film Device Fabrication

7.3.1 Organic Thin film Transistor (OTFT) Fabrication

Top-gate bottom-contact (staggered, top-gate) configuration was used for all OTFTs discussed in this thesis. The OTFTs were fabricated on glass substrates, which were VWR microscope slides cut with a glass pen to 1 inch square and sanded down with sand paper to give an exact fit in the substrate holder. After cutting the glass substrates were sonicated in acetone and IPA each for 10 minutes. Either silver or gold source and drain electrodes (35 nm) were thermally evaporated onto the substrates using a shadow mask.

The electrodes were left bare or modified with either polyethyleneimine (PEI) or pentafluorobenzenethiol (PFBT). For the PEI a solution in 2-methoxyethanol (0.04 wt%) was spin coated at 5000 rpm/ 60 seconds and annealed at 90 °C/ 5 minutes. For the PFBT a solution of 0.1 wt% in propan-2-ol was puddled onto the electrodes for 2-5mins and subsequently the electrodes were spin rinsed with propan-2-ol and dried with a Nitrogen gun before a 70 °C/ 5 minute anneal.

The NFA active layers were spin coated on top of the source and drain electrodes from 10 mg ml^{-1} solutions in chlorobenzene at 1000 rpm s^{-1} / 45 seconds under a Nitrogen atmosphere to give films between 45 - 52 nm thick. The films were exposed to various thermal anneals carried out in a glovebox. For solvent vapour annealed (SVA) samples thin films were first coated from either chloroform or chlorobenzene. These were then exposed to various solvent vapours for specific time periods using a petri dish lid under ambient conditions.

A CYTOP dielectric (900 nm) was then deposited by spin coating in air. The thickness of the CYTOP film was confirmed using a Dektak stylus profiler, however, there is likely to be some slight variation between coatings. Finally, an Aluminium gate electrode (45 nm) was thermally evaporated through a shadow mask.

7.3.2 Organic Photovoltaic (OPV) and Organic Photodetector (OPD) Fabrication

OPVs and OPDs were fabricated on prepatterned indium tin oxide (ITO) coated glass substrates with a sheet resistance of 15 Ω sq^{-1}, which were purchased from Psiotech Ltd. The substrates were cleaned by sonicating in acetone, Decon90, water, acetone and isopropanol for ten minutes each followed by a 7 minute ozone plasma treatment. Both conventional (p-i-n) and inverted (n-i-p) architectures OPVs and OPDs were fabricated according to the following procedures.

For the PTQ10 based OPDs discussed in *Chapters 3* and *4* an inverted device architecture was used (figure 91a) and the fabrication procedure was as follows. Zinc acetate dihydrate (219.5 mg) was dissolved in 2-methoxyethanol (2 ml) to which ethanolamine (60.5 µl) was added. This solution was dissolved overnight, filtered through 0.45 µm PTFE syringe filters (Pall Acrodisc®) and spin coated 4000 rpm / 40 seconds. Edges of the zinc oxide films were wiped with isopropanol prior to annealing to allow contact with the ITO during the measurement. The films were annealed at 150 °C/20 mins. For PTQ10:O-FBR and PTQ10:O-IDTBR the active layers were blade coated in air from 30 mg ml^{-1} solutions at a 1:2 weight ratio, with the gap between the blade and substrate set to 400 µm. Both the solution and substrate were at 60 °C during coating and the coating speed was 60 mm s^{-1}. For the PTQ10:O-IDTBCN blend the same processing conditions but with a weight ratio of 1:1.5 and concentration of 50 mg ml^{-1} were used.

Molybdenum oxide (MoO_x) (10 nm) and silver (Ag) (100 nm) were thermally evaporated under a pressure of less than 10^{-6} mbar using a shadow mask to give 0.045 cm^2 pixel areas. MoO_x was evaporated at a rate of 0.1 Å s^{-1} and Ag was evaporated at a rate of 0.1 Å s^{-1} for the first 10 nm and a subsequent rate of 0.4 – 0.7 Å s^{-1}.

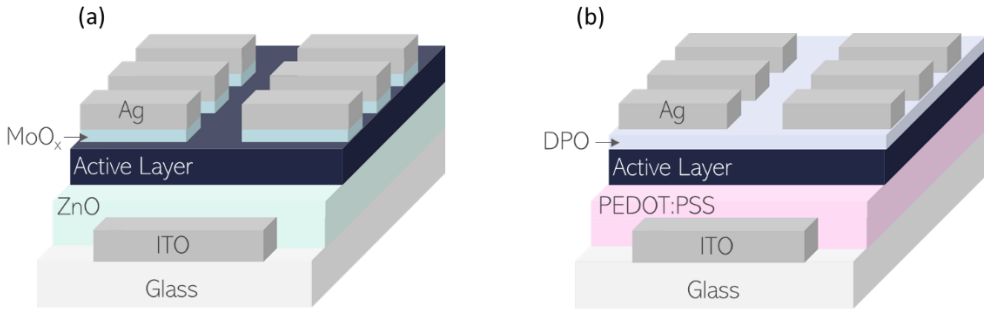

Figure 91| OPV/OPD architectures used in this work, both architectures use glass coated with indium tin oxide (ITO) as the substrate and silver (Ag) as the top electrode. (a) Inverted architecture (n-i-p), with zinc oxide (ZnO) electron transport layer and molybdenum oxide (MoO_x) hole transport layer. (b) Conventional architecture (p-i-n), with PEDOT:PSS hole transport layer and a Phen-NaDPO (DPO) electron transport layer.

For the PM6:O4TFIC based devices discussed in *Chapter 4*, a conventional OPV architecture was used (figure 91b). The PM6:Y6 and PM6:RS-Y6 based OPVs discussed in *Chapter 4* also used a conventional architecture either with DPO or replacing DPO with a PDINO ETL interlayer.

The device fabrication of the conventional architecture OPVs was as follows. The hole transport layer was PEDOT:PSS (Heraeus *Clevios*™ P VPAI 4083) spin coated at 3500 rpm/ 35 seconds and annealed at 140 °C/ 10 mins.

For the best performing OPVs based the PM6:O4TFIC active layer was spin coated in a N_2 filled glovebox from a 1:1 weight ratio solution at 30 mg ml^{-1} in chlorobenzene at 2000 rpm to give a 90 nm thick film and annealed at 130 °C/10mins. For the PM6:Y6 a 1:1.2 blend in chloroform with 0.5% chloronaphthalene was spin coated at 2000 rpm in the glovebox and annealed at 80 °C/10 mins.

Phen-NaDPO (figure 92) solution in isopropanol (0.5 mg ml^{-1}) was filtered through 0.45 µm PTFE filters and spin coated at 2000 rpm in the glovebox. When PDINO (figure 92) was used instead of DPO, a solution in methanol (0.5 mg ml^{-1}) was spin coated at 5000 rpm in a nitrogen filled glovebox.

Finally, 100 nm of Ag was thermally evaporated through a shadow mask at an evaporation rate of initially 0.1 Å s^{-1} for the first 10 nm followed by 1.0 Å s^{-1} for the remaining thickness. The pressure during the evaporation was 2 x 10^{-6} Torr and the six resulting pixels had an active area of 0.045 cm^2 each.

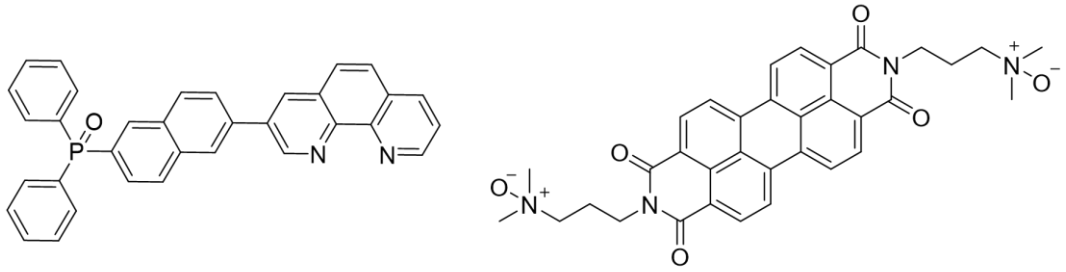

Figure 92| Chemical structures of Phen-NaDPO and PDINO.

7.4 Thin Film Device Characterisation

7.4.1 Organic Thin film Transistor (OTFT) Characterisation

Electrical characterisation of the OTFTs was performed in a glovebox under a Nitrogen atmosphere using a Keysight B2901A dual source measurement unit. Tungsten probe tips were used to manually contact the gate, source, and drain electrodes.

7.4.2 Organic Photovoltaic and Photodetector Characterisation

Current Density-Voltage Characteristics

Operation of the OPVs was determined by carrying out current-voltage (I-V) measurements using a Keithley 2400 source meter under illumination by a Xenon lamp (Oriel Instruments) calibrated to 1 sun AM1.5G intensity using a silicon reference cell. OPVs were tested under nitrogen using a sample chamber designed for this purpose. The silicon reference cell was covered with an equivalent UV-fused silica window as present in the sample chamber during the light source calibration.

Mismatch correction between the Xenon lamp spectrum, the reference AM1.5G spectrum, the responsivity of the reference silicon solar cell and the responsivity of the solar cells being tested was not performed. Notably, it has been highlighted that spectral mismatch can lead to overestimations in the current densities of OPVs, particularly those absorbing in the NIR.

Light Intensity Dependent Current Density-Voltage Characteristics

A Xenon lamp (Oriel Instruments) was calibrated to 1 sun AM1.5G intensity using a silicon reference cell. Neutral density filters were then used to attenuate the irradiance incident on the OPV devices. Light intensity dependent I-V measured using a Keithley 2400 source-measurement unit. During the measurements, light in the room was reduced as much as possible and dark cloth was placed over the setup. Absolute dark was likely not achieved as dark currents measured when the device measurement chamber was inverted were lower than those obtained in the light intensity dependent I-V measurements. Notably, the spectrum of the light attenuated by the neutral density filters was not measured.

External Quantum Efficiency (EQE) Measurements

The EQE of the OPVs was determined using a Bentham PVE300 EQE system operating in DC mode. The OPVs were tested under nitrogen using a sample chamber designed for this purpose. The EQE was calibrated with a silicon reference diode. An equivalent UV-fused silica window as that present in the sample chamber was placed on top of the reference diode during calibration. The EQEs of OPVs were determined without bias voltage or illumination.

Responsivity Measurements

Responsivity of the OPDs was determined using a Newport EQE system. Bias voltages of 0 to – 10V were applied to determine the responsivity at reverse bias.

Noise Current and Dark Current-Voltage Measurements

The current limit of a Keithley 2400 source measurement unit is around 10^{-10} A. In cases where the dark current of the 0.045 cm^2 OPD pixels was less than this, current-voltage characteristics in the dark were measured using a Keithley 4200 source measurement unit. Current as a function of time was also measured using a Keithley 4200 and applying a fast Fourier transform (FFT) to obtain the noise spectral density of the OPDs.

Transient OPD Measurements

Transient photocurrent (TPC) and measurements of the device damping were performed using a Thorlab DC2200 LED driver fitted to either an LED with peak wavelength at 880 nm (M880L3) or a neutral white light LED (MNWHL4). For both measurements the devices were placed 5 cm away from the IR LED. The photocurrent transients were obtained by measuring the voltage drop across a 50 Ω resistor using a Tektronix TDS3032B oscilloscope. For determination of the rise and fall time, a square wave pulse was applied to the LED using the function generator. For determination of the cut-off frequency, sinusoidal functions with varying frequencies between 20 Hz and 100 kHz were used to drive the LED.

References

[1] S. Fratini, M. Nikolka, A. Salleo, G. Schweicher, H. Sirringhaus, *Nat. Mater.* **2020**, *19*, 491.

[2] T. Yokota, P. Zalar, M. Kaltenbrunner, H. Jinno, N. Matsuhisa, H. Kitanosako, Y. Tachibana, W. Yukita, M. Koizumi, T. Someya, *Sci. Adv.* **2016**, *2*, e1501856.

[3] A. Wadsworth, M. Moser, A. Marks, M. S. Little, N. Gasparini, C. J. Brabec, D. Baran, I. McCulloch, *Chem. Soc. Rev.* **2019**, *48*, 1596.

[4] J. Kublitski, A. Hofacker, B. K. Boroujeni, J. Benduhn, V. C. Nikolis, C. Kaiser, D. Spoltore, H. Kleemann, A. Fischer, F. Ellinger, K. Vandewal, K. Leo, *Nat. Commun.* **2021**, *12*, 551.

[5] N. Strobel, N. Droseros, W. Köntges, M. Seiberlich, M. Pietsch, S. Schlisske, F. Lindheimer, R. R. Schröder, U. Lemmer, M. Pfannmöller, N. Banerji, G. Hernandez-Sosa, *Adv. Mater.* **2020**, *32*, 1908258.

[6] S. J. Lim, D. S. Leem, K. B. Park, K. S. Kim, S. Sul, K. Na, G. H. Lee, C. J. Heo, K. H. Lee, X. Bulliard, R. I. Satoh, T. Yagi, T. Ro, D. Im, J. Jung, M. Lee, T. Y. Lee, M. G. Han, Y. W. Jin, S. Lee, *Sci. Rep.* **2015**, *5*, 1.

[7] S. Park, K. Fukuda, M. Wang, C. Lee, T. Yokota, H. Jin, H. Jinno, H. Kimura, P. Zalar, N. Matsuhisa, S. Umezu, G. C. Bazan, T. Someya, *Adv. Mater.* **2018**, *30*, 1802359.

[8] T. Yokota, T. Nakamura, H. Kato, M. Mochizuki, M. Tada, M. Uchida, S. Lee, M. Koizumi, W. Yukita, A. Takimoto, T. Someya, *Nat. Electron.* **2020**, *3*, 113.

[9] J.-L. Bredas, *Mater. Horiz.* **2014**, *1*, 17.

[10] J. Nelson, *The Physics of Solar Cells*, Imperial College Press, **2003**.

[11] A. Melianas, F. Etzold, T. J. Savenije, F. Laquai, O. Inganäs, M. Kemerink, *Nat. Commun.* **2015**, *6*, 8778.

[12] M. Kasha, H. R. Rawls, M. Ashraf El-Bayoumi, *Pure Appl. Chem.* **1965**, *11*, 371.

[13] B. A. Gregg, M. C. Hanna, *J. Appl. Phys.* **2003**, *93*, 3605.

[14] J.-L. Brédas, J. Cornil, A. J. Heeger, *Adv. Mater.* **1996**, *8*, 447.

[15] V. Coropceanu, J. Cornil, D. A. da Silva Filho, Y. Olivier, R. Silbey, J.-L. Brédas, *Chem. Rev.* **2007**, *107*, 926.

[16] V. Coropceanu, J. Cornil, D. A. da Silva Filho, Y. Olivier, R. Silbey, J.-L. L. Brédas, *Chem. Rev.* **2007**, *107*, 926.

[17] R. Noriega, J. Rivnay, K. Vandewal, F. P. V. V Koch, N. Stingelin, P. Smith, M. F. Toney, A. Salleo, *Nat. Mater.* **2013**, *12*, 1038.

[18] A. Salleo, T. W. Chen, A. R. Völkel, Y. Wu, P. Liu, B. S. Ong, R. A. Street, *Phys. Rev. B* **2004**, *70*, 115311.

[19] M. Stephen, K. Genevičius, G. Juška, K. Arlauskas, R. C. Hiorns, *Polym. Int.* **2017**, *66*, 13.

[20] M. Moser, A. Wadsworth, N. Gasparini, I. McCulloch, *Adv. Energy Mater.* **2021**, *11*, 2100056.

[21] O. Almora, D. Baran, G. C. Bazan, C. Berger, C. I. Cabrera, K. R. Catchpole, S. Erten-Ela, F. Guo, J. Hauch, A. W. Y. Ho-Baillie, T. J. Jacobsson, R. A. J. Janssen, T. Kirchartz, N. Kopidakis, Y. Li, M. A. Loi, R. R. Lunt, X. Mathew, M. D. McGehee, J. Min, D. B. Mitzi, M. K. Nazeeruddin, J. Nelson, A. F. Nogueira, U. W. Paetzold, N. Park, B. P. Rand, U. Rau, H. J. Snaith, E. Unger, L. Vaillant-Roca, H. Yip, C. J. Brabec, *Adv. Energy Mater.* **2020**, 2002774.

[22] M. Riede, D. Spoltore, K. Leo, *Adv. Energy Mater.* **2021**, *11*, 2002653.

[23] Y. Wang, J. Lee, X. Hou, C. Labanti, J. Yan, E. Mazzolini, A. Parhar, J. Nelson, J. Kim, Z. Li, *Adv. Energy Mater.* **2021**, *11*, 2003002.

[24] I. Burgués-Ceballos, L. Lucera, P. Tiwana, K. Ocytko, L. W. Tan, S. Kowalski, J. Snow, A. Pron, H. Bürckstümmer, N. Blouin, G. Morse, *Joule* **2021**, 1.

[25] Y. Cui, L. Hong, J. Hou, *ACS Appl. Mater. Interfaces* **2020**, *12*, 38815.

[26] C. J. Traverse, R. Pandey, M. C. Barr, R. R. Lunt, *Nat. Energy* **2017**, *2*, 849.

[27] C. J. M. Emmott, J. A. Röhr, M. Campoy-Quiles, T. Kirchartz, A. Urbina, N. J. Ekins-Daukes, J. Nelson, *Energy Environ. Sci.* **2015**, *8*, 1317.

[28] W. Zhao, S. Li, H. Yao, S. Zhang, Y. Zhang, B. Yang, J. Hou, *J. Am. Chem. Soc.* **2017**, *139*, 7148.

[29] M. Zhang, L. Zhu, G. Zhou, T. Hao, C. Qiu, Z. Zhao, Q. Hu, B. W. Larson, H.

Zhu, Z. Ma, Z. Tang, W. Feng, Y. Zhang, T. P. Russell, F. Liu, *Nat. Commun.* **2021**, *12*, 309.

[30] M. Azzouzi, T. Kirchartz, J. Nelson, *Trends Chem.* **2019**, *1*, 49.

[31] G. Yu, J. Gao, J. C. Hummelen, F. Wudl, A. J. Heeger, *Science (80-.).* **1995**, *270*, 1789.

[32] J. J. M. Halls, C. A. Walch, N. C. Greenham, E. A. Marseglia, R. H. Friend, S. C. Moratti, A. B. Holmes, *Nature* **1995**, *376*, 498.

[33] H. Zhang, H. Yao, J. Hou, J. Zhu, J. Zhang, W. Li, R. Yu, B. Gao, S. Zhang, J. Hou, *Adv. Mater.* **2018**, *30*, 1800613.

[34] S. Zhang, Y. Qin, J. Zhu, J. Hou, *Adv. Mater.* **2018**, *30*, 1800868.

[35] Y. Zhang, B. Kan, Y. Sun, Y. Wang, R. Xia, X. Ke, Y.-Q.-Q. Yi, C. Li, H.-L. Yip, X. Wan, Y. Cao, Y. Chen, *Adv. Mater.* **2018**, *30*, 1707508.

[36] J. Yuan, Y. Zhang, L. Zhou, G. Zhang, H.-L. Yip, T.-K. Lau, X. Lu, C. Zhu, H. Peng, P. A. Johnson, M. Leclerc, Y. Cao, J. Ulanski, Y. Li, Y. Zou, *Joule* **2019**, *3*, 1140.

[37] Q. Liu, Y. Jiang, K. Jin, J. Qin, J. Xu, W. Li, J. Xiong, J. Liu, Z. Xiao, K. Sun, S. Yang, X. Zhang, L. Ding, *Sci. Bull.* **2020**, *65*, 272.

[38] C. Zhan, J. Yao, *Chem. Mater.* **2016**, *28*, 1948.

[39] Y. He, Y. Li, *Phys. Chem. Chem. Phys.* **2011**, *13*, 1970.

[40] W. Zhao, D. Qian, S. Zhang, S. Li, O. Inganäs, F. Gao, J. Hou, *Adv. Mater.* **2016**, *28*, 4734.

[41] X. Zhang, Z. Lu, L. Ye, C. Zhan, J. Hou, S. Zhang, B. Jiang, Y. Zhao, J. Huang, S. Zhang, Y. Liu, Q. Shi, Y. Liu, J. Yao, *Adv. Mater.* **2013**, *25*, 5791.

[42] X. Song, N. Gasparini, L. Ye, H. Yao, J. Hou, H. Ade, D. Baran, *ACS Energy Lett.* **2018**, *3*, 669.

[43] Y. Liu, J. Zhao, Z. Li, C. Mu, W. Ma, H. Hu, K. Jiang, H. Lin, H. Ade, H. Yan, *Nat. Commun.* **2014**, *5*, 5293.

[44] M. T. Dang, L. Hirsch, G. Wantz, *Adv. Mater.* **2011**, *23*, 3597.

[45] Y. Lin, Z.-G. Zhang, H. Bai, J. Wang, Y. Yao, Y. Li, D. Zhu, X. Zhan, *Energy Environ. Sci.* **2015**, *8*, 610.

[46] J. K. J. van Duren, V. D. Mihailetchi, P. W. M. Blom, T. van Woudenbergh, J. C. Hummelen, M. T. Rispens, R. A. J. Janssen, M. M. Wienk, *J. Appl. Phys.* **2003**, *94*, 4477.

[47] V. D. Mihailetchi, J. K. J. van Duren, P. W. M. Blom, J. C. Hummelen, R. A. J. Janssen, J. M. Kroon, M. T. Rispens, W. J. H. Verhees, M. M. Wienk, *Adv. Funct. Mater.* **2003**, *13*, 43.

[48] R. Pacios, J. Nelson, D. D. C. Bradley, C. J. Brabec, *Appl. Phys. Lett.* **2003**, *83*, 4764.

[49] P. H. Wöbkenberg, D. D. C. Bradley, D. Kronholm, J. C. Hummelen, D. M. de Leeuw, M. Cölle, T. D. Anthopoulos, *Synth. Met.* **2008**, *158*, 468.

[50] B. W. Larson, J. B. Whitaker, X.-B. Wang, A. A. Popov, G. Rumbles, N. Kopidakis, S. H. Strauss, O. V. Boltalina, *J. Phys. Chem. C* **2013**, *117*, 14958.

[51] S. Yoo, J. Kum, S. Cho, *Nanoscale Res. Lett.* **2011**, *6*, 545.

[52] T. Niinomi, Y. Matsuo, M. Hashiguchi, Y. Sato, E. Nakamura, *J. Mater. Chem.* **2009**, *19*, 5804.

[53] Y. Li, M. Gu, Z. Pan, B. Zhang, X. Yang, J. Gu, Y. Chen, *J. Mater. Chem. A* **2017**, *5*, 10798.

[54] S. Holliday, R. S. Ashraf, C. B. Nielsen, M. Kirkus, J. A. Röhr, C.-H. Tan, E. Collado-Fregoso, A.-C. Knall, J. R. Durrant, J. Nelson, I. McCulloch, *J. Am. Chem. Soc.* **2015**, *137*, 898.

[55] H. Yao, L. Ye, J. Hou, B. Jang, G. Han, Y. Cui, G. M. Su, C. Wang, B. Gao, R. Yu, H. Zhang, Y. Yi, H. Y. Woo, H. Ade, J. Hou, *Adv. Mater.* **2017**, *29*, 1700254.

[56] Y. Wu, H. Bai, Z. Wang, P. Cheng, S. Zhu, Y. Wang, W. Ma, X. Zhan, *Energy Environ. Sci.* **2015**, *8*, 3215.

[57] P. Sonar, J. P. Fong Lim, K. L. Chan, *Energy Environ. Sci.* **2011**, *4*, 1558.

[58] S. Li, W. Liu, M. Shi, J. Mai, T.-K. Lau, J. Wan, X. Lu, C.-Z. Li, H. Chen, *Energy Environ. Sci.* **2016**, *9*, 604.

[59] H. Cha, J. Wu, A. Wadsworth, J. Nagitta, S. Limbu, S. Pont, Z. Li, J. Searle, M. F. Wyatt, D. Baran, J.-S. Kim, I. McCulloch, J. R. Durrant, *Adv. Mater.* **2017**, *29*, 1701156.

[60] F. B. Kooistra, V. D. Mihailetchi, L. M. Popescu, D. Kronholm, P. W. M. Blom, J. C. Hummelen, *Chem. Mater.* **2006**, *18*, 3068.

[61] D. Baran, N. Gasparini, A. Wadsworth, C. H. Tan, N. Wehbe, X. Song, Z. Hamid, W. Zhang, M. Neophytou, T. Kirchartz, C. J. Brabec, J. R. Durrant, I. McCulloch, *Nat. Commun.* **2018**, *9*, 2059.

[62] B. Verreet, B. P. Rand, D. Cheyns, A. Hadipour, T. Aernouts, P. Heremans, A. Medina, C. G. Claessens, T. Torres, *Adv. Energy Mater.* **2011**, *1*, 565.

[63] X. Lian, L. Zhang, Y. Hu, Y. Zhang, Z. Yuan, W. Zhou, X. Zhao, Y. Chen, *Org. Electron.* **2017**, *47*, 72.

[64] D. Sun, D. Meng, Y. Cai, B. Fan, Y. Li, W. Jiang, L. Huo, Y. Sun, Z. Wang, *J. Am. Chem. Soc.* **2015**, *137*, 11156.

[65] Y. Kim, C. E. Song, S.-J. Moon, E. Lim, *Chem. Commun.* **2014**, *50*, 8235.

[66] Z. Zhang, W. Liu, T. Rehman, H.-X. Ju, J. Mai, X. Lu, M. Shi, J. Zhu, C.-Z. Li, H. Chen, *J. Mater. Chem. A* **2017**, *5*, 9649.

[67] D. Baran, T. Kirchartz, S. Wheeler, S. Dimitrov, M. Abdelsamie, J. Gorman, R. S. Ashraf, S. Holliday, A. Wadsworth, N. Gasparini, P. Kaienburg, H. Yan, A. Amassian, C. J. Brabec, J. R. Durrant, I. McCulloch, *Energy Environ. Sci.* **2016**, *9*, 3783.

[68] A. Wadsworth, R. S. Ashraf, M. Abdelsamie, S. Pont, M. Little, M. Moser, Z. Hamid, M. Neophytou, W. Zhang, A. Amassian, J. R. Durrant, D. Baran, I. McCulloch, *ACS Energy Lett.* **2017**, *2*, 1494.

[69] Y. Lin, J. Wang, Z.-G. Zhang, H. Bai, Y. Li, D. Zhu, X. Zhan, *Adv. Mater.* **2015**, *27*, 1170.

[70] Q. Fan, Q. Zhu, Z. Xu, W. Su, J. Chen, J. Wu, X. Guo, W. Ma, M. Zhang, Y. Li, *Nano Energy* **2018**, *48*, 413.

[71] H. Yao, Y. Cui, R. Yu, B. Gao, H. Zhang, J. Hou, *Angew. Chemie Int. Ed.* **2017**, *56*, 3045.

[72] J. Yuan, T. Huang, P. Cheng, Y. Zou, H. Zhang, J. L. Yang, S.-Y. Chang, Z. Zhang, W. Huang, R. Wang, D. Meng, F. Gao, Y. Yang, *Nat. Commun.* **2019**, *10*, 570.

[73] C. G. Shuttle, N. D. Treat, J. D. Douglas, J. M. J. Fréchet, M. L. Chabinyc, *Adv. Energy Mater.* **2012**, *2*, 111.

[74] N. Gasparini, M. Salvador, T. Heumueller, M. Richter, A. Classen, S. Shrestha, G. J. Matt, S. Holliday, S. Strohm, H.-J. Egelhaaf, A. Wadsworth, D. Baran, I. McCulloch, C. J. Brabec, *Adv. Energy Mater.* **2017**, *7*, 1701561.

[75] J. C. Blakesley, F. A. Castro, W. Kylberg, G. F. A. Dibb, C. Arantes, R. Valaski, M. Cremona, J. S. J.-S. Kim, J. S. J.-S. Kim, *Org. Electron.* **2014**, *15*, 1263.

[76] J. A. Röhr, D. Moia, S. A. Haque, T. Kirchartz, J. Nelson, *J. Phys. Condens. Matter* **2018**, *30*, 105901.

[77] A. Melianas, V. Pranculis, Y. Xia, N. Felekidis, O. Inganäs, V. Gulbinas, M. Kemerink, *Adv. Energy Mater.* **2017**, *7*, 1602143.

[78] N. A. Mica, S. A. J. Thomson, I. D. W. Samuel, *Org. Electron.* **2018**, *63*, 415.

[79] A. F. Paterson, S. Singh, K. J. Fallon, T. Hodsden, Y. Han, B. C. Schroeder, H. Bronstein, M. Heeney, I. McCulloch, T. D. Anthopoulos, *Adv. Mater.* **2018**, *30*, 1.

[80] H. Yan, Z. Chen, Y. Zheng, C. Newman, J. R. Quinn, F. Dötz, M. Kastler, A. Facchetti, *Nature* **2009**, *457*, 679.

[81] H. Li, N. Tessler, J. Brédas, *Adv. Funct. Mater.* **2018**, *1803096*, 1803096.

[82] I. McCulloch, A. Salleo, M. Chabinyc, *Science (80-.).* **2016**, *352*, 1521.

[83] H. H. Choi, K. Cho, C. D. Frisbie, H. Sirringhaus, V. Podzorov, *Nat. Mater.* **2017**, *17*, 2.

[84] C. Liu, G. Li, R. Di Pietro, J. Huang, Y.-Y. Noh, X. Liu, T. Minari, *Phys. Rev. Appl.* **2017**, *8*, 034020.

[85] Z. Chen, Y. Zheng, H. Yan, A. Facchetti, *J. Am. Chem. Soc.* **2009**, *131*, 8.

[86] S. G. Bucella, A. Luzio, E. Gann, L. Thomsen, C. R. McNeill, G. Pace, A. Perinot, Z. Chen, A. Facchetti, M. Caironi, *Nat. Commun.* **2015**, *6*, 8394.

[87] G. Simone, M. J. Dyson, S. C. J. Meskers, R. A. J. Janssen, G. H. Gelinck, *Adv. Funct. Mater.* **2019**, 1904205.

[88] M. Babics, H. Bristow, W. Zhang, A. Wadsworth, M. Neophytou, N. Gasparini, I. McCulloch, *J. Mater. Chem. C* **2021**, *9*, 2375.

[89] Y. Khan, D. Han, A. Pierre, J. Ting, X. Wang, C. M. Lochner, G. Bovo, N. Yaacobi-Gross, C. Newsome, R. Wilson, A. C. Arias, *Proc. Natl. Acad. Sci.* **2018**,

115, E11015.

[90] S. Gielen, C. Kaiser, F. Verstraeten, J. Kublitski, J. Benduhn, D. Spoltore, P. Verstappen, W. Maes, P. Meredith, A. Armin, K. Vandewal, *Adv. Mater.* **2020**, *2003818*, 1.

[91] J. Lee, S. Song, J. Huang, Z. Du, H. Lee, Z. Zhu, S.-J. Ko, T.-Q. Nguyen, J. Y. Kim, K. Cho, G. C. Bazan, *ACS Mater. Lett.* **2020**, 395.

[92] P. C. Y. Chow, T. Someya, *Adv. Mater.* **2020**, *32*, 1902045.

[93] C. J. Heo, T. Motoyama, G. H. Lee, S. Yun, S. Park, Y. Lim, K. Tsutsumi, Y. Kim, Y. Park, J. Park, J. Lee, S. J. Lim, Y. S. Choi, T. Ro, S. Kim, Y. W. Jin, K. B. Park, *Org. Electron.* **2021**, *95*, 106154.

[94] Y. Wang, J. Kublitski, S. Xing, F. Dollinger, D. Spoltore, J. Benduhn, K. Leo, *Mater. Horizons* **2022**, *9*, 220.

[95] T. Zhu, Y. Yang, L. Zheng, L. Liu, M. L. Becker, X. Gong, *Adv. Funct. Mater.* **2020**, *30*, 1909487.

[96] G. Simone, M. J. Dyson, C. H. L. Weijtens, S. C. J. Meskers, R. Coehoorn, R. A. J. Janssen, G. H. Gelinck, *Adv. Opt. Mater.* **2020**, *8*, 1901568.

[97] H. Bristow, K. J. Thorley, A. J. P. White, A. Wadsworth, M. Babics, Z. Hamid, W. Zhang, A. F. Paterson, J. Kosco, J. Panidi, T. D. Anthopoulos, I. McCulloch, *Adv. Electron. Mater.* **2019**, *5*, 1900344.

[98] T. Lei, J. Y. Wang, J. Pei, *Chem. Mater.* **2014**, *26*, 594.

[99] Y. Cui, H. Yao, J. Zhang, K. Xian, T. Zhang, L. Hong, Y. Wang, Y. Xu, K. Ma, C. An, C. He, Z. Wei, F. Gao, J. Hou, *Adv. Mater.* **2020**, *32*, 1908205.

[100] J. Nelson, J. J. Kwiatkowski, J. Kirkpatrick, J. M. Frost, *Acc. Chem. Res.* **2009**, *42*, 1768.

[101] J. E. Anthony, D. L. Eaton, S. R. Parkin, *Org. Lett.* **2002**, *4*, 15.

[102] K. J. Thorley, T. W. Finn, K. Jarolimek, J. E. Anthony, C. Risko, *Chem. Mater.* **2017**, *29*, 2502.

[103] P. Mondelli, G. Boschetto, P. N. Horton, P. Tiwana, C.-K. Skylaris, S. J. Coles, M. Krompiec, G. Morse, *Mater. Horizons* **2020**, *7*, 1062.

[104] Y. Park, C. Fuentes-Hernandez, X. Jia, F. A. Larrain, J. Zhang, S. R. Marder, B. Kippelen, *Org. Electron.* **2018**, *58*, 290.

[105] X. Song, N. Gasparini, M. M. Nahid, H. Chen, S. M. Macphee, W. Zhang, V. Norman, C. Zhu, D. Bryant, H. Ade, I. McCulloch, D. Baran, *Adv. Funct. Mater.* **2018**, *28*, 1802895.

[106] F. Yang, C. Li, W. Lai, A. Zhang, H. Huang, W. Li, *Mater. Chem. Front.* **2017**, *1*, 1389.

[107] F. Zhang, Y. Hu, T. Schuettfort, C. A. Di, X. Gao, C. R. McNeill, L. Thomsen, S. C. B. B. Mannsfeld, W. Yuan, H. Sirringhaus, D. Zhu, *J. Am. Chem. Soc.* **2013**, *135*, 2338.

[108] A. Lv, S. R. Puniredd, J. Zhang, Z. Li, H. Zhu, W. Jiang, H. Dong, Y. He, L. Jiang, Y. Li, W. Pisula, Q. Meng, W. Hu, Z. Wang, *Adv. Mater.* **2012**, *24*, 2626.

[109] S. Holliday, R. S. Ashraf, A. Wadsworth, D. Baran, S. A. Yousaf, C. B. Nielsen, C.-H. Tan, S. D. Dimitrov, Z. Shang, N. Gasparini, M. Alamoudi, F. Laquai, C. J. Brabec, A. Salleo, J. R. Durrant, I. McCulloch, *Nat. Commun.* **2016**, *7*, 11585.

[110] D. Baran, R. S. Ashraf, D. A. Hanifi, M. Abdelsamie, N. Gasparini, J. A. Röhr, S. Holliday, A. Wadsworth, S. Lockett, M. Neophytou, C. J. M. Emmott, J. Nelson, C. J. Brabec, A. Amassian, A. Salleo, T. Kirchartz, J. R. Durrant, I. McCulloch, *Nat. Mater.* **2017**, *16*, 363.

[111] R.-Z. Liang, M. Babics, V. Savikhin, W. Zhang, V. M. Le Corre, S. Lopatin, Z. Kan, Y. Firdaus, S. Liu, I. McCulloch, M. F. Toney, P. M. Beaujuge, *Adv. Energy Mater.* **2018**, *8*, 1800264.

[112] P. E. Hopkinson, P. A. Staniec, A. J. Pearson, A. D. F. Dunbar, T. Wang, A. J. Ryan, R. A. L. Jones, D. G. Lidzey, A. M. Donald, *Macromolecules* **2011**, *44*, 2908.

[113] J. Kesters, P. Verstappen, J. Raymakers, W. Vanormelingen, J. Drijkoningen, J. D'Haen, J. Manca, L. Lutsen, D. Vanderzande, W. Maes, *Chem. Mater.* **2015**, *27*, 1332.

[114] M. Defour, N. Van den Brande, L. Van Lokeren, G. Van Assche, W. Maes, D. Vanderzande, B. Van Mele, *RSC Adv.* **2016**, *6*, 92981.

[115] Y. Diao, L. Shaw, Z. Bao, S. C. B. Mannsfeld, *Energy Environ. Sci.* **2014**, *7*, 2145.

[116] Z. Hamid, Structure-Phase Behavior-Performance Relationships in Non-Fullerene Acceptor Based Organic Solar Cells: Insight from Thermal and Spectroscopic Characterization, Doctoral Dissertation, Imperial College London, **2019**

[117] A. L. L. East, E. C. Lim, *J. Chem. Phys.* **2000**, *113*, 8981.

[118] A. S. Gertsen, M. K. Sørensen, J. W. Andreasen, *Phys. Rev. Mater.* **2020**, *4*, 075405.

[119] A. F. Paterson, R. Li, A. Markina, L. Tsetseris, S. MacPhee, H. Faber, A.-H. Emwas, J. Panidi, H. Bristow, A. Wadsworth, D. Baran, D. Andrienko, M. Heeney, I. McCulloch, T. D. Anthopoulos, *J. Mater. Chem. C* **2021**, *9*, 4486.

[120] H. Lai, F. He, *Adv. Energy Mater.* **2020**, *10*, 2002678.

[121] J. Kirkpatrick, *Int. J. Quantum Chem.* **2008**, *108*, 51.

[122] D. J. F. M. J. Frisch, G. W. Trucks, H. B. Schlegel, G. E. Scuseria, M. A. Robb, J. R. Cheeseman, G. Scalmani, V. Barone, B. Mennucci, G. A. Petersson, H. Nakatsuji, M. Caricato, X. Li, H. P. Hratchian, A. F. Izmaylov, J. Bloino, G. Zheng, J. L. Sonnenberg, M. Had, *Gaussian 09, Revision D.01*, Gaussian, Inc., Wallingford CT, **2013**.

[123] E. F. Valeev, V. Coropceanu, D. A. Da Silva Filho, S. Salman, J. L. Brédas, *J. Am. Chem. Soc.* **2006**, *128*, 9882.

[124] J. Wade, F. Steiner, D. Niedzialek, D. T. James, Y. Jung, D.-J. Yun, D. D. C. Bradley, J. Nelson, J.-S. Kim, *J. Mater. Chem. C* **2014**, *2*, 10110.

[125] Y. Park, K. S. Park, B. Jun, Y.-E. K. Lee, S. U. Lee, M. M. Sung, *Chem. Mater.* **2017**, *29*, 4072.

[126] L.-J. Riwar, N. Trapp, K. Root, R. Zenobi, F. Diederich, *Angew. Chemie Int. Ed.* **2018**, 1.

[127] C. L. Yaws, A. S. Y. Leh, D. Project, N. York, J. C. Educ, S. G. Sayegh, G. A. Ratcliff, F. P. Equilibria, in *Thermophys. Prop. Chem. Hydrocarb.*, **2009**, pp. 649–658.

[128] T. He, P. Leowanawat, C. Burschka, V. Stepanenko, M. Stolte, F. Würthner, *Adv. Mater.* **2018**, *30*, 1804032.

[129] S. Halaby, M. W. Martynowycz, Z. Zhu, S. Tretiak, A. Zhugayevych, T. Gonen, M. Seifrid, *Chem. Mater.* **2021**, *33*, 966.

[130] M. J. Kim, Y. W. Lee, Y. Lee, H. Y. Woo, J. Ho Cho, *J. Mater. Chem. C* **2018**, *6*, 5698.

[131] A. F. Paterson, A. D. Mottram, H. Faber, M. R. Niazi, Z. Fei, M. Heeney, T. D. Anthopoulos, *Adv. Electron. Mater.* **2019**, *1800723*, 1800723.

[132] Y. Zhou, C. Fuentes-Hernandez, J. Shim, J. Meyer, A. J. Giordano, H. Li, P. Winget, T. Papadopoulos, H. Cheun, J. Kim, M. Fenoll, A. Dindar, W. Haske, E. Najafabadi, T. M. Khan, H. Sojoudi, S. Barlow, S. Graham, J.-L. Bredas, S. R. Marder, A. Kahn, B. Kippelen, *Science (80-.).* **2012**, *336*, 327.

[133] O. Fenwick, C. Van Dyck, K. Murugavel, D. Cornil, F. Reinders, S. Haar, M. Mayor, J. Cornil, P. Samorì, *J. Mater. Chem. C* **2015**, *3*, 3007.

[134] P. I. Djurovich, E. I. Mayo, S. R. Forrest, M. E. Thompson, *Org. Electron.* **2009**, *10*, 515.

[135] J. I. Khan, M. A. Alamoudi, N. Chaturvedi, R. S. Ashraf, M. N. Nabi, A. Markina, W. Liu, T. A. Dela Peña, W. Zhang, O. Alévêque, G. T. Harrison, W. Alsufyani, E. Levillain, S. De Wolf, D. Andrienko, I. McCulloch, F. Laquai, *Adv. Energy Mater.* **2021**, *11*, 2100839.

[136] S. Karuthedath, J. Gorenflot, Y. Firdaus, N. Chaturvedi, C. S. P. De Castro, G. T. Harrison, J. I. Khan, A. Markina, A. H. Balawi, T. A. Dela Peña, W. Liu, R.-Z. Liang, A. Sharma, S. H. K. Paleti, W. Zhang, Y. Lin, E. Alarousu, S. Lopatin, D. H. Anjum, P. M. Beaujuge, S. De Wolf, I. McCulloch, T. D. Anthopoulos, D. Baran, D. Andrienko, F. Laquai, *Nat. Mater.* **2021**, *20*, 378.

[137] P. Makuła, M. Pacia, W. Macyk, *J. Phys. Chem. Lett.* **2018**, *9*, 6814.

[138] C. Liu, Y. Xu, Y. Y. Noh, *Mater. Today* **2015**, *18*, 79.

[139] B. Sun, W. Hong, H. Aziz, Y. Li, *Polym. Chem.* **2015**, *6*, 938.

[140] B. Sun, W. Hong, E. S. Thibau, H. Aziz, Z.-H. Lu, Y. Li, *ACS Appl. Mater. Interfaces* **2015**, *7*, 18662.

[141] Y. Kuzumoto, M. Kitamura, *Appl. Phys. Express* **2014**, *7*, 035701.

[142] W.-Y. Sit, F. D. Eisner, Y.-H. Lin, Y. Firdaus, A. Seitkhan, A. H. Balawi, F. Laquai, C. H. Burgess, M. A. McLachlan, G. Volonakis, F. Giustino, T. D. Anthopoulos, *Adv. Sci.* **2018**, *5*, 1700980.

[143] S. M. Tuladhar, D. Poplavskyy, S. A. Choulis, J. R. Durrant, D. D. C. Bradley, J. Nelson, *Adv. Funct. Mater.* **2005**, *15*, 1171.

[144] W. Huang, Y. H. Lin, T. D. Anthopoulos, *ACS Appl. Mater. Interfaces* **2018**, *10*, 10202.

[145] T. D. Anthopoulos, C. Tanase, S. Setayesh, E. J. Meijer, J. C. Hummelen, P. W. M. Blom, D. M. de Leeuw, *Adv. Mater.* **2004**, *16*, 2174.

[146] J. Rivnay, S. C. B. Mannsfeld, C. E. Miller, A. Salleo, M. F. Toney, *Chem. Rev.* **2012**, *112*, 5488.

[147] Suman, S. P. Singh, *J. Mater. Chem. A* **2019**, *7*, 22701.

[148] M. Ghasemi, N. Balar, Z. Peng, H. Hu, Y. Qin, T. Kim, J. J. Rech, M. Bidwell, W. Mask, I. McCulloch, W. You, A. Amassian, C. Risko, B. T. O'Connor, H. Ade, *Nat. Mater.* **2021**, *20*, 525.

[149] Z. Qian, L. Galuska, W. W. McNutt, M. U. Ocheje, Y. He, Z. Cao, S. Zhang, J. Xu, K. Hong, R. B. Goodman, S. Rondeau-Gagné, J. Mei, X. Gu, *J. Polym. Sci. Part B Polym. Phys.* **2019**, *57*, 1635.

[150] Y. Qin, N. Balar, Z. Peng, A. Gadisa, I. Angunawela, A. Bagui, S. Kashani, J. Hou, H. Ade, *Joule* **2021**, 1.

[151] Y. Qin, Y. Xu, Z. Peng, J. Hou, H. Ade, *Adv. Funct. Mater.* **2020**, *30*, 2005011.

[152] A. Wadsworth, H. Bristow, Z. Hamid, M. Babics, N. Gasparini, C. W. Boyle, W. Zhang, Y. Dong, K. J. Thorley, M. Neophytou, R. S. Ashraf, J. R. Durrant, D. Baran, I. McCulloch, *Adv. Funct. Mater.* **2019**, *29*, 1.

[153] C. M. Proctor, J. A. Love, T.-Q. Nguyen, *Adv. Mater.* **2014**, *26*, 5957.

[154] D. Qian, L. Ye, M. Zhang, Y. Liang, L. Li, Y. Huang, X. Guo, S. Zhang, Z. Tan, J. Hou, *Macromolecules* **2012**, *45*, 9611.

[155] Z. Chen, P. Bi, X. Yang, M. Niu, K. Zhang, L. Feng, X. Hao, *J. Phys. Chem. C* **2019**, *123*, 12676.

[156] S. E. Root, M. A. Alkhadra, D. Rodriquez, A. D. Printz, D. J. Lipomi, *Chem. Mater.* **2017**, *29*, 2646.

[157] H. Bristow, P. Jacoutot, A. D. Scaccabarozzi, M. Babics, M. Moser, A. Wadsworth, T. D. Anthopoulos, A. Bakulin, I. McCulloch, N. Gasparini, *ACS Appl. Mater. Interfaces* **2020**, *12*, 48836.

[158] A. Armin, M. Hambsch, I. K. Kim, P. L. Burn, P. Meredith, E. B. Namdas, *Laser Photon. Rev.* **2014**, *8*, 924.

[159] C. Fuentes-Hernandez, W. Chou, T. M. Khan, L. Diniz, J. Lukens, F. A. Larrain, V. A. Rodriguez-Toro, B. Kippelen, *Science (80-.).* **2020**, *370*, 698.

[160] N. Gasparini, A. Gregori, M. Salvador, M. Biele, A. Wadsworth, S. Tedde, D. Baran, I. McCulloch, C. J. Brabec, *Adv. Mater. Technol.* **2018**, *3*, 1800104.

[161] R. Shidachi, H. Jinno, S. Lee, T. Yokota, T. Someya, *ACS Appl. Electron. Mater.* **2019**, *1*, 1054.

[162] J. Huang, J. Lee, H. Nakayama, M. Schrock, D. X. Cao, K. Cho, G. C. Bazan, T.-Q. Nguyen, *ACS Nano* **2021**, *15*, 1753.

[163] C. Sun, F. Pan, H. Bin, J. Zhang, L. Xue, B. Qiu, Z. Wei, Z.-G. Zhang, Y. Li, *Nat. Commun.* **2018**, *9*, 743.

[164] H. Cha, Y. Zheng, Y. Dong, H. H. Lee, J. Wu, H. Bristow, J. Zhang, H. K. H. Lee, W. C. Tsoi, A. A. Bakulin, I. McCulloch, J. R. Durrant, *Adv. Energy Mater.* **2020**, *10*, 2001149.

[165] B. Qiu, S. Chen, C. Sun, J. Yuan, X. Zhang, C. Zhu, S. Qin, L. Meng, Y. Zhang, C. Yang, Y. Zou, Y. Li, *Sol. RRL* **2020**, *4*, 1.

[166] C. K. Lo, R. M. W. Wolfe, J. R. Reynolds, *Chem. Mater.* **2021**, *33*, 4842.

[167] L. Meng, C. Sun, R. Wang, W. Huang, Z. Zhao, P. Sun, T. Huang, J. Xue, J.-W. Lee, C. Zhu, Y. Huang, Y. Li, Y. Yang, *J. Am. Chem. Soc.* **2018**, *140*, 17255.

[168] R. A. J. Janssen, J. Nelson, *Adv. Mater.* **2013**, *25*, 1847.

[169] Y. Fang, A. Armin, P. Meredith, J. Huang, *Nat. Photonics* **2019**, *13*, 1.

[170] G. Liu, T. Li, X. Zhan, H. Wu, Y. Cao, *ACS Appl. Mater. Interfaces* **2020**, *12*, 17769.

[171] P. Hartnagel, T. Kirchartz, *Adv. Theory Simulations* **2020**, *3*, 1.

[172] H. Ko, S. Park, H. J. Son, D. S. Chung, *Chem. Mater.* **2020**, *32*, 3219.

[173] A. Salleo, R. J. Kline, D. M. DeLongchamp, M. L. Chabinyc, *Adv. Mater.* **2010**, *22*, 3812.

[174] Y. Jiang, L. Sun, F. Jiang, C. Xie, L. Hu, X. Dong, F. Qin, T. Liu, L. Hu, X. Jiang, Y. Zhou, *Mater. Horizons* **2019**, *6*, 1438.

[175] J. Luke, L. Corrêa, J. Rodrigues, J. Martins, M. Daboczi, D. Bagnis, J. Kim, *Adv. Energy Mater.* **2021**, *11*, 2003405.

[176] D. Meng, R. Zheng, Y. Zhao, E. Zhang, L. Dou, Y. Yang, *Adv. Mater.* **2022**, 2107330.

[177] Q. Li, Y. Guo, Y. Liu, *Chem. Mater.* **2019**, *31*, 6359.

[178] H. Yao, Y. Cui, R. Yu, B. Gao, H. Zhang, J. Hou, *Angew. Chemie Int. Ed.* **2017**, *56*, 3045.

[179] J. Lee, S. J. Ko, M. Seifrid, H. Lee, B. R. Luginbuhl, A. Karki, M. Ford, K. Rosenthal, K. Cho, T. Q. Nguyen, G. C. Bazan, *Adv. Energy Mater.* **2018**, *8*, 1.

[180] J. Huang, J. Lee, J. Vollbrecht, V. V Brus, A. L. Dixon, D. X. Cao, Z. Zhu, Z. Du, H. Wang, K. Cho, G. C. Bazan, T. Nguyen, *Adv. Mater.* **2020**, *32*, 1906027.

[181] P. Cheng, G. Li, X. Zhan, Y. Yang, *Nat. Photonics* **2018**, *12*, 131.

[182] E. Ravishankar, R. E. Booth, C. Saravitz, H. Sederoff, H. W. Ade, B. T. O'Connor, *Joule* **2020**, *4*, 490.

[183] J. Lee, H. Cha, H. Yao, J. Hou, Y.-H. Suh, S. Jeong, K. Lee, J. R. Durrant, *ACS Appl. Mater. Interfaces* **2020**, *12*, 32764.

[184] T. Jiang, G. Zhang, R. Xia, J. Huang, X. Li, M. Wang, H.-L. Yip, Y. Cao, *Mater. Today Energy* **2021**, *21*, 100807.

[185] CIE, "Luminous Efficiency Functions," can be found under http://www.cvrl.org/cie.htm, **1924**, accessed 01/06/2021

[186] NREL, “Reference Air Mass 1.5 Spectra,” can be found under https://www.nrel.gov/grid/solar-resource/spectra-am1.5.html, **n.d.** accessed 01/06/2021

[187] C. Yang, D. Liu, M. Bates, M. C. Barr, R. R. Lunt, *Joule* **2019**, *3*, 1803.

[188] Y. Xiong, R. E. Booth, T. Kim, L. Ye, Y. Liu, Q. Dong, M. Zhang, F. So, Y. Zhu, A. Amassian, B. T. O’Connor, H. Ade, *Sol. RRL* **2020**, *4*, 2000328.

[189] R. R. Lunt, V. Bulovic, *Appl. Phys. Lett.* **2011**, *98*, 113305.

[190] D. Corzo, E. Bihar, E. B. Alexandre, D. Rosas-Villalva, D. Baran, *Adv. Funct. Mater.* **2021**, *31*, 2005763.

[191] Z. Hu, Z. Wang, Q. An, F. Zhang, *Sci. Bull.* **2020**, *65*, 131.

[192] B.-H. Jiang, H.-E. Lee, J.-H. Lu, T.-H. Tsai, T.-S. Shieh, R.-J. Jeng, C.-P. Chen, *ACS Appl. Mater. Interfaces* **2020**, *12*, 39496.

[193] R. Xia, C. J. Brabec, H. L. Yip, Y. Cao, *Joule* **2019**, *3*, 2241.

[194] T. Someya, Z. Bao, G. G. Malliaras, *Nature* **2016**, *540*, 379.

[195] A. E. London, L. Huang, B. A. Zhang, M. B. Oviedo, J. Tropp, W. Yao, Z. Wu, B. M. Wong, T. N. Ng, J. D. Azoulay, *Polym. Chem.* **2017**, *8*, 2922.

[196] A. Armin, R. D. Jansen-van Vuuren, N. Kopidakis, P. L. Burn, P. Meredith, *Nat. Commun.* **2015**, *6*, 6343.

[197] B. Siegmund, A. Mischok, J. Benduhn, O. Zeika, S. Ullbrich, F. Nehm, M. Böhm, D. Spoltore, H. Fröb, C. Körner, K. Leo, K. Vandewal, *Nat. Commun.* **2017**, *8*, 15421.

[198] K. Vandewal, S. Albrecht, E. T. Hoke, K. R. Graham, J. Widmer, J. D. Douglas, M. Schubert, W. R. Mateker, J. T. Bloking, G. F. Burkhard, A. Sellinger, J. M. J. Fréchet, A. Amassian, M. K. Riede, M. D. McGehee, D. Neher, A. Salleo, *Nat. Mater.* **2014**, *13*, 63.

[199] J. Lee, S. J. Ko, H. Lee, J. Huang, Z. Zhu, M. Seifrid, J. Vollbrecht, V. V. Brus, A. Karki, H. Wang, K. Cho, T. Q. Nguyen, G. C. Bazan, *ACS Energy Lett.* **2019**, *4*, 1401.

[200] D. Han, Y. Khan, J. Ting, J. Zhu, C. Combe, A. Wadsworth, I. McCulloch, A. C. Arias, *Adv. Mater. Technol.* **2020**, *1901122*, 1901122.

[201] P. Li, Z.-H. Lu, *Small Sci.* **2021**, *1*, 2000015.

[202] D. Baierl, L. Pancheri, M. Schmidt, D. Stoppa, G. F. Dalla Betta, G. Scarpa, P. Lugli, *Nat. Commun.* **2012**, *3*, 1.

[203] W. Li, Z. Xiao, J. Cai, J. A. Smith, E. L. K. Spooner, R. C. Kilbride, O. S. Game, X. Meng, D. Li, H. Zhang, M. Chen, R. S. Gurney, D. Liu, R. A. L. Jones, D. G. Lidzey, L. Ding, T. Wang, *Nano Energy* **2019**, *61*, 318.

[204] Z. Xiao, S. Yang, Z. Yang, J. Yang, H. Yip, F. Zhang, F. He, T. Wang, J. Wang, Y. Yuan, H. Yang, M. Wang, L. Ding, *Adv. Mater.* **2019**, *31*, 1804790.

[205] T. J. Aldrich, M. Matta, W. Zhu, S. M. Swick, C. L. Stern, G. C. Schatz, A. Facchetti, F. S. Melkonyan, T. J. Marks, *J. Am. Chem. Soc.* **2019**, *141*, 3274.

[206] J. H. Kim, T. Schembri, D. Bialas, M. Stolte, F. Würthner, *Adv. Mater.* **2021**, 2104678.

[207] D. Wang, H. Liu, Y. Li, G. Zhou, L. Zhan, H. Zhu, X. Lu, H. Chen, C. Z. Li, *Joule* **2021**, *5*, 945.

[208] P. Bi, S. Zhang, Z. Chen, Y. Xu, Y. Cui, T. Zhang, J. Ren, J. Qin, L. Hong, X. Hao, J. Hou, *Joule* **2021**, *5*, 2408.

[209] K. Jiang, Q. Wei, J. Y. L. Lai, Z. Peng, H. K. Kim, J. Yuan, L. Ye, H. Ade, Y. Zou, H. Yan, *Joule* **2019**, *3*, 3020.

[210] N. Gasparini, S. H. K. Paleti, J. Bertrandie, G. Cai, G. Zhang, A. Wadsworth, X. Lu, H.-L. Yip, I. McCulloch, D. Baran, *ACS Energy Lett.* **2020**, *5*, 1371.

[211] C. M. Cardona, W. Li, A. E. Kaifer, D. Stockdale, G. C. Bazan, *Adv. Mater.* **2011**, *23*, 2367.

[212] S. M. Swick, T. Gebraad, L. Jones, B. Fu, T. J. Aldrich, K. L. Kohlstedt, G. C. Schatz, A. Facchetti, T. J. Marks, *ChemPhysChem* **2019**, *20*, 2608.

[213] E. Gutierrez-Fernandez, A. D. Scaccabarozzi, A. Basu, E. Solano, T. D. Anthopoulos, J. Martín, *Adv. Sci.* **2021**, *2104977*, 2104977.

[214] S. Limbu, K.-B. Park, J. Wu, H. Cha, S. Yun, S.-J. Lim, H. Yan, J. Luke, G. Ryu, C.-J. Heo, S. Kim, Y. W. Jin, J. R. Durrant, J.-S. Kim, *ACS Nano* **2021**, *15*, 1217.

[215] H. F. Iqbal, E. K. Holland, J. E. Anthony, O. D. Jurchescu, *Mater. Horizons* **2020**, *7*, 2390.

[216] I. D. Baikie, A. C. Grain, J. Sutherland, J. Law, *Energy Procedia* **2014**, *60*, 48.

[217] K. Vandewal, J. Benduhn, V. C. Nikolis, *Sustain. Energy Fuels* **2018**, *2*, 538.

[218] SHELXTL v5.1, Bruker AXS, Madison, WI, 1998

[219] SHELX-2013, G.M. Sheldrick, *Acta Crystallogr*., 2015, C71, 3

Appendix A: List of Publications

- **H. Bristow**, K. J. Thorley, A. J. P. White, A. Wadsworth, M. Babics, Z. Hamid, W. Zhang, A. F. Paterson, J. Kosco, J. Panidi, T. D. Anthopoulos, I. McCulloch, Impact of Nonfullerene Acceptor Side Chain Variation on Transistor Mobility, *Adv. Electron. Mater*., 1900344 (2019)
- **H. Bristow**, P. Jacoutot, A. D. Scaccabarozzi, M. Babics, M. Moser, A. Wadsworth, T. D. Anthopoulos, A. Bakulin, I. McCulloch, and N. Gasparini, Nonfullerene-Based Organic Photodetectors for Ultrahigh Sensitivity Visible Light Detection, *ACS Appl. Mater. Interfaces*, 12, 43, 48836–48844 (2020)
- Y. Dong, H. Cha, **H. Bristow**, J. Lee, A. Kumar, P. Shakya Tuladhar, I. McCulloch, A. Bakulin, J. R. Durrant, Correlating Charge-Transfer State Lifetimes with Material Energetics in Polymer:Non-Fullerene Acceptor Organic Solar Cells, *J. Am. Chem. Soc*., 143, 20, 7599–7603 (2021)
- M. Babics, **H. Bristow**, W. Zhang, A. Wadsworth, M. Neophytou, N. Gasparini, I. McCulloch, Non-fullerene-based organic photodetectors for infrared communication, *J. Mater. Chem. C*, 9, 2375-2380 (2021)

- S. Griggs, A. Marks, **H. Bristow**, I. McCulloch, n-Type organic semiconducting polymers: stability limitations, design considerations and applications, *J. Mater. Chem. C* (2021)
- T. Carey, A. Arbab, L. Anzi, **H. Bristow**, F. Hui, S. Bohm, G. Wyatt-Moon, A. Flewitt, A. Wadsworth, N. Gasparini, J. M. Kim, M. Lanza, I. McCulloch, R. Sordan, F. Torrisi, Inkjet Printed Circuits with 2D Semiconductor Inks for High-Performance Electronics, *Adv. Electron. Mater*., 2100112 (2021)
- A. J. Clarke, J. Luke, R. Meitzner, J. Wu, Y. Wang, H. K.H. Lee, E. M. Speller, **H. Bristow**, H. Cha, M. J. Newman, K. Hooper, A. Evans, F. Gao, H. Hoppe, I. McCulloch, U. S. Schubert, T. M. Watson, J. R. Durrant, W. C. Tsoi, J.-S. Kim, Z. Li, Non-fullerene acceptor photostability and its impact on organic solar cell lifetime, *Cell Reports Physical Science*, 2, 100498 (2021)
- T. Zhang, M. Moser, A. D. Scaccabarozzi, **H. Bristow**, P. Jacoutot, A. Wadsworth, T. D. Anthopoulos, I. McCulloch, N. Gasparini, Ternary organic photodetectors based on pseudo-binaries nonfullerene-based acceptors, *J. Phys. Mater*., 4, 045001 (2021)
- A. F. Paterson, R. Li, A. Markina, L. Tsetseris, S. MacPhee, H. Faber, A.-H. Emwas, J. Panidi, **H. Bristow**, A. Wadsworthh, D. Baran, D. Andrienko, M. Heeney, I. McCulloch, T. D. Anthopoulos, N-Doping improves charge transport and morphology in the organic non-fullerene acceptor O-IDTBR, *J. Mater. Chem. C*, Just Accepted (2021)
- H. Chen, M. Moser, S. Wang, C. Jellett, K. Thorley, G. T. Harrison, X. Jiao, M. Xiao, B. Purushothaman, M. Alsufyani, **H. Bristow**, S. De Wolf, N. Gasparini, A. Wadsworth, C. R. McNeill, H. Sirringhaus, S. Fabiano, I. McCulloch, Acene Ring Size Optimization in Fused Lactam Polymers Enabling High n-Type Organic Thermoelectric Performance, *J. Am. Chem. Soc.*, 143, 260–268 (2021)
- Z. Hamid, A. Wadsworth, E. Rezasoltani, S. Holliday, M. Azzouzi, M. Neophytou, A. A. Y. Guilbert, Y. Dong, M. S. Little, S. Mukherjee, A. A. Herzing, **H. Bristow**, R. J. Kline, D. M. DeLongchamp, A. A. Bakulin, J. R. Durrant, J. Nelson, I. McCulloch, Influence of Polymer Aggregation and Liquid Immiscibility on Morphology Tuning by Varying Composition in PffBT4T-2DT/Nonfullerene Organic Solar Cells, *Adv. Energy Mater.*, 10, 201903248 (2020)
- M. Alsufyani, R. K. Hallani, S. Wang, M. Xiao, X. Ji, B. D. Paulsen, K. Xu, **H. Bristow**, H. Chen, X. Chen, H. Sirringhaus, J. Rivnay, S. Fabiano, I. McCulloch, The effect of aromatic ring size in electron deficient semiconducting polymers for n-type organic thermoelectrics, *J. Mater. Chem. C*, 8, 15150-15157 (2020)
- H. Cha, Y. Zheng, Y. Dong, H. H. Lee, J. Wu, **H. Bristow**, J. Zhang, H. K. H. Lee, W. C. Tsoi, A. A. Bakulin, I. McCulloch, J. R. Durrant, Exciton and Charge Carrier Dynamics in Highly Crystalline PTQ10:IDIC Organic Solar Cells, *Adv. Energy Mater.*, 10, 202001149 (2020)
- A. Wadsworth, H. Chen, K. J. Thorley, C. Cendra, M. Nikolka, **H. Bristow**, M. Moser, A. Salleo, T. D. Anthopoulos, H. Sirringhaus, I. McCulloch, Modification of Indacenodithiophene-Based Polymers and Its Impact on Charge Carrier Mobility in Organic Thin-Film Transistors, *J. Am. Chem. Soc*., 142, 2, 652–664 (2020)
- R. K. Hallani, M. Moser, **H. Bristow**, M. V. C. Jenart, H. Faber, M. Neophytou, E. Yarali, A. F. Paterson, T. D. Anthopoulos, I. McCulloch, A low temperature crosslinking benzocyclobutene based polymer dielectric for organic thin film transistors on plastic substrates, *J. Org. Chem*., 85, 1, 277–283 (2019)
- A. Wadsworth, **H. Bristow**, Z. Hamid, M. Babics, N. Gasparini, C. W. Boyle, W. Zhang, Y. Dong, K. J. Thorley, M. Neophytou, R. Shahid Ashraf, J. R. Durrant, D. Baran, I. McCulloch, End Group Tuning in Acceptor–Donor–Acceptor Nonfullerene Small Molecules for High Fill Factor Organic Solar Cells, *Adv. Funct. Mater.*, 1808429 (2019)